

Experimental analysis of spatial states in broad-area vertical-cavity surface-emitting lasers

Malte Arved Schulz-Ruhtenberg

2008

Experimentelle Physik

Experimental analysis of spatial states in broad-area
vertical-cavity surface-emitting lasers

Inaugural-Dissertation
zur Erlangung des Doktorgrades
der Naturwissenschaften im Fachbereich Physik
der Mathematisch-Naturwissenschaftlichen Fakultät
der Westfälischen Wilhelms-Universität Münster

vorgelegt von

Malte Arved Schulz-Ruhtenberg

aus Berlin

– 2008 –

Dekan: Prof. Dr. J. P. Wessels
Erster Gutachter: Dr. T. Ackemann
Zweiter Gutachter: Prof. Dr. W. Lange
Tag der mündlichen Prüfung: 30.06.2008
Tag der Promotion: 30.06.2008

Abstract

In this thesis, the properties of the transverse patterns emitted by oxide-confined vertical-cavity surface-emitting lasers (VCSELs) with a large aperture are studied experimentally. These include lasers with square (30 and 40 μm side length) and circular aperture (80 μm diameter). The lasers tend to emit highly divergent modes due to their large Fresnel number, which reduces the beam quality drastically. It is thus of some interest for applications to understand the processes that lead to the formation of these transverse modes. The lasers also offer the opportunity to study spontaneous pattern formation in a system which is easy to operate and available in many different designs.

Due to the symmetric shape of the active zone of the VCSELs the polarization anisotropy - which is strong for edge-emitting semiconductor lasers - is intrinsically very weak. Thus the polarization of the emission adds another degree of complexity to the pattern formation in large VCSELs. One central subject of this thesis is the analysis of the complex coupling of polarization and spatial degrees of freedom.

The transverse modes originate from the preference of tilted waves inside the laser cavity due to a detuning between the emission wavelength and the longitudinal resonance. The emission wavelength is controlled by the spectral position of the maximum of the gain curve. Since both the longitudinal resonance and the maximum gain wavelength red-shift with the device temperature, but at markedly different rates, the temperature serves as a control of this detuning. The transverse wave vector of a mode supported by the detuned laser is dependent on the absolute value detuning. This dependence is analyzed quantitatively for VCSELs for the first time in this work. A square-root dependence of the wave number on the detuning is found independently of the shape of the aperture, confirming theoretical predictions.

The experiments show that the detuning also influences the shapes of the emission patterns and the polarization distribution. Systematic measurements are presented that lead to an understanding of the underlying mechanisms. Three regions are defined with respect to the length of the transverse wave vector. In each region distinct pattern shapes and polarization distributions are found.

Modes in region I, which have very small transverse wave numbers, are characterized by irregularly modulated patterns covering the whole aperture or by localized intensity peaks. The Fourier transform is in some cases ring-shaped, in others it forms an area of emission centered around the optical axis. The polarization is found to be homogeneous. In region II the modes at threshold are dominated by four Fourier components, located at the corners of an elongated rectangle. This corresponds to wavy stripe patterns covering the whole aperture. The polarization is in tendency aligned with one of the boundaries, though small deviations from this rule are observed. With increasing transverse wave number this rectangle converges to a square with the Fourier components at the diagonals of the wave vector plane. The patterns created by these Fourier modes resembles a

diamond-shaped closed periodic orbit and are attributed to region III. In this case only a fraction of the aperture is emitting. The polarization distribution is found to be very complex.

Tilted waves travelling inside the cavity need to be confined by total internal reflection at the index step formed by the oxide confinement. If the transverse part of the wave vector of a laser mode is too large, the angle of incidence upon the side boundary of the VCSEL becomes too steep and the light wave is scattered into the material outside the laser aperture. This increases the losses of such a mode drastically. This cut-off condition is experimentally observed only in VCSELs with square geometry. It explains the shifting of the Fourier components of the emitted modes toward the diagonal for very large transverse wave numbers.

In circular lasers the emission is in general concentrated along a ring close to the laser aperture. The wavelength of the azimuthal modulation of this ring is dependent on the detuning. The effect of current crowding at the device boundary known from VCSELs with large apertures is responsible for the observed pattern shapes. For small wave numbers a homogeneous polarization distribution is found, for large wave numbers the polarization is orthogonal to the wave vector (in correspondence with region I and II of the square lasers).

The observed polarization distribution is explained with a combination of the anisotropic reflection of the Bragg mirrors forming the VCSEL cavity and the influence of the side boundary. The Bragg mirrors have a higher reflectivity for s-waves, whose polarization is orthogonal to the plane of incidence upon the mirror, due to the properties of Fresnel reflection. For small transverse wave numbers the DBR-induced anisotropy is negligible and the polarization is determined by the material anisotropy. Above a certain wave number the DBR-induced anisotropy dominates the polarization selection and the polarization is expected to be orthogonal to the transverse wave vector (“90°-rule”). For VCSELs with a circular aperture this is observed in the experiment. In the square devices the reflection of the travelling waves at the side boundaries results in a linear coupling of the polarization of different Fourier components. Thus the Fourier modes can not all represent s-waves, which results in an alignment of the polarization with the boundaries. The “90°-rule” determines to which boundary the polarization of a mode aligns. At the diagonal of the wave vector plane this results in a degeneracy of the polarization orientation, which explains the complex scenario observed for modes with very large transverse wave numbers.

The properties of the patterns described above, the length scales, the pattern shapes, and the polarization distribution can also be controlled directly when the laser is submitted to feedback. In this thesis, experiments with (spatial) frequency-selective feedback are described. By adjusting the feedback frequency the pattern length scale can be controlled. When adding Fourier filters to the feedback beam path the pattern shape can be influenced. The polarization of the patterns follows that of the feedback.

In conclusion, in this work the quantitative dependence of the pattern length scales on the detuning is analyzed and the mechanisms of pattern and polarization selection in VCSELs with square and circular geometry are clarified to a large extent.

Kurzfassung

In dieser Doktorarbeit werden die Eigenschaften von transversalen Mustern, die von oxidgeführten oberflächenemittierenden Halbleiterlasern (“Vertical-cavity surface-emitting lasers”, kurz VCSEL) mit großer Apertur emittiert werden, experimentell untersucht. Laser mit quadratischer (30 und 40 μm Seitenlänge) und runder Apertur (80 μm Durchmesser) waren für die Experimente verfügbar. Diese Laser neigen zur Emission von stark divergenten Moden aufgrund ihrer hohen Fresnelzahl, welche die Strahlqualität erheblich einschränken. Für Anwendungen ist es daher von einigem Interesse die Prozesse zu verstehen, die zur Bildung der transversalen Moden führen. Die Laser bieten außerdem die Möglichkeit, spontane Musterbildung in einem System zu untersuchen, welches vielen verschiedenen Ausführungen verfügbar und leicht zu bedienen ist.

Im Gegensatz zu Kantenemittern ist die Polarisationsanisotropie aufgrund der symmetrischen Struktur in VCSELn sehr schwach. Daher kann das Szenario der Musterbildung in VCSELn mit großer Apertur durch den Polarisationszustand zusätzlich komplexer werden. Ein zentraler Gegenstand dieser Arbeit ist dementsprechend die Analyse der Kopplung zwischen Polarisationsfreiheitsgraden und räumlichen Strukturen.

Transversale Moden werden angeregt, wenn die Verstimmung zwischen der Emissionswellenlänge und der longitudinalen Resonanz “verkippte Wellen” (“tilted waves”) innerhalb des Resonators bevorzugt. Die Emissionswellenlänge wird von der spektralen Position des Maximums der Verstärkungskurve kontrolliert. Sowohl die longitudinale Resonanz als auch die Verstärkungskurve verschieben sich zu größeren Wellenlängen wenn die Temperatur des VCSELs erhöht wird, allerdings mit deutlich unterschiedlichen Raten. Daher kann die Verstimmung durch die Temperatur kontrolliert werden, wodurch wiederum die transversale Wellenzahl einer Lasermode kontrolliert wird. Die Abhängigkeit der Wellenzahl von der Verstimmung wird in dieser Arbeit zum ersten Mal quantitativ für VCSEL untersucht. Für beide Aperturgeometrien wird eine wurzelförmige Abhängigkeit gefunden, die mit theoretischen Vorhersagen übereinstimmt.

Die Experimente zeigen, dass die Verstimmung auch die Form der Emissionsmuster und die Polarisationsverteilung beeinflusst. Systematische Messungen werden präsentiert, die zu einem Verständnis der zugrunde liegenden Mechanismen führen. Drei Bereiche werden in Bezug auf die Länge des transversalen Wellenvektors definiert. Jedem dieser Bereiche können spezifische Musterformen und Polarisationsverteilungen zugeordnet werden.

Bereich I ist durch Moden mit kleiner Wellenzahl charakterisiert. Sie werden von unregelmäßig modulierten Mustern charakterisiert, welche die ganze Apertur abdecken. Außerdem treten lokalisierte Intensitätsmaxima auf. Die Intensitätsverteilung der Fouriertransformierten ist in einigen Fällen ringförmig, in anderen konzentriert sie sich in einem kleinen Bereich um die optische Achse. Die Polarisation ist in beiden Fällen homogen. In Bereich II werden die Moden an der Schwelle von vier Fourierkomponenten dominiert, welche an den Eckpunkten eines länglichen Rechtecks liegen. Dies entspricht einem welli-

gen Streifenmuster, welches die ganze Apertur füllt. Die Polarisation ist tendenziell an den Rändern der Lasers ausgerichtet, allerdings werden geringe Abweichungen davon beobachtet. Mit steigender transversaler Wellenzahl konvergiert das Rechteck zu einem Quadrat, dessen Eckpunkte, und damit die Fourierkomponenten, auf der Diagonale der Fourierebene liegen. Die entsprechenden Muster ähneln rautenförmigen periodischen Orbits und werden Bereich III zugeordnet. Diese Muster werden nur auf einem kleinen Teil der Apertur emittiert. Eine komplexe Polarisationsverteilung wird beobachtet.

Verkippte Wellen, die innerhalb des transversalen Resonators propagieren, werden vom Brechungsindexsprung totalreflektiert, der von der Oxidbarriere erzeugt wird. Ist die transversale Komponente des Wellenvektors zu groß kann keine Totalreflexion mehr auftreten und die Welle erfährt wesentlich größere Verluste. Dies erzeugt eine Einschränkung des Existenzbereichs für transversale Moden in VCSELn mit quadratischer Apertur und ist verantwortlich für die Verschiebung der Fourierkomponenten zur Diagonalen.

In den runden Lasern ist die Emission aufgrund der inhomogenen Verteilung der Ladungsträger im Allgemeinen auf den Rand der Apertur beschränkt. Die Wellenlänge der azimuthalen Modulation dieser Ringe ist abhängig von der Verstimmung. Für kleine Wellenzahlen wird eine homogene Polarisationsverteilung beobachtet. Für größere Wellenzahlen ist die Polarisation orthogonal zum Wellenvektor orientiert.

Die beobachtete Polarisationsverteilung kann im Wesentlichen durch die anisotrope Reflexion an den Bragg-Spiegeln und den Einfluss der Laserbegrenzung erklärt werden. Aufgrund der Eigenschaften der Fresnel-Reflexion erfahren s-Wellen, die senkrecht zur Einfallsebene polarisiert sind, an den Bragg-Spiegeln eine höhere Reflexion als p-Wellen, die parallel zur Einfallsebene polarisiert sind. Für kleine transversale Wellenzahlen ist dieser Effekt vernachlässigbar und die Polarisation wird von der Materialanisotropie bestimmt. Oberhalb einer bestimmten Wellenzahl wird die Anisotropie der Bragg-Spiegel zum dominierenden Effekt und eine Orientierung der Polarisation senkrecht zum Wellenvektor wird erwartet ("90°-Regel"). Für VCSEL mit runder Apertur wird dies auch im Experiment beobachtet. In quadratischen VCSELn erzeugt die Reflexion an den Seitenrändern eine lineare Kopplung der Polarisation verschiedener Fourierkomponenten. Daher können nicht alle Fouriermoden gleichzeitig s-Wellen sein und die Polarisation richtet sich an den Seitenrändern aus, wobei die "90°-Regel" bestimmt, an welchem Rand die Polarisation sich ausrichtet. An der Diagonalen resultiert daraus eine Entartung der Polarisation, was für die komplexe Polarisationsverteilung für Moden mit sehr hoher Wellenzahl verantwortlich ist.

Die oben beschriebenen Eigenschaften der Muster – die Längenskalen, die Musterformen und die Polarisationsverteilung – können durch optische Rückkopplung auch direkt kontrolliert werden. In dieser Arbeit werden Experimente mit (räumlich-) frequenzselektiver Rückkopplung beschrieben. Durch Änderung der rückgekoppelten Wellenlänge kann die Längenskala der Muster kontrolliert werden. Werden Fourierfilter in den Strahlengang eingesetzt, können die Musterformen beeinflusst werden. Die Polarisation der Emission folgt in diesen Experimenten der Polarisation des rückgekoppelten Lichts.

Zusammengefasst werden in dieser Arbeit die quantitative Abhängigkeit der Musterlängenskalen von der Verstimmung analysiert und die Mechanismen der Muster- und Polarisationsselektion weitgehend aufgeklärt.

Contents

1	Introduction	5
2	Scope of the thesis	7
2.1	Semiconductor lasers	7
2.2	Vertical-cavity surface-emitting lasers	9
2.3	Polarization effects in small-area VCSELs	11
2.4	Pattern formation by tilted waves in Fabry-Perot cavities	12
2.5	Transverse patterns in VCSELs	14
2.6	Emission control by optical feedback	17
3	Basic properties of the VCSELs	19
3.1	The VCSELs under study	19
3.1.1	Square VCSELs	19
3.1.2	Circular VCSELs	20
3.2	Basics of the setup	21
3.2.1	Mounting and control of the VCSELs	21
3.2.2	Optical components	21
3.2.3	Detection	22
3.3	Basic experimental characteristics	23
3.3.1	L–I curves	23
3.3.2	V–I curves	25
3.3.3	Spectral measurements	28
3.4	Analysis and interpretation	29
3.4.1	AlGaAs refractive indices	29
3.4.2	Laser thresholds	30
3.4.3	Laser efficiencies	33
3.4.4	Spectral characteristics	34
3.4.4.1	Temperature-induced shift	35
3.4.4.2	Current-induced shift	36
3.4.4.3	Joule heating coefficients	37
3.4.4.4	Temperature dependence of the longitudinal resonance	39
3.4.4.5	Dependence of gain peak frequency on temperature	40
3.4.4.6	Indicators of zero detuning	41
4	Length scales and spatial structures	43
4.1	Experimental setup	43
4.1.1	Spatially resolved detection	43
4.1.2	Devices for spectral measurements	44

4.1.2.1	Plano-planar FPI	44
4.1.2.2	Confocal FPI	45
4.2	Experimental observations	45
4.2.1	Types and length scales of spatial states	45
4.2.1.1	Temperature dependence of the emission	46
4.2.1.2	Dependence on injection current	49
4.2.1.3	Temperature dependence at constant current	53
4.2.1.4	Uncommon emission patterns	54
4.2.2	Details of the billiard-type patterns	56
4.2.3	Characteristics of the emission below threshold	59
4.2.4	Temperature dependence of the Fourier mode position	62
4.2.5	Optical and spatial spectra	65
4.3	Analysis and interpretation	68
4.3.1	On-axis emission and thermal lensing	68
4.3.2	Existence region of tilted waves	73
4.3.3	Diamond patterns as quantum billiards in the semiclassical limit	76
4.3.4	Quantitative analysis of the pattern length scales	78
4.3.5	Transverse mode selection above threshold	82
4.3.6	The model describing the VCSELs	83
4.3.7	Results of the model and comparison with the experiment	84
5	Polarization of spatial states	87
5.1	Experimental setup	87
5.1.1	Spatially resolved Stokes parameters	87
5.1.2	Pulsed excitation	89
5.2	Experimental observations	90
5.2.1	Averaged Stokes parameters	90
5.2.2	Degree of circular polarization with spatial resolution	93
5.2.3	Emission with small transverse wave numbers	95
5.2.4	Patterns with intermediate wave numbers	97
5.2.5	Diamond-shaped patterns	100
5.2.6	Circular VCSELs	103
5.2.7	Characteristics of the spontaneous emission	104
5.2.8	Pulsed excitation	108
5.2.8.1	Transient behavior of the transverse patterns	109
5.2.8.2	Influence of the current on the transient behavior	111
5.2.8.3	Snapshots for zero time delay	112
5.3	Analysis and interpretation	113
5.3.1	Polarization state below threshold and transition through threshold	113
5.3.2	Pulsed excitation	116
5.3.3	Material anisotropies	118
5.3.4	Description and discussion of the improved model	119
5.3.5	Polarization selections mechanisms: square VCSELs	121
5.3.6	Polarization selections mechanisms: circular VCSELs	125
5.3.7	Extent of the three regions	126

6	Control of pattern properties with feedback	129
6.1	Experimental setup	129
6.2	Experimental observations	131
6.2.1	Scanning the Feedback frequency	131
6.2.2	Polarization measurements	134
6.2.3	Measurements with spatial-frequency-selective feedback	135
6.3	Analysis and interpretation	137
6.3.1	Control of the length scales	137
6.3.2	Control of the pattern shapes	138
6.3.3	Modal threshold with frequency-selective feedback	139
7	Conclusions	141
A	Polarization coupling for a reflection at the laser boundary	147
B	Device structures	149
C	Calculation of necessary device parameters	153
D	Electronic circuit for pulsed excitation experiments	157

1 Introduction

Vertical-cavity surface-emitting lasers (VCSELs) are a special kind of semiconductor lasers with a high potential for applications: their design uses a high-quality Fabry-Perot cavity with the optical axis orthogonal to the plane of the semiconductor layers (i.e. parallel to the epitaxial growth direction). Thus they allow a circular beam profile, which is important, e.g., for the coupling of the beam into optical fibers. Mostly due to this feature VCSELs have replaced other types of semiconductor lasers in short-range data communication networks.

Commercially available VCSELs commonly have an output power of several milliwatt only. However, for many applications higher output power is desirable. This is achieved by increasing the transverse size of the aperture of the VCSEL. Since the resonators of VCSELs are very short, typically of the order of one wavelength, increasing the transverse size over about $15\ \mu\text{m}$ results in the formation of highly divergent modes. This reduces the beam quality drastically and makes broad-area VCSELs less attractive for applications.

It is thus of some importance for applications to analyze the mechanisms involved in the formation of these transverse modes. On the other hand the emission characteristics of broad-area VCSELs also pose an opportunity to study spontaneous pattern formation¹ in a system that is readily available and easy to operate. In addition to the intensity distribution of the transverse modes the state of polarization is also worth investigating: due to the isotropy in the transverse plane the polarization of the modes is in principle degenerate, though in real devices it is weakly pinned by unavoidable inhomogeneities [1, 2].

Spontaneous pattern formation occurs in a spatially extended system with a nonlinearity and spatial coupling, e.g. diffraction or diffusion, if it is driven out of equilibrium. Beyond some threshold, typically a spatially modulated state arises from homogeneous pumping. Such a modulational instability creates a periodic pattern and can occur in many different systems. This phenomenon is well understood in most cases [3].

Spontaneous pattern formation is not restricted to optics, but can occur in many systems, e.g. gas discharges [4], chemical reactions [5], granular matter [6], or skin pigmentation [7]. Nonetheless it is especially important to study optical pattern formation since in this subject all types of patterns and all relevant phenomena reported from other fields are found together with some that are specific for optics [8]. The spectrum of experimentally observed patterns in nonlinear optical systems is very rich and includes the formation of hexagons [9], optical vortices [10], labyrinths [11], solitons [12], and many others. These effects arise from a nonlinear dependence of the material polarization on the amplitude of the light field. The consequences include frequency conversions and a

¹The term “pattern” commonly refers to periodic spatial structures. The structures studied in this work are generally periodic, though often perturbed by imperfections, thus this term is used here.

dependence of the refractive index or the absorption coefficient on the light intensity. Especially semiconductors have a high resonant nonlinearity.

Lasers play a significant role in this field because they provide the optical power needed to excite nonlinear effects in most systems. They are used as an intense coherent light source that pumps another medium (e.g. alkali metal vapor [13] or photorefractive crystals [14]) or as the subject of research themselves: pattern formation in the emission of lasers, i.e. inside the laser cavity where electro-magnetic fields of immense amplitude can occur, is reported in numerous articles [15–19]. More recent publications show that this field is still of great interest [20–23].

In this thesis the optical pattern formation in the emission of broad-area VCSELs is studied. The Maxwell-Bloch equations describing the interaction of the light field with the gain material in semiconductor lasers are nonlinear coupled partial differential equations. They predict the formation of so-called tilted waves, which are resonant in the Fabry-Perot cavity when they have a non-zero transverse wave vector [24, 25]. In VCSELs these were first seen experimentally by Hegarty et al. [18], though here no quantitative study was provided. The authors reported the observation of a superposition of several Fourier modes located on a ring in the Fourier plane centered around the optical axis, represented by a wavy stripe pattern in the transverse section of the VCSEL. The spatial patterns arise because the tilted waves travelling inside the transverse cavity undergo total internal reflection at the index step created by the oxide confinement. Thus a standing wave pattern is formed. The important question of the selection of shapes and symmetries of the spatial structures was not addressed. In addition, a coupling between spatial and polarization degrees of freedom was mentioned, but not investigated in detail.

In [26, 27] another intriguing type of spatial structure was reported in the form of a diamond-shaped closed periodic orbit, explained phenomenological as a superposition of selected Fourier modes. These phenomena allow a study of the correspondence between wave and ray optics in billiard problems due to the reflection at the side boundaries.

A quantitative explanation of the connection between these types of patterns and the transition between the different regimes was not established. Also details on the state of polarization are scarcely known, which is surprising regarding the wealth of publications on polarization effects in small-area VCSELs. As will be shown in this work, the sparse observations of earlier works are partly wrong or incomplete.

This work is organized as follows: in the next chapter an overview over semiconductor lasers and specifically VCSELs is given, followed by an explanation of the mechanism leading to the emission of tilted waves. A review of the relevant literature and a description of the aims of this thesis are also given there. In chapter 3 the VCSELs under study are described and basic properties of the lasers are considered, such as laser thresholds, series resistances, and spectral characteristics. Chapter 4 focusses on the quantitative study of the length scales of the transverse patterns and their shape. The polarization characteristics of these patterns are described in chapter 5 together with an explanation of the mechanisms leading to these characteristics. A means of direct control of the properties of the emission is demonstrated in chapter 6 in the form of (spatial) frequency-selective feedback.

2 Scope of the thesis

2.1 Semiconductor lasers

The first laser (Light Amplification by Stimulated Emission of Radiation), based on stimulated emission in ruby, was invented in 1960 [28]. This proved to be a revolution for many fields of science, especially optics, because of the groundbreaking new properties of laser light: a laser is a source of coherent, monochromatic, and highly directional and intense light. In the following years and decades many different types of lasers were developed, but the one with the greatest impact on everyday life followed already in 1962: at this time laser emission was demonstrated in a semiconductor p-n junction for the first time [29]. Nowadays semiconductor lasers are the type of lasers that are most commonly found outside scientific applications and research. They have proven to be efficient, low-cost, small, and reliable sources of laser light, that are used in optical disc players (CD, DVD, Blue-ray), in optical data communication (fast internet connections over fiber optic cables), for medical applications, and so on.

The semiconductor laser has several advantages over other light sources and lasers: it is highly efficient, power conversion efficiency values of greater than 50% are reported [30]; the structure of the standard semiconductor laser allows it to be as small as a few micrometers; this type of laser is known to be highly reliable (tests at increased temperature indicate a room temperature life time of the order of millions of hours [31]); only a small current source is necessary for the operation; and due to the boom of the microchip industry the growth and processing of semiconductor materials has become a standard technology that allows the production of hundreds of semiconductor lasers on one wafer, making them comparatively cost-effective.

For a semiconductor diode the main component is the p-n junction, which is a combination of two semiconductor materials: acceptors (atoms providing holes, i.e. missing electrons, with increased mobility) are inserted into the p-doped material, donators (atoms providing electrons with increased mobility) into the n-doped material. Note that the doped materials are still electrically neutral. The electrons are at first found in the valence band. If voltage of the correct polarity is applied they are raised into the conduction band, leaving positively charged holes behind. Both can then move freely through the semiconductor. The p-n junction is responsible for the diode function, because it serves as a conductor when voltage is applied in forward-bias direction and as an insulator for reverse-bias direction.

As stated above the first working semiconductor laser consisted of nothing more than a p-n junction. At the junction itself the free electrons and holes recombine under the emission of photons when the voltage is applied in forward-bias direction. The recombination energy is of the order of the band gap of the semiconductor material. The p-n junction then serves as active medium of the laser. Due to the diode function of the p-n junction

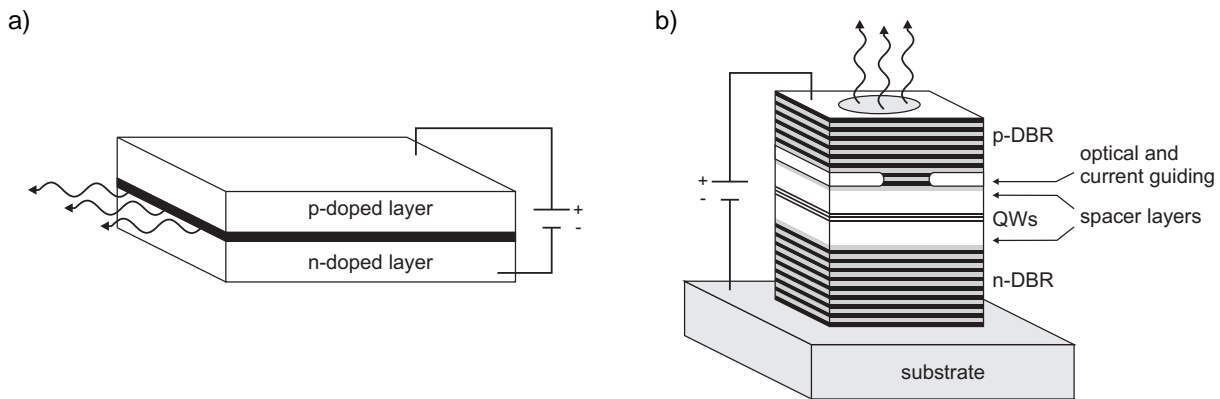


Figure 2.1: Schematic drawing of an edge-emitting semiconductor laser (a) and a vertical-cavity surface-emitting laser (b). See text for details.

semiconductor lasers are also called laser diodes.

A simple p-n junction does not form a very efficient laser. A more efficient design was found to be the double heterostructure [32]. For this type of structure two different semiconductor materials with different band gaps are combined. They form three layers on top of each other. The outer layers consist of the material with the larger band gap, the central area of the other semiconductor. The outer layers are p-, respectively n-doped, the center is undoped. This results in a so-called p-i-n structure. At the points where the materials meet energy discontinuities are formed which confine the free carriers to the central layer. Thus a two-dimensional potential well for the carriers is formed and the recombination only takes place in this layer. If the thickness of the central layer is of the order of the de Broglie wavelength of the carriers the energy states available for the carriers become discrete [33]. Such thin layers are called quantum wells. In modern semiconductor laser designs quantum wells are often used as active medium, because the reduction of the density of states results in higher quantum efficiency (conversion efficiency of carriers to photons) and lower laser thresholds¹.

A typical double heterostructure laser diode design is shown in fig. 2.1(a). The electrical voltage is applied to top and bottom of the structure. The black area in the center represents the active region. The left and right ends of the flat structure are polished and due to the index step from semiconductor to air they have a reflectivity of about 30%. Thus they serve as resonator mirrors. The wafer, on which the semiconductor materials are grown as thin layers, is cut into rectangles, typically between several hundred micrometers and some millimeters in size. Due to the thinness of the active layer the beam is elliptic and highly divergent in the vertical direction. The selection of the semiconductor materials for the active region (commonly combinations of elements from groups III and V, e.g. AlGaAs, InGaAs, GaN, GaAsP) and their relative concentration selects the emission wavelength of the diode. If the active medium consists of quantum wells the thickness of these also affects the wavelength.

The structure shown in fig. 2.1(a) is commonly referred to as an edge-emitting laser

¹The laser threshold denotes the current, where the stimulated emission surmounts the spontaneous emission, the gain exceeds the losses, and a coherent light field develops.

(EEL). Many modifications of the standard design are common, e.g. distributed feedback lasers [34], distributed Bragg reflector lasers [35], and quantum well lasers [36]. The drawback of an elliptical beam profile with high divergence in one direction motivated the invention of another laser geometry leading to the vertical-cavity surface-emitting lasers [37]. These lasers are the subject of this work and are described in more detail in the following.

2.2 Vertical-cavity surface-emitting lasers

The first surface-emitting semiconductor laser was developed in 1979 [38], though the name “vertical-cavity surface-emitting laser” (VCSEL), which is commonly used nowadays, was introduced years later. The inventors achieved continuous wave operation at room temperature in 1988 [37] and since then the VCSEL has become an important tool for research and applications, as well as an object of research itself. The optimization of the basic components gain material, cavity mirrors [39], and current and optical confinement [40] has led to great improvements in the efficiency [41] and the threshold current [42] of VCSELs, surpassing those of EELs. For applications needing high output power VCSEL arrays were developed [43, 44]. Today VCSELs replaced the EELs in optical data communication over short ranges, such as fast local area networks [45]. They are also used in laser printers, for optical sensors (e.g. in computer mice), and for spectroscopy [46].

The greatest difference to EELs is the orientation of the optical axis: orthogonal to the semiconductor layers instead of parallel. A typical VCSEL structure is shown in fig. 2.1(b). In the scheme the laser emission leaves the VCSEL at the top (bottom-emitting VCSELs are common as well). The laser structure is grown on top of a substrate that serves as one contact for the current source. The active medium is in most cases realized as a group of quantum wells. These are located at an anti-node of the optical field, which increases the gain by nearly a factor of 2. Around the active medium spacer layers are grown so that a cavity length of about one wavelength is obtained. The cavity is sandwiched between mirrors forming a plano-planar resonator. These mirrors are typically distributed Bragg reflectors (DBRs) [47], highly reflective mirrors consisting of quarter-wavelength layers with alternating refractive index. At the transition between the layers the light field is partly reflected and interference effects lead to reflectivities of more than 99.5%. The mirrors of modern VCSELs are made of semiconductor material, which allows current injection through the mirrors [48]. Graded layers with a continuous change of the material composition are inserted between the Bragg layers to decrease the electrical resistance [49]. The highly reflective DBRs are needed because in a VCSEL the light field experiences an amplification per pass of only about 1% [50], due to the thin active medium. The mirrors are doped to serve as p- and n-type semiconductors necessary for the diode function. Between the top mirror and the active zone a specially treated layer is located, serving as optical waveguide and current guide. Several types of guiding are common.

In gain-guided devices H^+ ions are implanted into one of the DBRs, except for the area of the aperture. The ion implantation results in a strong increase of the resistance, hence the current is flowing through the aperture only. This area is heated up, which

changes the refractive index in such a way that a lens is formed inside the VCSEL. This so-called thermal lensing effect results in a self-induced index guiding which forms an optical waveguide.

Another method is to build an index guide into the semiconductor structure. By changing the refractive index in selected layers, omitting the area of the aperture, an optical waveguide is formed. This can e.g. be achieved by etching away the material around the aperture, which creates a so-called etched air-post VCSEL. The index difference between the semiconductor material and the air leads to optical confinement. At the same time the current flow is confined to the area of the aperture.

Nowadays the most common method, especially for VCSELs based on aluminum gallium arsenide (AlGaAs), is index guiding by a thin laterally oxidized layer, because this design proved to yield VCSELs with the highest efficiency and lowest laser thresholds [48]. For the semiconductor layer designated as oxide confinement a high amount of aluminum is used in the composition, because the oxidation rate is proportional to the amount of aluminum. After the epitaxial growth process the side walls of the VCSEL are exposed by etching a mesa structure similar to the process of creating an air-post VCSEL. Oxidation takes place for a specific amount of time in a hot steam environment, which creates an oxide layer with a low refractive index [51]. The oxidation starts at the outer walls of the mesa, moving inward. By adjusting the oxidation time the size of the aperture, i.e. the area where the layer is not oxidized, is controlled. The oxide layer serves also as an insulator that confines the current flow to the area of the aperture. The VCSELs used in this work are all oxide-confined devices.

The structure of the VCSEL has several advantages over the design of EELs: the shape of the beam emitted by the VCSEL is defined by the confinement and thus the size and the shape can be selected during the fabrication. In contrast, EELs always have an elongated beam with a higher divergence in the vertical direction. The beam of a VCSEL with circular aperture e.g., is much easier coupled into an optical fibre, compared to the astigmatic beam of an EEL.

Another advantage of the VCSEL design is the possibility of on-wafer testing, since the exit aperture is located at the front side of the wafer, while EELs have to be cleaved and treated before testing is possible making VCSELs even more cost-effective than edge emitters. The same argument makes clear that two-dimensional VCSEL arrays can be produced in a straight-forward way. And since all components consist of semiconductor materials (at least in modern VCSEL designs) the whole laser can be produced by common semiconductor growth methods and needs much less special treatment after this production step.

The typical VCSEL structure is only several micrometers high and the cavity length is of the order of the wavelength. Due to the short cavity and the highly reflective mirrors the free spectral range of the cavity is of the order of 100 THz, while the stop-band of high reflectivity of the DBRs and the width of the gain curve is typically of the order of only 10 THz. Thus inside the range of the gain curve and the mirror reflectivity only one longitudinal cavity mode is found, i.e. VCSELs always operate on one longitudinal mode.

As long as a VCSEL operates on the fundamental spatial mode its beam quality is superior to this of EELs. However, due to the thin gain medium their output power is limited, typically to one mW for aperture sizes of a few micrometer [52]. To achieve higher output

power, which is demanded for many applications such as material treatment, free space communication, and laser pumping [43], VCSELs with a larger aperture are necessary. For example VCSELs with aperture diameters of several hundred micrometers are used for special applications, particularly in research [53–55]. Due to the short longitudinal cavity such lasers have a very high Fresnel number² and thus tend to emit highly divergent transverse modes, which reduces the beam quality drastically. In this work the emission of broad-area VCSELs (with sizes of 30, 40, and 80 μm) is studied, because these systems prove to be ideal for the study of the spontaneous formation of spatial patterns.

Another interesting attribute of VCSELs is the weak polarization determinism due to the cylindrical symmetric structure. Thus the polarization forms an additional degree of freedom which makes the pattern formation even more complex. The characteristics of the state of polarization in small VCSELs were reported in a large number of publications. The central points are described in the following section.

2.3 Polarization effects in small-area VCSELs

In contrast to EELs, where the thin active region results in a strong polarization anisotropy (i.e. one fundamental polarization state is dominant), due to the intrinsic rotational symmetry with respect to the optical axis no preference of a specific polarization orientation is expected in VCSELs. In reality most VCSELs emit a defined linear polarization state at threshold, which is due to effects like stress and strain and the resulting tendency of the electric field to align to the crystal axes of the semiconductor material [1, 2].

The sources of this polarization anisotropy are two effects: the electro-optic effect and the elasto-optic effect [2, 57, 58]. The first effect is induced by the electrical field inside the VCSEL, which induced small differences of the refractive index for orthogonally polarization modes. This index difference results in different resonance conditions and thus the orthogonally polarized modes are frequency-split. In addition, the elasto-optic effect creates a frequency splitting and a difference in the gain of the orthogonal polarization components due to (unintentional) stress or strain (e.g. from the fabrication process). The effective difference of the frequencies of the orthogonally polarized modes is called birefringence.

Due to the birefringence and the frequency-dependence of the gain and the losses orthogonally polarized modes experience different net gain (all gain sources minus all loss sources) [1]. These effects are summarized in a quantity called dichroism. It is obtained from the linewidth difference between the spectral lines of the two orthogonally polarized modes [59]. In the presence of dichroism generally one of the two modes is excited at threshold, while the other is suppressed to the level of amplified spontaneous emission [60–62]. In this case effects like polarization switching [59] and bistability [63] were reported.

²The Fresnel number of a Fabry-Perot cavity is defined as the dimensionless number calculated from the quotient of the square of the aperture radius and the product of the mirror distance and the wavelength. It quantifies the potential of a resonator to support transverse modes. See [56] for further information.

However, due to the weakness of the polarization anisotropies a diversity of polarization dynamics are observed in VCSELs above threshold. In the last ten years numerous studies of polarization dynamics were published, mostly on small-area VCSELs up to a diameter of 15 μm . Polarization switching between the two polarization states [59, 64–68] and regions of hysteresis and bistability [63, 69] are found in the fundamental TEM_{00} or higher order Gaussian modes when varying the injection current. The temporal dynamics were studied with and without external feedback [61, 62, 70–73]. Feedback was also used to control the polarization state [74].

For broad-area VCSELs only individual phenomena of the polarization selection were studied (e.g. [75]) and a comprehensive picture is missing. Hence, in this work the polarization state of the highly divergent modes emitted by broad-area VCSELs is investigated. For this the polarization is characterized by spatially-resolved Stokes parameters. These parameters provide a complete description of the polarization, including the degree of linear and circular polarization and the orientation of the polarization ellipse. The spatially-resolved measurement of the polarization is a technique known in medical optics [76], astronomy [77], or the tomography of stress [78]. To the knowledge of the author the experiments described in this work are the first to apply spatially-resolved Stokes parameters to the study of the emission of lasers.

2.4 Pattern formation by tilted waves in Fabry-Perot cavities

In the introduction a short overview over the mechanisms leading to optical pattern formation is given. Here this is explicitly discussed for patterns forming in plano-planar Fabry-Perot cavities, since a VCSEL cavity is of this type.

A model capable of describing the interaction of the light field with the active medium in a laser cavity are the Maxwell-Bloch equations [79]. They are a combination of the Maxwell equations for the electro-magnetic field and the Bloch equation for the material polarization. The Maxwell-Bloch equations were used to predict pattern formation on the basis of so-called tilted waves [80]. Theoretical works were done on several different systems, e.g. in plano-planar Fabry-Perot cavities [24, 81], two-level lasers [25, 82], optical parametric oscillators [83], and ring cavities [84].

Tilted waves are travelling or standing waves in a resonator that have a non-zero transverse component of the wave vector, thus they are not aligned with the optical axis but tilted at some angle with respect to that axis. Generally the transverse components of the wave vector are much smaller than the longitudinal part, i.e. the one aligned with the optical axis. Interference between several of these tilted waves leads to the formation of a spatially modulated structure, called a pattern in the following. In the following the mechanisms leading to the formation of tilted waves in a Fabry-Perot cavity are explained by means of a simple geometrical example.

The distance L between two mirrors forming a Fabry-Perot cavity defines a maximal longitudinally resonant wavelength λ_c with the wave number $k_c = 2\pi/\lambda_c$. Light waves with a wave number $k = m \times 2\pi/\lambda_c$ (where m is a nonzero integer) experience constructive interference inside the cavity. In the following the description is limited to light waves

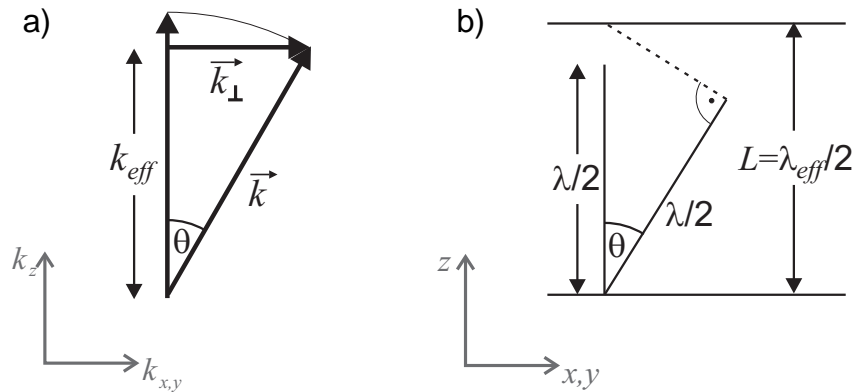


Figure 2.2: Illustration of the resonance condition for tilted waves. (a) Wave vector of the emission \vec{k} , emitted under tilt angle θ , is longer than the longitudinal resonance of the cavity. Nonetheless the projection onto the optical axis, k_{eff} is equal to the resonance. \vec{k}_\perp is the transverse wave vector. (b) The emission wavelength λ is shorter than the longitudinal resonance wavelength λ_c . λ_{eff} , the wavelength corresponding to the resonant wave number k_{eff} , is equal to λ_c . The respective coordinate systems are shown on the lower left of each subfigure.

with a wavelength of the order of λ_c (i.e. $m = 1$) for simplicity. Consider a light wave with the wave number $k > k_c$ and the wavelength $\lambda < \lambda_c$ that is not resonant inside the Fabry-Perot cavity. In other words this wave is detuned with respect to the cavity resonance by the wavelength difference $\delta = \lambda - \lambda_c < 0$, called detuning in the following. Such a wave has to be tilted with respect to the optical axis to restore the resonance condition.

This case is illustrated in fig. 2.2. In (a) the wave vector of the light wave \vec{k} is tilted at an angle θ . The transverse component is k_\perp . k_{eff} indicates the length of the projection of \vec{k} onto the optical axis. When resonance is restored $k_{eff} = k_c$ is obtained. In (b) the same is illustrated in real space. $L = \lambda_c/2$ is the longitudinal resonance, λ the wavelength of the light wave. For the tilted wave the resonance condition is restored because $\lambda_{eff} = \lambda_c$ is the wavelength that has the same phase as the tilted wave at the planes of the cavity mirrors (indicated by the dashed line). In effect, the light wave that is blue-shifted with respect to the longitudinal resonance is again resonant in the cavity when it is tilted at a certain angle θ .

This argument is true for waves injected into the cavity and for those excited inside the cavity, i.e. for lasers. For the latter the detuning is created by a wavelength mismatch between the longitudinal resonance and the maximum of the gain curve. Note that the argument above is only true if the tilted wave is blue-shifted, i.e. the detuning δ is negative. If it is positive the resonance condition can not be established at all.

The tilted wave argument seems to be rather simple, but is quite difficult to demonstrate it experimentally since a large plano-planar cavity is necessary for this. However, such a cavity has only marginally stable modes [56] and thus this situation is difficult to realize. Despite these experimental difficulties the tilted wave mechanism was shown to be responsible for pattern formation in photorefractive oscillators, in which intra-cavity lenses were used to stabilize the transverse modes [85]. The first study on tilted waves in lasers, in particular in VCSELs, was published in 1999 [18]. VCSELs are ideally suited

for this type of studies due to the large aperture and the high-quality planar cavity. Nonetheless, these were only qualitative studies that did not establish the dependence of the tilt angle θ , respectively the transverse component k_{\perp} of the wave vector, on the detuning δ .

A quantitative study of the dependence of the length scales of the transverse patterns, represented by the transverse wave number k_{\perp} , on the detuning is given in [86] and [87] for different realizations of photorefractive oscillators, but in both cases intra-cavity lenses were used to stabilize the transverse modes. In the publications a linear proportionality is found between the square of the transverse wave number and the detuning.

2.5 Transverse patterns in VCSELs

As described above the cavity of a VCSEL is very short and thus large apertures result in very large Fresnel numbers, which in turn leads to the formation of highly divergent transverse modes. In addition, VCSELs have a highly planar resonator. In principle, in this regime the tilted wave argument introduced in the previous section can be studied quite easily.

However, early works were devoted to small to medium sized VCSELs (up to radii of about $15\ \mu\text{m}$), which emit a spectrum of Gauss-Hermite and Gauss-Laguerre modes, both types appearing simultaneously in one laser [88]. In those medium sized VCSELs thermal effects lead to the formation of a thermal lens (see section 2.2) which stabilizes the plano-planar VCSEL cavity. High order non-Gaussian modes were described to appear in VCSELs larger than $10\ \mu\text{m}$ in [89], in the form of so-called whispering gallery modes, azimuthally modulated rings along the circular boundary of the VCSEL. Similar modes were observed in ring lasers [90]. In that publication the temperature was used to change the emission wavelength of the laser and thereby tune the length scales of the patterns: decreasing the temperature resulted in modes with larger transverse wave numbers (i.e. larger divergence angles). Other influences on the transverse patterns, like the pump profile and thermal properties [91], were also reported for medium sized circular VCSELs.

The mechanism of thermal tuning of the laser wavelength is a key component for investigating the tilted wave mechanism. It was described in [47] that the emission wavelength changes with temperature due to the temperature-dependent band gap. A lowering of the band gap with temperature results in a red-shift of the gain curve and thus the emission wavelength. A second effect is the temperature-dependence of the refractive index that results in a red-shift of the longitudinal resonance with temperature. The latter shift is considerably smaller than the gain shift. The result of this is that the emission wavelength λ is detuned with respect to the longitudinal cavity resonance λ_c . The detuning $\delta = \lambda - \lambda_c$ is thus found to be temperature dependent.

A major publication regarding the formation of high-order non-Gaussian patterns in broad-area square VCSELs (between $15\ \mu\text{m}$ and $40\ \mu\text{m}$ side length) is found in [18, 92]. The authors find irregular stripe patterns in the images of the laser aperture (corresponding to the coordinate space, the so-called near-field) at threshold for negative detuning δ . These modes correspond to a Fourier transform (corresponding to the wave num-

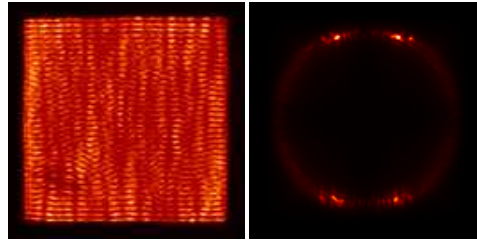


Figure 2.3: Example of the emission of square broad-area VCSELs for nonzero negative detuning δ . On the left the near-field image and on the right the far-field image is shown. Similar patterns were reported in [18, 26, 92].

ber space, the so-called far-field) presenting four pronounced Fourier components with large transverse wave numbers (i.e. the mode is highly divergent) located close to one of the axes spanning the transverse wave vector plane (with the optical axis at the zero). An example of such a transverse state is shown in fig. 2.3, obtained from the VCSELs studied in this thesis. The detuning is reported to be dependent on temperature due to a temperature-dependent refractive index that modifies the resonance of the VCSEL cavity. A dependence of the pattern length scales (i.e. the transverse wavelength of the near-field pattern, respectively the length of the transverse wave vectors in the far-field pattern) on the detuning is found: for an increasing absolute value of the detuning the length scales also increase. However, this dependence was only described phenomenological: a quantitative analysis was not reported.

The observations in [18, 92] are interpreted by the tilted wave mechanism: each of the four Fourier components found in the far-field pattern at threshold for negative detuning δ corresponds to the wave vector of a wave travelling inside the cavity. A standing wave pattern is formed due to total internal reflection at the index step created by the oxide confinement. The travelling wave pattern has only one frequency and is found to be a coherent Fourier mode, which is expected for tilted waves.

The authors also report that at threshold the polarization of the mode is orthogonal to the four dominant Fourier components. For injection currents above threshold the polarization becomes unstable and the orthogonal fundamental polarization is excited in addition. The corresponding transverse pattern is also oriented orthogonal to the first. The statement that the polarization is orthogonal to the transverse wave vector of the excited modes will be referred to as “90°-rule” in chapter 5.

The length scales of transverse patterns in circular lasers were studied in [93]. The authors describe the emission of flower-like modes with a geometry similar to high order Gauss-Laguerre modes and modes with Cartesian symmetry. A first quantitative study of the detuning dependence of the transverse length scales in VCSELs was given in [94], but for a VCSEL with external injection. Thus the tilted waves were externally driven and not self-excited.

For positive detuning δ the models based on the Maxwell-Bloch equations predict a homogenous solution [24, 80]. This was not found in the emission of the VCSELs. Rather a complex low divergence pattern composed of several wavelength in the optical spectra is reported [92, 93]. A detailed explanation of this is not known.

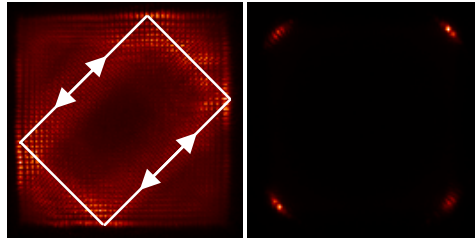


Figure 2.4: Example of the emission of a square broad-area VCSEL for large negative detuning δ . On the left the near-field image and on the right the far-field image is shown. Such patterns are reported in [26, 27] and interpreted as scars of the trajectory of closed periodic orbits in the limit between wave and ray optics.

The types of transverse patterns with large divergence angles emitted by square broad-area VCSELs was further investigated in [26, 27]. The authors found patterns similar to those described above and a new type of pattern for considerably lower temperatures. While for the first type the emission covers the whole aperture, the new type features a regular diamond shape that is reduced to parts of the aperture. In the corners and the center of the aperture the near-field image remains on the level of spontaneous emission. The pattern was reported to be linearly polarized. An example of such a pattern as emitted from lasers studied in this thesis is shown in fig. 2.4. The authors of [26, 27] interpret these states as closed periodic orbits of the transverse part of the travelling waves at the limit between wave and ray optics. The waves travel in the two-dimensional potential well formed by the transverse VCSEL cavity due to total internal reflection at the oxide confinement. The standing wave pattern is created by the interference of waves travelling in opposite direction. In the figure the corresponding classical ray trajectory is indicated by the white arrows. In analogy to quantum mechanical particles in potential wells these states are called quantum billiards. In a later publication the same authors also reported the formation of vector vortex lattices in the polarization distribution of quantum billiards [95]. The physical mechanisms leading to these complex structures remained unclear.

The complexity of the pattern formation observed in the emission of thermally-detuned broad-area VCSELs was numerically simulated using the Maxwell-Bloch equations and details of the device structure [96]. To include polarization effects the spin-flip model [97], an expansion of the Maxwell-Bloch models, was used, e.g. in [98]. It was demonstrated that a crucial component needed for the explanation of the experimental observations is the anisotropic reflection of the DBRs for tilted waves. These show different reflectivities for transverse electric (TE) and transverse magnetic (TM) waves due to the properties of Fresnel reflection. For a TE-wave, also called s-wave, the electrical component of the field, ergo the polarization, is orthogonal to the plane of incidence (formed by the incident and the reflected wave vector of the light). For a TM-wave, also called p-wave, the polarization is parallel to the plane of incidence. For Fresnel reflection the reflectivity is higher for an s-wave than for a p-wave. This was also treated as a qualitative explanation of the polarization state reported in [18, 92].

Since the models describing the emission of broad-area VCSELs are quite complex numerical simulations of the patterns observed in the experiment are sparse. Application

of the models to numerical simulations of close to real broad-area VCSEL structures can be found in [98, 99] for square and [100] for circular aperture geometry. The complexity of the experimental observations is not fully met in these publications.

The publications on transverse patterns in VCSELs reported several scenarios for very specific parameters without fully revealing the underlying mechanisms. The aim of this thesis is to systematically investigate these phenomena over a broad range of parameters and explain the connection between three seemingly incoherent scenarios: 1. the polarization selection and dynamics in the Gaussian beam known from small-area VCSELs; 2. the non-Gaussian high divergence modes represented by the wavy stripe patterns and the coupling between their spatial and polarization orientation; 3. the diamond-shaped quantum billiard modes occurring for very low temperatures. The connection between the types of patterns, their length scale, the laser temperature, and the detuning δ is investigated quantitatively. In this way the correspondence between the optical wavelength of the transverse modes and the wave numbers of the corresponding Fourier components is established. The mechanisms leading to the coupling between spatial and polarization degrees of freedom are clarified.

2.6 Emission control by optical feedback

One important aim of the research on transverse modes in the emission of VCSELs is the control of these modes by different means, usually to achieve the emission of TEM_{00} [101] which is desirable for applications, e.g. for easier coupling into optical fibers. Another aim can be the creation of arbitrary pattern shapes on demand. Publications like [102] demonstrate that this field is still very important for fundamental research as well as applications. In addition to the pattern shape, the control of the polarization state is also of interest [103].

Several different methods of transverse mode control are known, including the injection of the laser beam of a second laser into the VCSEL [94], modifications of the VCSEL structure (e.g. by etching gratings [103, 104] or photonic crystals [102, 105] into the top semiconductor layer), or optical feedback from an external cavity, which is explained in more detail below. In recent years the combination of optical feedback and external injection was reported to allow the formation of small localized spots, so-called cavity solitons, in the emission of broad-area VCSELs [55, 106–111].

Optical feedback is probably the most versatile method since it allows many different realizations. In general, with this method a part of the optical output is reflected back into the laser, in the simplest case by a plane mirror. The front mirror of the laser and the feedback mirror form an external cavity. The beam incident on the laser has the same characteristics as the beam leaving the laser, except for the propagation distance and the resulting delay. An increase of the efficiency and a decrease of the threshold current of VCSELs under the influence of feedback was reported [112]. The non-zero round-trip time of the light in the feedback beam path leads to dynamics that were studied in EELs and VCSELs [113–115]. In other feedback configurations the beam incident on the laser is filtered by optical components like polarizers, Fourier filters, or spectral filters. For example, it is possible to favor certain length scales or shapes of transverse patterns by

adding spatial Fourier filters to the feedback beam path (e.g [116] for EELs). Only a small number of publications are known that cover the effect of feedback on the transverse mode structure of VCSELs [117, 118]. These studies are restricted to low-order Gaussian modes.

When a reflective grating is used instead of a mirror the feedback becomes frequency-selective, if the first reflected order is directed back into the VCSEL. Since the grating divides the incident beam into its spectral components only a narrow band of frequencies is reflected back into the VCSEL, favoring these frequencies in the cavity. By changing the angle of incidence of the VCSEL output beam on the grating the feedback frequency can be changed.

Two common configurations are used to realize frequency-selective feedback: the Littmann configuration [119] consists of the grating and an additional mirror. The beam coming from the VCSEL is reflected by the grating onto the mirror and back to the grating. The double-pass increases the frequency-resolution of the feedback. When tilting the grating to change the feedback frequency the mirror has to be adjusted too, which is a drawback of this setup. The second setup is called Littrow configuration [120]. Here the first order of the beam reflected from the grating is directed back into the VCSEL. These feedback configuration are commonly used to tune EELs over a wide wavelength range [121–123], e.g. for spectroscopical applications [124]. Tunable semiconductor lasers with high output power using one of these configurations are commercially available nowadays.

In this thesis frequency-selective feedback in Littrow configuration is used to demonstrate direct control over the transverse pattern length scales. With spatial-frequency-selective feedback, i.e. the combination of a Fourier filter and a mirror to close the external cavity, the selection of several pattern shapes is demonstrated. In addition, the control of the state of the polarization is shown.

3 Basic properties of the VCSELs

In this chapter the VCSELs studied in this thesis and their basic properties are described and analyzed. These properties include L–I and V–I curves, series resistance, conversion efficiency, temperature dependence of thresholds, and spectral characteristics. These considerations provide important basic principles and parameters for the discussions in the later chapters.

3.1 The VCSELs under study

Several different VCSELs were studied in this thesis. They are all oxide-confined devices, in which the oxide layer serves both as current guide and optical waveguide. Two basic shapes of the oxide aperture were investigated: square and circular. Most experiments were done with the square devices with side lengths of 30 and 40 μm , respectively. For comparison, circular lasers with 80 diameter were studied as well. Schematics can be found in fig. 3.1. The VCSELs are consecutively numbered in the format (size)–(number) (e.g. 30–1 for the first 30 μm device).

More than ten square VCSELs were investigated and it was found that though often the details are different for different devices the general characteristics are the same. Hence it is not necessary to describe the emission characteristics for each device individually. Rather there are a number of features, which are typical for most devices with similar design. Thus, in most descriptions of experimental observations throughout this work only an exemplary selection is shown. Some emphasis will be put on laser 40–5, since it shows the broadest scope of effects in a comprehensive way.

3.1.1 Square VCSELs

The research focussed on the square devices that were already described in several publications by the Taiwanese group of K.F. Huang (e.g. [26, 95, 125]), who provided these VCSELs for our studies. Four lasers with an aperture side length of 30 μm and eight with 40 μm were studied. A schematic of the VCSEL structure is shown in fig. 3.1(a), a chart listing the parameters of the structure is given in appendix B. These VCSELs are top-emitting VCSELs with an emission wavelength around 780 nm. The design was nominally the same for all lasers: The active region consists of three 8 nm thick $\text{Al}_{0.11}\text{Ga}_{0.89}\text{As}$ ¹ quantum wells alternated with 7 nm thick $\text{Al}_{0.36}\text{Ga}_{0.64}\text{As}$ barrier layers. These are sandwiched between two distributed Bragg reflectors (DBRs). The bottom mirror consists of 47 double layers, the top mirror of 31 double layers, both with an alternating composition

¹All layers of the square and most of the circular VCSELs consist of the semiconductor material $\text{Al}_x\text{Ga}_{1-x}\text{As}$, where x is the fraction of aluminum.

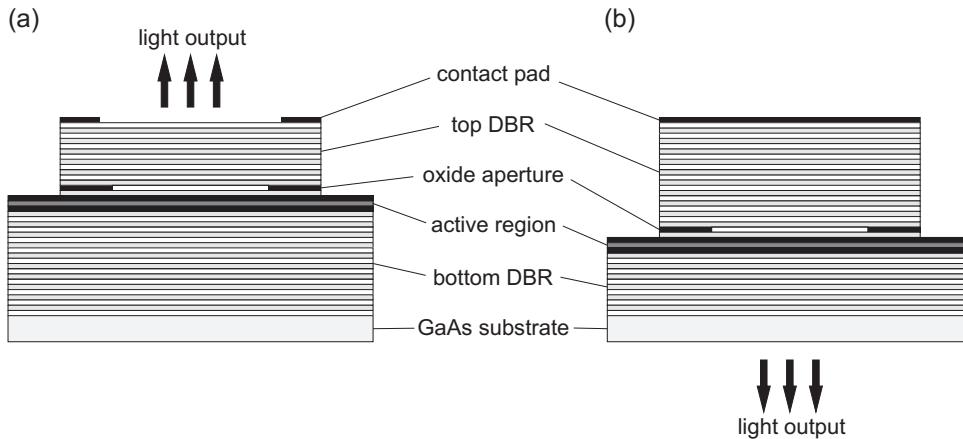


Figure 3.1: Schematic cross-section of the square top-emitting VCSELs (a) and the circular bottom-emitting VCSELs (b).

($\text{Al}_{0.3}\text{Ga}_{0.7}\text{As}$ and $\text{Al}_{0.9}\text{Ga}_{0.1}\text{As}$). This results in a reflectivity of 99.99% for the bottom mirror and 99.6% for the top mirror at 783 nm (see appendix C for details on the calculation). In order to reduce the electrical resistance of the lasers the interfaces between different semiconductor layers are graded using layers with a smooth change of the Al fraction [126]. A part of the third double layer of the top mirror is laterally oxidized to create the essential oxide confinement. For this a sub-layer with a 97% Al fraction of 30 nm thickness is inserted, which enables a very high oxidation rate. Hence this layer defines the aperture size of the VCSEL [48].

Together with a 15 nm GaAs layer at the top and a 500 nm GaAs substrate at the bottom the whole structure is about 10 μm long. The structure is topped by a metal contact pad with a square cut-out. The substrate serves as the other contact. Originally the VCSELs were packaged in TO-type housings. To avoid any influence of the glass window of the housing on the emission (e.g. by feedback or filtering) the caps were removed.

Note that the 40 μm VCSELs can be separated into two groups: one batch, consisting of lasers 40–1 through 40–4, was produced earlier than the other, lasers 40–5 through 40–9. Though the design parameters and the structure are nominally equal, some small differences between the two groups were found in the emission characteristics during the experiments for this thesis.

3.1.2 Circular VCSELs

The circular VCSELs were provided by ULM-Photonics. Three devices with a diameter of 80 μm were studied. These are bottom-emitting VCSELs that have an intrinsically higher uniformity of current and carrier distribution [43, 94, 127] than top-emitters of the same size, hence larger sizes with acceptable uniformity are possible. A schematic is shown in fig. 3.1(b). The details of the structure are given in appendix B. The emission passes through a GaAs substrate that serves as one contact. A metal contact fully covers the top of the laser. The active region of the lasers consists of three 8 nm $\text{In}_{0.2}\text{Ga}_{0.8}\text{As}$ quantum wells, separated by 9 nm barrier layers. The emission wavelength is around 980 nm. The active zone is put between two 48.5 nm GaAs spacer layers and separated

from the bottom DBR by another 150 nm $\text{Al}_{0.5}\text{Ga}_{0.5}\text{As}$ layer. The 30 nm $\text{Al}_{0.99}\text{Ga}_{0.01}\text{As}$ oxide layer with two 135 nm $\text{Al}_{0.5}\text{Ga}_{0.5}\text{As}$ spacer layers is placed between active zone and top DBR.

The mirrors consist of double-layers of 70 nm GaAs and 83 nm AlAs. The bottom mirror has 22 such layers (n-side), the top mirror 33.5 (p-side). This results in a reflectivity of 99.59% for the bottom mirror and 99.99% for the top mirror. The whole structure is approximately 9 μm long. The GaAs substrate below the bottom mirror is 208 μm thick, the output facet is anti-reflection coated. For these lasers the TO housing cap was also removed. Fig. 3.1(b) shows a schematic view of the lasers.

3.2 Basics of the setup

3.2.1 Mounting and control of the VCSELs

Temperature and current are the two basic control parameters that influence the emission characteristics of a semiconductor laser (e.g. [128, 129]). Current control is easily achieved with a low-noise dc current source. Here a LDC 201 ULN laser diode controller from Profile is used. It provides a setting accuracy of ± 0.05 mA and fluctuations of less than 5 μA . Temperature control is a bit more involved, especially when temperatures below 0 $^{\circ}\text{C}$ are desired. To ascertain that the temperature of a laser is set to the designated value the device under study is clamped between two copper plates, which sit on a Peltier electric cooling element. This Peltier element is controlled by a feedback circuit consisting of a PID controller and a thermistor as sensor. Details on the temperature controller can be found in [130]. The thermistor is inserted into a hole drilled into the front copper plate as close as possible to the VCSEL. Heat-conductive paste is used to increase thermal conductance between all parts of the mount, the sensor, and the laser. The actual temperature is measured with an accuracy of 0.1 $^{\circ}\text{C}$ by a thermo couple that is placed in a second hole in the front copper plate. The maximal temperature fluctuations over time for a fixed set-point are 0.04 K, measured with the monitor signal of the PID controller.

To avoid condensation at temperatures below 5 $^{\circ}\text{C}$ the mounted laser is put into an airtight box together with silica gel bags. The Peltier element has a cooling capacity of about ± 40 K only, because the brass wall of the box is used as a heat spreader, instead of a more efficient heat sink with milled ribs. To reach temperatures below -20 $^{\circ}\text{C}$ an additional water-cooling system is used: water at a temperature of about 5 $^{\circ}\text{C}$ is circulating through a large heat-sink, that is attached to the outside of the airtight box, cooling the brass walls of the box. Thus the hot side of the Peltier element is cooled down, allowing an overall improvement of the cooling capacity. The possible temperature range is from 45 $^{\circ}\text{C}$ (with the water-cooling switched off) to -35 $^{\circ}\text{C}$ (with activated water-cooling).

3.2.2 Optical components

Since the emission of the VCSELs under study can be highly divergent (half cone divergence angles of up to 32 $^{\circ}$ were observed) a collimating lens with a high numerical aperture (NA) is needed. For early experiments an aspheric lens with an NA of 0.68

was used. This was found to create aberrations for the highly divergent beams. The lens was replaced by a microscope objective (Nikon CFI LU Plan EPI ELWD) with an NA of 0.8 and anti-reflection coating for the visible spectrum. Such an objective with a comparatively long working distance is preferable because the output facet of the VCSEL is several millimeters below the front plate of the laser mount. The microscope objective is put into the airtight box directly in front of the mounted VCSEL. The collimated beam then leaves the box through a window and passes through polarizing elements: a half-wave zero-order retardation plate from CVI and a linear polarizer (Glan-Thompson prism, measured extinction 18000:1) from EKSMA. The polarizer is set to horizontal transmission, which defines the reference axis for all polarization sensitive measurements. Since the polarization is a central parameter studied in this work it is imperative that it is not modified by the optical elements in the beam path (apart from the linear polarizer). Most optical elements, such as mirrors and beam splitters, do modify the polarization. Hence the linear polarizer has to be set as close to the VCSEL as possible. For this reason the two polarizing elements are placed behind the collimating lens, directly outside the airtight box (it was checked that the box window does not influence the polarization). The half-wave plate is used to select the polarization component to be transmitted through the linear polarizer. The influence of the polarization sensitivity of the remaining optical elements is thus eliminated.

3.2.3 Detection

In order to automate most of the experiments a largely computer-controlled measuring station was set up. For the first set of experiments the total output power of the lasers is measured with a low-bandwidth photo detector with a built-in amplifier. The signal of the detector is digitized by an analog-digital converter (ADC, National Instruments Lab-PC 1200) with 12-bit resolution. For quick visualization a digital oscilloscope (LeCroy Wavepro 960) is used that can be computer-controlled via a GPIB-link. To calibrate the photo diode signal to power levels a simple hand-held power meter and a Thorlabs power meter are used. The ADC is also used to measure the voltage drop across the VCSEL. The input impedance of the device is given as $100\text{ G}\Omega$, i.e. it does not influence the measurements.

For optical spectra a SpectraPro-500 0.5 m grating monochromator (Acton Research Corporation) is used, which is operated in a spectrometer-like setup by placing a charge-coupled device (CCD) camera after the exit slit. Thus a spectral range of 3 nm can be detected with one measurement. The maximum nominal resolution of the device is 0.05 nm (which corresponds to 25 GHz at 780 nm). Linewidth measurements from typical spectra yield a resolution of down to 0.06 nm. The laser light is coupled into the spectrometer via a multi-mode fibre. Beams with different divergence angles experience different coupling efficiencies at the entry facet of the fibre. This strongly affects the relative height of spectral lines. Also the adjustment of the beam at the fibre entry facet and even a bending of the fibre influences the relative height of the lines. Hence the relative intensity of the spectral lines is unreliable and is thus disregarded in the analysis of the data.

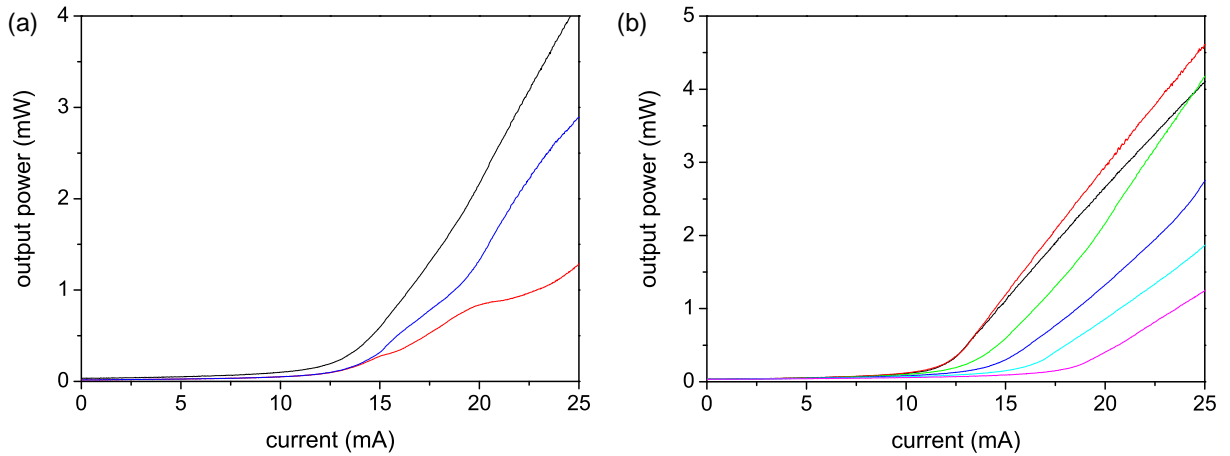


Figure 3.2: L–I curves of device 40–5. (a) Heat sink temperature $10\text{ }^{\circ}\text{C}$. The overall output power (black curve) is obtained by adding the horizontally (red) and vertically (blue) polarized components. (b) Temperature dependence of the L–I curves of laser 40–5. $T = 42\text{ }^{\circ}\text{C}$ (black), $25\text{ }^{\circ}\text{C}$ (red), $10\text{ }^{\circ}\text{C}$ (green), $0\text{ }^{\circ}\text{C}$ (blue), $-10\text{ }^{\circ}\text{C}$ (cyan), and $-20\text{ }^{\circ}\text{C}$ (magenta).

3.3 Basic experimental characteristics

3.3.1 L–I curves

The L–I (light-current) curve is an important characteristic for semiconductor lasers, since it contains a lot of information. Firstly it yields the output power of the device at a certain input current, which directly leads to the efficiency of the laser. Secondly, the threshold current can be determined. The temperature dependence of the L–I curve provides an insight into the performance of a laser diode at a certain operation temperature, which is of great importance for applications.

Fig. 3.2 shows the experimental L–I curves of device 40–5. Nearly all VCSELs under study show similar curves. The only exception is described below. Subfigure (a) shows the measured horizontally and vertically polarized components (red and blue curves) for a heat sink temperature $T = 10\text{ }^{\circ}\text{C}$. Note that though there is noticeable change of the distribution of power into the two polarization directions, this change is always very smooth. The sum of the two curves yields the total output power (black curve). All L–I curves discussed here were created by summing up the horizontally and vertically polarized components. A direct measurement of the total output power is impractical, because a separate setup would be needed for that (cf. section 3.2.2). It was checked though that an L–I curve taken directly after the collimating lens without polarizing elements yields the same results.

Fig. 3.2(b) shows L–I curves for various temperatures of device 40–5. The L–I curves can be separated into two parts: for low currents the output power is very low and rises only slowly. This indicates spontaneous emission. The second part has a much larger slope and output powers are much higher. The kink between the two parts indicates the onset of lasing emission. For semiconductors the amount of spontaneous emission is typically rather high and the kink at laser threshold is less pronounced than for other types of lasers [56]. It is obvious that the laser threshold increases with decreasing temperature.

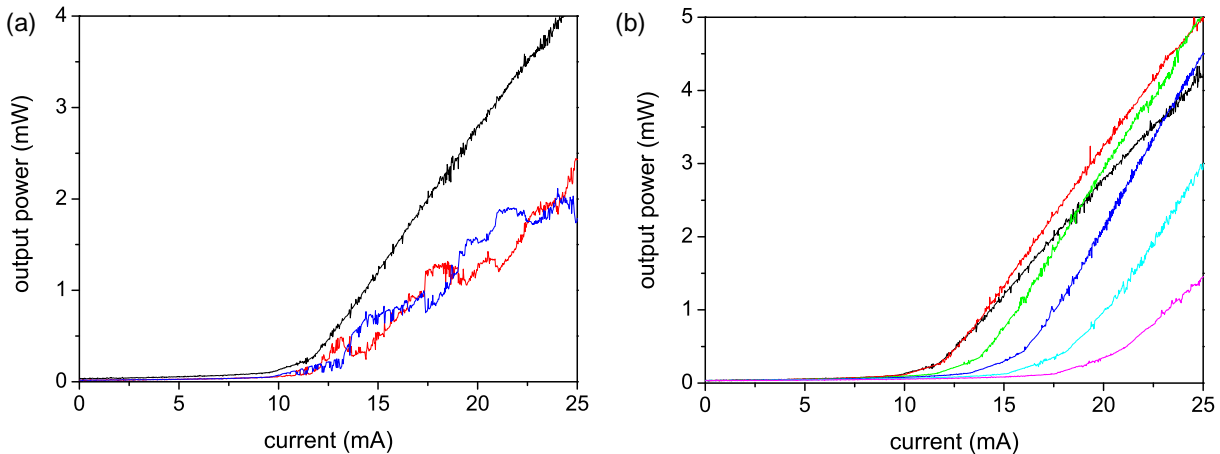


Figure 3.3: L-I curves of device 40-1. (a) Heat sink temperature 42°C. The overall output power (black curve) is obtained by adding the horizontally (red) and vertically (blue) polarized components. (b) Temperature dependence of the L-I curves of laser 40-1. $T = 42^\circ\text{C}$ (black), 25°C (red), 10°C (green), 0°C (blue), -10°C (cyan), and -20°C (magenta).

This will be addressed in detail in section 3.4.2. The red curve with $T = 25^\circ\text{C}$ has the highest output power for high currents, but not the lowest threshold, i.e. this curve has the largest slope. For higher (black curve with $T = 42^\circ\text{C}$) and lower (green curve with $T = 10^\circ\text{C}$) temperatures, the output power decreases. Note that thermal rollover does not occur in the investigated current range.

Fig. 3.3 shows the same plots for device 40-1. This laser exhibits much less regular L-I curves for the two polarization directions, as shown in subfigure (a). Here noise and abrupt changes in the distribution of power are visible. The details of the abrupt changes are strongly influenced by minute variations of injection current and laser temperature. Since the L-I curves of the two polarizations are measured one after the other minimal parameter changes are unavoidable. This affects the smoothness of the overall output power curve which is obtained by adding the two polarization resolved curves. A directly measured L-I curve of the overall power was checked to be as smooth as the curves of device 40-5. Fig. 3.3(b) shows the L-I curves of device 40-1 for the same heat sink temperatures as in fig. 3.2(b). It is obvious that these are much noisier than the L-I curves of device 40-5 for the reason discussed above. No other laser shows such pronounced jumps, but rather smooth curves for both polarizations similar to device 40-5.

In conclusion the overall power of laser 40-1 shows the same characteristics as other devices. Only when looking at the polarization-resolved measurements the difference between the devices becomes visible.

Another feature observed only in the emission of laser 40-1 is shown in fig. 3.4. Sub-figures (a) and (b) show the horizontally, respectively the vertically polarized part. The black curves were taken during an up-scan of the current, i.e. the current was changed from 0 to 25 mA. The red curves however are obtained from a down-scan, i.e. the current is decreased from 25 to 0 mA. Between 17 and 20 mA the black and red curves show different progressions. Here the laser exhibits bistability, i.e. there are two possible emission states for the current range between 17 and 20 mA. When increasing the current (black

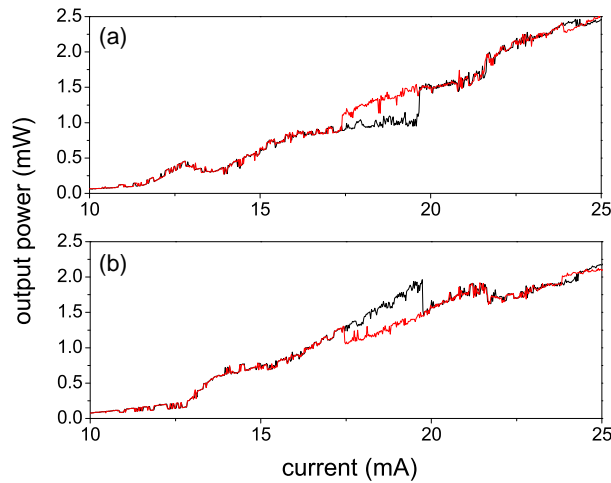


Figure 3.4: Example for the bistable behavior of laser 40–1, heat sink temperature $35\text{ }^{\circ}\text{C}$. The black curves in (a) and (b) show the L–I curve when scanning the current from 0 to 25 mA, the red curves show the scan from 25 to 0 mA. (a) Horizontally polarized part, (b) vertically polarized part. The bistability is evident between about 17 and 20 mA.

curves) the output power is rather smooth until reaching approximately 20 mA, where a large jump occurs (up for horizontally polarized light, down for vertical polarization). When decreasing the current (red curves), the output power is smooth down to 17 mA, where the jump occurs. Except for this portion the red and black curves are more or less equal. The bistability occurs in a small spot at one corner of the square VCSEL (cf. section 4.2.1.4) with a diameter of about $5\text{ }\mu\text{m}$.

Polarization bistability is a feature typically found in small VCSELs [62], but also in injection or feedback experiments with larger VCSELs [61, 69, 131]. The small spot in which the polarization bistability occurs is comparable to the situation found in small VCSELs. That device 40–1 is the only one that shows bistability without external feedback indicates that the polarization selection is weaker in this laser. This can be due to lower intrinsic material anisotropies [62]. Nonetheless all VCSELs have nominally the same design and thus such an effect can not be expected.

The L–I curves of the circular VCSELs are similar to those found in the majority of the square VCSELs. They are not shown in this section, but the threshold of the circular lasers is discussed in section 3.4.2.

3.3.2 V–I curves

Since the VCSEL is electrically a semiconductor diode, the I–V (current-voltage) characteristic is of some interest. From it several insights can be obtained, such as the series resistance of the VCSEL and its conversion efficiency of electrical power to optical power. Here the reverse, the V–I curve, shall be discussed, because the current is the control parameter and the voltage measured quantity. Exemplary V–I curves are shown in fig. 3.5 for laser 40–5 at four temperatures. All but one of the square VCSELs under study show the same V–I curves. The one exception is again device 40–1, whose behavior is rather strange (see fig. 3.7). The circular devices were not available for these experiments.

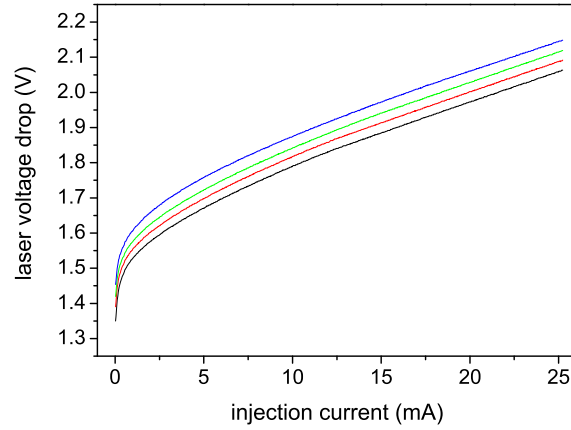


Figure 3.5: V–I curves for device 40–5 and heat sink temperatures 41 °C (black), 20 °C (red), 0 °C (green), and –20 °C (blue).

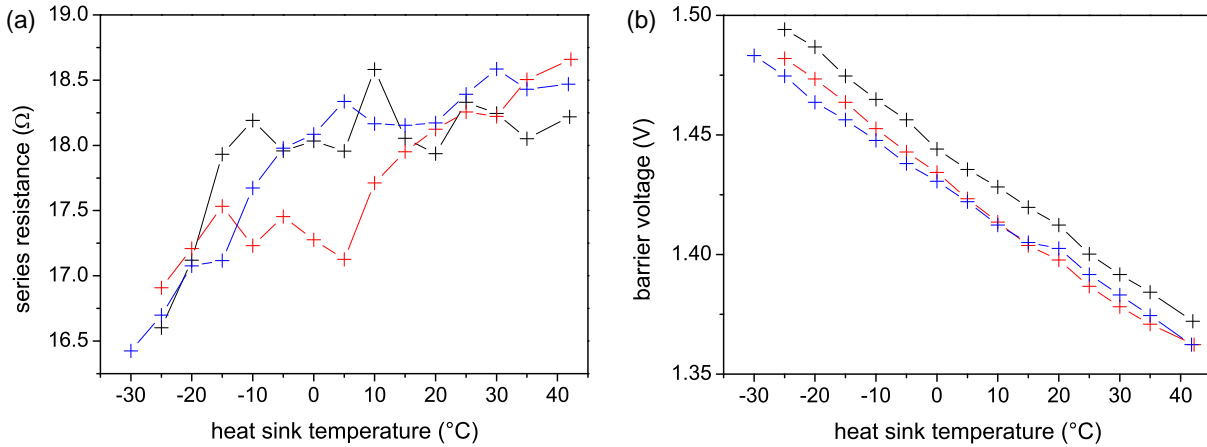


Figure 3.6: Temperature dependence of the series resistance (a) and the barrier voltage (b) for devices 30–2 (black), 40–4 (red), and 40–5 (blue).

The series resistance is important for a study of the VCSEL from the electrical point of view [42, 132]. A low series resistance is desired for applications [53, 88, 133], because it lowers the electrical power lost to heat and thus improves the conversion efficiency of the laser. In order to bring down the resistance, a grading of the semiconductor layers is used in most modern VCSEL designs [48].

The series resistance (sometimes also referred to as differential resistance) can be obtained by linear regression of the part of the V–I curve above threshold where it is linear. This was done for lasers 30–2, 40–4, and 40–5 for various heat sink temperatures. The regression was done for the current range from laser threshold to 1.2 times threshold. The results are plotted in fig. 3.6(a). Values of around 17 Ω are rather large compared to the 10 Ω given in [92] for a 25 μm VCSEL of similar design. This is probably due to the somewhat larger number of layers in the Bragg mirrors of the lasers studied here.

The barrier voltage U_b , defined here as the voltage that is applied as soon as current flows through the VCSEL, is a measure for the electrostatic barrier of the p–n junction. The electrostatic barrier is formed as a result of diffusion processes of electrons and holes,

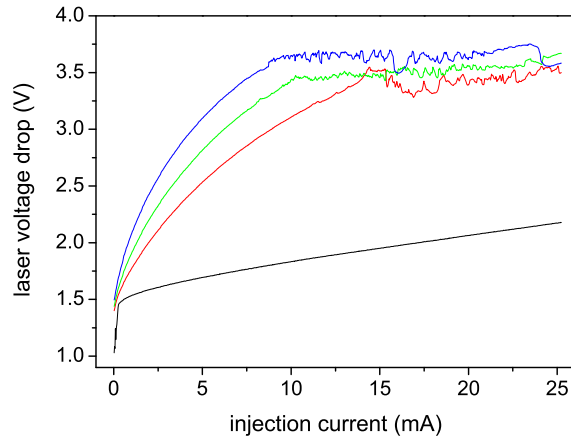


Figure 3.7: V–I curves for device 40–1 and heat sink temperatures 41 °C (black), 20 °C (red), 0 °C (green), –20 °C (blue).

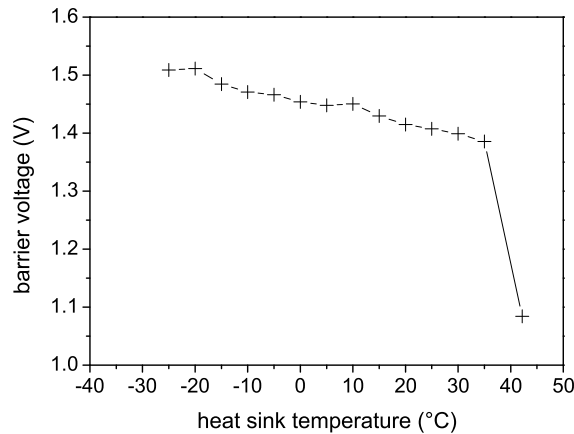


Figure 3.8: Temperature dependence of the barrier voltage for device 40–1.

when n- and p-doped semiconductors are brought together. In equilibrium the diffusion current is equalized by an electric field. U_b is the voltage needed to surmount this field. The temperature dependence of the barrier voltage is shown in fig. 3.6(b) for devices 30–2, 40–4, and 40–5. The voltage decreases linearly with temperature. This is expected since it is known that the bandgap energy is also reduced by an increasing temperature [47].

The energy of the electrons eU_b should be of the order of the bandgap energy and thus the photon energy [134]. The barrier voltage found here is around 1.425 eV, which corresponds to 870 nm. The energy of photons with an emission wavelength of 780 nm is around 1.6 eV. That means that the energy necessary to surmount the electrostatic barrier is somewhat lower than the energy necessary for laser operation, in agreement with the expectation.

Fig. 3.7 shows the dependence of the V–I curves of device 40–1 on temperature. The difference to laser 40–5 is obvious: only the curve for 41 °C resembles those of laser 40–5, though also here some differences, like the much lower barrier voltage and the steep slope near zero current followed by a sharp kink, are apparent. The other three curves

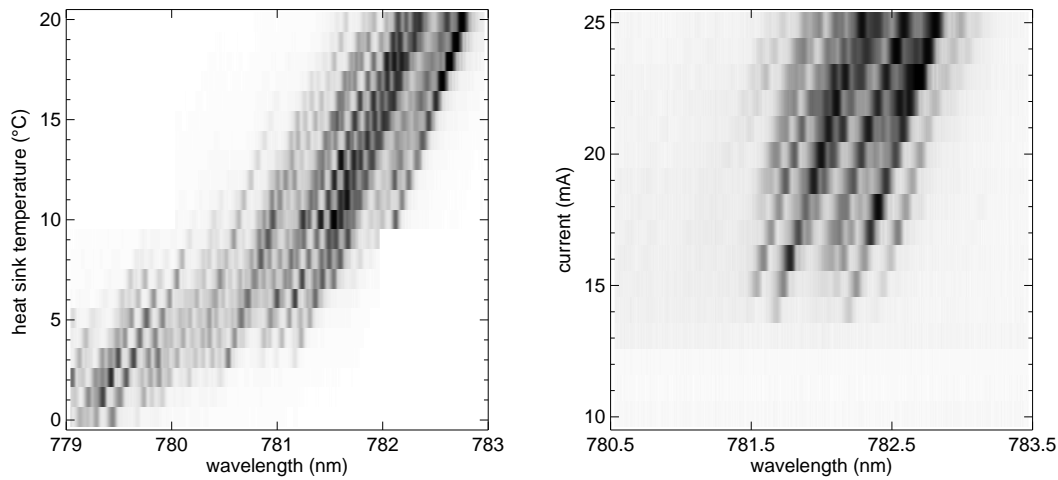


Figure 3.9: (a) Heat sink temperature and (b) current dependence of optical spectra of device 40–5 as grey-scale maps. Black denotes highest intensity, the spectra are normalized to the global maximum and slightly over-exposed to enhance the contrast of weak modes. The injection current in (a) is 25 mA, heat sink temperature in (b) is 20 °C.

feature a much stronger voltage increase (up to 3.5 V compared to around 2 V maximum for 40–5) with a sudden saturation and a noisy continuation for currents above 10 mA. The transition from a smooth to an erratic curve shifts to lower currents with decreasing temperature. It is around 14 mA for 20 °C, around 10 mA for 0 °C, and around 8 mA for –20 °C. Note that this does not correspond to the laser threshold, which is also temperature dependent (see section 3.4.2). At 20 °C the threshold is considerably lower (9 mA), for 0 °C and –20 °C it is well above the transition to the noisy part of the V–I curve (12, respectively 15.8 mA).

Since the V–I curves have an erratic form above threshold, a linear regression is not applicable to this part and thus no series resistance values can be obtained for this laser. Though the barrier voltage curve has a more typical form, it is more noisy than the one of laser 40–5. As discussed later in chapters 4 and 5, device 40–1 shows other distinctive features that are quite unique compared to the other lasers.

3.3.3 Spectral measurements

In this section the spectral characteristics of the emission of the VCSELs is considered. From the optical spectra taken with the spectrometer some very important insights can be obtained. For easier comparison and illustration of trends found in the spectra they are composed to so-called “spectra maps”. Two examples are shown in fig. 3.9. For these maps optical spectra are taken while varying one of the operating parameters (temperature or current). The result is a three-dimensional data set with the optical wavelength, the varied operating parameter, and the intensity as axes. When plotting the operating parameter as the vertical and the wavelength as the horizontal axis and representing the intensity in

grey-scale (with white denoting no emission, black highest intensity) the spectra map is obtained, as shown in fig. 3.9. Thus each horizontal stripe in the spectra maps corresponds to one spectrum at the respective parameter setting.

In fig. 3.9(a) the heat sink temperature and in (b) the current is scanned. The coarse resolution along the vertical axis is due to 1 °C steps, respectively 1 mA steps, between the spectra. In both spectra maps several tilted continuous lines are apparent. Each line corresponds to a transverse mode excited in the laser. The tilt is due to a red-shift of the wavelength of each mode with temperature, respectively current. This red-shift is approximately equal for each mode. The temperature- and current-induced red-shifts will be discussed in detail in section 3.4.4.

Keeping these shifts in mind other features become apparent: in subfigure (a), where the temperature is varied, the low wavelength modes exist only for low temperatures and fade out with increasing temperature, while modes with larger wavelengths are excited. In other words the broad band of excited transverse modes red-shifts faster than each individual line. It was stated before (cf. section 2.4) that a simple understanding of transverse mode selection is connected to the detuning between the longitudinal resonance and the wavelengths of the gain maximum. These two wavelengths shift with temperature at different rates. Applying this knowledge to the shifts visible in the spectra maps shows two things: firstly, the shift of each individual line with temperature and current corresponds to the shift of the longitudinal resonance wavelength. The second shift, only visible in subfigure (a), then corresponds to the shift of the maximum gain wavelength. The spectral position of the gain curve determines which band of wavelengths is amplified. Inside this band the resonance condition of the cavity selects the wavelengths that are actually supported. This consideration of the spectral characteristics already gives a deep insight into the selection mechanisms of the transverse modes.

3.4 Analysis and interpretation

In this section the experimental results are analyzed and the parameters necessary for the discussion in later chapters are obtained. At first the sources for refractive index values for $\text{Al}_x\text{Ga}_{1-x}\text{As}$ are evaluated. This is followed by an analysis of the laser thresholds, which play a role in the later chapters, because the emission characteristics of the lasers mainly depend on the distance to the laser threshold, not so much on the absolute current values. This is followed by a short discussion of the efficiencies of the VCSELs.

The longest section is about the spectral characteristics of the VCSELs. There the first puzzle piece necessary to understand the selection mechanisms of transverse modes is obtained.

3.4.1 AlGaAs refractive indices

For all calculations regarding the behavior of light inside the VCSELs the refractive index of the semiconductor material is needed. This is especially involved here, since the index is strongly dependent on the fraction x of aluminum in the individual layers of $\text{Al}_x\text{Ga}_{1-x}\text{As}$ and on the temperature. Several sources were found for the indices. A

reference value for each x used in the VCSEL design was provided by the manufacturers. These are compared to publications on material parameters. In [135] the Sellmeier equation is applied to calculate the indices, but it was found that the resulting values differ from the reference values. Values with a better agreement are obtained from [136], where a complex interpolation scheme is applied to experimental values found in the literature. It turns out that for small x this equation yields no indices for $\lambda = 780$ nm because the material becomes absorbing. A third comprehensive source was found in an online database [137], where n is given for several compositions of $\text{Al}_x\text{Ga}_{1-x}\text{As}$ and for several wavelengths. This is of great advantage, since it enables the calculation of the group index

$$n_{gr} = n(\lambda) - \lambda \frac{dn}{d\lambda}. \quad (3.1)$$

A good agreement with the reference values is also found. Using a linear interpolation scheme, values for n and n_{gr} for every x are obtained. The resulting refractive and group indices are given in appendix B. They are calculated for $\lambda = 780$ nm, which is in most cases not the actual wavelength of the emission, but the deviation was checked to be negligible.

For the circular lasers the situation is similar. For the wavelength of those lasers, around 980 nm, nearly identical values are obtained from the sources [136] and [137]. Since the equations in [136] simplify the calculation of the index and group index values, this source is used for the circular VCSELs. A refractive index for $\text{In}_{0.2}\text{Ga}_{0.8}\text{As}$ - the material of the quantum wells of the circular lasers - can in principle be obtained from [138]. It turns out that for $x = 0.2$ the equations again yield no result, because the material becomes absorbing. For the calculation of the average refractive index of the whole structure the refractive index of the thin quantum wells has only a marginal significance, thus it is omitted.

3.4.2 Laser thresholds

The laser threshold defines at which current the gain inside the active laser medium overcomes the losses and laser operation sets in. Below threshold current spontaneous emission is dominant, above threshold current stimulated emission gets the upper hand. In this section the temperature dependent threshold values for several lasers are determined.

Together with the threshold values I_{th} , the pump rate can be defined from the injection current I as

$$p = \frac{I - I_{th}}{I_{th}}. \quad (3.2)$$

The pump rate is a more meaningful parameter than the absolute current, because it relates the state of the laser to the laser threshold, and most emission characteristics depend on the distance to the threshold rather than the absolute current values.

There are four ways to extract the laser threshold from the L-I curves described in section 3.3.1 [139]:

1. Linear fit: a linear regression to the linear part of the curve after the kink indicating the threshold. The threshold value is given by the intersection with the horizontal axis.

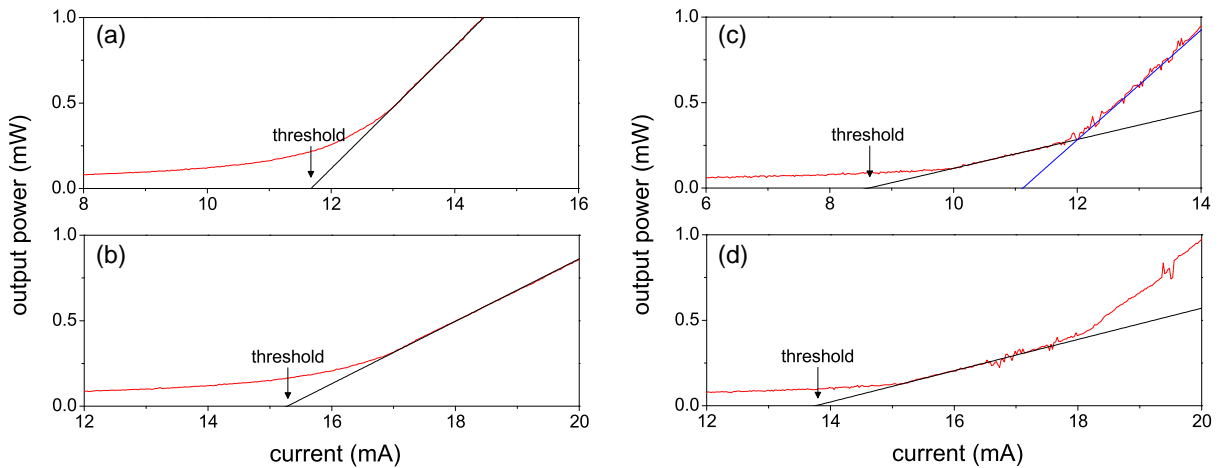


Figure 3.10: Determination of the laser threshold. (a) and (b): device 40–5, heat sink temperature 25 and 10 °C, respectively. (c) and (d): device 40–1, same temperatures as (a) and (b). The red curves represent the measured L–I curves, the black lines show the linear fit to the part of the L–I curves with the first strong increase of the slope. The additional blue line in (c) illustrates the ambiguity sometimes encountered in the determination of the threshold current.

2. Two-segment fit: in addition to the first linear fit a second fit to the L–I curve before the kink (the spontaneous emission part) is done. The intersection of the two lines yields the threshold current.
3. First-derivative method: the kink results in a rise of the first derivative of the L–I curve at threshold. The half-maximum value of the rise yields the threshold current.
4. Second-derivative method: the second derivative of the L–I curve shows a peak at the position of the kink, where the curvature is highest. The threshold current is obtained from the position of the maximum of the peak.

All methods have certain advantages and disadvantages: method 1 is rather simple to apply but makes it necessary to select an appropriate linear part of the L–I curve for the linear fit. This is not always definite, especially when the laser is operating on several transverse modes already close to threshold, which is often the case for the VCSELs under study. Method 2 has the same drawback and in addition, a second line has to be fitted to the spontaneous emission portion of the L–I curve. It is quite difficult to obtain the threshold with method 3, since it is difficult to locate the half maximum of the rise when the kink in the L–I curve is not sharp (as is typical for semiconductor lasers). The fourth method also works best for sharp kinks. Applied to the data gathered here the peak in the second derivative is in most cases very broad and shallow.

Especially when the analysis shall be (at least) semi-automatic method 1 is most suited in the case under study here. It was used for all L–I curves. Comparison of the threshold values obtained with the other methods yields similar values, though details are different. Examples of the threshold determination are shown in fig. 3.10. While the method is straight-forward for device 40–5, it is more involved for other lasers. An example of the problem is shown in subfigure (c). The black line shows the fit applied to the very first

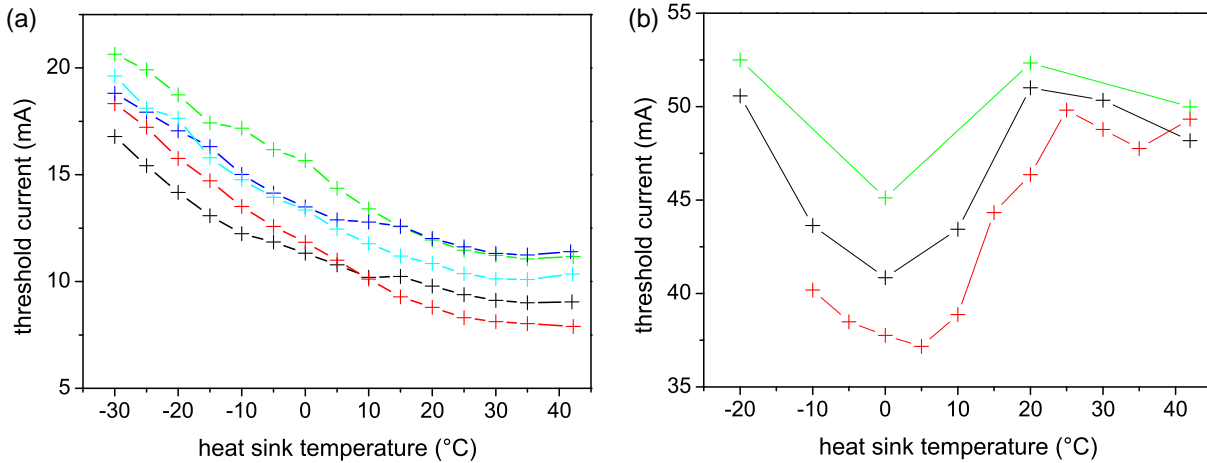


Figure 3.11: Temperature dependence of the laser thresholds of several devices. (a): square VCSELs. 30–2 (black), 40–1 (red), 40–4 (green), 40–5 (blue), 40–9 (cyan). (b): circular VCSELs. 80–1 (black), 80–2 (red), 80–3 (green).

rise in output power, while the blue line shows the fit applied to the portion of the L–I curve with the much higher slope. The two resulting threshold values differ by more than 2 mA. It is necessary to establish precisely to which part of the L–I curve the linear fit is applied and to use the same procedure for all sets of measurements. In this case the linear fit was always applied to the very first increase of the slope of the L–I curve, as indicated by the black lines in fig. 3.10. This problem generally occurs for low temperatures.

Fig. 3.11 summarizes the temperature dependence of the threshold values, subfigure (a) for the square lasers, subfigure (b) for the circular lasers. It is obvious that the dependence is more or less the same for each group of lasers (square and circular) included in the plot.

While for the square lasers the threshold dependence on temperature is rather smooth, this is not the case for the thresholds of the circular lasers. To understand this it is first necessary to say that all lasers studied here show a strong dependence of the transverse wave number emitted at threshold on the heat sink temperature (this will be discussed in detail in chapter 4). The overall L–I curve is in principal the sum of the contributions of individual L–I curves of each transverse mode. These individual L–I curves have different threshold dependencies on temperature. The threshold obtained from the overall output power is at the same time the threshold of the transverse mode that starts lasing first. A pronounced kink in the curve in fig. 3.11(b) is found in the black curve (laser 80–1) between 10 and 20 °C. This coincides with a distinct change of the transverse wave number emitted at threshold (see fig. 4.5(h) and (i) in the next chapter for far-field images).

The threshold curves of the square lasers shown in fig. 3.11(a) are much smoother than those of the circular lasers, though some bumps are visible here as well (e.g. in the black curve around 10 °C). The threshold current is decreasing with temperature, the shape of the curves is similar to a second degree polynomial. The lowest threshold values are found for the highest temperatures. The point of lowest threshold is discussed in more detail in section 3.4.4.6.

The smoothest curve is the red one corresponding to laser 40–1. This device has the specialty that it always emits (close to) on-axis emission at threshold, which will be

shown in section 4.2.1.4. The form of this curve can be understood with the help of the detuning between gain maximum wavelength and longitudinal resonance wavelength which was introduced in section 2.4. Lowering the temperature means that the detuning between the two parameters increases. Thus the on-axis mode emitted by laser 40–1 at threshold is less and less preferred by the resonator which in turn means an increase in laser threshold. This is also true for the other lasers, but they adapt by emitting transverse modes of increasing wave number at threshold. In effect the threshold should remain constant with decreasing temperature because the resonator should always start lasing at the point where the gain maximum overcomes the losses. This is obviously not the case, which can stem from several effects, e.g. the transverse modes could have higher losses than the longitudinal resonance mode.

The bumps visible in the threshold curves of the square lasers can also be related to the onset of transverse modes at threshold, as it was done above with the curves of the circular lasers. Such a bump occurs when the change in temperature results in a change of the order of the transverse mode excited at threshold.

As a final note the expectation that the threshold current is related to the size of the VCSEL [53] is somewhat visible in the figure. The black curve in fig. 3.11(a) corresponding to the 30 μm VCSEL is at least lower than the other curves, with the exception of laser 40–1 which is special in many aspects.

3.4.3 Laser efficiencies

The efficiency of a laser indicates how well it converts input power to output power. Two common types of efficiency are found in the literature: the slope efficiency and the power conversion efficiency. These are calculated here for some of the VCSELs under study.

To obtain the slope efficiency the output optical power is plotted against the input pump power. The slope efficiency is then defined as the slope of the part of the curve above the laser threshold. In this way the efficiency values are always quite high, since the amount of pump power necessary to reach the laser threshold is neglected. Slope efficiency and threshold current together characterize the L–I curve of a laser [140]. Here the pump power is the electric power $P_{el} = UI$, with the injection current I and U the voltage obtained from the V–I curves shown in section 3.3.2. The slope is calculated with a linear regression. The resulting slope efficiencies are plotted in fig. 3.12(a) over the heat sink temperature. All lasers show a similar dependence of the slope efficiency on temperature. The highest values of 15 to 20% are found between 0 and 15 $^{\circ}\text{C}$ with a drop-off toward lower and higher temperatures.

The other important parameter is the power conversion efficiency. This is obtained by simply dividing the output optical power by the input electrical power. The conversion efficiency has to be given for a certain injection current value. The electrical power is then obtained by multiplying the current with the voltage drop at the laser taken from the V–I curves. In this way the current needed to reach the laser threshold is included. The conversion efficiency is very low below laser threshold, since the output power is near zero. Only above threshold values above 1% are reached. In subfigure (b) the conversion efficiency is given in percent for three lasers at 1.2 times laser threshold. Maximum values

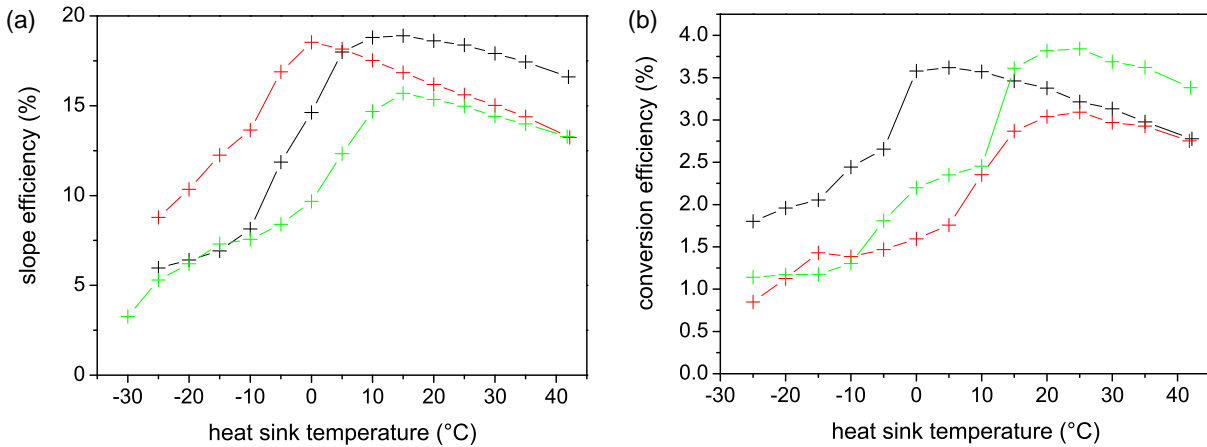


Figure 3.12: Temperature dependence of (a) the slope and (b) the power conversion efficiencies at 1.2 times laser threshold of various lasers: 30–2 (black), 40–4 (red), 40–5 (green).

between 3 and 4% are found in a temperature range from 0 to 25°C. For higher and lower temperatures the efficiency decreases. The current dependence of this efficiency is very analogous to the L–I curves, only the vertical axis changes from current to electrical power. The point of maximal conversion efficiency is not reached within the investigated current region (up to 25 mA).

Note that the temperature where the efficiencies are maximal does not coincide with the lowest threshold value (cf. fig. 3.11). Also the maxima of slope and conversion efficiency are found at different temperatures. This is due to the fact that the conversion efficiency strongly depends on the laser threshold, while the slope efficiency only depends on the slope above threshold.

Compared to optimized VCSELs the efficiencies are very low. For example in [141] a maximum slope efficiency of 78% and a maximum power conversion efficiency of 50% is achieved. Generally semiconductors are known for their superb conversion efficiencies: 50% slope efficiency is common [140]. The devices under study here are an exception of this rule. This can be attributed to the fact that the emission of the large VCSELs covers only a part of the aperture in most cases.

3.4.4 Spectral characteristics

From spectral maps similar to those shown in fig. 3.9 the values of the red-shifts of the emission with temperature and with current can be obtained. Both current and temperature-induced shifts arise from the same source: the change of the longitudinal resonance due to a thermal expansion of the medium and the temperature dependence of the refractive index. It is shown in the following that the shift values are easily quantifiable. This is helpful later on because by removing the shifts from the spectra it becomes possible to compare the wavelengths of modes that are emitted at different parameter settings. This is used in section 4.3.4 to calculate the detuning between gain peak and longitudinal cavity resonance.

The current affects the temperature via Joule heating. The latter effect describes the

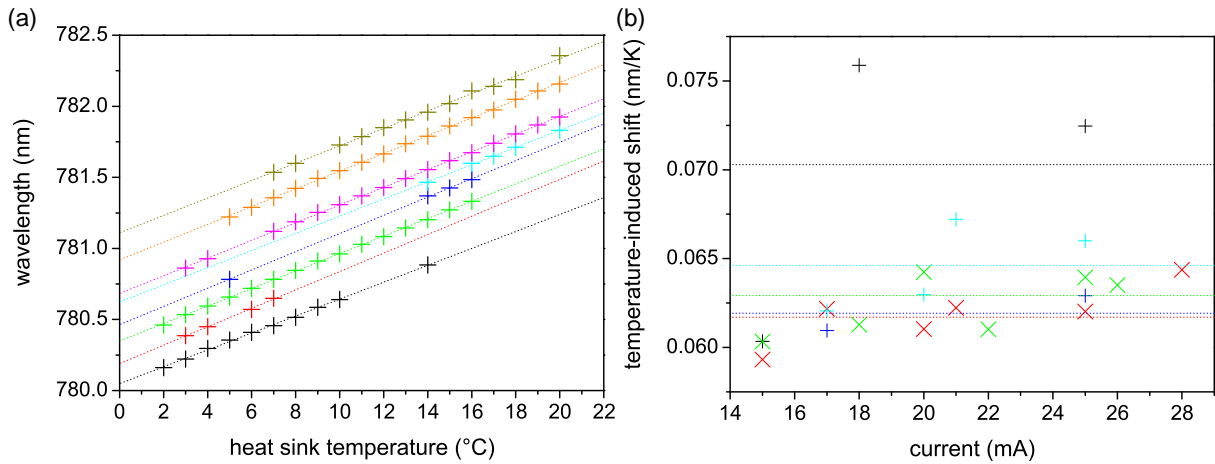


Figure 3.13: (a) Wavelengths of strong modes extracted from optical spectra, similar to the spectra map in fig. 3.9(a). Laser 40–5, $I = 25$ mA, the temperature is scanned from 0 to 20 °C. For clarity only the positions of some of the modes found in the optical spectra are plotted. An individual color is assigned to each mode, the dashed lines are linear fits to the position of the corresponding modes. (b) Current dependence of the temperature-induced shifts for various VCSELs: 30–3 (black), 40–4 (red), 40–5 (green), 40–7 (blue), and 40–9 (cyan). To make hardly separated data points distinguishable, the symbol type is alternating between cross- and plus-shape. The similarly colored dotted lines give the average temperature-induced shift for each device. The shift values are given in table 3.1.

heating-up of a material due to its series resistance. Dividing the current-induced shift by the temperature-induced shift results in the Joule heating coefficient in Kelvin per milliampere. Using this coefficient the effective temperature T_{eff} inside the laser can be derived [59].

In the following sections temperature and current-induced shifts, and their origins are discussed individually. The results are compared to values obtained from the literature. This is followed by a discussion of the Joule heating coefficients.

The second trend found in the optical spectra, the shift of the gain curve, is discussed in section 3.4.4.5. The origin of this shift is the change of the bandgap with temperature. The value is obtained again from spectral measurements and compared to those found in the literature. The last section uses all these shift values for the purpose of calculating the point where longitudinal resonance wavelength and gain maximum wavelength are equal, i.e. where the detuning is zero.

In large parts the analysis was only done for the square lasers, since here a lot more measurements could be done. For the circular devices only the resulting shift values and the Joule heating coefficient are given.

3.4.4.1 Temperature-induced shift

At first the red shift of the wavelengths of excited transverse modes with temperature is analyzed. The analysis includes the lasers 30–3, 40–4, 40–5, 40–7, 40–9, and 80–3. It is relatively easy to obtain a linear temperature-induced shift from the spectra by tracking spectral lines over a large temperature range. An example is shown in fig. 3.13(a) for laser

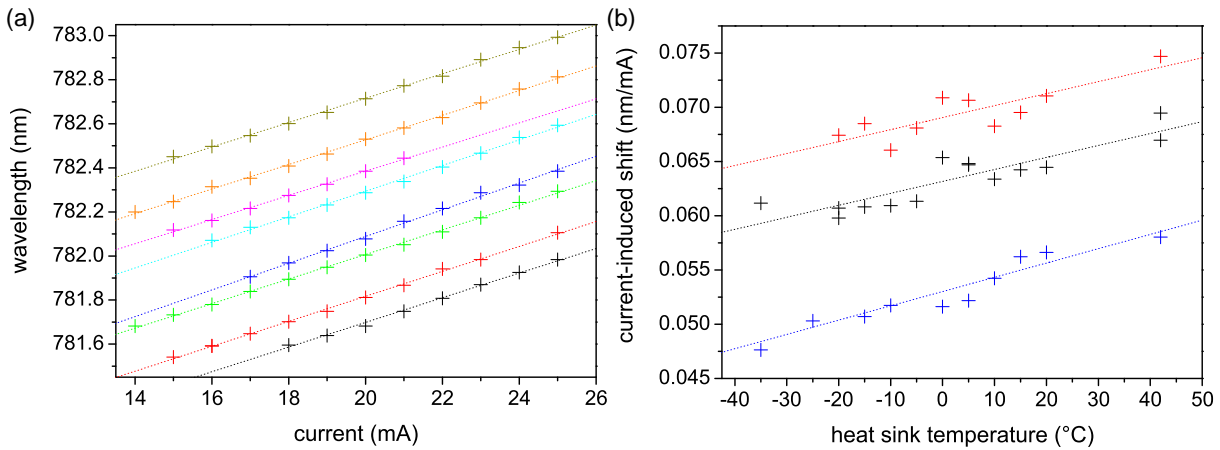


Figure 3.14: (a) Wavelengths of strong modes extracted from optical spectra, similar to the spectra map in fig. 3.9(b). Laser 40–5, $T = 20^\circ\text{C}$, the current is scanned from 10 to 25 mA. For clarity only the positions of modes found over large current ranges are plotted. An individual color is assigned to each mode, the dashed lines are linear fits to the position of the corresponding modes. (b) Temperature dependence of the current-induced shifts for various VCSELs: 30–3 (black), 40–4 (red), and 40–9 (blue). Each data point is obtained from a current scan from threshold to a maximum of 25 mA, similar to the one shown in (a). Linear fits to the data of each laser are plotted as dotted lines. The fit parameters are given in table 3.1.

40–5 with $I = 25$ mA, which corresponds to the spectra map in fig. 3.9(a). Only some of the modes in the spectral map are displayed in this plot. An individual color is assigned to each mode. The dashed lines in the same colors are corresponding linear fits. It is found that within an error of less than 3% the shift of the wavelength with temperature of each mode is linear. The standard deviation of the slopes of the linear regressions is less than 5%. It is thus reasonable to assume a linear shift and average over the shifts of the individual modes.

It remains to be checked if the temperature-induced shift changes with current. Fig. 3.13(b) shows the dependence of the temperature-induced shift on current for various lasers. The dashed lines corresponding to each set of data points indicate the average value. It shows that in some cases a slight tendency of an increase of the shift with current is found, but not for each laser. Since the error of each data point is of the order of 5% and the current range encountered in the experiments (from laser threshold to a maximum of 25 mA) is rather small, the current dependence of the temperature-induced shift is neglected and the averaged shifts are used in the following. The resulting shift values for all lasers are given in table 3.1.

3.4.4.2 Current-induced shift

For the current-induced shift the range from threshold to 25 mA was analyzed for various temperatures. The current range for each data point is thus rather small, in many cases less than 10 mA. An example of modes found in laser 40–5 at $T = 20^\circ\text{C}$ and varied current is shown in fig. 3.14(a). Similar to the plot in fig. 3.13(a) an individual color is assigned to each identified mode. The dashed lines indicate linear regressions to the

wavelengths of the modes. It is obvious that the shift is linear, the errors of the linear fits are smaller than 3%. The standard deviation of the slopes is less than 4%. Thus again the average shift is used.

The temperature dependence of the current-induced shift is shown for various lasers in fig. 3.14(b). Here a systematic tendency is found for each laser: the current shift increases slightly with temperature. Though the slope is very small a significant change of the shift (more than 15%) is found over the accessible temperature range (−35 to 40 °C). In conclusion the current-induced shift is linear and dependent on temperature. The values for all lasers are given in table 3.1.

Note that the current-induced shifts for lasers 40–5, 40–7, and 40–9 found in the table are significantly smaller than those of the other devices. For the 30 μm lasers this is understandable, since the current flow is confined to a smaller area and thus the shift is expected to be stronger (i.e. the thermal resistance is higher [43]). Where the difference between the two groups of 40 μm devices originates is not clear. As stated before lasers 40–1 through 40–4 were produced some years before the second batch, 40–5 through 40–9. Nonetheless the nominal design is the same and only some optimization of growth parameters can be expected.

The experimental data available for the circular lasers was not sufficient to enable the same in-depth analysis as for the square VCSELs. The dependence of the current-induced shift on temperature is neglected for these devices.

3.4.4.3 Joule heating coefficients

To calculate the Joule heating effect the current-induced shift is simply divided by the temperature-induced shift. This invokes the assumption that the current-induced shift is a purely thermal effect. In other words, the wavelength shift with current originates only from the heating-up of the laser, not from other effects. The results for all lasers, including the circular devices, are given in table 3.2. For a given heat sink temperature T the Joule heating coefficient γ can now be calculated. With the injection current I and

$$T_{eff} = T + \gamma(T) \cdot I \quad (3.3)$$

the effective temperature inside the laser is obtained.

Joule heating creates a current-dependent temperature rise in the laser. The rise can be obtained from eq. (3.3) by subtracting the heat sink temperature T , i.e. $\Delta T = \gamma I$. Considering device 40–5 at a constant current $I = 10$ mA the dependence of the temperature rise on the heat sink temperature is plotted in black in fig. 3.15. The slope relates to the temperature dependence of the Joule heating coefficient given in table 3.2.

The set of red data points in fig. 3.15 is calculated with the following equation, obtained from the definition of the heat conductivity:

$$\Delta T = \frac{P \cdot l}{A \cdot K(T)}, \quad (3.4)$$

where P is the dissipated power, l the distance to the heat sink, and A the area of the heat flow, and ΔT the amount of heat created. The heat conductivity $K(T)$ is obtained from [142] for GaAs as $K = 0.5 - 0.0024 \times T/^\circ\text{C}$ [W/cmK]. A reference value of 0.44 W/cmK

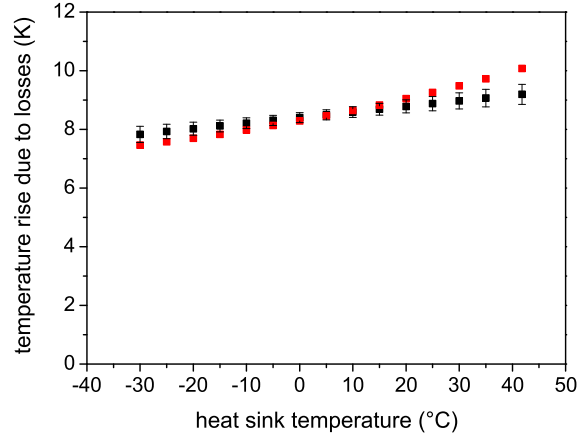


Figure 3.15: The dependence of the temperature rise on heat sink temperature for laser 40–5. Black: experimental values ($\Delta T = T_{eff} - T = \gamma \cdot I$), featuring in principal the change of the Joule heating coefficient with temperature. Red: calculated values using the literature values for the thermal conductivity and the length l in eq. (3.4) as a fit parameter.

Table 3.1: Values for current and temperature-induced shift for all VCSELs studied in this work. T is the heat sink temperature. For the current-induced shift the error of the linear regression is used, the standard deviation gives the error for the temperature-induced shift. For the circular lasers the standard deviation yields both errors.

Laser	current-induced shift (nm/mA)	temperature-induced shift (nm/K)
30–1 ... 30–4	$0.00011(2)T/^\circ\text{C} + 0.0632(4)$	0.070(7)
40–1 ... 40–4	$0.00011(3)T/^\circ\text{C} + 0.0691(5)$	0.062(3)
40–5	$0.00012(2)T/^\circ\text{C} + 0.0530(2)$	0.063(4)
40–7	$0.00013(4)T/^\circ\text{C} + 0.053(1)$	0.062(2)
40–9	$0.00014(1)T/^\circ\text{C} + 0.0528(3)$	0.065(5)
80–1 ... 80–3	0.008(1)	0.06(1)

is given in [53]. This fits very well to the previous value with $T = 25^\circ\text{C}$. Note that the dependence on temperature in [142] is not linear. This was neglected for the comparatively small temperature range studied here.

The dissipated power P is approximately equal to the electrical power $P_{el} = UI$, because at 10 mA the optical output power is negligible. The values for $P_{el}(T)$ can be obtained from V–I curves. For A a reasonable approximation is the size of the oxide aperture because it guides the current flow, i.e. $A = (40 \mu\text{m})^2$. The remaining parameter l is used as a fitting parameter. The best agreement between experiment and theory is obtained for $l = 36 \mu\text{m}$. The resulting temperature rise is plotted in fig. 3.15 in red. It changes with temperature only due to the temperature dependence of K . A linear regression to the curve yields a slope nearly two times larger than the one of the experimentally obtained values. This may be due to other temperature dependent parameters, such as the heat conduction length l or a different temperature dependence of K obtained when the real VCSEL structure is taken into account.

Table 3.2: Values for Joule heating coefficients for all VCSELs studied in this work. T is the heat sink temperature. The error for the Joule heating coefficient is obtained with error propagation from the values in table 3.1.

Lasers	Joule heating coefficient (K/mA)
30-1 ... 30-4	$0.0016(13)T/^\circ\text{C} + 0.90(3)$
40-1 ... 40-4	$0.0018(8)T/^\circ\text{C} + 1.12(2)$
40-5	$0.0019(7)T/^\circ\text{C} + 0.84(2)$
40-7	$0.0021(6)T/^\circ\text{C} + 0.86(1)$
40-9	$0.0021(9)T/^\circ\text{C} + 0.82(2)$
80-1 ... 80-3	0.13(3)

3.4.4.4 Temperature dependence of the longitudinal resonance

It remains to be seen, from where the shifts originate. As it was said before, defining the Joule heating coefficient as the ratio of current-induced shift and temperature-induced shift invokes the assumption that the current-induced shift is a purely thermal effect. Thus both temperature and current-induced shifts have the same source: the change of the longitudinal resonance with temperature. Two possible sources are conceivable for this: thermal expansion of the material and the temperature dependence of refractive index.

The thermal expansion coefficient for $\text{Al}_x\text{Ga}_{1-x}\text{As}$ is given in [136] as $\alpha = (6.4 - 1.2x) \cdot 10^{-6} \text{ K}^{-1}$. The device structure of the square VCSELs is given in appendix B. Weighted averaging yields $x = 0.58$ for the aluminum fraction of the whole structure. Thus we have $\alpha = 5.7 \cdot 10^{-6} \text{ K}^{-1}$ and a wavelength change with temperature of $\lambda \cdot \alpha = 4.4 \text{ pm/K}$ for $\lambda = 780 \text{ nm}$ (the actual length change of the material $L \cdot \alpha$ is irrelevant, since λ is only influenced by the change of the resonance). This is one order of magnitude smaller than the experimentally obtained shift values.

Data on the temperature dependence of the refractive index n of $\text{Al}_x\text{Ga}_{1-x}\text{As}$ are sparse. There are some papers on GaAs and AlAs, but for unsuitable wavelength (mostly far above $1 \mu\text{m}$) [143–145]. [146, 147] provides both GaAs and AlAs values for wavelengths down to 960 nm . Though this is quite distant from the wavelengths under study here, the values provided there are best suited here. For GaAs the given change of n is $3.66 \cdot 10^{-4} \text{ K}^{-1}$, for AlAs $1.63 \cdot 10^{-4} \text{ K}^{-1}$. A linear interpolation for $\text{Al}_{0.58}\text{Ga}_{0.42}\text{As}$ yields $\beta = 2.81 \cdot 10^{-4} \text{ K}^{-1}$. The wavelength shift generated by the temperature dependence of the refractive index is then $\beta\lambda/\bar{n} = 0.067 \text{ nm/K}$, where $\bar{n} = 3.3$ is the average index of the whole laser structure (cf. appendix C).

The overall result for the change of the longitudinal resonance with temperature is 0.071 nm/K , which is only slightly larger than the experimental values for the temperature-induced shift. This is a good agreement for a comparison on this level, since the value of β was not derived for the correct wavelength.

Of course the refractive index is also dependent on the wavelength. For example the average index of the VCSEL structure changes from 3.276 to 3.273 in the wavelength range from 779 to 783 nm (where the emission is typically found). This change is well

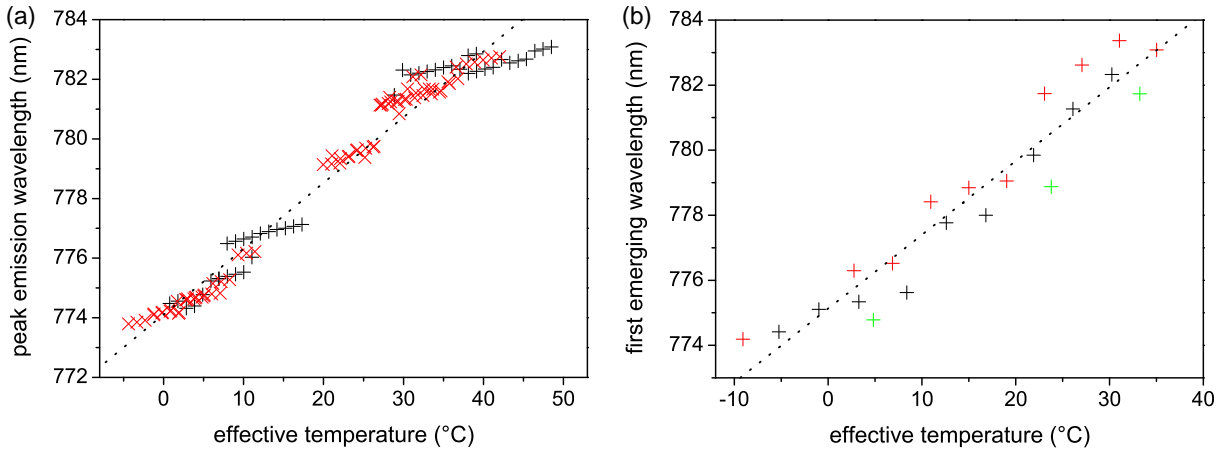


Figure 3.16: (a) Dependence of the wavelengths of the emission maxima on effective laser temperature for lasers 30–3 (black) and 40–5 (red). A linear fit is plotted for both sets of data in dotted lines with corresponding colors. (b) Dependence of the wavelengths of the first emerging modes at threshold on effective laser temperature for laser 30–3 (black), 40–4 (red), and 40–5 (green). The linear fit through all three sets of data is given as a dotted line.

below the accuracy of the available data. The effect on the calculated wavelength shift is even smaller (it affects the fourth significant digit), and definitely negligible.

Finally the results are compared to values found in the literature. The cavity resonance is in most cases deduced from injection experiments, where the wavelength of the injected beam is tuned and the Fabry-Perot resonance of the slave VCSEL is found at a dip in the intensity of the reflected light. Most values found are for smaller (0.055 nm/K [88], 0.056 and 0.067 nm/K for two positions on a wafer [148], 0.06 nm/K [149]) or gain-guided VCSELs (0.06 nm/K [47]). A value for a broad-area laser similar to the ones studied here is 0.075 nm/K from [92]. All values are very close together and agree quite well with the ones found here experimentally and theoretically.

3.4.4.5 Dependence of gain peak frequency on temperature

As mentioned in section 3.3.3 the second effect responsible for the temperature dependence of the detuning is the shift of the gain curve with temperature. This is investigated in this section and compared to values found in the literature.

Fig. 3.16 shows the experimental data from which the gain shift can be derived. The data points represent the wavelength of the emission maximum for several sets of temperature and current (a), and the wavelength of the first emerging mode at threshold for various temperatures (b). Both are derived from optical spectra obtained with the spectrometer. To correctly represent the state of the cavity both data sets are plotted versus the effective temperature, calculated from eq. (3.3).

In the data in Fig. 3.16(a) two slopes are apparent: over small temperature ranges the emission wavelength slowly increases with temperature. The slope obtained from a linear regression to all data points is much larger (indicated by the black dotted line). The first smaller slope shows the shift of the longitudinal resonance, while the larger slope corresponds to the gain curve shift. The dashed black line is obtained from a linear

regression to all data points in the plot. The slope is 0.22 nm/K. The slope of the regression to the data in subfigure (b) is 0.23 nm/K.

Values of the shift of the gain peak are also found in the literature. In [47] it is given for GaAs as 0.27 nm/K. It is due to the lowering of the bandgap energy with temperature. In [136] the bandgap of $\text{Al}_x\text{Ga}_{1-x}\text{As}$ with $x=0.11$ (the Al fraction of the quantum wells) is given as 1.56 eV at 300 K. The change with temperature is $-4.1 \cdot 10^{-4}$ eV/K. This corresponds to a wavelength shift of -0.21 nm/K at 794 nm (the wavelength corresponding to the bandgap energy), which is in very good agreement with the experimentally obtained shift value. Note that the bandgap wavelength is significantly higher than the emission wavelengths encountered in the experiments. This is always the case with quantum well semiconductor lasers, since the laser transition takes place between levels inside the conduction and valence bands, respectively. Thus the photon energy is higher than the bandgap energy [134].

3.4.4.6 Indicators of zero detuning

In section 3.4.2 it was discussed that with simple assumptions (e.g. same losses for all transverse modes) the dependence of the threshold on temperature is a constant for negative detuning ($\delta = \lambda - \lambda_c < 0$), and rises for positive detuning. This can be assumed because for $\delta < 0$ the laser adapts by emitting tilted waves with the frequency of the gain maximum. For $\delta > 0$ this is not possible, since there tilted waves are not supported by the cavity and the emission should be homogenous [24]. This state will become more and more disfavored with rising detuning, thus the threshold increases. With this simple considerations it can be deduced that zero detuning is encountered before the threshold rises again for high temperatures.

In real devices, and also in the experiments shown here, the threshold also rises for negative detuning (cf. fig. 3.11(a)). The point of zero detuning should thus be indicated by the threshold minimum [150, 151]. In the following the point of zero detuning is estimated from the threshold curves and this is compared to a second method.

This second access to the point of zero detuning are the wavelengths of the longitudinal resonance and the gain peak. Where the two quantities are equal the detuning is zero (i.e. at the intersection of the respective linear dependence on temperature). To calculate the temperature where $\delta = 0$ we need the parameters of the following equations:

$$\lambda_{res} = \lambda_{0,res} + \sigma_T \cdot T \quad (3.5)$$

and

$$\lambda_{gain} = \lambda_{0,gain} + \sigma_{gain} \cdot T, \quad (3.6)$$

with λ_0 the respective wavelength at $T = 0^\circ\text{C}$, σ the respective shift, T the temperature in $^\circ\text{C}$.

The intersection is considered for devices 30–3 and 40–5. The values of σ_T and σ_{gain} were derived above. The absolute values for $T = 0^\circ\text{C}$ can be obtained easily from linear fits to the experimental data (cf. fig. 3.13 for the longitudinal resonance and fig. 3.16 for

the gain wavelength). We obtain for device 30–3

$$\lambda_{res} = (781.1(1) + 0.070(7) \cdot T/^\circ\text{C})\text{nm} \quad (3.7)$$

$$\lambda_{gain} = (774.3(1) + 0.22(1) \cdot T/^\circ\text{C})\text{nm} \quad (3.8)$$

$$\Rightarrow T(\delta = 0) = 45(4)^\circ\text{C} \quad (3.9)$$

and for device 40–5

$$\lambda_{res} = (781.2(1) + 0.063(7) \cdot T/^\circ\text{C})\text{nm} \quad (3.10)$$

$$\lambda_{gain} = (774.0(1) + 0.22(1) \cdot T/^\circ\text{C})\text{nm} \quad (3.11)$$

$$\Rightarrow T(\delta = 0) = 46(4)^\circ\text{C}. \quad (3.12)$$

The errors of the linear regressions are given in parentheses. The errors of the intersection temperatures are obtained by Gaussian error propagation. Note that the resulting temperatures as well as their errors strongly depend on the values of the gain shift. For this shift the error was estimated from several linear regressions that yielded slightly different results.

For some lasers the threshold minimum is outside the accessible temperature range. In fig. 3.11(a) a clear minimum can be found for lasers 40–4, 40–5, and 40–9. For those VCSELs the minimum is around 35°C . Since the threshold curve of laser 30-2 (the black curve in fig. 3.11(a)) is flat between 35 and 40°C the minimum is probably found there. The values derived above are somewhat higher. Taking into account that the material gain decreases with increasing temperature (or to be more precise: the gain curve broadens and flattens, see e.g. [134]) it can be reasoned that the threshold minimum is found at smaller temperatures than the point of zero detuning. This agrees with the results found here but can not be quantified any further.

It can be concluded that the point of lowest threshold is indeed an indication for zero detuning, though the comparison with the calculation above shows that on this level it can only be an estimation.

4 Length scales and spatial structures

In this chapter the experiments on the types of spatial structures emitted by the VCSELs and their length scales are reported and discussed in view of the results of the previous chapter. The first section details the setup used for the experiment. This is followed by the experimental observations and a discussion section where the observations are compared to theoretical calculations using results from section 3.4.

4.1 Experimental setup

The setup for the experiments described in this chapter was developed to enable simultaneous measurement of the near-field and far-field intensity distribution, as well as of optical spectra. A schematic of the setup can be found in fig. 4.1. The basic scheme of the setup described in section 3.2 was expanded by several detection beam paths. The details are described below. Various modifications were made during the work on the experiments. The actual realization of the setup may differ slightly between the various experiments, but these minor changes have no impact on the results.

4.1.1 Spatially resolved detection

Right after passing the polarization optics the beam is split, so that the image of the intensity distribution within the laser (near-field) and the spatial Fourier transform of the light field (far-field) can be captured simultaneously. A cooled charge-coupled device (CCD) camera (Apogee AP6-E) with a resolution of 1024x1024 pixels and 14 bit color depth is used for this. The pixels are 24 μm large, the typical near-field image of a 40 micron VCSEL is about 8 mm across (200-times magnification). The minimum exposure time of the camera is 0.02 s, thus all images taken are time averaged.

The Fourier images of the laser emission taken with the CCD camera have to be calibrated from pixels to divergence angles or (which is more appropriate for this work) to wave numbers (in units of $1/\mu\text{m}$). A separate setup is used to measure the divergence angles of the VCSELs at appropriate parameter settings. This setup consists only of the VCSEL on a mount with heat sink (without the airtight box) and the CCD camera, with an adequate neutral density filter in between. Since the (half cone) divergence angle can be as large as 32° , the camera has to be very close to the VCSEL to capture the whole beam. For practical reasons only modes with smaller divergence angles are selected for this measurement. By increasing the distance between camera and VCSEL and taking a picture for each distance setting, the divergence angle of a specific mode can be determined. Since the size of this same mode in pixels can be obtained with the standard

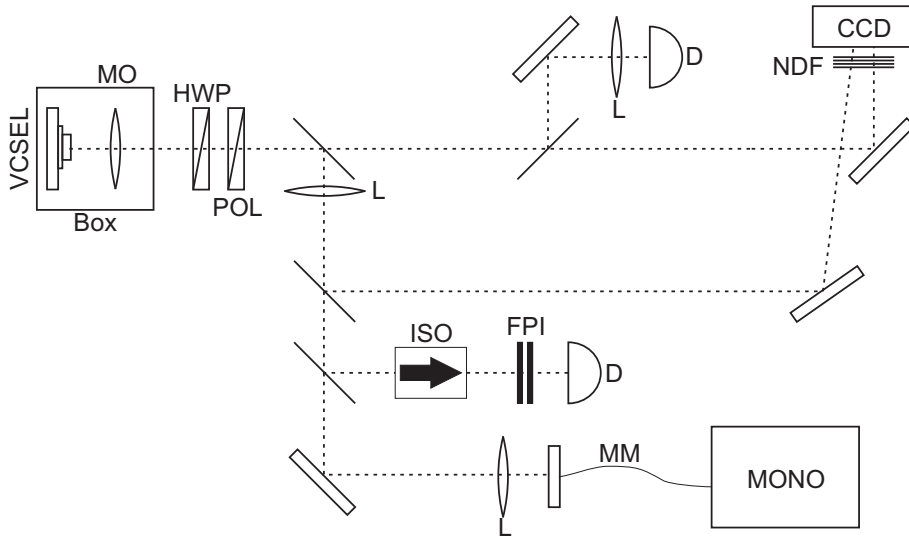


Figure 4.1: Schematic of the setup used for the experiments in chapters 4 and 5. The abbreviations denote the following components: MO – microscope objective, Box: airtight box around the VCSEL and the MO, HWP – half-wave plate, POL – linear polarizer, L – lenses, D – photo detectors, NDF – neutral density filters, CCD – CCD camera, ISO – optical isolator, FPI – scanning Fabry-Perot interferometer, MM – multi-mode fibre, MONO – monochromator.

setup, a calibration factor for pixels to divergence angles is thus obtained. With

$$\alpha = \arcsin \frac{k_{\perp}}{k_0} \quad \text{and} \quad k_0 = \frac{2\pi}{\lambda}, \quad (4.1)$$

(with $\lambda = 780$ nm for the square lasers and $\lambda = 980$ nm for the circular lasers) the transverse wave number k_{\perp} can be determined.

4.1.2 Devices for spectral measurements

4.1.2.1 Plano-planar FPI

For optical spectra with higher resolution than those obtained with the spectrometer a plano-planar scanning Fabry-Perot interferometer (FPI) is used. It is made up of two highly reflective mirrors ($> 99\%$) from EKSMA with the reflective sides facing toward each other. The back sides are anti-reflection coated and have a wedge of 1° to avoid interference effects due to parasitic reflections. The mirrors are put into two mounts, whose distance and respective orientation can be change with three piezoelectric actuators (from Thorlabs). The actuators enable motion along the optical axis and tilting around all three axes. They are powered by three individual high voltage supplies. The free spectral range (FSR) and finesse of the FPI is selected individually for each experiment. To avoid feedback into the VCSEL an optical isolator (DLI 1 from Linos) is put in front of the FPI.

In a second type of plano-planar FPI, piezo actuators with strain gauges are used. This enables a variation of the mirror distance in small steps (minimum $0.1 \mu\text{m}$) with high accuracy, good reproducibility, and without hysteresis. This allows a very high

resolution, only limited by the mirror transmissivity, the adjustment of the mirrors, and the stability of the laser operation. A system with three actuators and three individually calibrated voltage amplifiers from Piezosysteme Jena is used for this. This system allows measurements with spatial and spectral resolution simultaneously. The experiments will be described in section 4.2.5.

4.1.2.2 Confocal FPI

One of the major drawbacks in using a plano-planar FPI for experiments with broad-area VCSELs is that it is less suited for highly divergent modes, since the overlap of iteratively reflected tilted waves and thus their ability to interfere decreases with the divergence angle. The best case when using a plano-planar FPI is a collimated gaussian beam with its beam waist between the two mirrors and a marginal divergence. A more suitable device for large divergence angles is the confocal Fabry-Perot interferometer (cFPI). In such a device the frequencies of the modes with odd order (in terms of Gauss-Laguerre or Gauss-Hermite modes) are grouped together at the frequency of the axial mode and all modes with even order are grouped together shifted by half an FSR. That means that the mode order is of no importance when using a cFPI, accordingly it is applicable even for highly divergent modes. This argument is also true for non-Gaussian modes, since they can be expanded from Gaussian modes.

The scanning cFPI used here consists of two highly reflective concave mirrors from Laseroptik with a radius of curvature of -50 mm. One is mounted onto a holder with a single built-in piezo actuator, enabling scanning operation. The second is set at a distance of $d = 50$ mm from the other. The beam is focussed into the center between the mirrors. The FSR of the cFPI is $c/4d = 1.5$ GHz, thus a very high resolution is possible already with rather low finesse values.

4.2 Experimental observations

The experiments detailed here focus on the characterization of the transverse patterns emitted by the VCSELs. For this the near-field and far-field emission is studied for different settings of the operating parameters temperature and current in the first section. This is followed by a more in-depth analysis of the rather special diamond-shaped billiard patterns. It turns out that the emission of the VCSELs can be attributed to three different categories, corresponding to three regions in the far-field emission.

Section 4.2.3 considers the spontaneous emission below threshold, where several interesting features are found in the comparison between below and above threshold emission. This is followed by the investigation of the spectral characteristics, which provide some insight into the correlation between the emitted spatial states and their wavelengths.

4.2.1 Types and length scales of spatial states

In the following sections all images of near-fields and far-fields show the total intensity, i.e. the sum of horizontally and vertically polarized light. The optical axis always lies in the center of the far-field images. To enable a direct comparison between the injection current

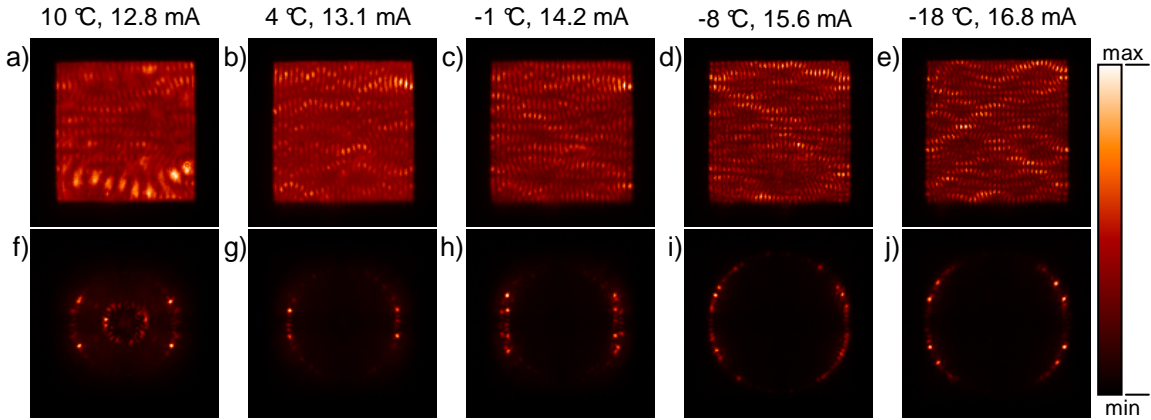


Figure 4.2: Temperature dependence of the laser emission (total intensity, near-field (a-e) and far-field images (f-j)) of laser 30-3 just above threshold. Temperatures and injection currents are given at the top of each column. The current was selected to be just above threshold. The respective pump rates are 0.16, 0.13, 0.16, 0.18, 0.14. The range of the far-field images is -4.9 to $4.9 \mu\text{m}^{-1}$ horizontally and vertically. The color table indicated on the right (black to red to white) is used for all intensity images throughout this thesis. Images are scaled to the respective maximum in order to enhance the contrast.

and the laser threshold the pump rates are given in the captions of the figures (see section 3.4.2 for the definition of the pump rate). All intensity images throughout the thesis are color-coded as indicated on the right of fig. 4.2. Note that the given temperatures are not the effective temperatures inside the laser but the heat sink temperatures read out from the thermometer attached to the copper block around the laser.

During systematic measurements of the intensity distributions of near-field and far-field it was found that the far-field distribution is better suited for a characterization and interpretation of the underlying mechanisms. Thus in most descriptions of the experimental observations the far-field distribution is considered first.

4.2.1.1 Temperature dependence of the emission

For the square lasers 30-3, 40-5, and 40-7 operating at threshold figures 4.2, 4.3, and 4.4 show the dependence of the emission patterns on the heat sink temperature. The injection current is chosen so that the first pattern emerging at threshold is clearly visible (i.e. the pump rate is well above zero). The temperatures were selected to show the variety of patterns observed in the emission of these VCSELs.

The far-field images show emission along rings, predominantly with well defined transverse wave numbers. In most cases only one transverse mode is excited near threshold (theoretically at threshold exactly one mode is excited [56]). Sometimes the thresholds of the modes are very close together, e.g. in fig. 4.2(f) two rings are evident. In many cases, with decreasing temperature and increasing wave number, the number of peaks excited on one ring decreases as well. A good example for this is the transition from fig. 4.3(g) to (h) to (i).

An important feature that is conspicuous in all far-field images is the dependence of the radius of the rings on temperature. In each figure from left to right the temperature

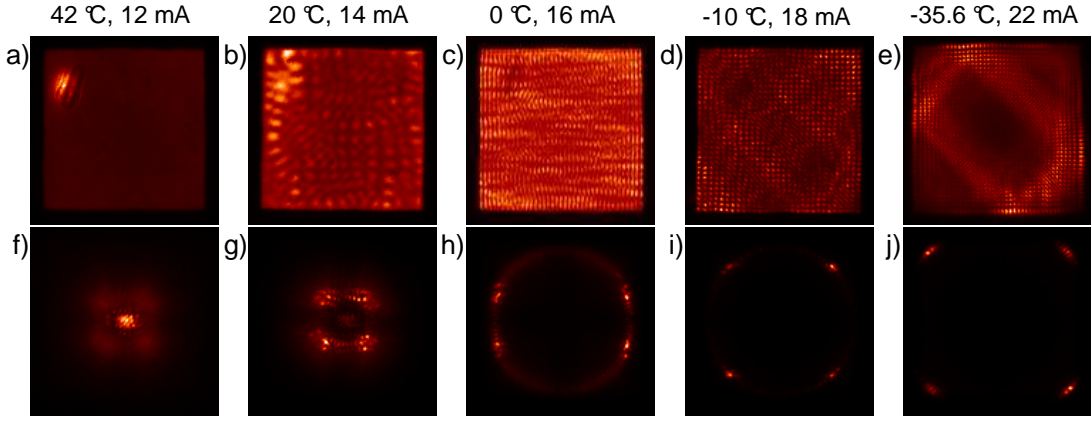


Figure 4.3: Temperature dependence of the laser emission (total intensity, near-field (a-e) and far-field images (f-j)) of laser 40–5 just above threshold. The respective pump rates are 0.05, 0.16, 0.19, 0.20, 0.15. The range of the far-field images is -4.7 to $4.7 \mu\text{m}^{-1}$. See caption of fig. 4.2 for further details.

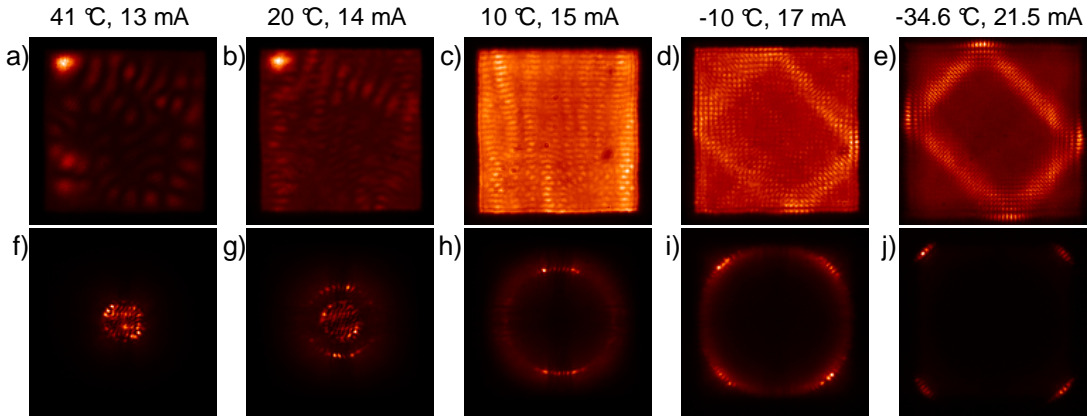


Figure 4.4: Temperature dependence of the laser emission (total intensity, near-field (a-e) and far-field images (f-j)) of laser 40–7 just above threshold. The respective pump rates are 0.18, 0.18, 0.20, 0.13, 0.13. The range of the far-field images is -4.7 to $4.7 \mu\text{m}^{-1}$. See caption of fig. 4.2 for further details.

is decreased and a correlated increase of the wave number is evident. Corresponding to this trend it is possible to classify the patterns shown in figures 4.2, 4.3, and 4.4 into three categories related to the transverse wave number k_{\perp} , respectively the heat sink temperature T :

1. Region I: typical values $T \gtrsim 20^{\circ}\text{C}$, $k_{\perp} \lesssim 1.8 \mu\text{m}^{-1}$. The far-field emission is found close to the optical axis. Single-humped peaks (fig. 4.3(f)), rings with small k_{\perp} (central ring in fig. 4.2(f)), or small circular areas filled with ripples and distinct peaks (fig. 4.4(f)) are observed.
2. Region II: typical values $-20^{\circ}\text{C} \lesssim T \lesssim 20^{\circ}\text{C}$, $1.5 \mu\text{m}^{-1} \lesssim k_{\perp} \lesssim 3.8 \mu\text{m}^{-1}$. Here the far-field emission is in general dominated by four intense Fourier components, which are situated rather close to one of the axes (small k_x and large k_y or vice versa), which

means they are either oriented horizontally or vertically (e.g. fig. 4.2(g), 4.3(h), 4.4(h)). Also less ordered states are found (e.g. fig. 4.2(h-j)).

3. Region III: typical values $T \lesssim -10^\circ\text{C}$, $k_\perp \gtrsim 4.0\ \mu\text{m}^{-1}$. The far-field consists of four groups of Fourier components which are located close to the diagonal. These groups consist of several Fourier components, the internal structure differs between different lasers. Typical patterns belonging to this region are shown in fig. 4.3(j) and fig. 4.4(j). Note that fig. 4.2(j) represents a not attributed to region III but rather region II.

Some emission patterns are superpositions of the three cases, e.g. fig. 4.4(g). Other cases are less easily categorized, e.g. fig. 4.3(g) or (i). This categorization into three regions is a rather robust feature observed in all VCSELs under study.

The near-field patterns correspond to the far-field emission in a straight-forward way: every Fourier component found in the far-field images constitutes a tilted wave and the superposition of the various waves creates a wavy stripe pattern as seen in most near-field images. The general trends described above are analogously valid here: an increasing length scale denotes a decreasing transverse wavelength. The decreasing number of peaks on a circle found in the far-field emission for low temperatures corresponds to more regular stripe patterns.

The classification of the far-field emission into three regions is analogously applicable to the near-field patterns:

1. Region I: Here localized spot (fig. 4.3(a)) and irregular long-wavelength patterns (fig. 4.4(a)) are observed. It is important to point out that true on-axis emission would correspond to a homogeneous intensity distribution in the near-field. This is never observed in the experiment. The single-humped on-axis emission found in some far-field images corresponds to a strongly localized peak in one corner of the laser aperture. Such localized spots are found in several but not all devices.
2. Region II: The near-field emission shows more or less well ordered wavy stripe patterns, i.e. two-dimensional sine waves oriented in one direction, modulated more slowly in the orthogonal direction (a rather nice example is shown in 4.4(c)).
3. Region III: Diamond-shaped patterns of different geometry are found in this region. The emission is strongly localized to the diamond shape and large areas of the aperture remain inactive. This type of pattern is described in details in section 4.2.2.

It was described in section 2.4 and investigated in section 3.4.4 that the selection of transverse modes in the VCSELs is in part controlled by the detuning δ between the longitudinal resonance of the cavity and the wavelength of the gain maximum. This detuning in turn is controlled by the heat sink temperature. The behavior of the VCSELs shows that this mechanism is responsible for the selection of the pattern length scales. This will be quantitatively analyzed in section 4.3.4.

The emission of the circular lasers shows less complexity: figure 4.5 illustrates near-field and far-field emission with the same layout as before. Again the dependence on

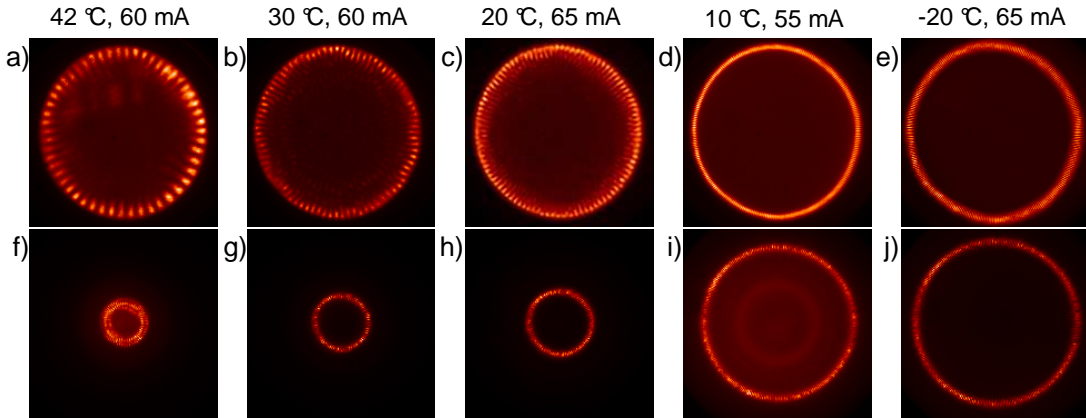


Figure 4.5: Temperature dependence of the laser emission (total intensity, near-field (a-e) and far-field images (f-j)) of laser 80–1 just above threshold. The respective pump rates are 0.25, 0.19, 0.27, 0.27, 0.29. The range of the far-field images is -2.8 to $2.8 \mu\text{m}^{-1}$. See caption of fig. 4.2 for further details.

temperature is depicted for modes found close to threshold. The divergence angles are lower in these lasers (compared to the square lasers at the same temperature settings), thus the area of the far-field images is somewhat smaller (see caption).

As with the square lasers the emission shows a dependence of the dominant length scale on temperature. A difference is that here rings are found in the far-field as well as the near-field emission for all temperatures. With decreasing temperature the ring in the far-field grows, together with the transverse wavelength of the azimuthally modulated ring in the near-field. Such patterns are typical for this type of VCSELs [91, 93]. Note that the rings in subfigures (d,e,i,j) are still modulated azimuthally, but due to the small modulation wavelength the intensity appears to be nearly homogeneous.

The near-field images show that the circular lasers tend to operate close to their circular boundary. The reason for this behavior, which is typical for the circular lasers but not observed in the square devices, will be discussed in section 4.2.3.

It is apparent that the wavelength of the azimuthal modulation of the ring decreases with temperature. The simple geometries of near-field and far-field emission serve as a way to calculate the wave number of the pattern from the order of the azimuthal standing wave: the ring in the near-field image has 52 humps on a $2\pi \cdot 40 \mu\text{m}$ circumference, which results in a wavelength for the electrical field (which is decisive for the optical Fourier transformation) of $9.7 \mu\text{m}$. With $k = 2\pi/\lambda$ the transverse wave number should be $0.65 \mu\text{m}^{-1}$. The measured wave number of the outer ring in the far-field image (fig. 4.5(f)) is indeed $0.65 \mu\text{m}^{-1}$. This confirms the value of the constant which is used to calibrate the far-field images to wave numbers (cf. section 4.1.1).

4.2.1.2 Dependence on injection current

The next step is to look at the development of the emission with increasing injection current. This is illustrated for device 30–3 in fig. 4.6 and for VCSEL 40–5 in figures 4.7 and 4.8, respectively. Here the heat sink temperature is held constant and the injection

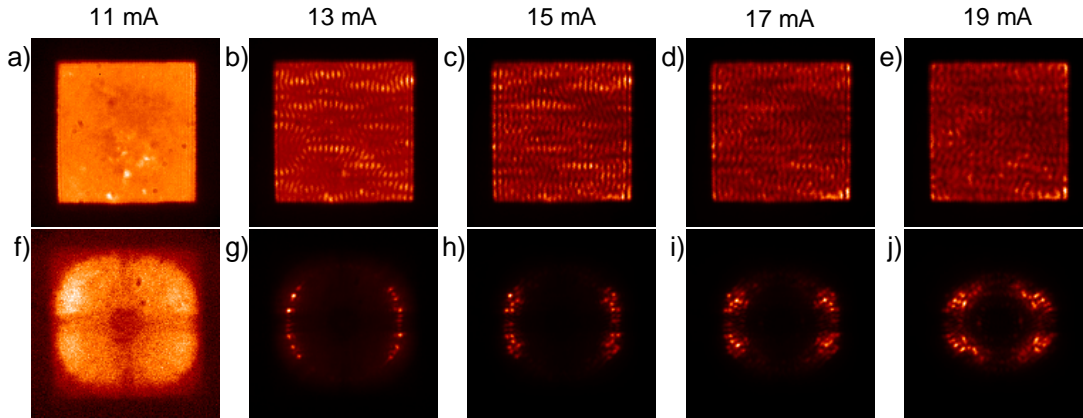


Figure 4.6: Current dependence of near-field (a-e) and far-field images (f-j) emission of laser 30-3 at 5°C heat sink temperature. The respective pump rates are -0.05 , 0.12 , 0.29 , 0.47 , 0.64 . The range of the far-field images is -4.9 to $4.9 \mu\text{m}^{-1}$. See caption of fig. 4.2 for further details.

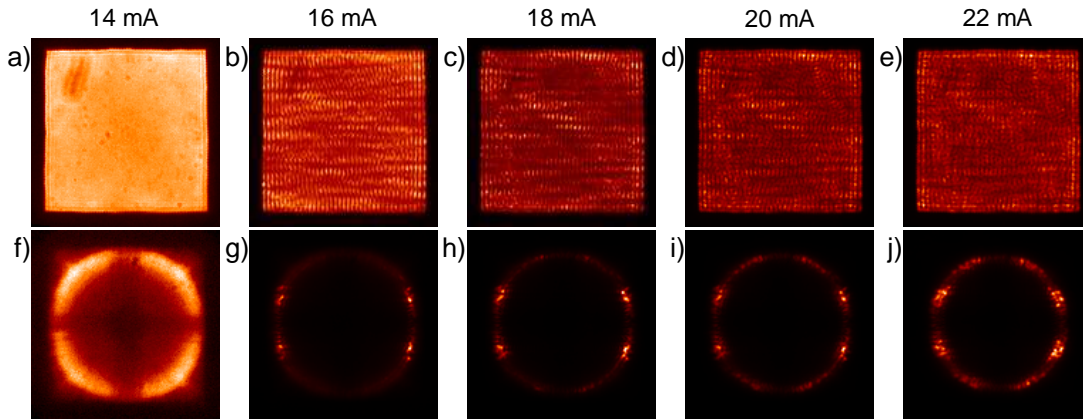


Figure 4.7: Current dependence of near-field (a-e) and far-field images (f-j) emission of laser 40-5 at 0°C heat sink temperature. The respective pump rates are 0.03 , 0.19 , 0.33 , 0.48 , 0.63 . The range of the far-field images is -4.7 to $4.7 \mu\text{m}^{-1}$. See caption of fig. 4.2 for further details.

current is changed. For the first column the current is set below laser threshold, i.e. the amplified spontaneous emission¹ (ASE) is shown. While the near-field distribution is more or less homogeneous (disregarding the spots of debris from the transition through the neutral density filters), the far-field images exhibit a concentration of the emission to a certain range of wave numbers. Comparing figures 4.7(f) and 4.8(e), it is apparent that this dominant wave number also changes with temperature. This means that also below threshold the length scales are controlled by the detuning δ , though the hump in the far-field distribution below threshold is much broader than the rings of the modes above threshold. This and other characteristics of the emission below threshold are described in more detail in section 4.2.3.

The other columns in each figure illustrate the emission characteristics with increasing positive pump rate. It is important to note that though the heat sink temperature is

¹Amplified spontaneous emission denotes the spontaneous emission of a laser that is amplified by stimulated emission in the gain material and filtered by the resonance condition of the laser cavity.

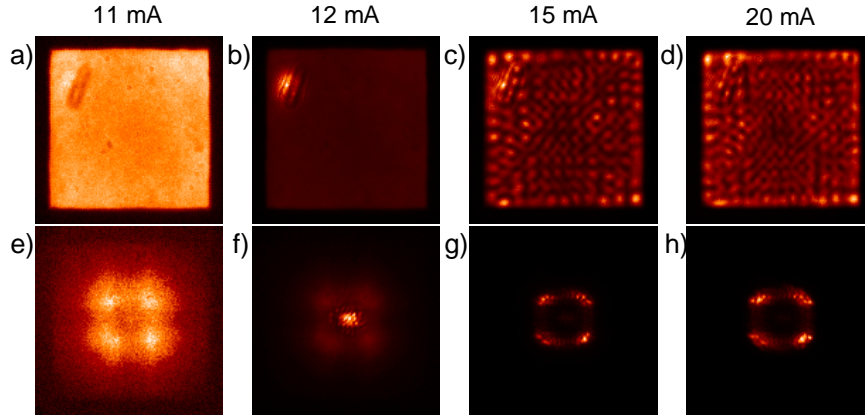


Figure 4.8: Current dependence of near-field (a-d) and far-field images (e-h) emission of laser 40–5 at 42°C heat sink temperature. The respective pump rates are -0.01 , 0.08 , 0.35 , 0.79 . The range of the far-field images is -4.7 to $4.7 \mu\text{m}^{-1}$. See caption of fig. 4.2 for further details.

held constant, the temperature inside the laser is rising with current due to the effect of Joule heating. This is investigated in more detail in section 4.2.5. Here it is sufficient to keep in mind that the laser temperature rises with current, which in turn also affects the detuning.

Several general features are observed above threshold: quite apparent in fig. 4.6 is the decrease of the dominant transverse wave number(s) with increasing current. At 13 mA the single ring has a wave number of $3.0 \mu\text{m}^{-1}$, at 19 mA the innermost mode has a wave number of $2.0 \mu\text{m}^{-1}$. At the same time the number of modes increases as the current goes beyond the thresholds of modes less favored by the gain and the cavity resonances.

In principle the observed trends – the decrease of the transverse wave number(s) and the increase of the number of excited modes with current – are general characteristics valid for all VCSELs. One exception is the category of patterns called region I. fig. 4.8 shows the emission of laser 40–5 at 42°C, which is a typical example for patterns attributed to region I. Just above threshold (12 mA, subfigure (g)) the far-field image shows an irregular spot at the optical axis (radius about $0.46 \mu\text{m}$), the near-field emission is dominated by a peak at the upper left corner. With rising current the far-field distribution concentrates on a ring with a radius of $1.5 \mu\text{m}^{-1}$ with a dominant four-fold symmetry. The near-field pattern shows a roughly square symmetry. Here the first trend mentioned above is reversed: with the increase of the injection current the dominant transverse wave number increases. In fact this increase of the wave number with current for patterns in region I is also a general characteristic valid for all lasers.

Comparing figures 4.7(g) and (j) another important feature can be illustrated: it was stated above that modes belonging to region II predominantly consist of four intense Fourier components aligned horizontally (i.e. with $k_x \gg k_y$) or vertically (i.e. with $k_y \gg k_x$). A horizontally aligned mode is shown in fig. 4.7(g). It was stated above that the increase of the injection current excites additional modes. In some cases these extra modes are oriented orthogonally with respect to the orientation of the mode at threshold. That means that the four Fourier components oriented horizontally are joined by four vertically oriented components in the present example. In fig. 4.7(i) the transverse wave

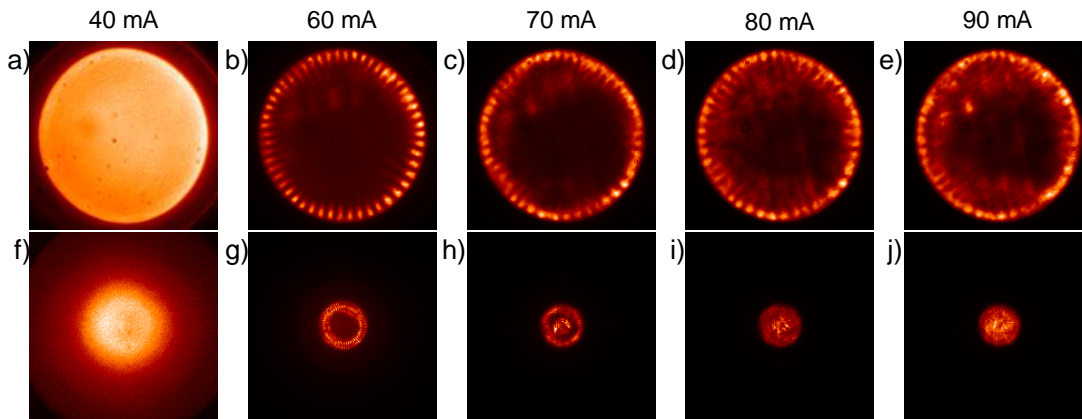


Figure 4.9: Current dependence of near-field (a-e) and far-field images (f-j) emission of laser 80-1 at 42°C heat sink temperature. The respective pump rates are -0.17 , 0.25 , 0.45 , 0.66 , 0.87 . The range of the far-field images is -2.8 to $2.8 \mu\text{m}^{-1}$. See caption of fig. 4.2 for further details.

numbers of the two orthogonally oriented modes are very close together. In other devices, a separation of up to $0.5 \mu\text{m}^{-1}$ was observed. It will be discussed in detail in chapter 5 that these orthogonally oriented modes also have orthogonal polarizations.

The general behavior can be summarized and interpreted as follows: with increasing current the effective laser temperature also increases due to Joule heating. This leads to an increase of the detuning and thus the dominant transverse wave number shrinks. At the same time the pump rate increases, which results in a broadening of the gain spectrum (filtered by the transverse cavity resonances). This in turn leads to an excitation of additional modes. As a general rule it can be stated that the lasers start to emit at the outermost wave number for a given temperature. If the mode at threshold belongs to region II or III only modes with smaller radius are excited with increasing current. Generally the additional modes are excited starting at 10 to 30% above the laser threshold. This range decreases with temperature. For the lowest temperature settings in some cases two modes are observed already at or only slightly above threshold.

In region I the detuning is already small. At threshold a mode with a low transverse wave number is excited. Increasing the injection current at some point the detuning becomes positive (i.e. the emission wavelength is higher than the longitudinal resonance). For positive δ no pattern formation is expected [24, 94] and the near-field intensity distribution should be homogenous. However in larger VCSELs homogeneous emission is never observed, which can in part be attributed to a complex interplay of anisotropies and inhomogeneities [100]. To a certain degree the experimental observations suggest that the transverse wave number increases again for increasing positive detuning. The possible origins of the localization of the spots to a corner of the aperture is discussed in section 4.3.1.

Again the same scenario for the circular lasers is simple. Figure 4.9 and 4.10 show the current dependence of the emission of device 80-1 at 42°C and 10°C. The first column shows the ASE just below threshold. Note that the pump rate for fig. 4.10(a) and (f) is $p = 0.15$, though a negative value is expected since the near-field and far-field

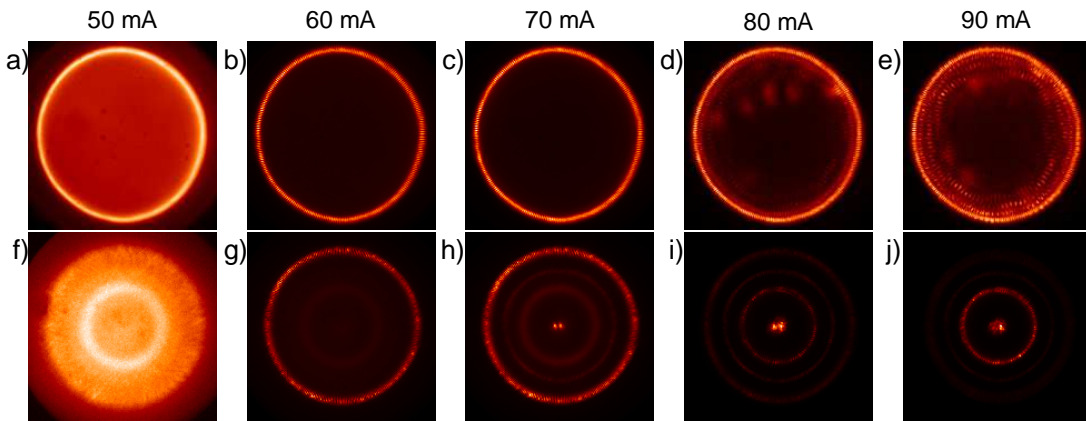


Figure 4.10: Current dependence of near-field (a-e) and far-field images (f-j) emission of laser 80-1 at 10°C heat sink temperature. The respective pump rates are 0.15, 0.38, 0.61, 0.84, 1.07. The range of the far-field images is -2.8 to $2.8 \mu\text{m}^{-1}$. See caption of fig. 4.2 for further details.

images can only be interpreted as representing emission below threshold. This is due to the difficulties in determining the laser threshold addressed in section 3.4.2. Though the injection current is set above the threshold value derived in that section, the intensity of the emerging mode is still of the order of the spontaneous emission intensity.

Some of the general trends observed in the square lasers can be found here as well: Images taken at a high temperature are shown in fig. 4.9. The transverse wave number excited at threshold is small, around $k_{\perp} = 0.64 \mu\text{m}^{-1}$. With increasing current additional modes with lower k_{\perp} are excited until at 90 mA the whole central area inside the initial ring is emitting. In the near-field images a long wavelength pattern consisting of a ring with azimuthal modulations around the border of the laser aperture is apparent. With increasing current ripples inside this ring, covering parts of the aperture, are excited.

For a lower temperature setting (fig. 4.10) the emission starts at a large wave number ($k_{\perp} = 0.64 \mu\text{m}^{-1}$ in subfigure (g)) and lower order modes are excited for higher currents. It is also visible that the modes initially excited at threshold fade out with increasing current. Note that the on-axis mode is somewhat favored in the circular lasers and thus it is emerging already at 70 mA (subfigure (h)), at lower current than the ring visible in subfigure (j).

In fig. 4.10 it is clearly visible that the wave number of the modes does not change continuously. Rather only the intensity of certain modes changes, while the wave number is constant. The impression of a continuous change of the wave number stems from the small mode separation found in the square VCSELs. Nonetheless, the analysis of the experimental observations showed that also for square VCSELs a discrete transverse mode spacing is found.

4.2.1.3 Temperature dependence at constant current

For completeness the temperature dependence of the emission of laser 40-7 is shown again in figure 4.11, but for a constant injection current (in contrast to fig. 4.4, where a more or less constant pump rate and thus a different injection current for each temperature

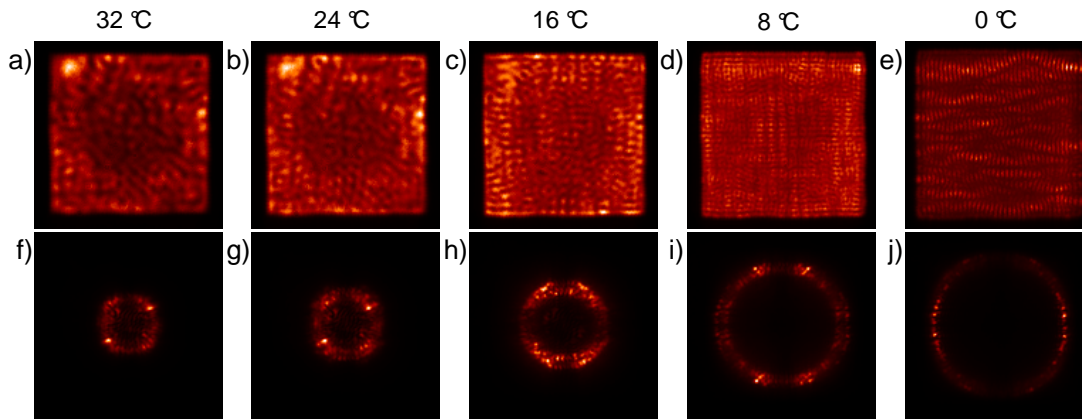


Figure 4.11: Temperature dependence of near-field (a-e) and far-field images (f-j) emission of laser 40–7 at 17 mA injection current. The respective pump rates are 0.53, 0.48, 0.40, 0.35, 0.27. The range of the far-field images is -4.7 to $4.7 \mu\text{m}^{-1}$. See caption of fig. 4.2 for further details.

was selected). For high temperatures a continuous ring with a small wave number and some sharp peaks on it is observed in the far-field images, corresponding to an irregular near-field pattern. With decreasing temperature the dominant transverse wave number increases, while the number of excited modes decreases. At 0°C only one wave number is visible in the far-field image. Accordingly the transverse wavelength of the near-field patterns decreases while the patterns get more regular.

A superposition of two effects is visible here: the decrease of the temperature and thus an increase of the negative detuning; and a decrease of the pump rate due to the rising laser threshold with decreasing temperature (cf. section 3.4.2 for the threshold values). This corresponds to the two trends visible in the figure: the growing dominant wave number and the decrease of the number of excited modes.

4.2.1.4 Uncommon emission patterns

Up to now general characteristics valid for all VCSELs under study were presented. In addition, also some interesting and insightful phenomena were observed that are only found in individual devices. In particular lasers 40–1 and 40–9 show rather special emission characteristics that are described in the following.

The temperature dependence of the near-threshold emission for laser 40–9 is shown in fig. 4.12. The general behavior is quite typical: with decreasing temperature, the dominant transverse wave number increases. For high temperatures (here $T = 15^\circ\text{C}$, subfigure (a) and (f)) the typical localized peak is observed in the near-field, corresponding to a far-field emission close to the optical axis. Here this type of emission ranges to significantly lower temperatures than in other devices and it is always found to be a double-humped peak (in near-field and far-field images). For the lowest temperature ($T = -25^\circ\text{C}$, subfigure (e) and (j)) the diamond-shaped patterns described above are observed.

In addition to these observations that are consistent with general trends discussed above, the rather special shape of the patterns attributed to region II is unique for this devices: instead of the known four-fold symmetry, the far-field images show two groups

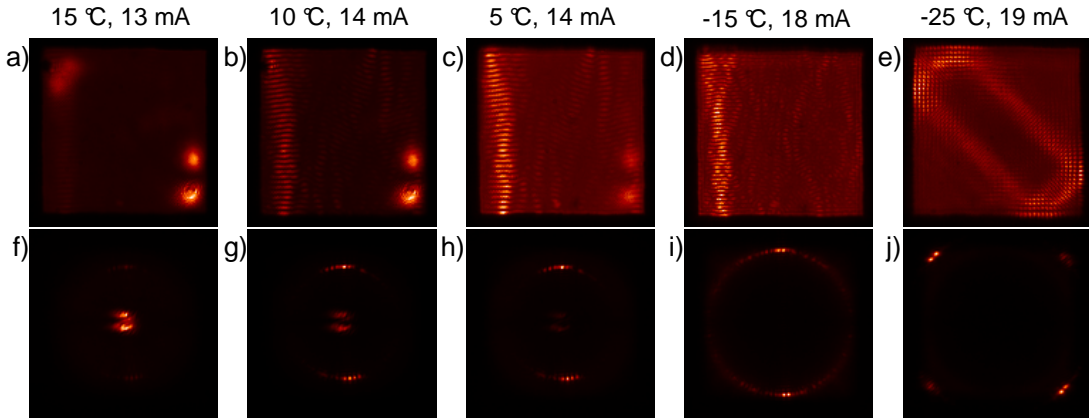


Figure 4.12: Temperature dependence of near-field (a-e) and far-field images (f-j) emission of laser 40–9 just above threshold. This laser shows rather uncommon emission in region II, instead of the usual four-spot modes two elongated spots with $k_y \approx 0$. The respective pump rates are 0.16, 0.19, 0.12, 0.14, 0.05. The range of the far-field images is -4.7 to $4.7 \mu\text{m}^{-1}$. See caption of fig. 4.2 for further details.

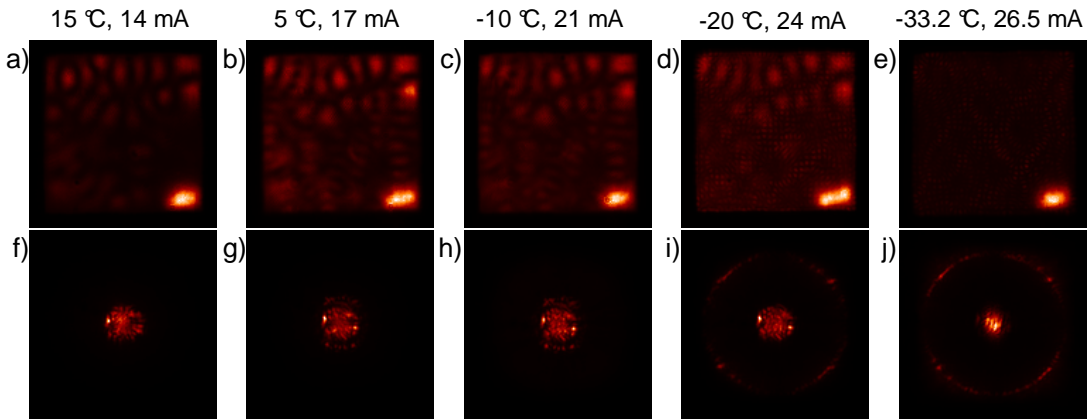


Figure 4.13: Temperature dependence of near-field (a-e) and far-field images (f-j) emission of laser 40–1 just above threshold. This laser has a strong “hot-spot” in one corner of the aperture, which has always the lowest laser threshold. To display also high transverse modes the laser has to be driven considerably above threshold. The respective pump rates are 0.50, 0.54, 0.55, 0.53, 0.40. The range of the far-field images is -4.7 to $4.7 \mu\text{m}^{-1}$. See caption of fig. 4.2 for further details.

of spots diametrically opposed to each other and with $k_x \approx 0$. The groups are quite broad along the ring with the respective wave number and three or more distinct peaks are visible. In the near-field emission this constitutes a stripe pattern, which is not covering the whole aperture, but only one side. Nonetheless this is the closest resemblance to the two-dimensional stripe pattern that is predicted by the simple model discussed in section 4.3.6. Thus this structure is of some interest for comparisons with this model.

Device 40–1, depicted in fig. 4.13, has the specialty that the spot in the lower right corner of the near-field images is present for nearly all temperature and current settings. Corresponding to this the far-field always features a peak close to the optical axis. This

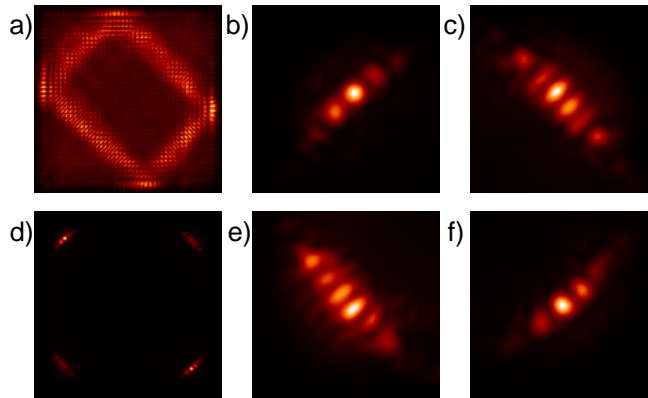


Figure 4.14: Details of the billiard-type emission for laser 40–7 at $T = -34.6\text{ }^{\circ}\text{C}$ and $I = 22\text{ mA}$. (a) near-field, (d) far-field images. The other subfigures show a 5 times magnification of the four Fourier components (upper left (b), upper right (c), lower left (e), lower right (f)). The diametrically opposed Fourier constituents ((b) and (f), resp. (c) and (e)) are sufficiently identical and only one of each pair is shown in the other figures (4.15, 4.16, 4.17). The width of the magnified far-field images is $1.9\text{ }\mu\text{m}^{-1}$.

mode always has the lowest threshold, hence the currents in the figures are selected far above threshold to illustrate that the laser also emits off-axis patterns. Though some other devices also feature localized spots over large parameter ranges (e.g. laser 40–9, as described above), device 40–1 is unique in this way. The persistent on-axis spot will be of some importance later on, because it yields a convenient access to the longitudinal resonance wavelength of the cavity (cf. section 4.3.4).

Possible sources for the spot – e.g. an enhanced carrier density at that corner of the aperture or thermal lensing due to increased non-radiative losses – are discussed in section 4.3.1.

4.2.2 Details of the billiard-type patterns

For heat sink temperatures below $-20\text{ }^{\circ}\text{C}$ the emission characteristic changes drastically: at some point the Fourier mode position in the far-field images changes to the diagonal and the near-field images show a regular diamond-shaped pattern that covers a much smaller area of the aperture than the patterns in region II. This type of emission is attributed to region III. The transition from region II to III will be detailed below, in section 4.2.4. Here, the patterns found in region III are described.

One examples is depicted in fig. 4.14, where near-field (a) and far-field images (d) are shown for device 40–7 and $-34.6\text{ }^{\circ}\text{C}$ heat sink temperature. The other subfigures display the four Fourier components magnified 5 times. The other examples, figures 4.15, 4.16, and 4.17, only include two adjacent Fourier peaks and the near-field image, because the diametrically opposed components are sufficiently identical. Note that not all lasers show this kind of unusual emission patterns. In some cases even for the lowest possible heat sink temperatures diamond-shaped patterns were not observed. In those VCSELs also the other types of patterns appear at lower temperatures and to reach emission of diamond-shaped patterns temperatures below the accessible minimum are necessary.

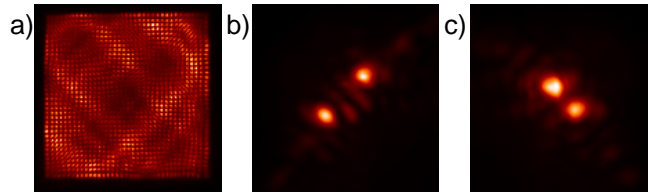


Figure 4.15: Details of the billiard-type emission for laser 40–3 at $T = -36.5^\circ\text{C}$ and $I = 21.5\text{ mA}$. Only the near-field image (a) and the upper left (c) and upper right (d) Fourier components are shown.

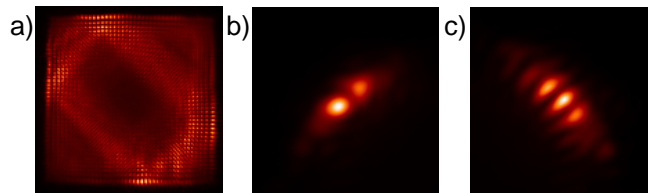


Figure 4.16: Details of the billiard-type emission for laser 40–5 at $T = -35.6^\circ\text{C}$ and $I = 22\text{ mA}$. Only the near-field image (a) and the upper left (c) and upper right (d) Fourier components are shown.

The patterns belonging to region III are equal to the quantum billiard structure described in [26, 27]. The patterns arise from transverse standing waves with a small wavelength that are reflected at the side boundaries due to total internal reflection and form a closed periodic orbit. In this region the trajectories are always aligned with the diagonal. Of course, trajectories with other tilt angles than 45° would be conceivable. Transverse modes belonging to region II can resemble such billiard-type patterns that are not aligned with the diagonal. These are much less regular and in most cases not perfectly periodic due to dislocations. Thus they are much more difficult to recognize. An example is shown in fig. 4.2(i). In [26] such patterns are called bouncing balls, to distinguish them from the diamond-shaped patterns with perfect periodicity. In the following the patterns belonging to region III are called “billiard-type” patterns, excluding the less regular patterns in region II.

The billiard-type patterns from different lasers show some differences. The pattern of device 40–9, e.g., is rather elongated compared to the others, i.e. two of the diagonal parts of the diamond are shorter than the others. This means that the phase relation between the four diagonally oriented waves is different for different lasers.

The localization of the standing wave in the near-field distribution demands the existence of additional side peaks to the main Fourier components of the far-field emission. These are found in the internal structure of each group of Fourier peaks. This structure is shown in the magnified far-field images in figures 4.14, 4.15, 4.16, and 4.17. The difference between the Fourier peaks located in the upper left corner and those located in the upper right corner of the far-field images is apparent (the diametrically opposed peaks are approximately equal). The internal structure of the groups of Fourier peaks is also different for different devices. It is found that a shorter diagonal path along the diamond-shaped localized wave in the near-field emission corresponds to a larger number of Fourier peaks

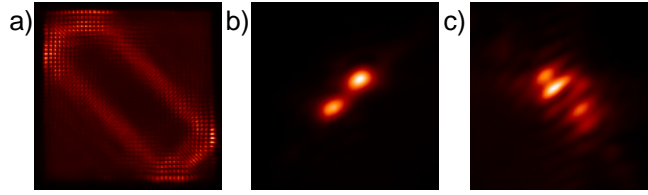


Figure 4.17: Details of the billiard-type emission for laser 40–9 at $T = -34.4^\circ\text{C}$ and $I = 22\text{ mA}$. Only the near-field image (a) and the upper left (c) and upper right (d) Fourier components are shown.

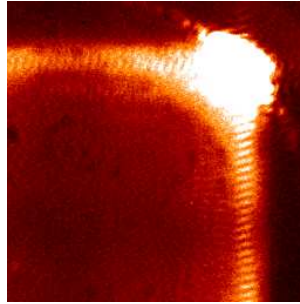


Figure 4.18: Magnified and strongly contrast enhanced area of the far-field image of the billiard-type pattern emitted by laser 40–5 at -36°C and 22 mA . The upper right group of Fourier peaks is shown together with the band of ripples connecting this group of peaks with the bottom right and the top left ones.

in the corresponding corner of the far-field images. In addition to different numbers of peaks, their mutual distance is also different for different shapes of the diamond-shaped pattern.

Note that nearly all lasers always show the same pattern shape in region III, even when the value of the transverse wave number changes. Only some devices, one example is shown in fig. 4.15, emit several different diamond-shaped patterns. In section 4.3.3 this type of patterns and their far-field distribution will be compared to numerical calculations.

The billiard-type patterns allow a comparison of near-field and far-field images similar to the one discussed in section 4.2.1.1 for the circular lasers. In the following this is done for the billiard pattern emitted by laser 40–5 (cf. fig. 5.14). By counting the stripes along the diamond shaped trajectory the corresponding wave number can be calculated with

$$k_{bill} = \frac{2\pi}{\Lambda} = m \frac{\pi}{a}. \quad (4.2)$$

Here k_{bill} is the transverse wave number of the Fourier components of the mode. Λ is the corresponding transverse wavelength, m is half the number of stripes counted in the near-field (half the number because we look at the intensity, which has twice the number of stripes as the optical field), and a the path length along which the stripes are counted. With $m \approx 56$ and $a = 40\ \mu\text{m}$ we obtain $k_{bill} \approx 4.4\ \mu\text{m}^{-1}$. The value obtained from the far-field images is $4.8\ \mu\text{m}^{-1}$. The agreement is not as good as in the comparison of near-field and far-field scaling of the modes emitted by the circular lasers.

In some cases the far-field images also show sequences of ripples connecting the Fourier

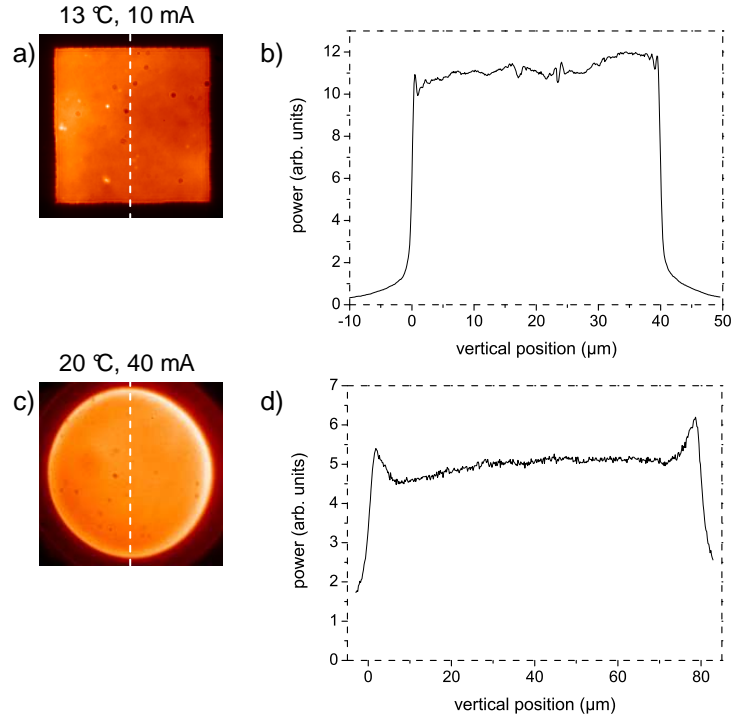


Figure 4.19: Near-field images of lasers 40–7 and 80–1 operating below threshold (a,c) with plots of vertical cuts through the images (b,d). The locations of the cuts are illustrated by the dashed lines through the near-field images. The respective pump rates are -0.19 and -0.22 .

components. These are hardly visible in intensity images, but can be made visible with strong contrast enhancing as shown in fig. 4.18. The spacing between the ripples corresponds to the minimal wave number step, i.e. to the boundary condition created by the oxide aperture. With the number of stripes, e.g. here in horizontal direction, k_x can be calculated. With $m = 40$ $k_x = 3.1 \mu\text{m}^{-1}$ is obtained, which corresponds to $k_{bill} = \sqrt{2}k_x = 4.4 \mu\text{m}^{-1}$. This is equal to the value obtained above. The origin of the ripples is considered in section 5.3.4.

4.2.3 Characteristics of the emission below threshold

It was mentioned above that also the ASE yields details worth inspecting. In this section the spatial homogeneity of the ASE is investigated, serving as an indication of the distribution of the carriers. Two other features of the ASE are investigated, namely the increased intensity near the diagonal in the far-field distribution and the intensity minima along the vertical and horizontal axes. This is followed by a study of the change of the observed length scale with temperature and current.

As seen in figures 4.6(a), 4.7(a), and 4.8(a) the near-field emission is in most cases essentially homogeneous. This is shown again in fig. 4.19(a) and (c) for lasers 40–7 and 80–1. Vertical cuts, as indicated by the dashed lines, are plotted in subfigure (b) and (d). For the square device the aperture has steep edges and is rather flat-topped. The slight gradient and the ripples and indentations are due to small inhomogeneities in the beam

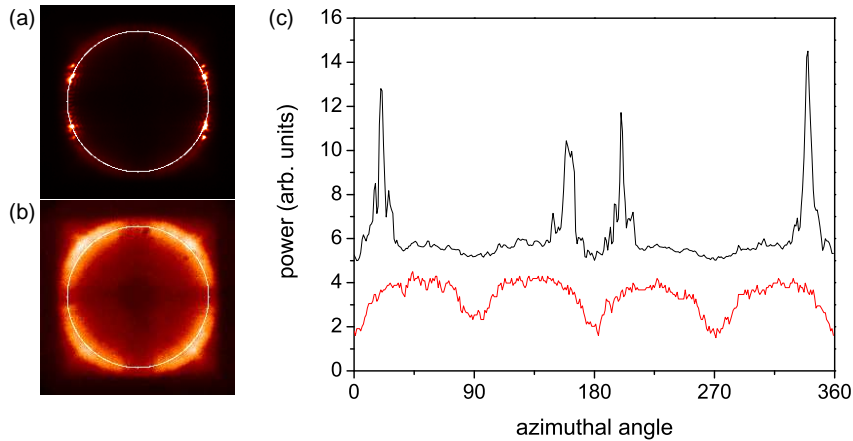


Figure 4.20: Laser 40–5 at $T = 0^\circ\text{C}$ above threshold ((a), 16 mA) and below threshold ((b), 14 mA). The rings denote the dominant wave number at 16 mA ($3.4 \mu\text{m}^{-1}$). (c) shows the azimuthal plots along the rings above threshold (black curve) and below threshold (red curve).

path as well as in the laser itself. The circular laser shows a rather pronounced rise of spontaneous emission at the boundary.

Note that the ASE well below threshold filtered by the laser mirrors is often used as an indication of the homogeneity of the pump current profile [18, 100]. In this case, where the difference between square and circular laser is very pronounced, it gives some insight into the selection of modes at threshold. In particular, the square devices show no pronounced pump inhomogeneity, while in the circular VCSELs a stronger spontaneous emission around the boundary is visible. For large area lasers a concentration of the current flow to the perimeter of the confinement is expected [152]. This can explain the fact that the emission above threshold of these lasers (nearly) always concentrates on a ring just inside the oxide aperture (as seen in fig. 4.5 e.g.).

Another feature of the ASE is illustrated in fig. 4.20. In (a) and (b) the far-field emission of laser 40–5 at $T = 0^\circ\text{C}$ and 14, respectively 16 mA injection current is shown. Above threshold the typical four Fourier components are apparent. The circles in both far-field images denote $k_\perp = 3.4 \mu\text{m}^{-1}$, the wave number of the emission above threshold. In subfigure (c) the azimuthal plots along these rings for (a) in black and for (b) in red are shown. The positions of the four Fourier components above threshold are visible as sharp peaks. Note that these positions differ from the positions of maximum intensity below threshold. The latter are found around the diagonals. It is found that this is a general feature: well below threshold the diagonal wave vector is favored.

An example of the evolution of far-field emission with temperature is shown in fig. 4.21. It is obvious that the peak emission wave number increases with decreasing temperature, as was already discussed for the emission above threshold. Another apparent feature are the indentations at $k_x = 0$ and $k_y = 0$. These can be seen as “forbidden” areas, where emission is not supported by the transverse cavity. These are typical features in all devices. They are responsible for the predominant four-fold symmetry in the emission above threshold (laser 40–9 is the only exception).

In the following the dependence of the dominant transverse wave number observed

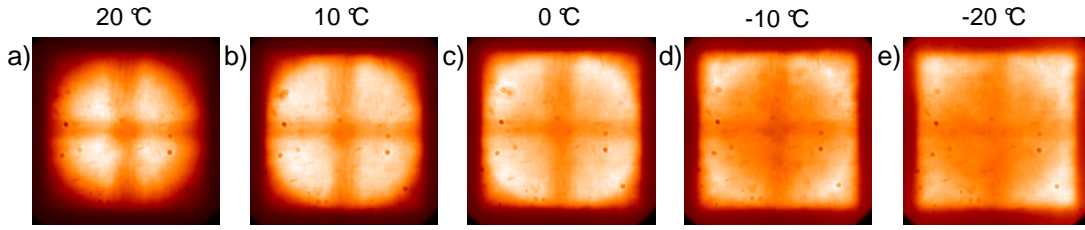


Figure 4.21: Temperature dependence of the below threshold far-field emission of laser 40–5 at $I = 10$ mA. The respective heat sink temperature is given at the top of each image. The respective pump rates are -0.17 , -0.22 , -0.26 , -0.33 , and -0.41 .

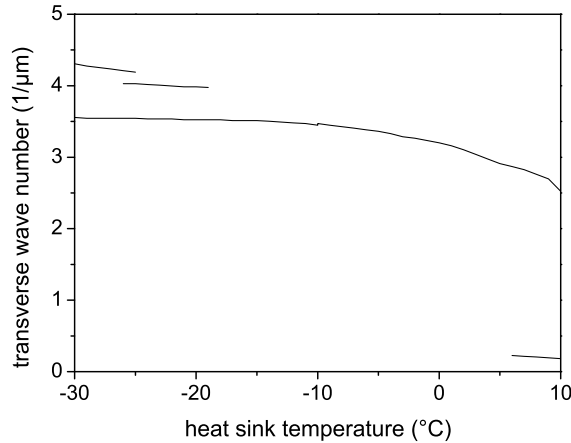


Figure 4.22: Temperature dependence of the critical wave number of device 40–9 below threshold. The laser is driven at 12 mA (10 to -10 °C) and 14 mA (-10 to -30 °C). See text for details on the critical wave number.

below threshold on temperature and current is investigated in more detail. The intensity of the ASE is maximal at the transverse wave number that corresponds to the tilted wave favored by the cavity resonance at a given detuning. Close to threshold it is an indication of the mode that will emerge above threshold. The wave number of the ring with higher intensity found in the ASE is termed “critical wave number” in the following. To analyze this quantity radial profiles of the far-field images are created. The local maxima of all peaks found in such a profile are recorded.

The detuning δ is controlled by the heat sink temperature. Therefore, fig. 4.22 shows the evolution of the critical wave number with temperature for device 40–9. The plot is made from two measurements: one at 14 mA for temperatures between -30 and -10 °C, the second at 12 mA for temperatures between -10 and 10 °C. The predominant feature of the plot is the continuous curve between $2.5 \mu\text{m}^{-1}$ and $3.6 \mu\text{m}^{-1}$. This represents emission in region II. Some on-axis emission tail is visible for temperatures above 5 °C. The high wave number tails on the left indicate emission in region III.

One apparent feature of the curves is that the critical wave number changes continuously with detuning δ . This is interesting insofar, as it was earlier shown that the wave number of the emission above threshold changes discretely, which is most evident in the circular lasers (cf. fig. 4.10). Nonetheless, also the critical wave number shows jumps at some

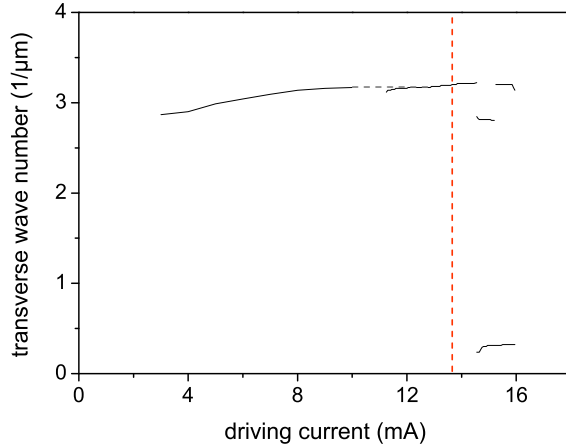


Figure 4.23: Dependence of the critical wave number of device 40–9 below and above threshold on injection current at $T = 0^\circ\text{C}$. The laser threshold is given by the red dashed line. Between 10 and 11 mA the neutral density filters in front of the CCD camera were changed. The dashed grey line serves to guide the eye over the gap between the disconnected curves.

points, namely at the transitions between the wave number ranges attributed to the three regions.

The current dependence of the critical wave number is plotted in fig. 4.23 for the same device as before and $T = 0^\circ\text{C}$. The laser threshold is indicated by the dashed red line. Note that also here the critical wave number changes continuously, but in the direction opposed to expectation based on earlier deductions: it was established that the increasing current also increases the laser temperature due to Joule heating. With increasing temperature the wave number should decrease. This is true above threshold, but apparently not below threshold. This illustrates that below threshold Joule heating is not the predominant effect. Below threshold the increase of the number of carriers in the conduction band with current leads to a change of the refractive index of the corresponding material. This in turn induces a blue-shift of the wavelength [134]. Since a lower wavelength corresponds to a higher detuning the transverse wave number increases. This effect and the red-shift induced by the Joule heating oppose each other. In the VCSELs under study the observed increase of the wave number with increasing current below threshold shows that the carrier-induced blue-shift dominates. Note that above threshold the number of carriers is constant and the thermal red-shift persists.

4.2.4 Temperature dependence of the Fourier mode position

In this section the dependence of the far-field patterns on the heat sink temperature is investigated quantitatively. For this purpose the coordinates (k_x, k_y) of the dominant Fourier components found in the far-field images are gathered from measurements covering the whole temperature range (-35 to 40°C) and several currents above threshold. The transverse wave number $k_\perp = \sqrt{k_x^2 + k_y^2}$ and the mode angle α , defined as the angle between the Fourier component and the horizontal axis, are calculated from the coordinates.

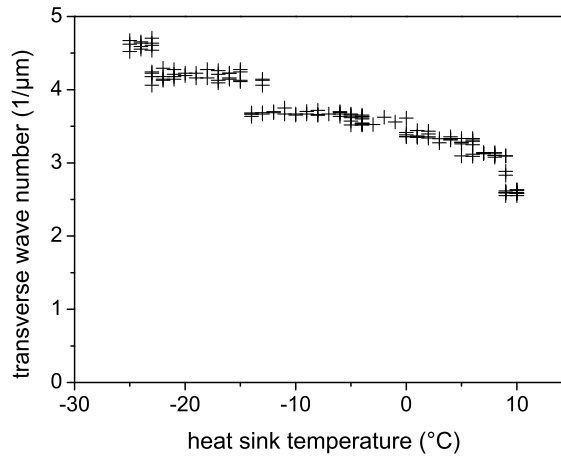


Figure 4.24: Temperature dependence of the wave numbers of transverse modes at threshold for device 40–5.

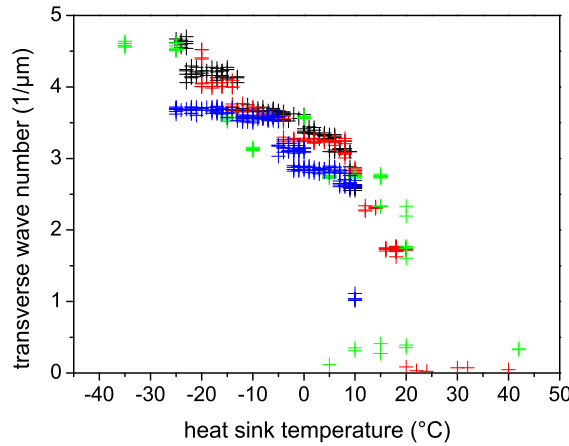


Figure 4.25: Temperature dependence of the wave numbers of transverse modes at threshold for various lasers: 40–5 (black), 40–7 (red), 40–9 (green), 30–3 (blue).

The dependence of the dominant wave number on temperature is quantified in fig. 4.24 for device 40–5. The graph is obtained by plotting the transverse wave number k_{\perp} of each dominant Fourier component against the respective temperature. The result shows the already discussed increase of the wave number with decreasing temperature. The dependence is apparently not linear. Temperature ranges where the wave number stays (more or less) constant are evident, interrupted by jumps to higher wave numbers (with decreasing temperature). The data points with $T < -15^{\circ}\text{C}$, separated from the rest by a rather large gap in the transverse wave number, represent diamond-shaped patterns whose Fourier components are found at the diagonal.

To show that the temperature dependence of the transverse wave number is a general feature, it is plotted in fig. 4.25 for four VCSELs. Here the temperature range covers all possible values, so that also on-axis emission is included. The large gap between the on-axis data points ($k_{\perp} < 1\ \mu\text{m}^{-1}$) and the others is typical for the transition from region I and II. This gap is in most cases of the order of $1\ \mu\text{m}^{-1}$. Note that the blue curve,

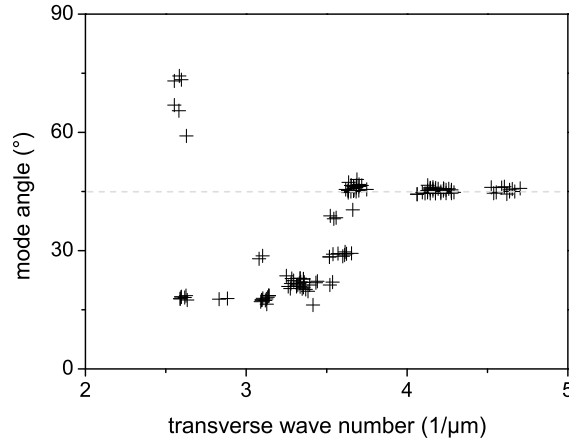


Figure 4.26: Dependence of the mode angle α on the transverse wave number for device 40–5 and several temperatures and currents. The dashed line highlights the diagonal ($\alpha = 45^\circ$), where the Fourier components of the billiard-type patterns are located. The plot includes the same data as the plot in fig. 4.24.

representing data from laser 30–3, does not show data points above $4 \mu\text{m}^{-1}$, since for this device emission of diamond-shaped modes was not observed in the studied temperature range. The plot shows that the temperature dependence of the transverse wave number is a universal feature in the type of VCSELs under study. A more quantitative discussion is given in section 4.3.4.

To simplify the illustration of the experimental data, in the following all dominant Fourier components are mapped into the first quadrant. That means that the absolute value of the transverse coordinates ($|k_x|, |k_y|$) is considered and the mode angle α is determined with respect to those absolute values. This is allowed due to the four-fold symmetry of the far-field emission.

In fig. 4.26 the mode angle α is plotted over the transverse wave number k_\perp . For small k_\perp Fourier components are located around $\alpha = 20^\circ$ and between 60° and 75° . The latter correspond to the orthogonally oriented mode discussed in section 4.2.1.2 and shown in fig. 4.7(j). In the wave number range between 2.5 and $3.5 \mu\text{m}^{-1}$ the most Fourier components have a mode angle around 20° . Between 3.5 and $3.7 \mu\text{m}^{-1}$ a transition to the diagonal is apparent. For higher wave numbers the mode angle is more or less constant at 45° .

Fig. 4.27 shows a plot of the position of the dominant Fourier components in the first quadrant of the (k_x, k_y) plane. Such a plot is termed “mode map” in the following. With the knowledge gained from the previous two plots the temperature dependence can be derived. It is indicated in the figure by the arrows. Starting at low wave numbers, the mode position moves outward with decreasing temperature, while the mode angle α is constant at first. At some point, around $k_\perp = 3.5 \mu\text{m}^{-1}$, k_x stops to increase while k_y starts to grow faster. Finally the mode position changes to the diagonal, where k_\perp increases further. The origin of this behavior, which has to do with a limited existence region for transverse modes, is discussed in section 4.3.2.

While laser 40–5 shows the described general features in the most complete way, similar

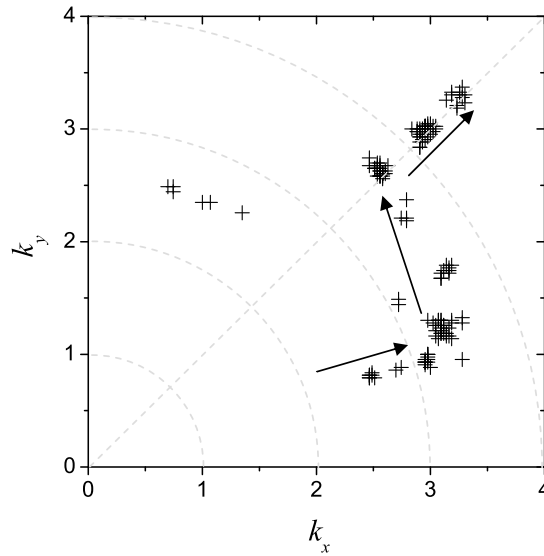


Figure 4.27: Positions of the dominant transverse modes in the first quadrant of the (k_x, k_y) plane for device 40–5. The dotted circular arcs indicate integer values of k_\perp . The dotted line indicates a mode angle of $\alpha = 45^\circ$, where the Fourier components of region III are found (cf. section 4.2.2). The arrows indicate the direction of the temperature-dependent change of the coordinates of the dominant modes (cf. fig. 4.24).

characteristics are found in the other lasers as well. Namely the angle α increases with decreasing temperature, the Fourier components with large wave numbers are always located close to the diagonal, and the transition between small α and $\alpha \approx 45^\circ$ around $k_\perp = 3.5 \mu\text{m}^{-1}$.

4.2.5 Optical and spatial spectra

The optical spectra obtained with the spectrometer introduced in section 3.3.3 are investigated here in more detail. To simplify the analysis of a group of spectra taken during a parameter scan they are displayed as intensity maps, similar to the example in fig. 3.9. In addition, spatial spectra are obtained from far-field images by creating radial profiles (i.e. the azimuthally averaged intensity is plotted against the wave number). These spatial spectra are composed to spectra maps analogous to the optical spectra maps described in section 3.3.3. To highlight the correspondence between wave number and wavelength the optical and spatial spectra maps are placed side by side and the wave number axis is reversed. In this way optical and spatial Fourier spectra can be compared directly.

An example of intensity maps of a temperature scan is shown in fig. 4.28. Subfigure (a) corresponds to optical spectra at temperature settings between 0 and 35 °C, changed in steps of 1 °C. Dashed lines marked with (a) to (e) correspond to the respective subfigures in fig. 4.11. Several continuous lines are visible in the spectra map, each corresponding to a transverse mode. Especially for high temperatures these lines are visible over a range of several degrees, shifting towards higher wavelengths with increasing temperature. This red-shift corresponds to the change of the longitudinal resonance discussed in section 3.4.4. A second trend, visible in the faster red-shift of the wavelength range in which modes are

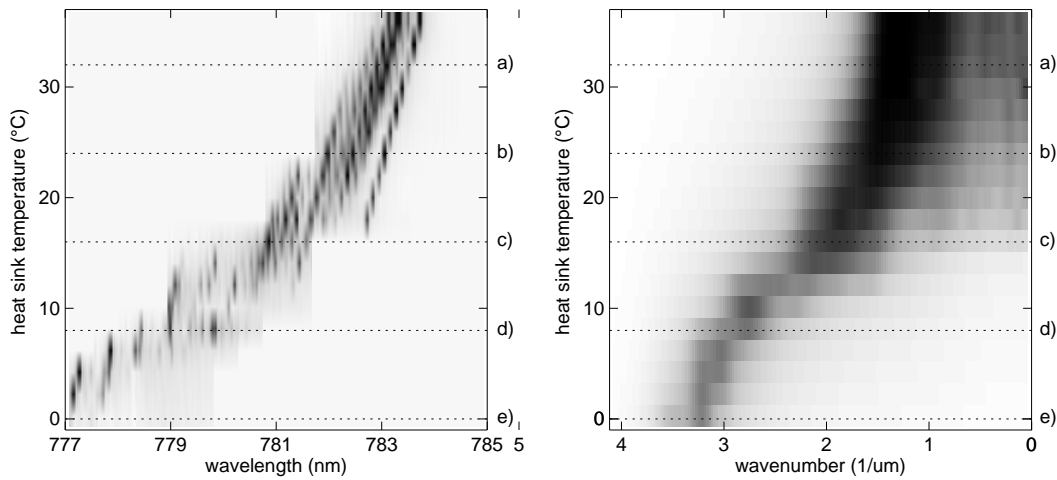


Figure 4.28: Intensity maps of a temperature scan for device 40–7 at 17 mA. (a) Optical spectra, (b) spatial Fourier spectra. The dashed lines and attached letters correspond to the respective subfigures in fig. 4.11.

emitted, corresponds to the change of the gain peak frequency with temperature. This second trend slows down for temperatures above 20 °C. Since the threshold drops for increasing temperature, the spectrum is broader and the lines are more intense for high temperatures.

Subfigure (b) shows the Fourier spectra for the same temperature scan. The wave number is decreasing from left to right. Here the change of the transverse wave number with temperature is visible: with increasing temperature the wave number decreases at first. This trend slows down until above 30 °C the wave number stays constant at around $1.2 \mu\text{m}^{-1}$. In comparison it becomes apparent that the optical spectra show much more details than the spatial spectra.

Fig. 4.29 shows optical and spatial spectra for a current scan from 10 to 25 mA in steps of 1 mA. The dashed lines marked with (a) to (e) correspond to the subfigures in fig. 4.6. In subfigure (a) at threshold (around 13 mA) one wavelength is emitted. The next spectrum already shows two additional peaks, one with a lower and one with a higher wavelength. For higher currents more and more wavelengths are excited, all of them higher than the one emitted at threshold. With increasing current each spectral line shifts toward higher wavelengths, which again corresponds to the shift of the longitudinal resonance. Around 20 mA the modes with the lowest wavelengths vanish. Overall the range of emitted wavelength shifts toward higher wavelength, faster than the shift of each individual line. This corresponds to the shift of the gain peak frequency.

The spatial spectra map in fig. 4.29(b) shows that a transverse mode with a radius of $3 \mu\text{m}^{-1}$ is excited at threshold (around 13 mA). With increasing current the spectrum broadens and red-shifts slightly, so that at 25 mA it is about $1 \mu\text{m}^{-1}$ wide and centered around $1.8 \mu\text{m}^{-1}$.

The claim that each transverse wave number corresponds to a different wavelength

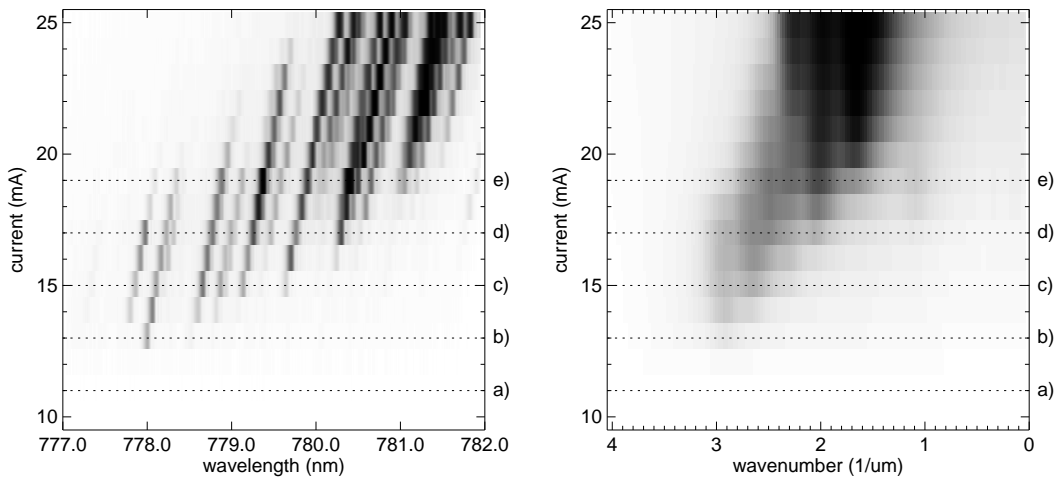


Figure 4.29: Intensity maps of a current scan for device 30-3 at 5°C. (a) Optical spectra, (b) spatial Fourier spectra. The dashed lines and attached letters correspond to the respective subfigures in fig. 4.6.

(cf. section 2.4) is supported by these experiments. To illustrate this correspondence further an experiment was realized that allows the visualization of the far-field emission with spectral resolution. This experiment is based on the strain-gauge FPI that is described in section 4.1.2. When imaging the far-field emission through this interferometer onto a CCD camera it is possible to vary the detected frequency by changing the distance between the FPI mirrors. This was achieved only with a rather low spectral resolution, similar to that of the Fourier spectra. Nonetheless this experiment provides a direct insight into the 1:1 correspondence between transverse wave number and optical wavelength: the filtered far-field images show rings with radius depending on the mirror distance. If a transverse mode falls into such a ring it is transmitted by the FPI.

The confocal FPI was used to determine the spectral characteristics of the emission with large wave numbers and especially to check if the emission of diamond-shaped patterns has only one frequency. The FSR of the cFPI is 1.5 GHz. The finesse in the experiment is about 15, which results in a spectral resolution of about 100 MHz.

Laser 40-7 is operated at -33°C , where it emits the known billiard-type pattern. The far-field emission slightly above threshold is shown in fig. 4.30(a). Subfigure (b) shows the corresponding cFPI spectrum. Two peaks are visible, separated by one FSR, which means that both peaks correspond to the same emission frequency and to one transverse mode. This mode is excited at threshold, at around 22.2 mA. With increasing current the height of the peaks of corresponding to the mode increase. At around 22.7 mA a second mode becomes visible in the spectrum, close to the first. The frequency spacing is about 300 MHz. Increasing the current further the state shown in fig. 4.30(c) is reached. Even with strong contrast enhancement no changes beyond the increase of intensity are visible in the far-field images within this current range. Thus only the image corresponding to the first spectrum is shown in the figure.

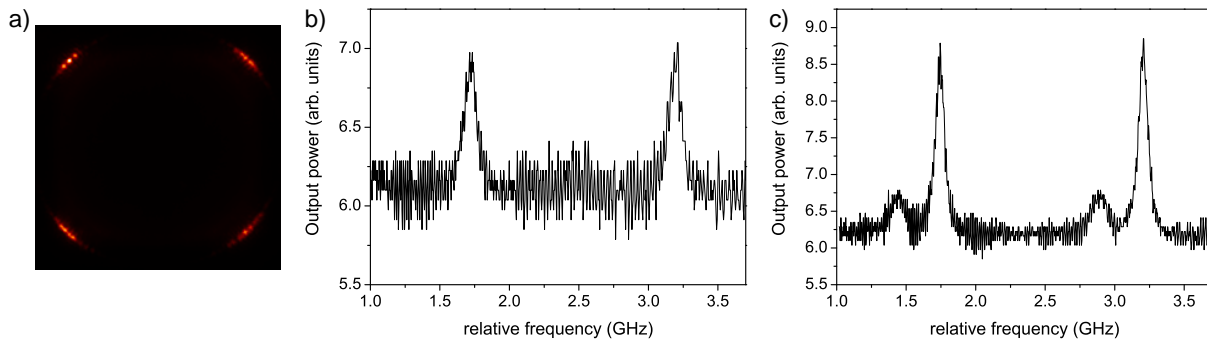


Figure 4.30: (a) Far-field image of the emission of laser 40-7 with $T = -33^\circ\text{C}$ and $I = 22.64$ mA. (b) Corresponding cFPI spectrum. (c) Spectrum with $I = 23.5$ mA.

This shows that the billiard-type patterns have only one frequency at threshold, but a second is emitted at slightly higher currents. The two modes have a very small frequency splitting. The change from single-frequency to two-frequency operation is not visible in the far-field images.

4.3 Analysis and interpretation

In this section the experimental observations are analyzed in more detail and compared to theoretical considerations. In the following subsection possible origins of the localized peaks observed in the emission of the square VCSELs for high temperatures are investigated. This is followed by a calculation of the region of existence for tilted waves, which ends at the point where the angle of incidence upon the transverse boundaries of the VCSELs becomes too steep for total reflection. In the next section, the diamond-shaped billiard patterns observed in the experiment for very low heat sink temperatures are compared to calculated images with emphasis on the far-field distribution.

The first publication of the quantitative dependence of the transverse wave number of the pattern on the detuning between maximum gain wavelength and longitudinal resonance is [153]. This analysis is described in section 4.3.4. This is followed by a brief analysis of the threshold of individual transverse modes. Finally, a brief description of the model used in many publications to simulate the emission of broad-area VCSELs is given and the results of the model are compared to the experimental observations.

4.3.1 On-axis emission and thermal lensing

As established before for negative values of the detuning a transverse stripe pattern corresponding to a certain wave number is observed. When the detuning is changed toward zero the dominant wave number decreases and for $\delta = 0$ on-axis emission is observed. In the near-field emission of a perfect laser a homogeneous intensity distribution is expected in this case, but this is not observed in the experiments. The near-field pattern corresponding to on-axis emission is in most lasers dominated by a single peak in one corner of the aperture (this is shown e.g. in fig. 4.3).

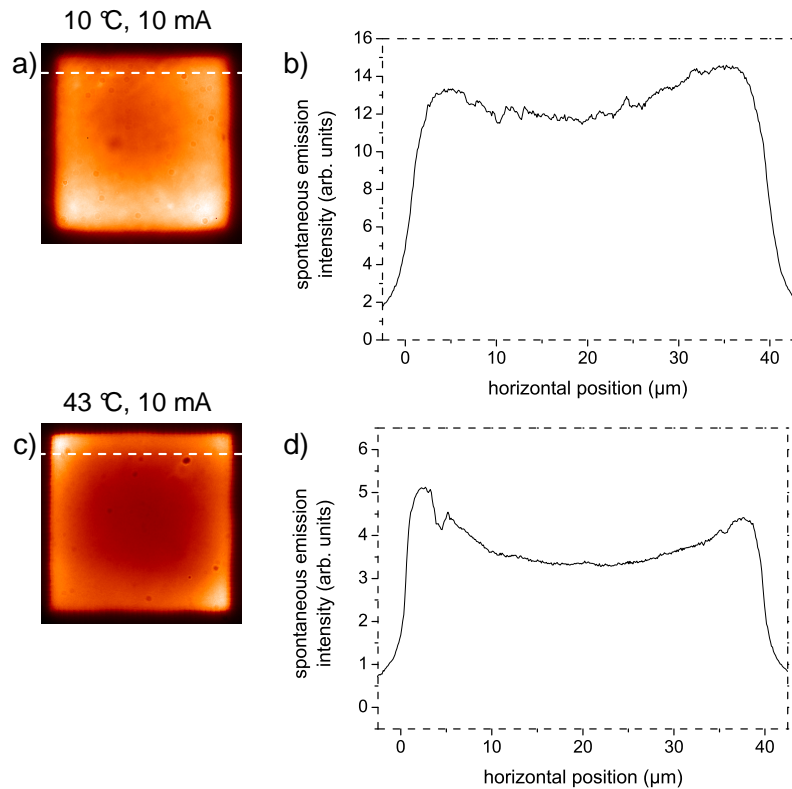


Figure 4.31: Near-field images of lasers 40–1 (a) and 40–7 (c) below threshold with an interference filter in the beam path. Pump rates -0.01 and -0.09 , respectively. The cuts plotted in (b),(d) are indicated by the respective white lines in (a),(c). In both lasers the hot spot is found in the upper left corner.

Here the possible origins of the localization of the (near-field) emission to a corner of the aperture (as seen in devices 40–1, 40–5, 40–7, and 40–9) are considered. With the exception of device 40–1 this occurs only for highest temperatures (i.e. for low or zero detuning) and in a small current range just above threshold. Far above threshold the spot is usually replaced by an irregularly modulated pattern that covers the whole aperture. In VCSEL 40–1 the hot spot is emitted at threshold for all temperatures and also far above threshold.

One obvious explanation is current crowding at the location of the spot. A good indicator of the carrier distribution is the homogeneity of the spontaneous emission below threshold. It can be accessed by detecting the emission outside the DBR stop-band. The width of the stop-band is about 47 nm (cf. table C.1), reaching from above 750 to below 810 nm. An interference filter (Thorlabs, bandpass width 10 nm) transmitting around 760 nm at perpendicular incidence is inserted into the beam path. By tilting the filter the transmitted wavelength can be reduced. In the following experiments the filter was tilted by approximately 20° . This results in a transmission wavelength range around 710 nm (i.e. well below the DBR stop-band).

With this modification of the setup near-field images of the emission of lasers 40–1 and 40–7 are taken at temperature settings where the hot spot is emitted. For both lasers the current is set below threshold. The results are illustrated in fig. 4.31. Subfigure (a)

shows the near-field image of device 40–1 at 10 °C and 10 mA. The white line indicates the location of the cut plotted in (b). The same was done in (c) and (d) for laser 40–7 with $T = 43$ °C and $I = 10$ mA. Corresponding images of the localized spots without interference filter are found in fig. 4.13(b) and 4.4(a), respectively. Note that the near-field images of laser 40–1 is rotated so that the localized spot is located at the upper left corner.

Both filtered near-field images feature an increase of carriers along the oxide boundary, especially in the corners of the aperture, which is much more pronounced in laser 40–7. This effect is known to occur in top-emitting oxide-confined VCSELs [43]. That the localized spots are found at the corners in all lasers studied here is an indication for the influence of the current crowding. The cut through the near-field image of laser 40–7 even indicates a global maximum of the spontaneous emission at the position of the localized spot (upper left corner). However, at the position of the localized spot in the image of laser 40–1 no global maximum is evident.

The current crowding can explain that the emission is found along the laser boundaries and especially at the corners. To favor one specific corner this symmetry has to be broken by another effect. One candidate is a perturbation in the length of the cavity. In very large lasers this effect is common [108], since it is difficult to produce perfectly parallel and smooth semiconductor layers. This effect changes the resonance condition locally which has a much larger impact on modes with a small detuning (according to the square-root shape of the curve in fig. 4.37).

In the following, the spot size is compared to the length scale that is minimally coupled by diffraction, i.e. the diffraction limit. The diffraction parameter [107] is

$$a = \frac{c}{2n\kappa k_z} = \frac{c\lambda}{4\pi n^2\kappa}, \quad (4.3)$$

where $\kappa = 1/(2\tau_p)$ is the decay rate of the field inside the cavity. κ can also be expressed as

$$\kappa = \frac{1}{2N_p\tau_{eff}} = \frac{c}{4nN_pL_{eff}}. \quad (4.4)$$

The values of τ_p , τ_{eff} , N_p , and L_{eff} are given in table C.1. Inserting eq. (4.4) into eq. (4.3) we obtain

$$a = \frac{\lambda}{\pi n} N_p L_{eff}. \quad (4.5)$$

The spot size corresponding to this diffraction parameter is $\sqrt{a} = 3.3$ μm . This constitutes a spot size with a divergence angle θ for which applies

$$\theta N_p L_{eff} = \sqrt{a}, \quad (4.6)$$

i.e. a spot of this size is self-consistently diffracted into itself over the propagation distance in the cavity. \sqrt{a} is only slightly smaller than the 3.4 μm obtained for the size of the localized emission of laser 40–5. Since the spots observed in the various lasers are of different size and also of different shape the diffraction limit is probably not the dominant mechanism but it establishes a minimal size for the localization.

Another candidate for an explanation is thermal lensing. This is a well known phenomenon in many lasers, especially high-power lasers, and also commonly found in

VCSELs [64, 154]. A thermal lens is an optical waveguide that can be created when temperature variations in the laser cavity influence the refractive index of the material. Possible sources of such temperature variations include an increased current flow that heats the material via Joule heating or increased non-radiative losses due to inhomogeneities in the material. In small VCSELs thermal lensing is often appreciated, because it increases the confinement of the light wave inside the cavity, which decreases the laser threshold [154]. In such small VCSELs the current flow induces a thermal lens for the whole aperture and this results in an increase of the intensity at the center of the aperture. In the large VCSELs under study this is not observed, thus local thermal lensing has to be involved to explain the localized peaks at the corners.

In the following calculations are presented that estimate the parameters of a thermal lens necessary to explain the localization of the near-field emission. For a waveguide with parabolic index profile

$$n^2(r) = n^2 \left(1 - \frac{n_2}{n} r^2 \right), \quad (4.7)$$

where n_2 is the (negative) curvature of the profile, the spot size resulting from the guiding effect is given by [155]

$$w_0 = \sqrt{\frac{\lambda}{\pi}} \left(\frac{1}{nn_2} \right)^{1/4}. \quad (4.8)$$

The curvature is thus obtained from

$$n_2 = \frac{\lambda^2}{\pi^2 w_0^4 n}. \quad (4.9)$$

It is obvious that n_2 strongly depends on the spot size. That means that a small error of the determination of w_0 leads to large errors of n_2 . Thus the following considerations can only be estimates.

From near-field images of device 40–5 $w_0 = 3.4 \mu\text{m}$ (half-width at $1/e^2$ point) is obtained. The resulting (negative) curvature of the profile (eq. (4.9)) is then $n_2 = 1.4 \cdot 10^{-4} \mu\text{m}^2$. Inserting this into eq. (4.7) yields the parabolic index profile. The index step (index difference between center of spot $w = 0$ and $w = w_0$) is only $8.1 \cdot 10^{-4}$. This can be converted to a temperature profile using $\beta = dn/dT = 2.81 \cdot 10^{-4} \text{K}^{-1}$ obtained in section 3.4.4.4 and

$$\Delta T(r) = \frac{n(r) - n}{\beta}. \quad (4.10)$$

The resulting temperature difference between the center of the spot and its border is $\Delta T = 2.9 \text{K}$. See Fig. 4.32 for plots of the index and temperature profiles. There the black curves represent the parabolic profiles. The borders of the spot are marked by dashed blue lines.

In the calculation above parabolic index and temperature profiles were assumed. This does not create a smooth transition from the thermal lens to the surrounding material. A more realistic assumption would be a Gaussian profile with the same curvature at the center as the parabolic one, i.e.

$$\frac{d^2 n(r)}{dr^2} (r = 0) = -n_2. \quad (4.11)$$

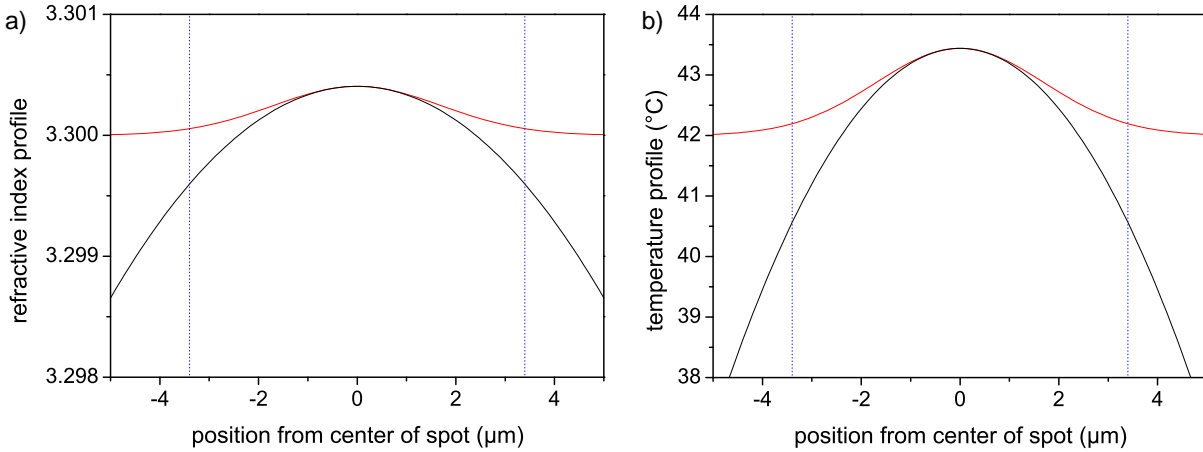


Figure 4.32: Calculated refractive index (a) and temperature (b) profiles of a thermal lens needed to explain the localized near-field emission observed near zero detuning. The black curves correspond to the assumption of parabolic profiles, while the red curves represent an ansatz with a Gaussian profile. The dashed blue lines indicate the width of the localized spot at the $1/e^2$ point of the intensity.

The following ansatz is used for the Gaussian refractive index profile:

$$n(r) = H \exp\left(-\frac{r^2}{2W^2}\right) \quad (4.12)$$

with H the height of the Gaussian and $W = 0.5w_0$ the width. Calculating the second derivative and inserting eq. (4.11) we get

$$H = n_2 W^2 = 4.05 \cdot 10^{-4}. \quad (4.13)$$

The resulting temperature difference (the height of the Gaussian temperature profile) is $\Delta T = H/\beta = 1.44$ K, which is even smaller than the value obtained with the parabolic profile. Fig. 4.32 summarizes the resulting index and temperature profiles. Note that here the width W of the Gaussian profile is set to $0.5w_0$, half the radius of the $1/e^2$ point of the spot. This is a minimum estimation, since it is probable that the temperature profile is broader than the intensity distribution. This means, that the temperature difference also represents a minimum value: a broader Gaussian with the same curvature at the peak has to be higher as well. With $W = 5 \mu\text{m}$ – a rough estimate of a more appropriate profile width – $\Delta T = 12.5$ K is obtained.

In conclusion it is shown that several effects can lead to the formation of localized emission. Some evidence was presented to illustrate the probable influence of current crowding and thermal lensing. The considerations about thermal lensing show that a very low temperature difference between the thermal lens and the surrounding material is sufficient to create spots of the observed size. Finally, this shows why homogeneous emission is never observed in broad-area VCSELs: small inhomogeneities are sufficient to destabilize the already marginally stable fundamental mode of the plano-planar cavity.

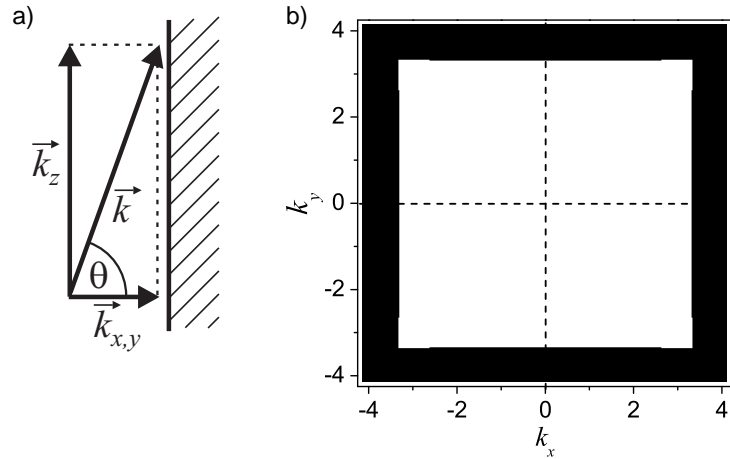


Figure 4.33: (a) Illustration of angles and wave vectors used for the calculation of the existence region. On the right the transverse boundary is depicted, the angle of incidence is θ . (b) The region of existence (white) for transverse wave vectors as calculated from equations 4.20 and 4.21. $k_x = 0$ and $k_y = 0$ are indicated by the dashed lines. This illustration is valid only for the square lasers.

4.3.2 Existence region of tilted waves

Tilted waves can only propagate in a finite laser cavity without significant losses if they undergo total internal reflection at the transverse boundaries [18, 26]. When the tilt angle of a wave gets too large, i.e. when the transverse component of the wave vector exceeds a certain value, the wave is scattered beyond the oxide aperture and its losses rise drastically. Thus the condition of total reflection defines an existence region for tilted waves. In the following the oxide aperture, nominally a 30 nm thick layer (see appendix B for details on the VCSEL structure), is represented by an effective waveguide, i.e. the guiding effect is considered to be “smeared out” over the whole laser structure. This approximation is based on the effective index model [156].

The derivation of the cut-off wave numbers is shown in [157] and will be illustrated here shortly. Total reflection occurs when

$$\epsilon_1 \sin^2 \theta \geq \epsilon_2, \quad (4.14)$$

with $\epsilon_1 = n_1^2$ being the susceptibility of the medium inside the cavity, $\epsilon_2 = n_2^2$ the susceptibility outside the cavity, and $\epsilon_1 > \epsilon_2$. The angle of reflection at the boundary is given by

$$\cos \theta = \frac{k_y}{|k|}, \quad (4.15)$$

with $|k| = \sqrt{k_x^2 + k_y^2 + k_z^2}$. This applies for k_x analogously. See fig. 4.33(a) for an explanation of the angles and vectors.

k_z is the longitudinal wave number in the medium of the cavity. For the square lasers it is given by $k_z = 2\pi\bar{n}/\lambda$, with $\bar{n} = 3.3$ the average refractive index of the whole VCSEL structure (cf. appendix C) and $\lambda = 780$ nm. For the small tilt angles ($< 10^\circ$ inside the device) encountered in the experiment k_z can be considered constant.

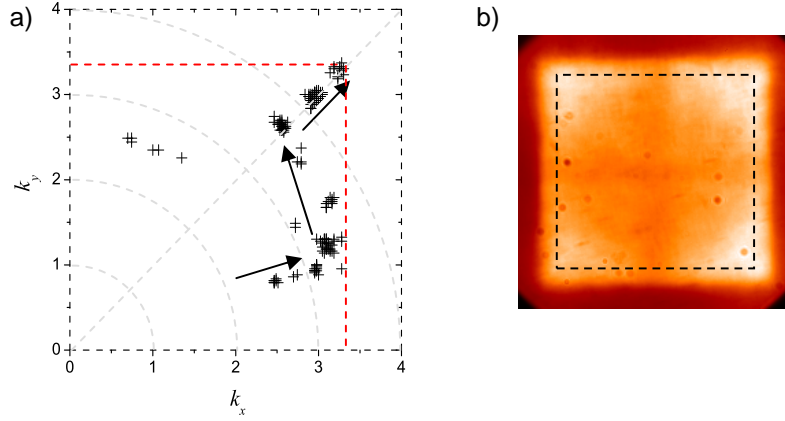


Figure 4.34: (a) Experimental mode map as shown in fig. 4.27 including the borders of the existence region (dashed red lines). $k_{x,max} = k_{y,max} = 3.3 \mu\text{m}^{-1}$ and $k_{\perp,max} = 4.6 \mu\text{m}^{-1}$ were found theoretically and are in very good agreement with the experiment. The arrows show the change of peak positions with decreasing temperature. (b) Far-field images of the spontaneous emission of laser 40–5 at -20°C and 10 mA. The existence region is indicated by dashed black lines and is also visible in the ASE.

Equations 4.14 and 4.15 combine to

$$\cos^2 \theta \leq 1 - \frac{\epsilon_2}{\epsilon_1} \quad (4.16)$$

$$\frac{k_y^2}{k_x^2 + k_y^2 + k_z^2} \leq 1 - \frac{\epsilon_2}{\epsilon_1}. \quad (4.17)$$

We set $\epsilon = 1 - \epsilon_2/\epsilon_1$ and obtain

$$k_y^2 \leq \epsilon (k_x^2 + k_y^2 + k_z^2) \quad (4.18)$$

$$\Leftrightarrow (1 - \epsilon)k_y^2 \leq \epsilon (k_x^2 + k_z^2). \quad (4.19)$$

Finally the conditions for k_y and analogously for k_x are

$$k_y^2 \leq \frac{\epsilon}{1 - \epsilon} (k_x^2 + k_z^2) \quad (4.20)$$

$$k_x^2 \leq \frac{\epsilon}{1 - \epsilon} (k_y^2 + k_z^2). \quad (4.21)$$

To calculate the maximal values of $k_{x,y}$ the cross-terms (k_x in eq. (4.20) and k_y in eq. (4.21)) are set to zero. Furthermore the index difference between the cavity medium and the surrounding oxide is needed. This can be obtained from a program [158] that utilizes the effective index method [156]. The effective waveguide produced by the oxide is calculated by weighted averaging including the distribution of the optical field inside the cavity. The calculated index step is $\Delta n = -0.026$. With the average index of the square VCSEL structure $n_1 = 3.3$ and $n_2 = 3.27$ are obtained. Using this we get $\epsilon = 0.016$ and

$$k_{x,max} = k_{y,max} = \sqrt{\frac{\epsilon}{1 - \epsilon}} k_z = 3.3 \mu\text{m}^{-1}. \quad (4.22)$$

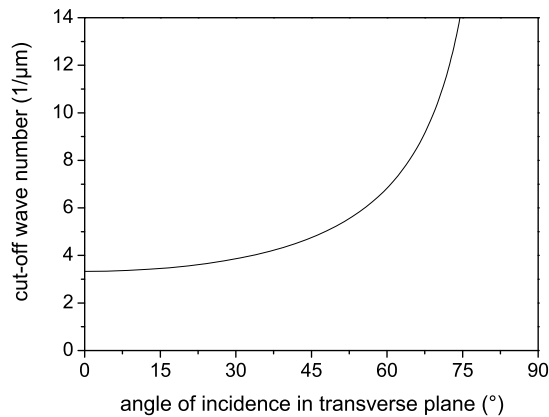


Figure 4.35: Plot of the calculated cut-off wave number on the angle of incidence in the transverse plane. For the square VCSELs angles of up to 45° are considered, but for the circular devices much larger angles can occur.

It is shown in detail in [157] that the calculations of the existence region are also true for mixed waves with both $k_x > 0$ and $k_y > 0$. Applying equations 4.20 and 4.21 to the whole transverse k -plane yields the existence region for tilted waves, which forms a (nearly perfect) square, as shown in fig. 4.33(b). Small deviations from the square, visible in the corners of the existence region, stem from the cross-terms in the equations. The overall maximal wave number (along the diagonal) is $k_{\perp,max} = \sqrt{k_{x,max}^2 + k_{y,max}^2} = 4.6 \mu\text{m}^{-1}$. This is in very good agreement with the highest wave numbers found in the experiment discussed in section 4.3.4.

These results allow also to explain why the transverse wave vectors change orientation as well as their length with temperature. Adding the existence region as dotted red lines to the mode map shown in section 4.2.5 fig. 4.34(a) is obtained. The agreement with the theoretical values is apparent: all the Fourier modes found in the far-field images are inside of the existence region. With help of this region the behavior of the Fourier modes with increasing detuning can be understood as follows: at first only the transverse wave number increases, while the direction of the transverse wave vector stays constant. At $k_{x,max} = 3.3 \mu\text{m}^{-1}$ the orientation changes, because in order to further increase in length the wave vector has to follow the border of the existence region. At some temperature value the jump to the diagonal takes place. It is obvious that the overall maximal wave vector with wave number $k_{\perp,max}$ has to be oriented along the diagonal.

The existence region is also visible in the far-field images of the ASE. Such an image is shown in fig. 4.34(b), together with a black square indicating the calculated values of the existence region. Obviously the same selection mechanisms are applicable to the ASE as well, though the square is somewhat smaller than the bright area inside the image. Note however that the maxima of the spontaneous emission are inside the square and only the drop from the maxima to the background level is outside of it. As a side note the darker areas at the corners of the image stem from the cut-off determined by the limited NA of the imaging microscope objective.

Up to now a maximum angle of incidence in the transverse plane of 45° was considered. This is justified for the square VCSELs since a larger angle of incidence upon one side

boundary would imply a steeper incidence upon the orthogonal boundary and the cut-off condition is valid for the steeper angle. For the circular lasers much larger angles can occur. In fig. 4.35 the cut-off wave number is plotted over the angle of incidence in the transverse plane. It is obvious that the cut-off wave number increases drastically above an angle of 60° . Since for the ring-shaped modes observed in the emission of the circular lasers an angle of incidence over 60° can be assumed, this shows that the cut-off plays no role in the pattern selection of the circular lasers.

In conclusion, these considerations show why patterns with markedly different geometries are emitted by the square VCSELs. Wavy stripe and diamond-shaped patterns similar to those observed here were already described in [26], but a reason for the existence of different patterns was not given. Note that the origin of the continuous rings observed in region I and the predominant four-fold symmetry in region II is not explained by this.

4.3.3 Diamond patterns as quantum billiards in the semiclassical limit

In [26, 27, 95] the billiard patterns observed for very low temperatures in the emission of the VCSELs under study are interpreted in a very interesting way: as a two-dimensional quantum billiard system. Responsible for this is the analogy between the Schrödinger equation (describing the movement of a particle in a quantum well) and the Helmholtz equation (describing the propagation of light waves). The VCSEL is regarded as a two-dimensional potential well, where a particle (the light wave) is trapped. The condition of total internal reflection, the importance of which was discussed in section 4.3.2, is analogous to infinitely high “hard” potential walls. The near-field pattern of certain modes is interpreted as the probability density of the particle position, the far-field as the momentum.

Since the transverse wavelength of these patterns is small they are considered to be semi-classical, i.e. located at the transition between the quantum mechanical probability density and classical periodic orbits. The pattern is then interpreted as the scar of a classical trajectory like those found for lowest temperatures in the experiments. Note that the VCSELs studied here are more or less identical to those studied in [26].

The model necessary to calculate such billiard patterns is illustrated in [27]. It is based on superpositions of eigenstates of the system (the VCSEL or the potential well), so-called coherent states. The authors show that only a few nearly degenerate eigenstates are sufficient to calculate a billiard pattern similar to those found in the experiment. The central equation in [27] is

$$\begin{aligned} \Psi_{N,M}^c(x, y; \phi) = & \frac{2}{a} \left[\sum_{K=q}^{N-q} \binom{N}{K} \cos^2 K\phi \right]^{-1/2} \cdot \sum_{K=q}^{N-q} \binom{N}{K}^{1/2} \cos(K\phi) \\ & \times \sin \left[(K+1) \frac{\pi x}{a} \right] \sin \left[(N-K+1) \frac{\pi y}{a} \right], \end{aligned} \quad (4.23)$$

where N is the order of the pattern and $M = N - 2q + 1$ is the number of eigenstates used in the wave function Ψ . A low value of M results in a less confined, broader trajectory.

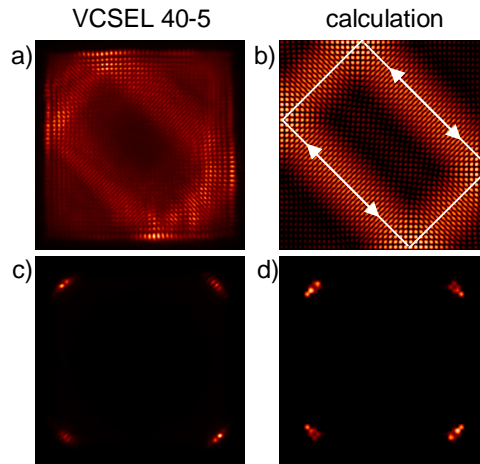


Figure 4.36: Near-field (a) and far-field (c) images of the billiard-type emission of laser 40–5 at -36°C and 22 mA. (b) shows $|\Psi_{N,M}^c|^2$ obtained with eq. (4.23). The parameters are $N = 80$, $M = 7$, and $\phi = 0.63\pi$. The square of the absolute value of the corresponding Fourier transform of Ψ is shown in (d). Both calculated images are shown in logarithmic scaling to enhance the contrast. The arrows in (b) indicate the trajectory of the travelling waves inside the transverse cavity.

ϕ is a parameter used to control the point at which the trajectory is reflected at the boundaries (e.g. $\phi = \pi/2$ results in a symmetric diamond). a is the transverse size of the VCSEL.

To compare the experimental results illustrated in this work with a calculated billiard pattern the parameters N , M , and ϕ have to be selected. In fact the value of N can be directly obtained from the number of stripes of the billiard pattern emission, which is $2N$. The parameters M and ϕ can be guessed relatively easily by comparing the experimental images with calculated ones. The calculated near-field is obtained from $|\Psi|^2$, while for the far-field the fast Fourier transform of Ψ is calculated and then the square of the absolute value is displayed. Note that in [26, 27] the far-field distribution is not discussed. Also the publications treat the subject rather phenomenological, without explaining details like the observed position of the dominant Fourier components at the diagonals.

Fig. 4.36 shows a comparison of an experimentally obtained (a) and a calculated billiard pattern (b) and the corresponding far-field images (c,d). The parameters chosen for the calculation are $N = 80$, $M = 7$, and $\phi = 0.63\pi$. N was obtained from the number of stripes in the experimental near-field image, M and ϕ were carefully selected to achieve a good agreement between the experimental and the calculated near-field images. The white arrows in (b) indicate the trajectories of the travelling waves as classical paths. If the transverse wave number would be increased further the billiard pattern would contract further to these classical trajectories.

The general characteristics of the experimental far-field images are found in the calculated one as well: four groups of Fourier components located at the diagonals are evident. Both in experimental and calculated far-field images a substructure is visible in each group of Fourier components. The groups corresponding to the longer diagonal paths in the near-field images are brighter than the other two.

Nonetheless, the details of the calculated far-field images show some differences compared to the experimental findings. It was found that the substructure of the four groups of Fourier peaks is equal for nearly all parameters, except for mirroring and a different intensities. Only for a few parameter pairs M, ϕ the substructure was different. In the experiment the substructure was found to be different in every observed far-field pattern.

By comparing the far-field images calculated with different values of M it was found that the number of peaks in one group of Fourier components increases with M . The form of each group changes with the value of ϕ . In the experiment it was observed that the parameter ϕ corresponds to the number of peaks in a group of Fourier components and also the size of the individual peaks and their mutual distance changes with ϕ (cf. section 4.2.2). An explanation of this would be a coupling of M and ϕ in the experiment.

It turns out that by tuning the parameters M and ϕ the calculated near-field image can become quite similar to the experimental images. In contrast it proved to be rather difficult to achieve an agreement between experimental and calculated far-field images.

4.3.4 Quantitative analysis of the pattern length scales

In this section the dependence of the pattern length scales on the detuning δ is studied in more detail and compared to theoretical considerations. Similar studies of VCSELs [93] and of other systems [86] revealed a linear dependence of the square of the transverse wave number on the detuning. This dependence is intrinsically included in the models that predict tilted waves in plano-planar resonators, e.g. [24]. Here it is explicitly calculated on the basis of our publication [153].

The simplest approach to calculate the length scales of the emission patterns is of geometrical nature. It was shown before (cf. section 3.4.4) that the maximum gain wavelength shifts considerably faster with temperature than the longitudinal resonance. If the maximum gain wavelength λ is blue-shifted with respect to the longitudinal cavity resonance λ_c , tilted waves are favored. The detuning $\delta = \lambda - \lambda_c$ is then negative. This scenario is schematically shown in fig. 2.2 for the corresponding wave vectors. $\vec{k} = (k_x, k_y, k_z) = (\vec{k}_\perp, k_z)$ denotes the wave vector of the lasing mode. The wave vector of the longitudinal cavity resonance is $\vec{k}_c = (0, 0, n\omega_c/c)$.

In the following we only consider the absolute values of the wave vectors $k = |\vec{k}|$. From the geometrical picture we get

$$k_z^2 = \frac{n^2(\omega)\omega^2}{c^2} - k_\perp^2, \quad (4.24)$$

where $n\omega/c = k$ the wave number of the mode, $\omega = 2\pi\nu = 2\pi c/\lambda$ the angular frequency. We approximate (valid for small dispersion)

$$n^2(\omega) \approx \left(n_0 + \Omega \frac{dn}{d\omega} \right)^2 \approx n_0^2 + 2n_0\Omega \frac{dn}{d\omega}, \quad (4.25)$$

where $\Omega = \omega - \omega_c$ is the detuning in terms of angular frequencies. Note that Ω is positive for negative δ . An analogous approximation is done for ω , i.e. $\omega^2 = \omega_c^2 + 2\omega_c\Omega$. In both

cases terms with Ω^2 are neglected. The two approximations are inserted into eq. (4.24), which leads to

$$k_z^2 = \frac{n_0^2 \omega_c^2}{c^2} + \frac{2n_0^2 \omega_c}{c^2} \Omega + \frac{2n_0 \omega_c^2}{c^2} \frac{dn}{d\omega} \Omega - k_\perp^2. \quad (4.26)$$

Now the Taylor expansion

$$\sqrt{a+x} = \sqrt{a} + \frac{1}{2\sqrt{a}}x \quad (4.27)$$

$$a = \frac{n_0^2 \omega_c^2}{c^2} \quad (4.28)$$

$$x = \frac{2n_0^2 \omega_c}{c^2} \Omega + \frac{2n_0 \omega_c^2}{c^2} \frac{dn}{d\omega} \Omega - k_\perp^2 \quad (4.29)$$

is used (valid for $x \ll a$). This leads to

$$k_z = \frac{n_0 \omega_c}{c} + \frac{n_0 \Omega}{c} + \frac{\omega_c \Omega}{c} \frac{dn}{d\omega} - \frac{c}{2n_0 \omega_c} k_\perp^2. \quad (4.30)$$

Using $k_c = n_0 \omega_c / c$ and $n_{gr} = \omega_c \frac{dn}{d\omega} + n_0$ (definition of the group index) we get

$$k_z = k_c + \frac{n_{gr} \Omega}{c} - \frac{1}{2k_c} k_\perp^2. \quad (4.31)$$

If we approximate $k_z = k_c$ this simplifies to

$$\frac{n_{gr} \Omega}{c} = \frac{1}{2k_c} k_\perp^2. \quad (4.32)$$

We insert $k_c = 2\pi/\lambda_c$, $\Omega/\omega_c = (\lambda_c - \lambda)/\lambda_c$, and $\omega_c = 2\pi n_0 c/\lambda_c$ and get

$$k_\perp^2 = 8\pi^2 n_0 n_{gr} \frac{\lambda_c - \lambda}{\lambda_c^3}. \quad (4.33)$$

The result is the linear dependence of the square of the transverse wave number on the detuning $\delta = \lambda_c - \lambda$, that was already predicted by the models [17] and reported experimentally for other systems [86, 87]. It is important to point out that this equation implies a 1:1 correspondence between wave number and wavelength. This correspondence is also found in the experiment.

From experimental data it is possible to extract k_\perp , λ , and λ_c for selected parameters T and I . One issue of this is to obtain λ_c , because when operating on off-axis modes most lasers do not emit on the longitudinal resonance simultaneously. Here the unusual behavior of laser 40-1 is useful: since this device always operates on the localized spot which corresponds (more or less) to on-axis emission it is possible to obtain λ_c for all temperature settings. With other lasers this is a bit more involved, since there the on-axis emission is only found for high temperatures. In those cases the shift values obtained in section 3.4.4 are helpful: it is possible to calculate the wavelength of a mode for given temperature and current values with the shifts, even if that mode is not emitted for those parameters. This solution is not applicable if the laser does not emit on the longitudinal

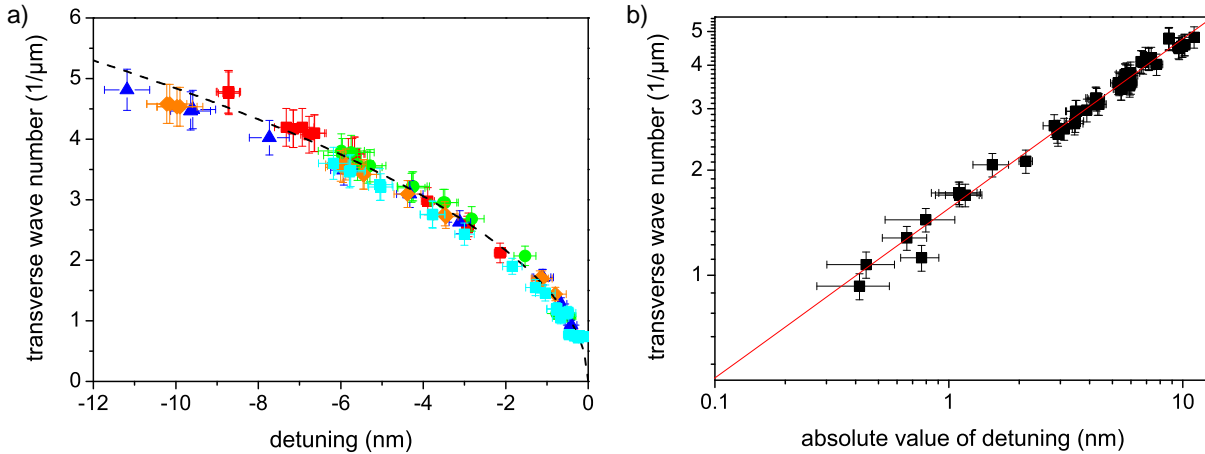


Figure 4.37: (a) Dependence of the transverse wave number of the emission on the detuning between cavity resonance and emission wavelengths. Experimental data points given for lasers 30–1 (red squares), 30–3 (green circles), 40–1 (cyan square), 40–7 (blue triangles), and 40–9 (orange diamonds). The dashed line is obtained from eq. (4.33) using $n_0 = 3.37$ and $n_{gr} = 4.20$. (b) Double-logarithmic plot of the transverse wave number over the absolute value of the detuning. The red line is a linear fit to the data and provides the scaling exponent of the experimental data.

resonance at all. Since this is only the case for a few devices, these are left out of the analysis.

Note that the term “longitudinal resonance” is used loosely in the considerations above. If a laser would operate truly on the longitudinal resonance with a plane wave a homogeneous near-field distribution would be expected. This is never observed in the experiment (cf. fig. 4.3(a)). It is a well known fact [159, 160] that a transversely confined Gaussian mode acquires a phase shift with respect to a plane wave. This is the so-called Gouy phase shift [161] and inside the laser resonator it leads to a change in the resonance frequency for a Gaussian mode. The Gouy phase shift of a mode with transverse wave number k_{\perp} (using the half-width of the $1/e^2$ point of intensity for the on-axis spot) can be calculated using [159]

$$\Phi = \frac{k_{\perp}^2 L}{k_0}, \quad (4.34)$$

with L the length of the cavity and $k_0 = 2\pi\bar{n}_{cav}/\lambda_0$ the longitudinal wave number. Using the appropriate values from table C.1 and $k_{\perp} = 0.7 \mu\text{m}^{-1}$ (spot in the emission of laser 40–1) we obtain $\Phi = 0.004$. This corresponds to a resonance wavelength change of about 0.5 nm. This is an acceptable error though slightly larger than the errors calculated from measurement uncertainties. A square root fit to the experimental data provides similar λ_c with an error of up to 0.8 nm. It is thus feasible to use the wavelength of the near on-axis emission observed in many lasers for high heat sink temperature as λ_c . Note that the origin of the localization of on-axis emission is discussed in section 4.3.1

The transverse wave numbers obtained from several parameters settings are plotted against the corresponding detuning in fig. 4.37(a). The error bars are calculated using error propagation and reasonable estimates for reading and measurement errors. The

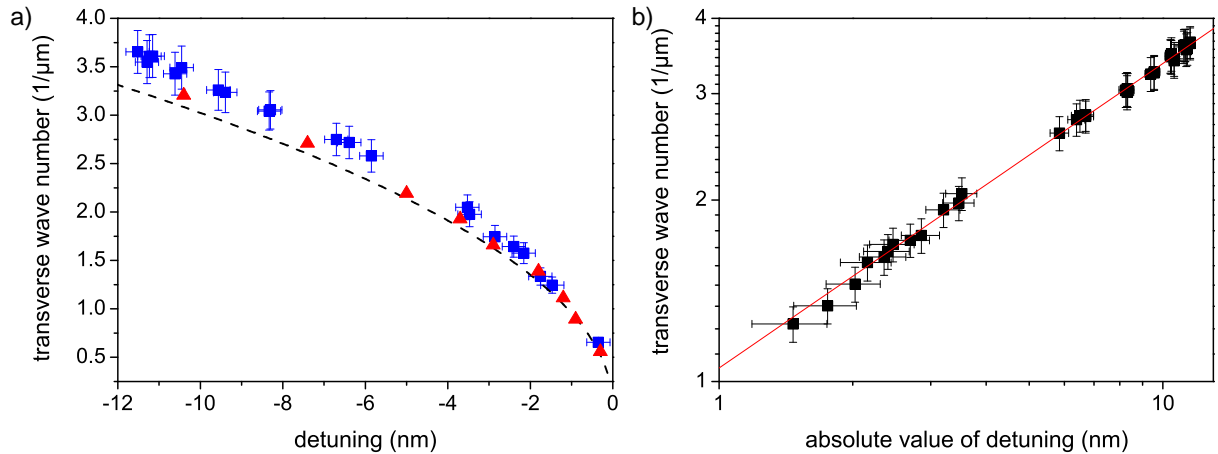


Figure 4.38: (a) Dependence of the transverse wave number of the emission on the detuning between cavity resonance and emission wavelengths. Experimental data points given for circular VCSEL 80–1. The dashed line is obtained from eq. (4.33) using $n_0 = 3.14$ and $n_{gr} = 3.47$. (b) Double-logarithmic plot of the transverse wave number over the absolute value of the detuning. The red line is a linear fit to the data and provides the scaling exponent of the experimental data.

data points from different lasers all fall on one curve. This is a further indication that the treatment of the experimental data yields correct results. That the transverse modes in different lasers are found at different detunings is an indication for growth inhomogeneities in the spacer layers leading to different absolute values of λ_c for given temperatures.

The shape of the curve on which all data points are located looks like a square-root. This is confirmed by the double-logarithmic plot of the transverse wave number over the absolute value of the detuning shown in subfigure (b). The linear fit to the data, plotted as a red line, has a slope of $0.49(1)$, which is a near perfect agreement with the assumed square-root shape.

With $n_0 = 3.37$ and $n_{gr} = 4.20$ obtained by weighted averaging over the layers of the cavity (layers 8–13, cf. section 3.4.1 and appendix B) the dashed black line is obtained using eq. (4.33). The agreement between the simple relation generally valid for Fabry-Perot resonators and the experimental data is very good for detunings up to -8 nm. Beyond that a slight drop of the transverse wave numbers can be seen for lasers 40–7 and 40–9. Though the theoretical curve is still inside the error intervals of the data points, this drop may in part be attributed to higher losses for modes with high wave numbers, e.g. due to a drop of the reflectivity of the DBRs (cf. section 5.3.4).

Despite this excellent agreement it has to be kept in mind that eq. (4.33) is only a simple model of a plano-planar Fabry-Perot cavity. It disregards the phase shift introduced by the DBRs. In [153] it was shown that this phase shift is also approximately proportional to the square of the transverse wave number in the wave number range under study. Thus the square root behavior is also found when the phase shift of the DBRs is included. Nonetheless the agreement between the simple Fabry-Perot equation and the experimental data is clearly better than the data calculated with the more rigorous model (see [153]).

A similar plot for the circular VCSELs is shown in fig. 4.38(a). Here the data shown

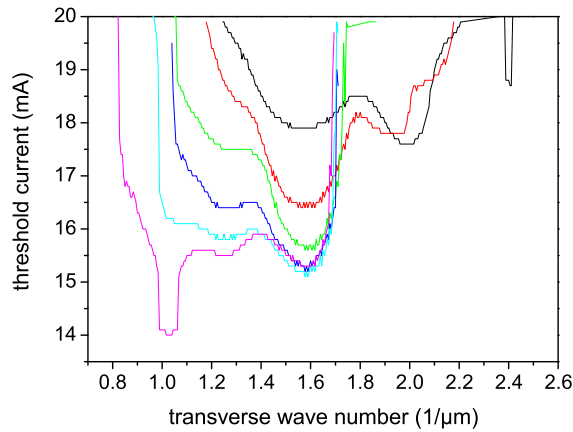


Figure 4.39: Plot of the dependence of the modal threshold on the transverse wave number for device 40-6 and various temperatures: 10 °C (black curve), 14 °C (red), 18 °C (green), 22 °C (blue), 26 °C (cyan), 30 °C (magenta).

in blue is obtained with laser 80-1, the errors again stem from error propagation of reasonable measurement and reading errors. As for the square VCSELs subfigure (b) shows the double-logarithmic plot of the data and a linear fit, which has a slope of 0.50(1), in perfect agreement with the expected square-root shape. The transverse wave numbers are somewhat smaller than for the square VCSELs. The red triangles in subfigure (a) stem from a program [162] that calculates the resonance condition for a cavity with DBRs similar to the structure of the circular VCSELs. They show reasonable agreement with the experimental data. The dashed black line is obtained with eq. (4.33) with $n_0 = 3.14$ and $n_{gr} = 3.47$ (obtained by weighted averaging of layers 8-13 in table B.3). The agreement between the calculated curve and the measured values is not as good as for the square VCSELs.

In conclusion, these results show a dependence of the square of the transverse wave number on the detuning between emission wavelength and longitudinal resonance. The results are independent of the transverse laser geometry. Before the publication of [153] this was not shown quantitatively for self-induced transverse modes in plano-planar laser cavities, though it was predicted by several theoretical calculations.

4.3.5 Transverse mode selection above threshold

In the last chapter, section 3.4.2, the threshold behavior was investigated only for the laser emission as a whole. More insights into mode spacing and mode selection mechanisms can be gained by looking at the threshold of each individual transverse mode and the behavior of these thresholds for varying temperature. Spatial Fourier spectra for currents around the laser threshold with high current resolution and for several temperatures are needed for this. Thus for each temperature a current resolved spatial Fourier map and a wave number dependent threshold are obtained.

In section 3.4.2 the threshold was determined by a linear regression to the slope of the L-I curve above threshold. It is found that here a different method is more appropriate: the threshold is defined as the current where the plot of intensity over current rises above

7% of the global maximum of the intensity (i.e. the maximum of the whole spectra map). In this way the often ambiguous linear regression to the steep slope of the same plot is avoided. The absolute values of the thresholds is not comparable to those determined by the linear fit, but here only the relative thresholds are of interest.

An exemplary result of this procedure for laser 40-6 is shown in fig. 4.39. Each curve corresponds to one temperature setting between 10 and 30 °C with a step of 4 °C. It is apparent that for each wave number (with a discretization step determined by the resolution of the far-field images) a threshold value is obtained. For those wave numbers where no transverse mode is emitted the threshold is very high. It is lowest for the central wave number of the dominant mode.

The cyan-colored plot corresponds to the highest temperature of 30 °C. Here two pronounced threshold minima are found at around $1 \mu\text{m}^{-1}$ and $1.6 \mu\text{m}^{-1}$. Another weaker mode is visible at $1.3 \mu\text{m}^{-1}$. Note that for decreasing temperature the established trend towards higher wave number is apparent. At the same time those higher modes are found at recurring positions: the cyan, blue, green, and red curves have their minimum at $1.6 \mu\text{m}^{-1}$, and also the black curve features a local minimum there. That means the mode with the wave number $1.6 \mu\text{m}^{-1}$ is found for all temperatures, always at approximately the same position. The same is true, but less pronounced, for the mode at $1.3 \mu\text{m}^{-1}$. The red and black curves feature another mode at $2.0 \mu\text{m}^{-1}$. Overall four clearly discernable transverse modes are found in this temperature range. Their wave numbers are constant and their thresholds differ by up to 5 mA. The threshold behavior changes with temperature, in agreement with the trend shown in fig. 4.25. The small number of modes inside the studied wave number range reflects the sparseness of data points in fig. 4.37. Note that this method does not necessarily show the mode spacing between all possible transverse modes.

This plot also demonstrates that a second mode is excited between 0.5 and 1.5 mA above threshold. In most cases the second mode has a lower wave number than the one excited at threshold. The exceptions in the figure are the cyan and the red curves. The tendency found in region I that secondary modes can have a larger wave number than the mode at threshold was discussed in section 4.2.1.2.

4.3.6 The model describing the VCSELs

In this section a model is described that explains some of the observations from the experiment. It also serves as a basis for the improved model described in the next chapter, section 5.3.4. The model is based on the spin-flip model [97] describing the interaction of the active medium with the light field and includes the anisotropic reflection at the DBRs. This model was developed by N. Loiko and I. Babushkin from the Institute of Physics at the National Academy of Sciences in Minsk, Belarus. Their work is published in many articles [96, 98–100, 163–166]. The most complete description of the model can be found in [98]. The author is very grateful to them for their support and the kind permission to use some additional numerical results for comparison with the experiments.

In [98] the interaction of the light field with the active medium is described by the spin-flip model [97]. This model is an extension of the standard Maxwell-Bloch equations for two-level semiconductor lasers (e.g. [81]). It includes a four-level description of valence

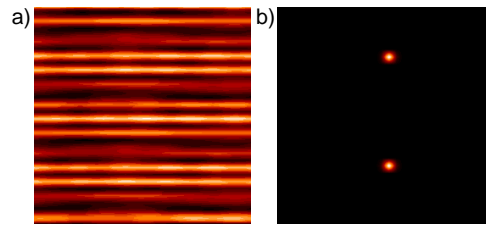


Figure 4.40: Numerical simulation of the transverse mode excited at threshold in a square VCSEL with strong amplitude anisotropy. Time averaged images of the near-field (a) and the far-field (b). The stripes in the near-field image are parallel to the polarization orientation.

and conduction band and the polarization of light. It is based on the Maxwell-Bloch equations for left- and righthanded circular polarization with the slowly varying envelope approximation. The model is often called “vectorial” as opposed to the “scalar” models that do not include polarization degrees of freedom. The material amplitude and phase anisotropies (corresponding to dichroism and birefringence, respectively) included into the model describe the degree of polarization determinism. If the amplitude anisotropy is very large ($\gamma_a \rightarrow \infty$) the model becomes similar to the scalar one described in [96]. In this case the polarization is fixed to one orientation and polarization dynamics are eliminated.

The propagation of the light field through the spacer layers is described by the paraxial wave equation. In [96, 98, 163] a model for the propagation is developed that describes the successive transit of the light wave through the parts of the cavity, including the diffraction in the spacer layers. Since the active medium is very thin compared to the optical wavelength, the diffraction during the transition is neglected and the electric field is given as the sum of the two incident fields and the material polarization.

The model takes a complex reflection at the DBRs into account that depends both on the wavelength and the transverse wave number. Due to the polarization dependent Fresnel reflection at thin layers the reflectivity is also dependent on the direction of the transverse wave vector. This is discussed in detail in the next chapter, section 5.3.4.

4.3.7 Results of the model and comparison with the experiment

The main mechanisms for the selection of the pattern shape and the length scales included in the model are as follows: the gain dispersion is mainly responsible for the length scale selection, which is equal to the detuning argument introduced in section 2.4 and observed also in the experiment. In addition, the reflectivity of the DBRs is weakly dependent on the transverse wave number q , which modifies the length scale selection slightly. The losses are independent of q , except in the DBRs.

In most publications (e.g. [24, 98]) the influence of transverse laser boundaries are neglected, i.e. the laser is assumed to have an infinite transverse size. In this case calculations result in a transverse travelling wave with a homogenous near-field emission at threshold. A standing wave composed of two counter-propagating waves is created by the reflections at the transverse boundaries when the boundaries are not neglected. Nonetheless, as shown in [165], a standing wave pattern can also arise in VCSELs with infinite transverse size from a secondary bifurcation.

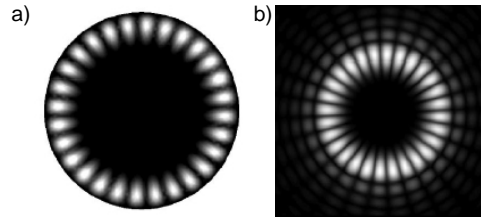


Figure 4.41: Numerical simulation of the transverse mode excited at threshold in a circular laser with current crowding around the boundary of the aperture. Time averaged images of the near-field (a) and the far-field (b).

An example of a numerical simulation at threshold with negative detuning $\delta = \lambda - \lambda_c$ (positive $\Omega = \omega - \omega_c$ in [96, 98]) and a high amplitude anisotropy (i.e. a strong polarization determinism) is shown in fig. 4.40. Similar results are also presented in [167]. The resulting temporally averaged near-field pattern shows a standing wave pattern consisting of perfect stripes. This corresponds to two Fourier components aligned with the vertical axis. Vertical or horizontal alignment of the pattern is controlled by the sign of the amplitude anisotropy.

A comparison with the experimentally observed transverse patterns shows that this model is not sufficient to explain all pattern selection mechanisms in the VCSELs. The perfect stripes found in the numerical simulations at threshold are never observed in the experiment. A symmetry breaking effect that is not included in the model is apparently responsible for the wavy stripe patterns observed in the experiments already at threshold, corresponding to the predominant four-fold symmetry of the far-field images.

For pump rates above threshold the numerical simulations also yield less ordered patterns, as shown in [98]. The snapshots of the temporal evolution show far-field patterns resembling rings with several pronounced Fourier components. The radius of the ring is defined by the detuning. Those patterns somewhat resemble the region I emission observed in the VCSELs under study.

In [100] the model is used to simulate the emission of large circular VCSELs. The effect of pump crowding along the edges of the aperture [43, 93] is included into the numerical calculations. The result are flower-like patterns as shown in fig. 4.41 excited at threshold. The near-field image consists of an azimuthally modulated ring close to the circular aperture. The area of the aperture is indicated by the black background. The Fourier transform is approximately self-similar for this kind of pattern.

The example is similar to the emission of the circular laser studied in this work. Figures 4.9(b) and (g) bear the closest resemblance to the simulated mode. As can be expected the modes shown in the experimental images are less regular. The ring in the far-field image is much broader and the modulation is smaller than in the numerical simulation. The different mode orders in simulation and experiment are due to different detuning values. In principle, the simulation can yield the same order when the detuning is selected accordingly.

In a simple interpretation the characteristics of the emission of the circular VCSELs arise from the azimuthal gain guiding at the border of the aperture, due to the current crowding there. Along the ring of heightened gain the emission forms an azimuthal

standing wave with a transverse wave number selected by the detuning. The shape of the guiding profile determines if the transverse mode represents a Gauss-Laguerre, Bessel, or Fourier mode. The imaging resolution of the experiments is not sufficient to clarify which type is present in the circular VCSELs under study.

In [100] also modes far above threshold are calculated. Those modes are located also at the central area of the aperture, not only along the boundary. This is somewhat similar to the case observed in the experiment for high currents. Examples are also shown in fig. 4.9.

In conclusion, it is found that the model is able to describe the emission of the circular VCSELs quite well, while the mechanisms responsible for the pattern selection in the square lasers are not explained in detail.

5 Polarization of spatial states

This chapter expands on the characterization of the emission of the VCSELs by introducing the polarization degree of freedom. It is shown that the three distinct pattern shapes found in the previous chapter also feature distinct mechanisms of polarization selection. On those mechanisms lies the focus of this chapter. In the first section the method of polarization measurement and some additions to the setup are described. In the next section the experimentally observed details of the state of polarization and experiments with temporal resolution are presented. The latter shows some aspects of the turn-on behavior and the onset of thermal effects in the lasers. In the last section the experimental observations are compared to numerical simulations and the polarization selection mechanisms are explained.

5.1 Experimental setup

The setup schematically shown in fig. 4.1 is used here to measure the state of polarization of the emission. Therefore the spatially resolved Stokes parameters are introduced in the first section. In the second section a modification to the setup is illustrated that allows experiments with a temporal resolution of the order of tens of nanoseconds.

5.1.1 Spatially resolved Stokes parameters

The Stokes parameters are a set of values that fully describe the polarization state of light. To calculate the complete set of Stokes parameters from experiments the measurements of four polarization states of the laser emission are necessary. In the experimental setup a linear polarizer and a half-wave plate are needed for this. The linear polarizer is oriented so that it transmits horizontally polarized light. The polarization angle φ is defined with respect to the horizontal axis, positive rotation direction is counter-clockwise when looking toward the laser.

The four measurements necessary to determine Stokes parameters are:

- horizontally polarized component I_x : the fast axis of the half-wave plate is aligned with linear polarizer,
- vertically polarized component I_y : the wave plate is rotated by 45° with respect to the horizontal axis,
- diagonally polarized component I_{45} : the wave plate is rotated by 22.5° with respect to the horizontal axis,

- one circular component I_{circ} : the half-wave plate is exchanged with a quarter-wave plate with the fast-axis set to 45° with respect to the horizontal axis.

With these measurements the Stokes parameters are calculated from the following equations:

$$S_0 = I_x + I_y, \quad (5.1)$$

$$S_1 = \frac{(I_x - I_y)}{S_0}, \quad (5.2)$$

$$S_2 = \left(\frac{2 \cdot I_{45}}{S_0} \right) - 1, \quad (5.3)$$

$$S_3 = \left(\frac{2 \cdot I_{circ}}{S_0} \right) - 1, \quad (5.4)$$

where S_0 represents the total intensity, S_1 describes the degree of horizontally (positive S_1) or vertically (negative S_1) polarized light, S_2 corresponds to the degree of polarization along the diagonal directions (positive for 45° , negative for -45°), and S_3 represents the degree of circular polarization (the sign denotes the direction of rotation). In addition, the fractional polarization (FP) and the distribution of the polarization direction φ can be calculated with

$$FP = \sqrt{S_1^2 + S_2^2 + S_3^2} \quad (5.5)$$

$$\varphi = \frac{1}{2} \cdot \arctan \left(\frac{S_2}{S_1} \right). \quad (5.6)$$

When calculating φ the four-quadrant variant of the arc tangent has to be used, which has a range from $-\pi$ to π . φ then has a range from -90° to 90° .

Here, this mechanism to measure polarization is extended to two dimensions: by taking near-field or far-field images for each I_x , I_y , I_{45} , and I_{circ} the polarization distribution in the laser aperture, respectively the Fourier plane is obtained. Note that to our knowledge spatially resolved Stokes parameters were not applied to the study of the polarization of laser radiation prior to this work. The error of the polarization measurement is estimated from a measurement with an additional linear polarizer between laser and the half-wave plate. In this way, the state of polarization of the laser beam is known and compared to the result of the measurement. It turns out that a maximum deviation of up to 5° is found. The standard deviation is around 1° .

Of course, in general the polarization orientation is defined with respect to the propagation direction of a beam, i.e. in the plane orthogonal to its wave vector. Images taken with the CCD camera naturally measure a projection of the polarization planes of the modes to the plane orthogonal to the optical axis (assuming the camera is properly aligned orthogonal to the optical axis). Since the emission of the VCSELs is often highly divergent, and the effect of this projection increases with the divergence angle, it has to be checked if the projection modifies the measured polarization angles noticeably. For this a different setup was used to measure the polarization of some selected modes directly. Laser 30-3 was mounted on a heat sink without the air-tight box. Also no collimation

lens was used. Instead a detector was put on a tiltable, movable stage in front of the laser, in some centimeters distance. The detector could thus be moved in lateral direction and tilted around two axes. In addition, a linear polarizer, an iris aperture (set to about 2 mm diameter), and a lens were put between detector and VCSEL. From the components k_x, k_y of the transverse wave vector of a selected Fourier component (taken from far-field images) the necessary tilt angle was calculated. The detector was tilted accordingly and the lateral position was adjusted so that the selected Fourier component was transmitted through the iris aperture. Turning the linear polarizer to horizontal, vertical, and diagonal transmission the data necessary for the Stokes parameters was obtained. The calculated polarization angles were inside a 1° interval around those obtained from the standard spatially-resolved measurements. Thus it is shown that the effect of the projection is small and can be neglected.

For a few measurements a different CCD camera (SVS-Vistek 285MSCL, 12 bit, 1360×1030 pixel) with pixels of $6.5 \mu\text{m}$ side length is used. Compared to the usually used CCD camera described in section 4.1.1 this allows a magnification of the near-field and far-field images by a factor of approximately 6. This is used to magnify selected Fourier components to better analyze the details of the polarization distribution.

5.1.2 Pulsed excitation

To analyze the temporal evolution of the emission of the VCSELs on time scales of tens of nanoseconds to several microseconds some additions were made to the standard setup. Firstly the current source was changed to the following setup: a pulse generator (Hewlett Packard 8005B) feeds a TTL signal of arbitrary length and repetition rate to an electronic circuit that converts TTL signals to ECL signals.¹ The resulting signal is sent to a high-speed laser diode driver (Hytek HY6110) that generates a current pulse from the ECL pulse with (nominally) the same parameters as the original TTL signal. Current pulses of down to 50 ns length can be generated in this way. The height and zero level of the current pulses can be controlled via a PC with a digital-analogue converter (DAC). The current pulse is then sent to the laser via a self-made electronic circuit (see appendix D for details on the circuit). Note that both pulse generators are synchronized by the same trigger signal, which is created in the HP pulse generator.

Secondly, an optical beam path is added to the setup, as shown in fig. 5.1. To analyze the modal structure of the far-field emission a fast shutter CCD camera (Proxitronic Nanocam HF4 S 5N, minimal shutter time 5 ns, CCD chip with 756×581 pixels) is used with a video sampling technique. For this the trigger from the pulse generator is fed to an electronic circuit specifically designed for this method. It combines the external trigger with the camera trigger (the camera can not be triggered faster than 50 Hz). The resulting synchronization signal shows a comparatively strong temporal jitter with a width of about 75 ns. This restricts the temporal resolution of the measurements. This signal is sent to the digital control unit of the camera. The unit controls the camera shutter, using the external trigger and an added gating time (0 to 65 ms in 1 ns steps). When the camera

¹TTL (transistor-transistor logic) and ECL (emitter-coupled logic) are different types of logics used for electronic circuits. Here the only difference of interest are the different power levels for on-state and off-state used in the two types.

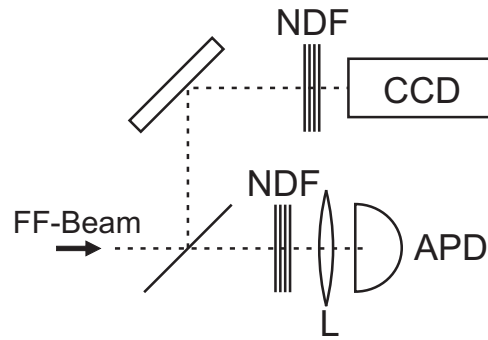


Figure 5.1: Addition to fig. 4.1 for pulsed excitation experiments. The beam coming from the left (“FF-Beam”) is diverted from the far-field beam path in the original setup, so that the far-field emission is imaged onto the CCD camera. The abbreviations denote the following components: NDF – neutral density filters, CCD – CCD camera, L – lens, APD – avalanche photo diode.

gating time is scanned in consecutive images, the temporal evolution of the camera image can be obtained. Note that this method does not enable temporal resolution of one event, but needs a periodic sequence to gather the time resolved images from consecutive events.

For time traces of the total output power an avalanche photo diode (APD, Silicon Sensor SSO-AD-230, analogue bandwidth 1.8 GHz) was connected to the oscilloscope (2 GHz maximal analogue bandwidth, 125 ps sampling interval).

5.2 Experimental observations

The experiments illustrated in this section all serve the purpose of understanding the polarization selection mechanisms occurring in the VCSELs. At first spatially averaged Stokes parameters are considered that give some insight into the general trends. This is followed by an analysis of the degree of circular polarization. It is established that this circular part can be neglected in the later experiments, which simplifies the analysis of the state of polarization considerably.

The main aspect of the experiments is the detailed description of the state of polarization in the three regions introduced in the last chapter. It is found that these regions also feature distinct polarization characteristics and can be analogously defined with respect to these characteristics. This is followed by a section about the polarization distribution of the ASE below threshold, which provides another important fragment along the way of understanding the polarization selection. Finally experiments with temporal resolution of down to tens of nanoseconds are described. There, the turn-on behavior is studied, especially considering the temporal evolution of the polarization distribution and the influence of thermal effects.

5.2.1 Averaged Stokes parameters

To study general trends, at first the Stokes parameters averaged over the whole beam are considered. Averaged Stokes parameters are obtained by sending the laser beam to a

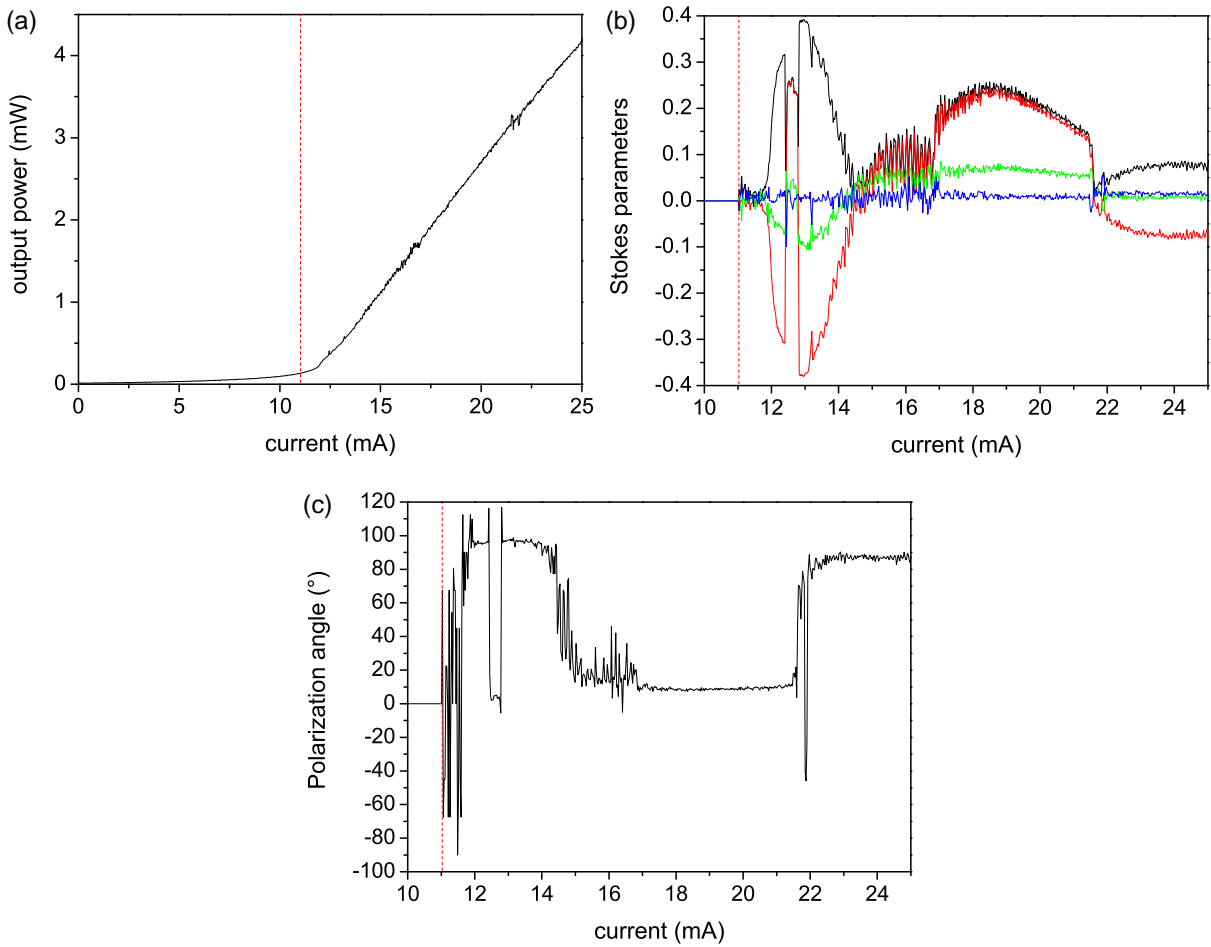


Figure 5.2: Current dependence of averaged Stokes parameters for laser 40–7 at 42°C. The laser threshold is indicated by the dotted red line. (a) Total intensity (S_0), same as L–I curve. (b) FP (black), S_1 (red), S_2 (green), and S_3 (blue). Below threshold the Stokes parameters are set to zero. (c) Polarization angle calculated from the Stokes parameters.

standard photo detector. The result is very similar to the L–I curves portrayed in section 3.3.1, but with added information about the state of polarization. Examples are shown in figures 5.2 and 5.3.

The figures show L–I curves and the corresponding Stokes parameters S_1 , S_2 , S_3 together with the FP and the polarization angle. The first figure characterizes the current dependence of the emission of laser 40–7 at 42°C. In (a) a typical L–I curve is shown. The blue curve in (b), representing S_3 , is very close to zero. This is expected for VCSELs, since circular polarization is the exception in such lasers due to the frequency-splitting between orthogonal linearly polarized modes which is induced by the linear birefringence [57, 168]. The polarization angle in (c) changes orientation five times between 0° and 90°. The FP is rather low (maximum about 0.4) and nearly vanishes each time the polarization angle changes. Apparently, the laser tends to operate on modes with either horizontal or vertical polarization orientation. Note that the switching between the two orthogonal directions does not take place in one transverse mode only. Near threshold

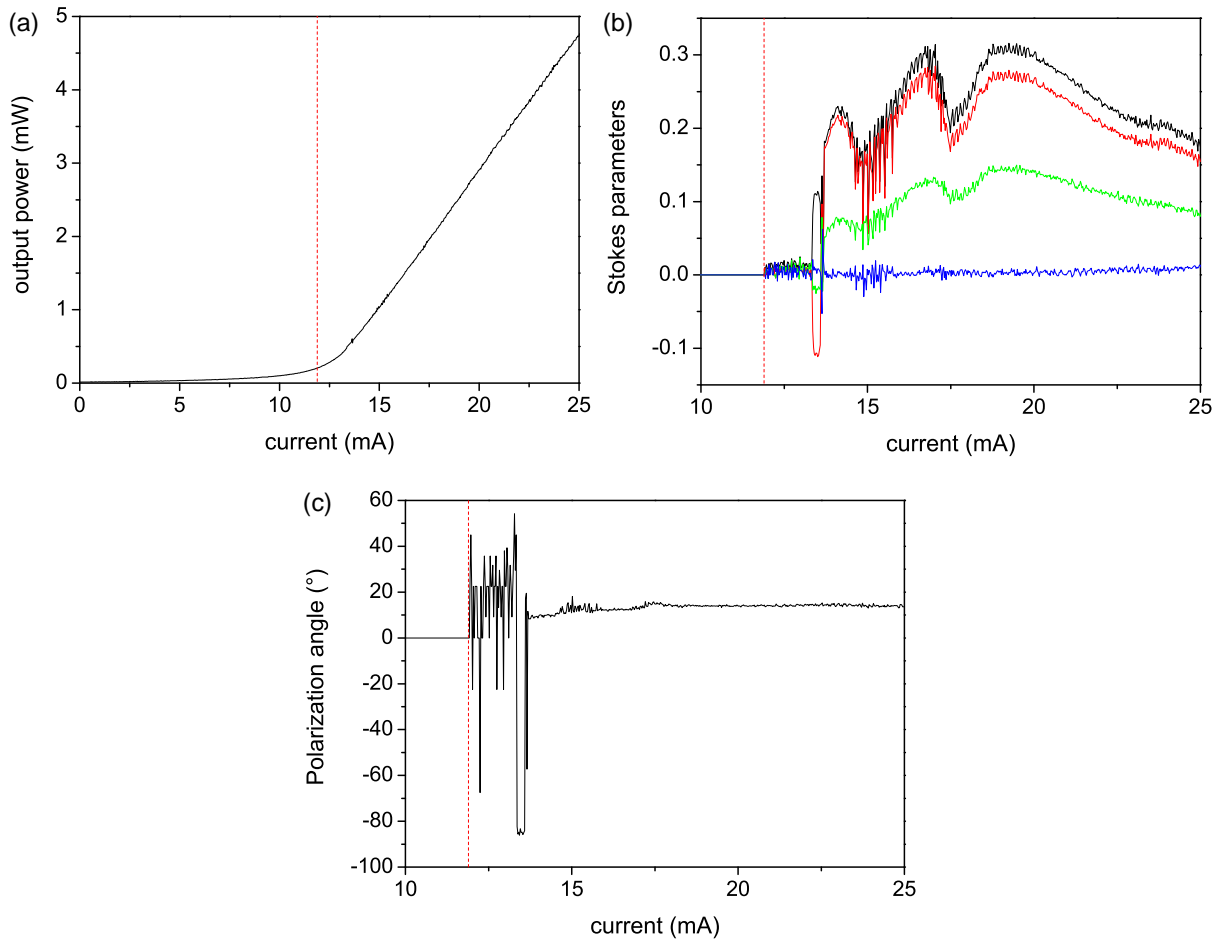


Figure 5.3: Current dependence of averaged Stokes parameters for laser 40-7 at 20°C. The laser threshold is indicated by the dotted red line. (a) Total intensity (S_0), same as L-I curve. (b) FP (black), S_1 (red), S_2 (green), and S_3 (blue). Below threshold the Stokes parameters are set to zero. (c) Polarization angle calculated from the Stokes parameters.

only a mode consisting of an irregular long wavelength pattern is excited (cf. fig. 4.4(a)), which is homogeneously polarized in vertical direction. Between 15 and 22 mA this mode switches to horizontal polarization. The change of the polarization around 22 mA is due to the redistribution of intensity to a vertically polarized higher order mode.

The second example, fig. 5.3 shows the emission of the same laser at 20°C. The layout is the same as before. Here, at first the polarization angle is very noisy due to the near-zero FP. A short polarization switch to -90° and back to 10° is apparent at the start of the increase of the FP. This is probably due to the onset of a weak vertically polarized mode at first, but already for slightly higher currents another mode is excited with horizontal polarization. The polarization then stays approximately constant up to 25 mA. The FP (black curve in (b)) changes quite strongly in this current range but stays below 0.3. The circular part is close to zero for all currents.

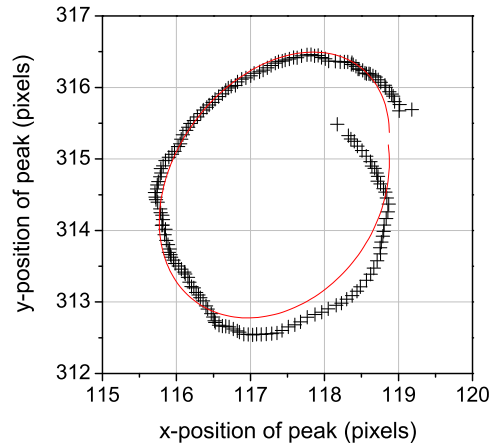


Figure 5.4: Illustration of the beam displacement encountered when using a quarter-wave plate. The plot shows the position of a Fourier component in the far-field emission of laser 40–7 at 16 mA and 0 °C, while turning the quarter wave-plate by 360° (in steps of 2°). The Fourier component is tracked after the image is strongly magnifying and smoothed. The red line is a 2-dimensional cosine fitted to the data. The grid visualizes the position of the pixels of the original image.

5.2.2 Degree of circular polarization with spatial resolution

If the degree of circular polarization is measured with spatial resolution the obtained values are much larger than those encountered in the averaged measurements described above. In this section it is checked if these large values of S_3 are real or arise due to artifacts in the measurement and analysis. A strong indication for measurement artifacts is given by a beam displacement observed when the half-wave plate is replaced by the quarter-wave plate. Though this displacement is quite small, of the order of some pixels of the CCD camera, the impact on the degree of circular polarization is large.

First, the problem connected with the measurement of I_{circ} , the intensity necessary to calculate S_3 , is illustrated. As explained in section 5.1.1, the half-wave plate in the setup must be replaced by a quarter-wave plate for this. While no noticeable beam displacement occurred in the comparison of images taken for different settings of the half-wave plate, this undesirable effect was quite pronounced when using the quarter-wave plate. In fig. 5.4 the central position of a Fourier component of a far-field image is plotted while the quarter-wave plate is turned by 360°. An image of I_{circ} with standard resolution is used for this and the selected Fourier component is magnified strongly and smoothed to facilitate the tracking of the component with a resolution better than the pixel size of the original image. The positions in the magnified image corresponding to pixels in the original image are marked by the grid lines in the plot. During the full turn of the quarter-wave plate the position of the peak also moves along an imperfect full circle. The diameter of the circle is about 4 pixels (on the original image). Though this may appear to be a very small beam displacement it strongly affects the values obtained from spatial Stokes measurements because the peaks in the far-field are very sharp. The red curve in the figure is obtained by fitting a two-dimensional cosine to the experimental data.

The impact of the beam displacement is illustrated in fig. 5.5 for a transverse mode

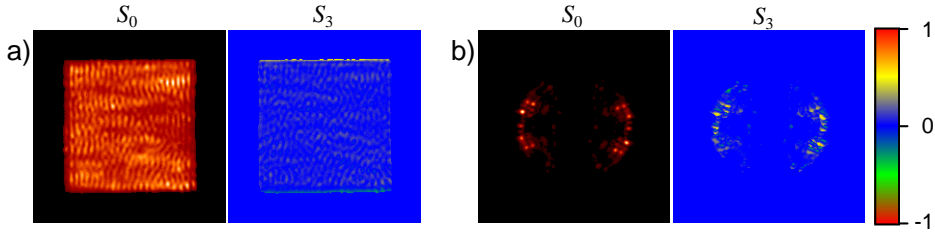


Figure 5.5: Near-field (a) and far-field images (b) of laser 30–3 at 13 mA and 10 °C. Each subfigure shows the total intensity (S_0) and the degree of circular polarization (S_3). The images of S_3 are color-coded as shown by the color bar on the right. They were obtained using the standard method for Stokes parameters detailed in section 5.1.1. Calculated S_3 values are within the interval $[-0.3, 0.7]$, but are actually artifacts of the beam displacement as discussed in the text.

emitted by VCSEL 30–3 operating at 10 °C and 13 mA. The near-field image is shown in (a), the far-field image in (b), in each subfigure the total intensity S_0 and the calculated degree of circular polarization S_3 is shown. Values of S_3 of up to 0.7 occur when S_3 is calculated with eq. (5.1). That this is in fact a result of an improper measurement method is demonstrated by the following measurement of S_3 with a different approach: in addition to the image taken with the quarter-wave plate set to 45° in relation to the horizontal orientation of the linear polarizer, images were taken at 135°, 225°, and 315° as well. The four measurements are called I_{45} , I_{135} , I_{225} , and I_{315} in the following. With these it is possible to calculate S_0 and S_3 independent of the measurements with the half-wave plate using the following set of equations:

$$I_1 = \frac{I_{45} + I_{225}}{2}, \quad (5.7)$$

$$I_2 = \frac{I_{135} + I_{315}}{2}, \quad (5.8)$$

$$S_0 = I_1 + I_2, \quad (5.9)$$

$$S_3 = \frac{2I_1}{S_0} - 1 = \frac{I_1 - I_2}{S_0}. \quad (5.10)$$

Here I_1 and I_2 are the respective averages of the measurements with 180° of quarter-wave plate rotation between them. In this way the effect of the beam displacement is reduced, but the spatial resolution is reduced slightly, since the averaging leads to a slight broadening of the peaks in the images. Instead of determining S_0 by adding two orthogonally linear polarized images (cf. eq. (5.1)), it is calculated as the sum of the two circularly polarized images of opposed helicity. S_3 is determined in the usual way.

The result of this method is illustrated in fig. 5.6, where the same state of emission is shown as in the previous figure. The largest (absolute) value of S_3 found here is 0.16. The maximum in the near-field image is only 0.05. It is clear that the beam displacement for the near-field images is lower, because the beam path is much shorter than for the far-field emission. Thus lower values of S_3 are expected. That this is supported by the experiment shows that the high values of S_3 obtained with the standard method are indeed results of the beam displacement. Remaining deviations from zero are likely due to imperfections in measurements and analysis.

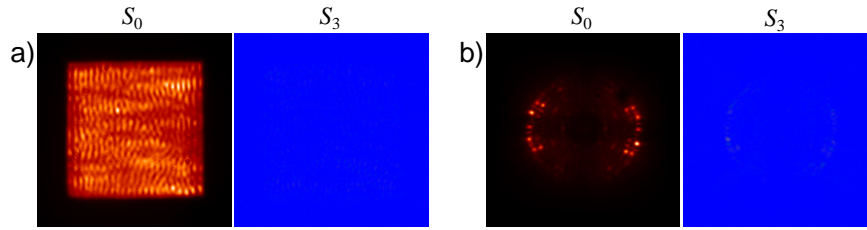


Figure 5.6: Near-field (a) and far-field images (b) of laser 30–3 at 13 mA and 10 °C. Each subfigure shows the total intensity (S_0) and the degree of circular polarization (S_3). The color-code for S_3 is shown in fig. 5.5. The images were obtained using the averaging method specifically designed for measurements of the degree of circular polarization (for details see text). S_3 values are within the interval $[-0.04, 0.05]$ for the near-field image and $[-0.09, 0.16]$ for the far-field image.

It is concluded that the circular component of the emission, at least for the VCSELs under study, is negligible. This is also in line with results from studies on small area VCSELs ($\leq 15 \mu\text{m}$), in which the birefringence is favoring the linear over the circular polarization (e.g. [169] and references therein).

5.2.3 Emission with small transverse wave numbers

In section 4.2.1 the emission of the VCSELs was characterized by introducing three regions that correspond to different pattern shapes as well as different length scales. This classification is even more clear when the polarization behavior is considered in addition. In this section the polarization distribution in region I will be analyzed, followed by region II and III in the next sections.

Figure 5.7 shows the near-field and figure 5.8 the far-field images of several lasers at the highest investigated temperature and for injection currents just above laser threshold (the actual values are given in the caption). Images (a)-(e) in the upper row show the total intensity which already appeared in the previous chapter. The middle row, subfigures (f)-(j), show the FP (cf. eq. (5.1)). These images are all scaled to a maximum of 1, since the FP ranges from 0 to 1 (in contrast to the images of S_0 that are scaled to the respective maximum). In this way the degree of polarization is visible in the brightness of the images. The third row, subfigures (k)-(o), shows the polarization distribution, color-coded with a cyclic palette as indicated on the right of fig. 5.7.

This special color-code is chosen due to several reasons:

- it has to be cyclic because the range of the polarization angle is inside the interval $[-90^\circ, 90^\circ[$, and the two extreme values represent the same angle of polarization.
- the colors black and white should not be used because they are easily mistaken for low and high intensity.
- at least four different colors are needed to facilitate the distinction of $\pm 90^\circ$, -45° , 0° , and $+45^\circ$ polarization. Fewer colors (e.g. only three, at $\pm 90^\circ$ and 0°) make it very difficult to identify different angles from the images.

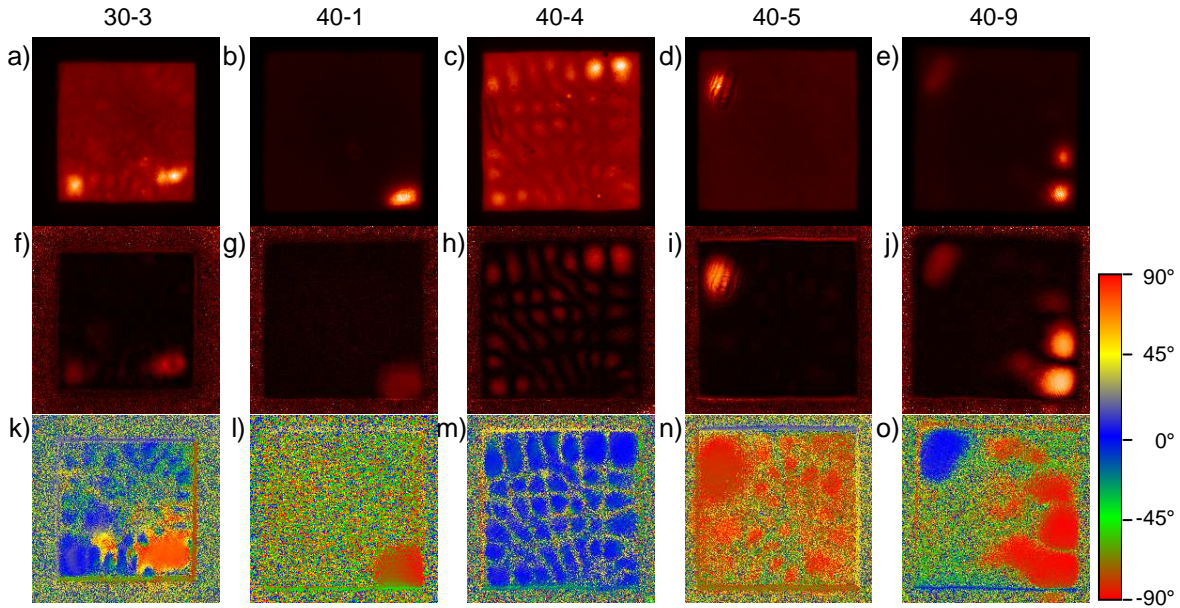


Figure 5.7: Near-field emission of various lasers just above threshold for high temperatures (region I). (a-e) S_0 , (f-j) FP, (k-o) polarization angle. The color-code of the polarization angle is shown on the right side. It is used for similar figures throughout the thesis. Parameters: $T = 42^\circ\text{C}$. 30-3: $I = 12\text{ mA}$, $p = 0.29$. 40-1: $I = 10\text{ mA}$, $p = 0.27$. 40-4: $I = 12\text{ mA}$, $p = 0.08$. 40-5: $I = 12\text{ mA}$, $p = 0.08$. 40-9: $I = 11\text{ mA}$, $p = 0.02$.

- colors of the same brightness should be used so that no polarization angle stands out from the others. For example a full circle in the HLS color model would do that. This idea was dropped in favor of the RGB colors red ($\pm 90^\circ$), green (-45°), blue (0°), and yellow ($+45^\circ$), because these colors are easily distinguishable. Though yellow is brighter than blue, it was found that this hardly influences the readability of the polarization images.

The angles between the four directions are filled by linear interpolation of the RGB values.

Of course, where the degree of polarization is (close to) zero the angle of polarization is not defined. Due to the intrinsic noise of the CCD camera (about 0.03% of the dynamic range) unpolarized light (or a low degree of linear polarization) generates a random distribution of all possible polarization angles. An example in the color-coded representation can be seen in fig. 5.7(l) outside the spot with high intensity in the lower right corner.

As seen in the previous chapter, the near-field emission is dominated by localized spots and irregular long wavelength patterns. The polarization distribution shows that these patterns are polarized homogeneously in one direction in most cases, both in the near-field as well as in the far-field images. An exception is shown in subfigures (k) and (o) in both figures: laser 30-3 emits a rather irregular pattern consisting of two bright spots with some weaker emission in between with at least three different polarization angles. The near-field emission of laser 40-9 consists of two bright spots in the lower right corner and a weaker one in the upper left. The polarization angle is $\pm 90^\circ$ (red) for the former and 0° (blue) for the latter. The vertical portion dominates, while the horizontal portion is

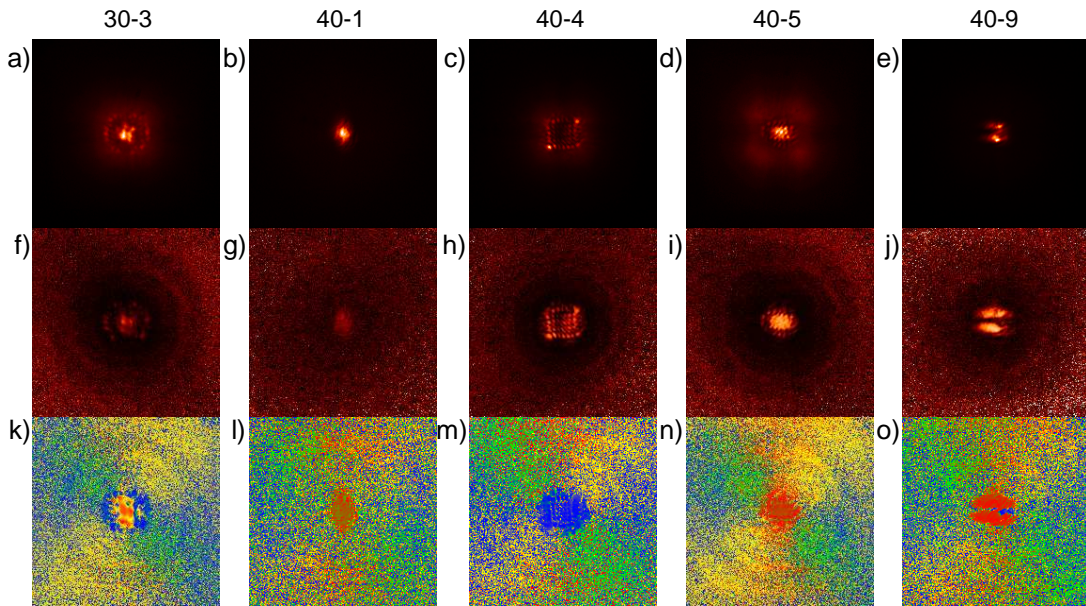


Figure 5.8: Far-field emission of various lasers just above threshold for high temperatures (region I). (a-e) S_0 , (f-j) FP, (k-o) polarization angle. Parameters: see fig. 5.7

weak in intensity and only found in a small region in both near-field and far-field images.

The lasers that tend to emit localized peaks for high temperatures sometimes also show polarization switching in those modes: when the current is changed the polarization switches from one state (horizontal or vertical) to the orthogonal one. Such a phenomenon is observed quite seldom, because the polarization switches back to the initial state already when the current is increased by a few tenths of a milliamperere. Such a switching scenario is documented in fig. 3.4, where also a bistable behavior is observed. Polarization switching (and bistability) is a phenomenon common in small VCSELs with a weak polarization anisotropy [169, 170].

Note that far above threshold when additional transverse modes are excited, the polarization distribution gets more and more complex due to the superposition of mostly horizontally or vertically polarized patterns.

In conclusion the emission of region I – at least close to threshold and as long as it is transversely single-moded – can in general be characterized by localized spots or long wavelength patterns that are polarized either vertically or horizontally.

5.2.4 Patterns with intermediate wave numbers

Transverse modes with intermediate wave numbers belonging to region II are emitted mostly between -10 and 20°C , but the parameter ranges vary from device to device. As described in the previous chapter the modes in region II that emitted at threshold generally consist of four intense Fourier components, one in each quadrant of the far-field image, and mostly with $k_x \ll k_y$ or vice versa.

Figures 5.9 and 5.10 show the near-field and far-field images of region II emission of various devices (the parameters are given in the caption). The polarization distribution

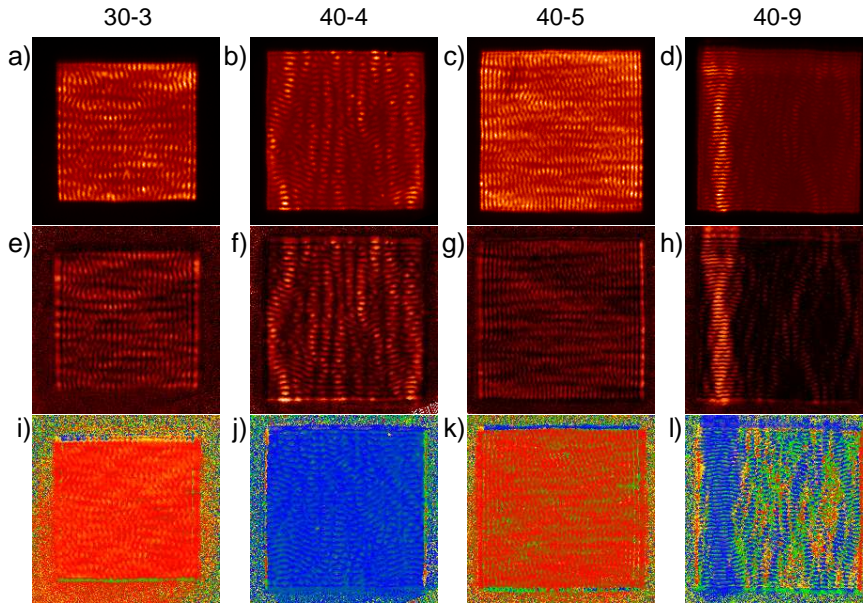


Figure 5.9: Near-field emission of various lasers just above threshold for intermediate temperatures (region II). (a-d) S_0 , (e-h) FP, (i-l) polarization angle. Parameters: 30-3: $T = 0^\circ\text{C}$, $I = 14\text{ mA}$, $p = 0.15$. 40-4: $T = -10^\circ\text{C}$, $I = 19\text{ mA}$, $p = 0.08$. 40-5: $T = 0^\circ\text{C}$, $I = 16\text{ mA}$, $p = 0.11$. 40-9: $T = 0^\circ\text{C}$, $I = 15\text{ mA}$, $p = 0.09$.

in the near-field images is again very homogeneous, though here the patterns have a shorter spatial wavelength and are more regular. Predominantly wavy stripe patterns are observed in the near-field images. The polarization of lasers 30-3 and 40-5 is vertical, which is parallel to the irregular stripes. Devices 40-4 and 40-9 show mainly horizontal polarization, again parallel to the orientation of the stripes.

The far-field images show the characteristic four-fold symmetry. Corresponding to the near-field the Fourier components of the patterns of laser 30-3 and 40-5 have a large k_x and a small k_y , i.e. they are oriented horizontally. The other two lasers emit patterns with vertical orientation of the Fourier components. The polarization is found to be either horizontal (lasers 30-3 and 40-5) or vertical (lasers 40-4 and 40-9), always orthogonal to the orientation of the Fourier components. In general the polarization is aligned with the laser boundaries and the orientation of the Fourier components selects between horizontal or vertical alignment. It can thus be said that a coupling between spatial and polarization degrees of freedom exists. This shows that the “90°-rule” introduced in section 2.5 is only valid at first glance and the details differ quite strongly from it.

Note that the far-field polarization distribution of laser 40-5 shows, in addition to the red areas on the left and right, also two blue areas at the top and the bottom. These correspond to the secondary modes excited above threshold. Though the secondary modes are not yet visible in the intensity, apparently the polarization changes to the above threshold orientation already before the onset of the modes.

Another feature found in most far-field images are ripples connecting the Fourier components, as described in section 4.2.2. Here it is found that their polarization is equal to that of the “parent” Fourier component.

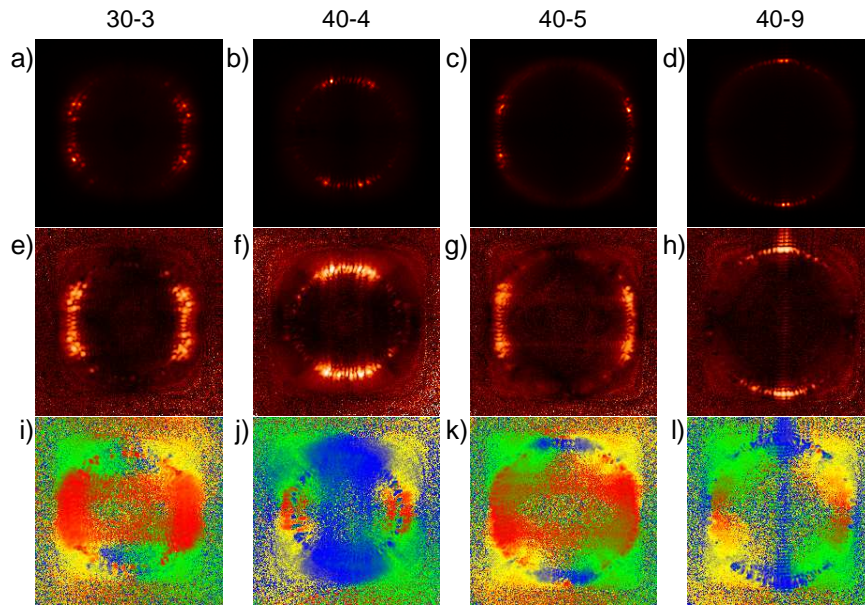


Figure 5.10: Far-field emission of various lasers just above threshold for intermediate temperatures (region II). (a-d) S_0 , (e-h) FP, (i-l) polarization angle. Parameters: see fig. 5.9.

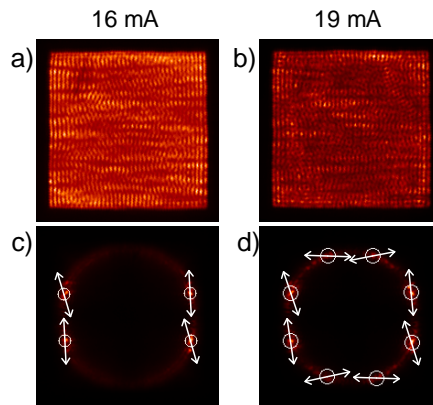


Figure 5.11: Near-field (a, b) and far-field images (c, d) of laser 40-5 at 0°C , illustrating the general characteristics of the polarization for region II modes. The locally averaged polarization angle is indicated by double-headed arrows in the far-field images for each dominant Fourier component. The respective pump rates are 0.11 and 0.32.

In fig. 5.11 the polarization orientation of the individual Fourier components illustrates the general behavior in region II in more detail. The left column displays near-field and far-field for the same mode already shown in figures 5.9(c) and 5.10(c). For the images shown in the right column the current was increased so that the secondary mode is excited. Arrows are added to the dominant Fourier components to show the averaged polarization orientation. The area of averaging is indicated by the circles, the averaging was weighted with the intensity and a threshold of 60% of the maximum intensity inside a circle was used to eliminate the spontaneous emission and noise.

The arrows in the figure illustrate the deviations from the “90°-rule” stated above. Both

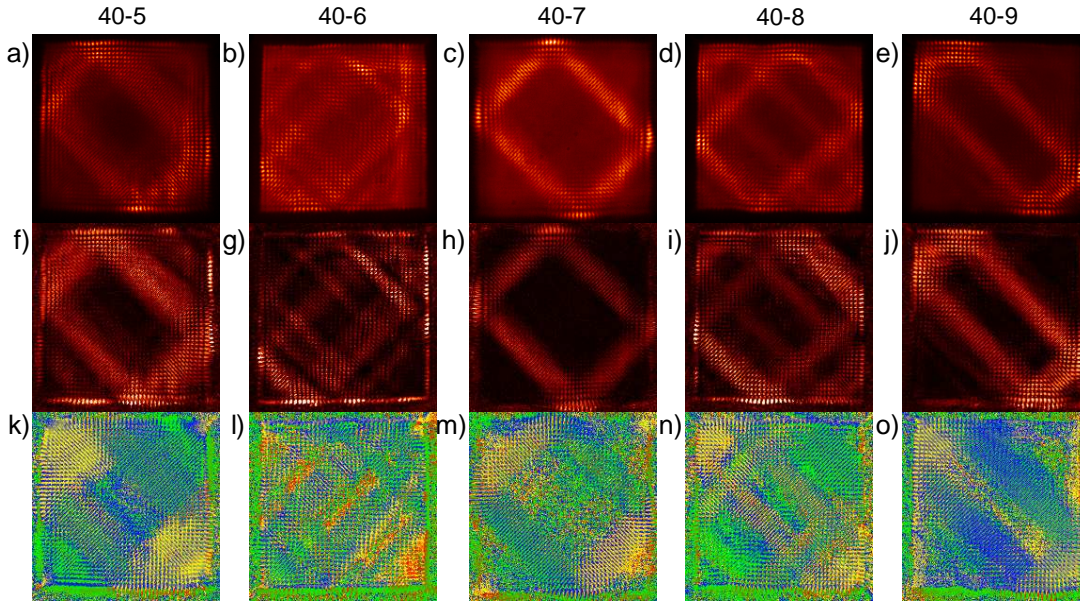


Figure 5.12: Near-field emission of various lasers just above threshold for lowest temperatures (region III). (a-e) S_0 , (f-j) FP, (k-o) polarization angle. Parameters: $T = -35^\circ\text{C}$. 40-5: $I = 22\text{ mA}$, $p = 0.11$. 40-6: $I = 24\text{ mA}$, $p = 0.10$. 40-7: $I = 21.5\text{ mA}$, $p = 0.11$. 40-8: $I = 24.5\text{ mA}$, $p = 0.12$. 40-9: $I = 21.5\text{ mA}$, $p = 0.05$.

the polarization of the mode at threshold in (c) and of the secondary mode in (d) are approximately aligned with the vertical, respectively the horizontal boundary. Nonetheless a pronounced deviation from this rule is apparent. For most Fourier components an additional rotation of the polarization towards the direction parallel to the wave vector is observed. The explanation of this is given in section 5.3.5.

As mentioned in section 2.5 in [18, 92] the polarization of a pattern similar to those described in this section was stated to be oriented parallel to the stripes in the near-field images and orthogonal to the corresponding four wave vectors. At first glance this is also found here, but the details show considerably more complexity. Firstly, the polarization is oriented approximately parallel to the boundaries. The deviation from the statements of the articles increases when the angle between the wave vectors of two adjacent Fourier components increases. Secondly, as shown above, there are also pronounced deviations from the alignment with the boundaries. As seen from the example in fig. 5.11(d) the polarization deviates in most cases strongly from the orientation orthogonal to the wave vectors.

5.2.5 Diamond-shaped patterns

For temperatures below -20°C the Fourier components of the far-field emission shift toward the diagonal. This was discussed and explained in section 4.3.2. While the origin of the pattern shape was clarified, the polarization of the billiard modes is a different matter. Since not all lasers emit pure billiard patterns, even at the minimum temperature of -35°C , the selection of devices in the following is different than in the previous two

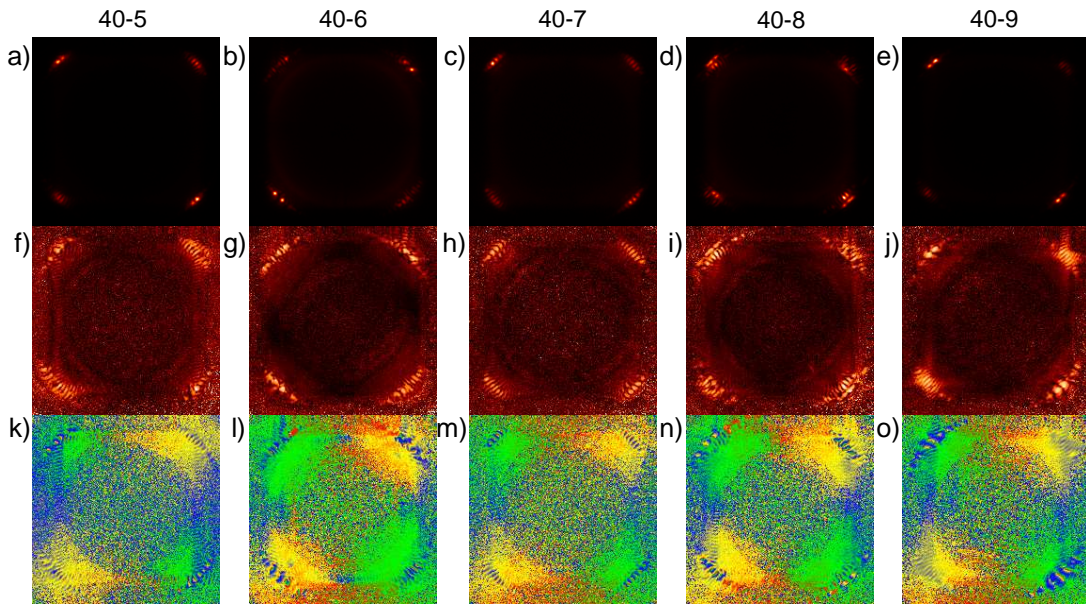


Figure 5.13: Far-field emission of various lasers just above threshold for lowest temperatures (region III). (a-e) S_0 , (f-j) FP, (k-o) polarization angle. Parameters: see fig. 5.12.

sections.

In figures 5.12 and 5.13 the emission at threshold for $T = -35^\circ\text{C}$ of several lasers is shown. The figures use the same layout as before. The first apparent feature in the near-field images is a very fine modulation of the polarization distribution. It seems that at least in some cases the near-field emission has two dominant polarization directions: one in the part of the pattern that is parallel to the diagonal direction from top left to bottom right, the other in the orthogonally oriented part. A good example of this is found in fig. 5.12(k) where dominantly yellow parts for one orientation and dominantly green-blue parts for the other are evident.

The far-field images show the typical four groups of Fourier components at the diagonals, each with a characteristic substructure. The polarization distribution is dominated by blue areas in the upper left and lower right peaks and yellow areas in the upper right and lower left peaks. The details differ between the lasers. Nonetheless in every image a substructure of the polarization distribution inside the groups of Fourier components is evident. Note that the dominantly green background in the upper left and lower right corners and the dominantly yellow background in the other two corners is due to a weakly polarized ASE. This will be described in detail in section 5.2.7.

To investigate the substructure in more detail in figures 5.14 and 5.15 a magnification of the Fourier components of the diamond-shaped patterns is shown. In both cases, (a) shows the upper left, (b) the upper right component, the black lines are contour plots of S_0 at 20, 40, and 60% of the maximum intensity.

In the first figure the left Fourier component is dominated by horizontal polarization (blue), the right one by $+45^\circ$ polarization (yellow). In the second figure the dominant directions are -45° (green) and $+45^\circ$. However it is apparent in both cases that this description is not sufficient. In the following only the area inside the contour plots is con-

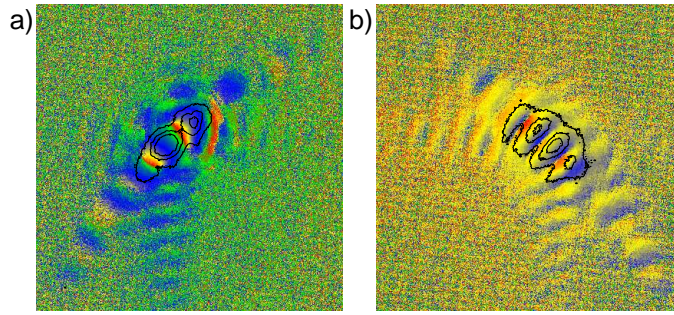


Figure 5.14: 3.9-times magnification of two Fourier components of the far-field emission of laser 40–5 with $I = 22$ mA and $T = -36$ °C. (a) Upper left Fourier component, (b) upper right component. The black lines are contour plots of S_0 (20, 40, and 60% of local maximum).

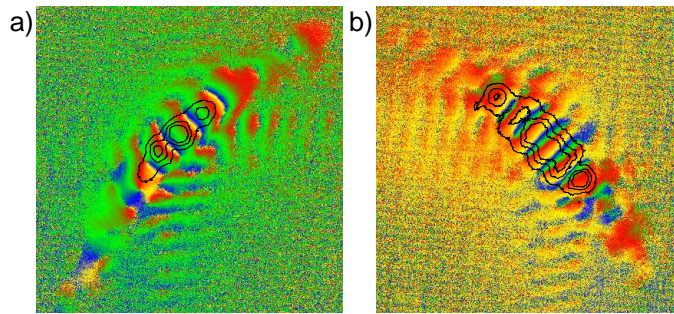


Figure 5.15: 3.9-times magnification of two Fourier components of the far-field emission of laser 40–7 with $I = 22$ mA and $T = -33$ °C. (a) Upper left Fourier component, (b) upper right component. The black lines are contour plots of S_0 (20, 40, and 60% of local maximum).

sidered. Along this area the polarization distribution is periodically changing, while the polarization orientation is equal for each intensity maximum. For example in fig. 5.14(a) starting at the bottom right and following the diagonal orientation of the contour plot the color changes from blue over green, red, and yellow to blue again, which is followed by another similar period. This constitutes two rotations of the polarization by 180° . Such a rotation of the direction of polarization is apparent in all the Fourier components, though sometimes it is less pronounced like in fig. 5.14(b). Note that a rotation by 180° corresponds to a full circle regarding polarization. In fact, the polarization rotates by a different number of full circles in each figure, two in fig. 5.14(a), four in 5.14(b), three in 5.15(a), and five in 5.15(b). This corresponds to the number of intense spots within the respective Fourier component (cf. fig. 4.14 and 4.16). In other words, for each intense peak within a Fourier component the polarization rotates by one full circle.

It was checked with some effort that the involved polarization distribution does not arise due to measurement errors (e.g. beam displacement as discussed in section 5.2.2 regarding the circular amount of polarization). For example, a modified setup with a much shorter far-field beam path was used to take similar images of the Fourier components of the billiards. The result was the exact same polarization distribution.

Figure 5.16 shows another way to illustrate the polarization distribution of the Fourier components. The four images show the intensity distribution of the upper left component

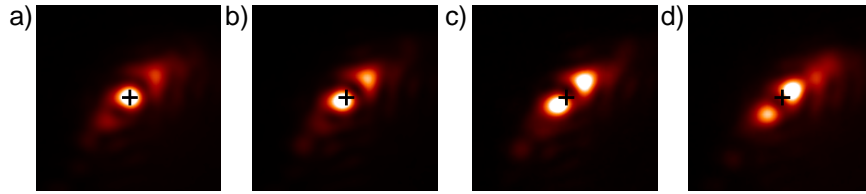


Figure 5.16: Magnification of the upper left Fourier component of the emission of laser 40–5 at $T = -35^\circ\text{C}$ and $I = 22\text{ mA}$. The four subfigures represent different orientations of the half-wave plate: (a) -45° , (b) 0° , (c) $+45^\circ$, (d) 90° . The cross in all images indicates the position of maximum intensity in subfigure (a). The images are slightly overexposed to enhance the contrast.

of the far-field emission of laser 40–5 at four different orientations of the half-wave plate. This is equivalent to turning the linear polarizer. Hence the images show the part of the light polarized at -45° (a), 0° (b), $+45^\circ$ (c), and 90° (d). In (a) the brightest peak is marked by a black cross. It is clearly visible that the intense spots that make up the Fourier component, change position when the detected polarization direction is changed. The behavior is cyclic: in (b) the marked spot shifts a bit to the left and down. In (c) it shifts further while another peak coming from the upper right gets brighter. Finally in (d) the first peak nearly disappears and the second peak moves toward the center. Then the procedure starts from the beginning. This is another evidence for the rotation of the polarization that was mentioned above.

The reason for this complex polarization scenario will be discussed in section 5.3.5.

5.2.6 Circular VCSELs

In the last chapter the emission of the circular VCSELs was described as being considerably less complex than that of the square lasers. The near-field images in general show an azimuthally modulated ring-shaped emission along the boundary. The far-field images correspondingly also feature rings with different radii according to the detuning between longitudinal resonance and gain peak frequency.

The polarization distribution is in some aspects very similar to the one found in the square devices. Fig. 5.17 shows the emission of laser 80–1 for two temperatures. The upper row again consists of intensity images, the lower one shows the polarization distribution. For each temperature the left column represents the near-field, the right one the far-field images.

The left case with $T = 20^\circ\text{C}$ shows the same characteristics as the emission of the square lasers in region I. The polarization is rather homogenous in near-field and far-field images, in this case vertical (red). The blue ring in the far-field emission corresponds to a higher order mode that is very weak in intensity. As for the square lasers, this case is encountered for rather high temperatures and corresponding low wave numbers.

In the other figure where $T = -20^\circ\text{C}$ the pattern in the near-field image is much finer corresponding to a higher wave number in the far-field image. The polarization distribution is drastically different, compared to the high temperature case. In both near-field and far-field images the polarization turns by 360° when tracing a full circle

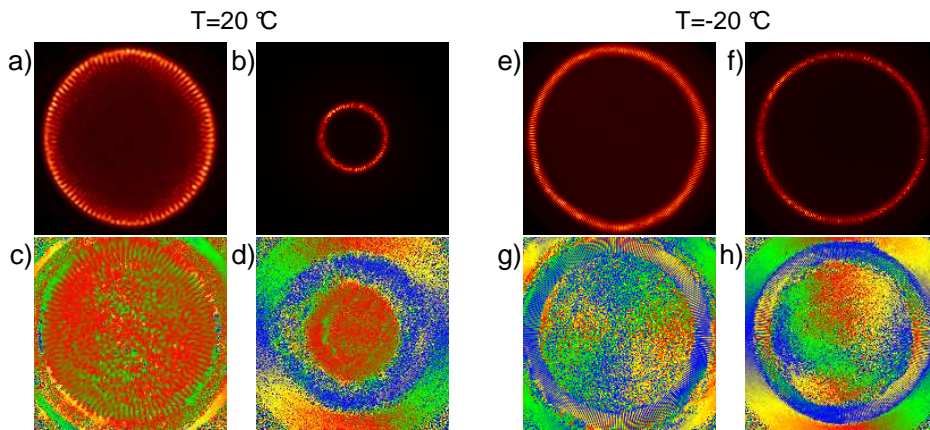


Figure 5.17: Intensity and polarization distribution images of laser 80–1 at two temperatures. Upper row: (a) near-field emission at 20°C, (b) corresponding far-field emission. (c) near-field emission at –20°C, (d) corresponding far-field emission. Lower row: same layout for the polarization distribution.

along the ring-shaped emission. However, the orientation is different: in the near-field image horizontal polarization (blue) is apparent on the left and the right side. The vertical portion is less prominent but still visible at the top and the bottom of the ring. Accordingly $\pm 45^\circ$ polarization can be found at the diagonal directions. In the far-field image this scenario is turned by 90° , otherwise it is equivalent: blue is found at the top and the bottom, red at the left and the right side.

This behavior corresponds to region II in the square lasers, but here the “ 90° -rule” is found to be nearly ideally realized: the polarization is always orthogonal to the wave vector. This also shows that in the near-field emission the polarization is parallel to the stripes along the ring (which is not really visible in the figure due to the limited resolution and the small spatial wavelength).

If the temperature is reduced farther the pattern length scale changes accordingly but the polarization distribution stays the same. That means that in the circular lasers a region III is not observed in the accessible temperature range.

5.2.7 Characteristics of the spontaneous emission

Not only the emission above threshold shows interesting polarization features, but also the (amplified) spontaneous emission below threshold and the transition through the threshold yield interesting insights into the mechanisms involved in the polarization selection. It is illustrated in the following that also the spontaneous emission below threshold is polarized, at least to some degree. This is followed by an investigation of the change of the polarization state at the transition to lasing emission.

Figures 5.18 and 5.19 show the color-coded polarization angle of the far-field emission of two lasers operating below threshold: the first figure for device 40–5 at constant current and varying temperature, the second for device 40–9 at constant temperature and varying current. One feature is evident in all images: the spatial distribution of the polarization angle shows a radial symmetry. To be more precise, the polarization is parallel to the

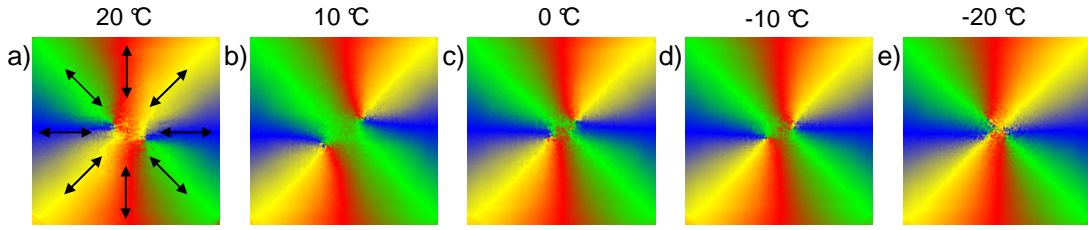


Figure 5.18: Spatially resolved polarization angle of the far-field emission of laser 40–5 below threshold ($I = 10$ mA) at various heat sink temperatures. The respective pump rates are -0.17 , -0.22 , -0.26 , -0.33 , and -0.41 . The arrows in (a) illustrate the polarization distribution.

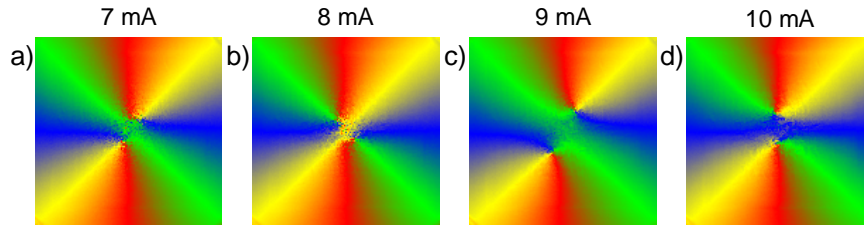


Figure 5.19: Spatially resolved polarization angle of the far-field emission of laser 40–9 for various currents below threshold ($T = 0$ °C). The respective pump rates are -0.48 , -0.40 , -0.33 , and -0.25 .

wave vector. For clarity this is indicated in fig. 5.18(a) by the black arrows. This feature is named “0°-rule” in the following, as opposed to the “90°-rule” introduced in conjunction with emission in region II above threshold.

The only exception from this rule in the presented figures is the center of the far-field images. Of course directly at the optical axis the wave number is zero and the polarization can not be parallel to the wave vector. This uncertainty of the polarization at the center is e.g. visible in fig. 5.18(e). In other images, e.g. (b) or fig. 5.19(c) the central area extends as far as a wave number of $0.9 \mu\text{m}^{-1}$. In such a case the simple “0°-rule” is somewhat modified for small wave numbers (visible e.g. in the “bending” of the red and blue areas in fig. 5.19(c)).

Fig. 5.20(a) shows the FP for the far-field image in fig. 5.19(d). The five differently colored curves correspond to radial cuts at different angles, the details are given in the caption. The curves are all equal with some minor deviations. They start at zero for low wave numbers (which is expected for unpolarized spontaneous emission), but increase to above 0.4 for high wave numbers. That shows that the effect that results in a polarized ASE is wave number dependent. The uncertainty of the polarization for $k_{\perp} = 0$ mentioned above is mirrored in the low FP around that point.

The “0°-rule” and the uncertainty near the optical axis are illustrated again in fig. 5.20(b). The figure also shows five radial plots at different angles. It is evident that the polarization is indeed parallel to the wave vector for $k_{\perp} > 2 \mu\text{m}^{-1}$ (i.e. for an FP above 0.05), with only small deviations. The orientation of the wave vector (i.e. the angle of the radial plot) is indicated by the dashed lines in corresponding colors. For lower wave numbers the polarization changes to around 0° , which fits well to the blue center of the corresponding far-field image (cf. fig. 5.19(d)).

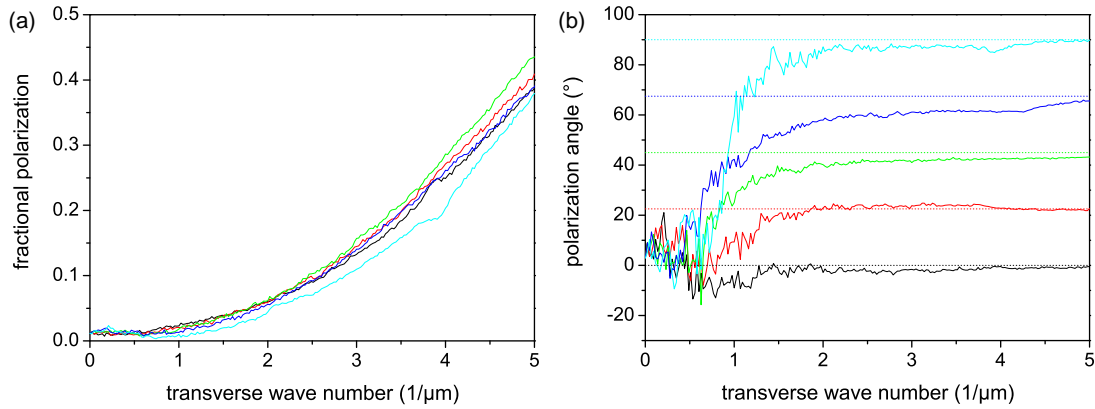


Figure 5.20: Radial plots of the FP (a) and the polarization angle (b) for the far-field image in fig. 5.19(d). The plots start at the optical axis ($k_\perp = 0$) going to higher wave numbers along cuts each with a different angle to the horizontal axis: 0° (black curve), 22.5° (red), 45° (green), 67.5° (blue), and 90° (cyan). (a) FP. (b) Polarization angle. The dashed lines correspond to a polarization parallel to the wave vector (i.e. following the “0°-rule”).

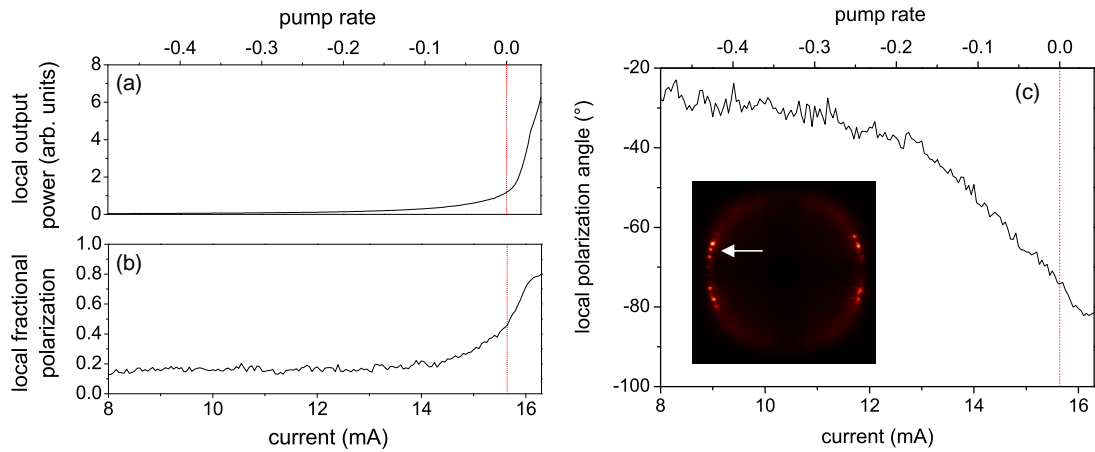


Figure 5.21: Illustration of the transition from below to above laser threshold for laser 40–5 at $T = 0^\circ\text{C}$. The studied Fourier component is indicated by the arrow in the far-field image on the right. The plots show the current dependence of (a) the local output power, (b) the local FP, and (c) the polarization angle. The (local) threshold is indicated by the dotted red line ($I_{th} = 15.6$ mA).

The interpretation of these experimental findings are given in section 5.3.1.

Obviously there has to be some transition from the “0°-rule” below threshold and the locking to the boundaries observed above threshold: at some point at or below laser threshold the polarization direction has to change. This transition is illustrated for two lasers in figures 5.21 and 5.22. For both figures one dominant Fourier component was selected from a far-field image (see captions for parameters) and the averaged Stokes parameters were calculated for it. The corresponding far-field images are shown in the respective insets in subfigure (c), the selected Fourier components are indicated by arrows. In each figure the current dependence of the local total intensity is plotted in (a), the FP in (b), and the (averaged) polarization direction in (c). The (local) laser threshold is

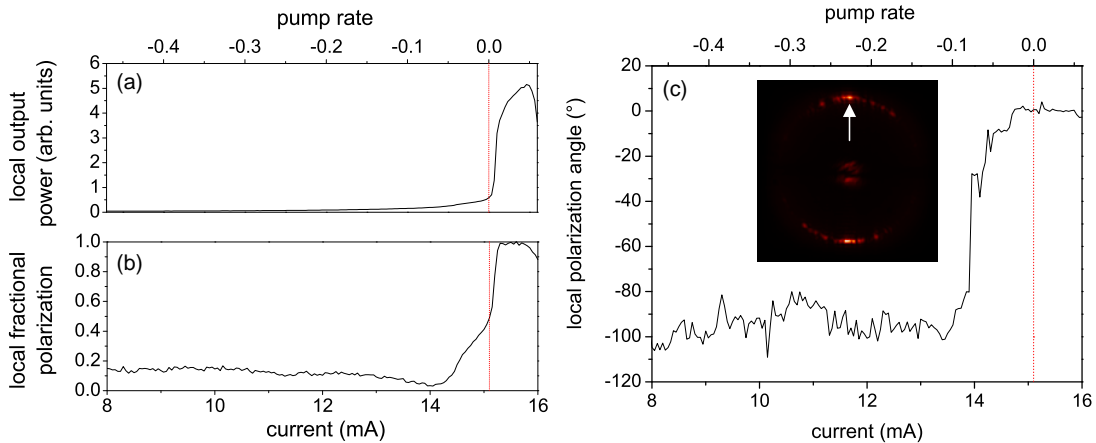


Figure 5.22: Illustration of the transition from below to above laser threshold for laser 40–9 at $T = 0^\circ\text{C}$. The studied Fourier component is indicated by the arrow in the far-field image on the right. The plots show the current dependence of (a) the local output power, (b) the local FP, and (c) the polarization angle. The (local) threshold is indicated by the dotted red line ($I_{th} = 15.1\text{ mA}$).

indicated in each subfigure by the dotted red line.

Both transitions show similar characteristics. The local output power shows a strong increase at threshold, typical for L–I curves of a lasers. Slightly below threshold in both cases the FP starts to increase. It reaches values close to one above threshold. The polarization follows the “0°-rule” for low currents but changes as the current nears the threshold. Above threshold the polarization orientation follows the characteristics of region II emission as expected from the polarization distributions shown in section 5.2.4.

The details show some differences between the two transitions. All curves are rather smooth for lasers 40–5 (fig. 5.21). The change of the polarization orientation starts well below threshold, covering a range of about 2 mA in which the polarization angle changes by 50° . Also at and slightly above threshold the polarization has not reached the final state. The FP also starts to increase below threshold, but much later than the polarization change. The maximal value of 0.8 is reached well above threshold.

For laser 40–9 the rise of (local) output power is steeper and the polarization change is rather abrupt. In a range of 1 mA the polarization angle shifts from around -100° to 0° . The fastest change is 50° in one current step of 0.02 mA. The final state of 0° is reached slightly below threshold. Another difference is the behavior of the FP. Instead of gradually increasing it decreases at first to just above zero. Then, about 1 mA below threshold, the FP increases at a faster rate than in the previous case, reaching the maximal value of 1 only slightly above threshold.

The differences in the transitions arise from the pattern shapes emitted above threshold. While the transverse mode in laser 40–5 has the typical four-fold symmetry and the polarization above threshold is not orthogonal to the wave vector, laser 40–9 shows a two-fold symmetry and the polarization is approximately orthogonal to the wave vector. That this is enough to explain the general characteristics of the two transitions is explained in more detail in section 5.3.1.

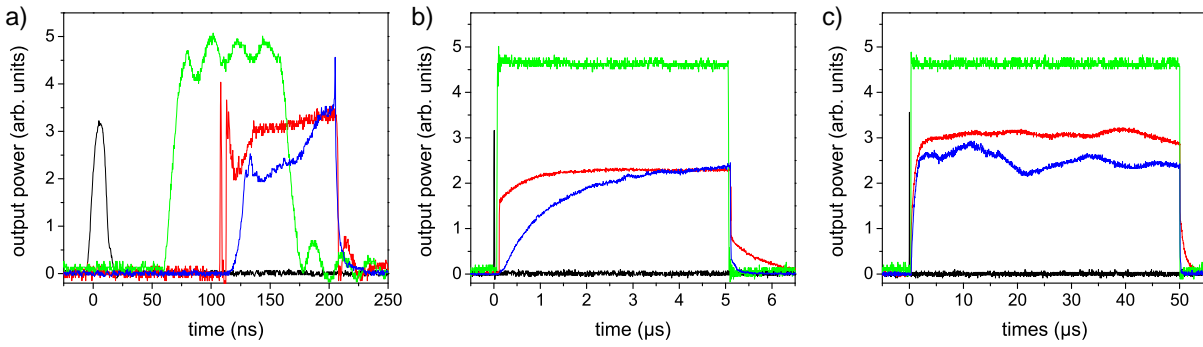


Figure 5.23: Scope traces of the relevant signals occurring in the experiments on pulsed excitation. Black: global trigger, green: TTL source signal, red: current pulse, blue: APD output. $I = 30.4 \text{ mA}$, $T = 42^\circ \text{C}$. (a) 100 ns pulse, 10 kHz repetition rate. (b) 5 μs pulse, 1 kHz. (c) 50 μs , 1 kHz. To increase the readability of the plots the individual plots were magnified appropriately.

5.2.8 Pulsed excitation

It was discussed in much detail already that the emission of the VCSELs is governed by the temperature inside the cavity. The laser temperature in turn is dependent on the heat sink temperature and the injection current (via Joule heating). While the heat sink can be considered constant, because all measurements are carried out after the temperature controller has reached the set-point, the action of the current is time-dependent, i.e. the Joule heating effect takes some time to heat up the device. The time evolution is analyzed here with a resolution of tens of nanoseconds. This enables the study of the turn-on behavior of the laser and the influence of thermal effects.

Fig. 5.23 shows the signals involved in the creation of a current pulse and the reaction of the laser to this pulse. The black curve represents the global trigger that defines the time $t = 0$. With an arbitrary delay it triggers the TTL pulse (green curves in the figure). The TTL pulse passes the conversion circuit and reaches the current pulse generator as an ECL pulse. Then it is converted to a current pulse (red curves). The current pulse is fed to the VCSEL and the light is detected by the APD (blue curves).

The different delays between the pulses originate from the electric propagation through cables and circuits. Their values are

- Trigger to TTL: adjustable at the pulse generator, minimum 66 ns,
- TTL to current pulse: 41 ns,
- current pulse to APD: 18 ns.

In each case also the delay from the device to the oscilloscope is included. For these paths BNC cables of equal length were used, so that this relative delay is equal for each signal and can thus be neglected. The only delay of interest, the one between the start of the current pulse and the laser turn-on (start of APD signal), is rather small. Since the time resolution is reduced by the jitter of the synchronization signal to around 75 ns (cf. section 5.1.2) this delay can also be neglected in the calculation of the overall delay.

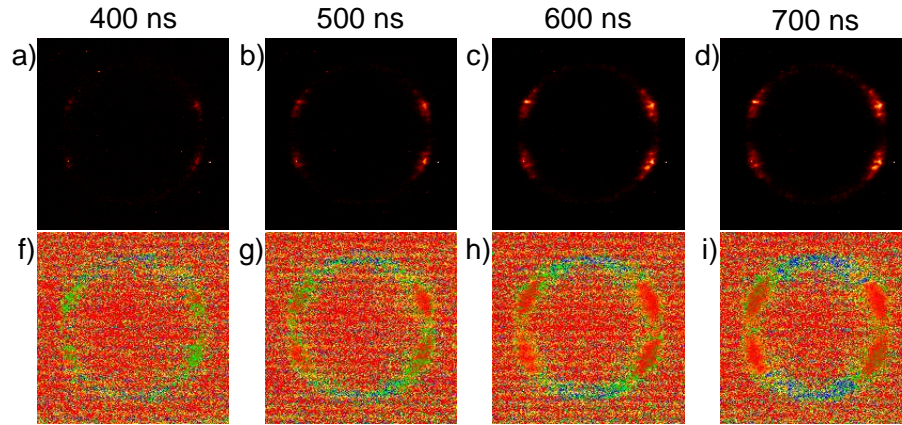


Figure 5.24: Time-resolved snap shots of the far-field emission of device 40–5 with a time step of 100 ns. (a)-(d) intensity, (e)-(i) polarization angle. Exposure time 35 ns, current 30.4 mA, heat sink temperature 10 °C. The delay times above the images are given with respect to the global trigger.

That means that the overall delay between the activation of the laser and the detection with the CCD camera is only dependent on the delay setting at the HP pulse generator and the camera control unit.

Fig. 5.23(a), (b), and (c) show the described signals for pulse lengths of 100 ns, 5 μ s, and 50 μ s, respectively. The shape of the source TTL signal is supposed to be a rectangle. This is indeed the case for the long pulses, but for the 100 ns pulse it is quite fluctuating. The resulting current pulse is even more irregular. The shape of the APD output is similar to that of the current pulse. Note that the repetition rate also influences the quality of the current pulse. For rates lower than 10 kHz the current pulses become even more irregular. It shows that for short pulse lengths the available pulse generators do not provide proper rectangular signals.

Note that there is a slowly decaying tail following the current pulse, which is most apparent in subfigure (b). This does not affect the measurements described below, since the exposure time of the CCD camera is always selected to be well within the current pulse.

5.2.8.1 Transient behavior of the transverse patterns

Various scans of the delay time are discussed in the following illustrating the temporal evolution of the patterns. Figures 5.24 and 5.25 show a scan for device 40–5 at a high current of 30.4 mA (pump rate approximately 1.4) and a heat sink temperature of 10 °C. The time steps are 100 ns and 2 μ s, respectively. In all images the exposure time is about 40 ns and for each measurement five images were taken successively and averaged afterwards (to reduce the effect of the temporal jitter in the camera trigger). Due to the temporal jitter and the averaging the temporal resolution is never greater than 75 ns.

For short time delays the turn-on is very similar to the time-averaged measurement at $T = 0$ °C (cf. fig. 5.10(d)), for the intensity as well as the polarization distribution. After about 2 μ s the current pulse reaches its maximum and the injection current is

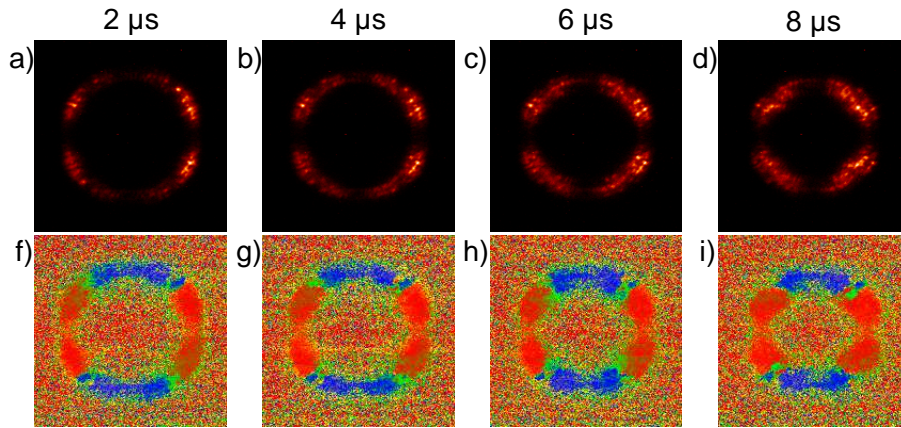


Figure 5.25: Time-resolved snapshots of the far-field emission of device 40–5 with a time step of $2 \mu\text{s}$. (a)-(d) intensity, (e)-(i) polarization angle. Exposure time 40 ns , current 30.4 mA , heat sink temperature 10°C . The delay times above the images are given with respect to the global trigger.

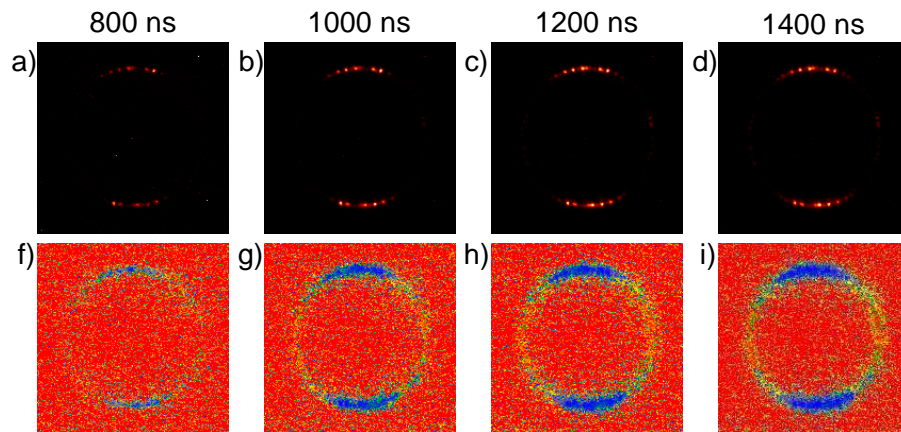


Figure 5.26: Time-resolved snapshots of the far-field emission of device 40–7 with a time step of 200 ns . (a)-(d) intensity, (e)-(i) polarization angle. Exposure time 80 ns , current 17.4 mA , heat sink temperature 20°C . The delay times above the images are given with respect to the global trigger.

constant for longer times (cf. fig. 5.23(b)). In fig. 5.25 images with a delay of 2 to $8 \mu\text{s}$ are shown. Though the injection current is supposed to be constant at this point the scenario is similar to the averaged case when the current is increased: a secondary mode with orthogonal polarization is excited. The transverse wave number shrinks. The polarization distribution is equivalent to the one described in section 5.2.4. After about $20 \mu\text{s}$ (not shown in the figures) the final state is reached and the pattern does not change any more.

Another scan is shown in figures 5.26 and 5.27 for laser 40–7 at a low current of 17.4 mA . The heat sink temperature is 20°C . The layout is the same as before but the time steps are different. Also here with 80 ns the exposure time is longer, because the current (and thus the intensity of the emission) is much lower than before. The observed patterns are

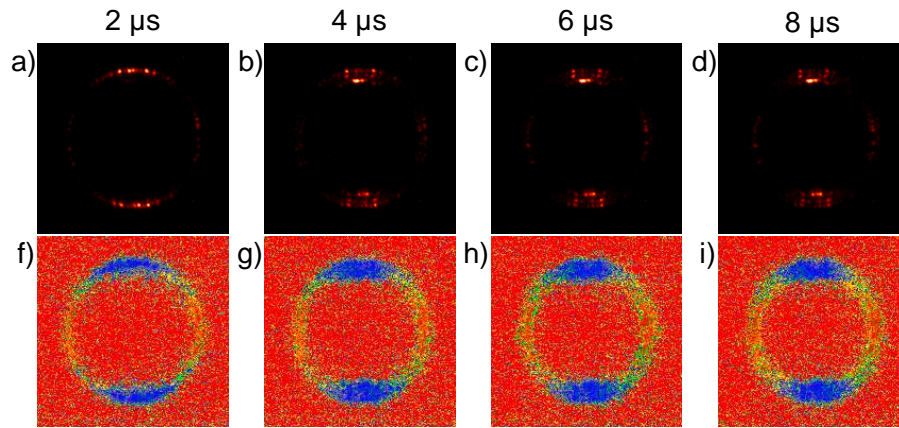


Figure 5.27: Time-resolved snap shots of the far-field emission of device 40–7 with a time step of $2 \mu\text{s}$. (a)-(d) intensity, (e)-(i) polarization angle. Exposure time 70 ns, current 17.4 mA, heat sink temperature 20°C . The delay times above the images are given with respect to the global trigger.

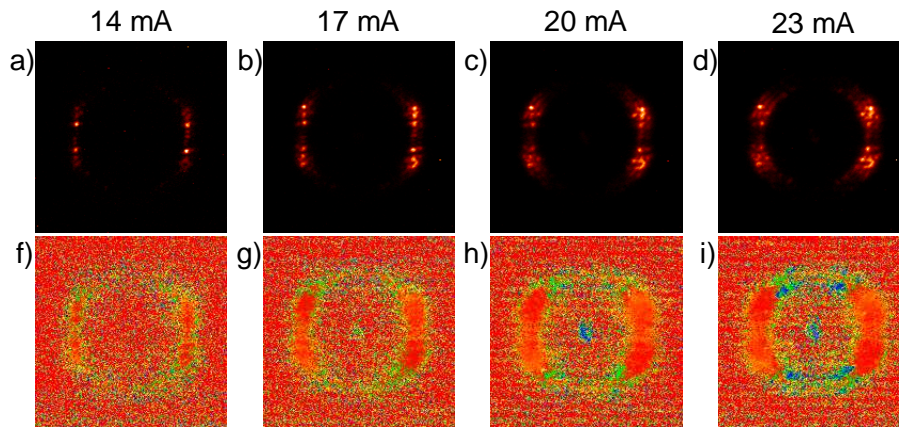


Figure 5.28: Time-resolved snap shots of the far-field emission of device 30–3 for different currents. (a)-(d) intensity, (e)-(i) polarization angle. Exposure time 35 ns, delay time $2 \mu\text{s}$, heat sink temperature 10°C . Pump rates 0.27, 0.54, 0.81, 1.08.

again very similar to the averaged case. With increasing time the transverse wave number shrinks. The pattern consisting of two Fourier modes, visible in the intensity images at 4, 6, and $8 \mu\text{s}$, is comparable to the typical far-field emission of laser 40–9, which is not observed in time-averaged images of laser 40–7.

5.2.8.2 Influence of the current on the transient behavior

A third set of figures shows snapshots of the emission of laser 30–3 for four different currents. The heat sink temperature is set to 10°C . In fig. 5.28 the delay time is set to $2 \mu\text{s}$. Again the behavior is very similar to the averaged measurements. With increasing current more transverse modes are excited and simultaneously the dominant wave number decreases.

After about $25 \mu\text{s}$ the change of the emission with time slows and reaches a more or

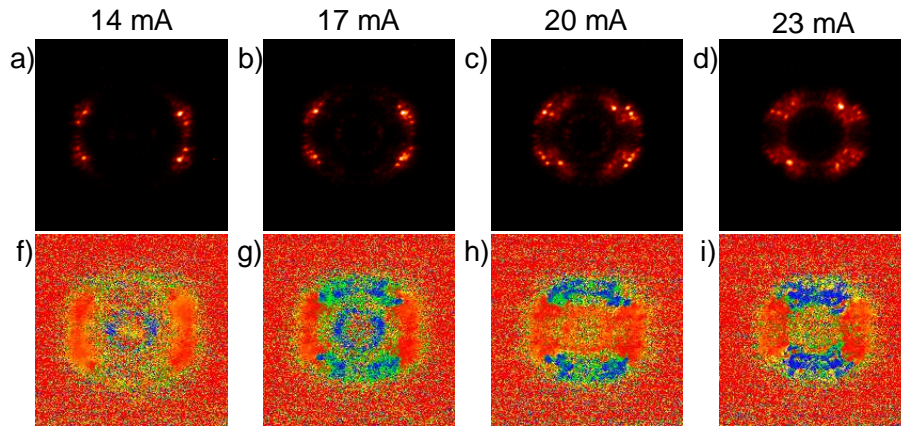


Figure 5.29: Time-resolved snap shots of the far-field emission of device 30-3 for different currents. (a)-(d) intensity, (e)-(i) polarization angle. Delay time $25 \mu\text{s}$, other parameters same as in fig. 5.28.

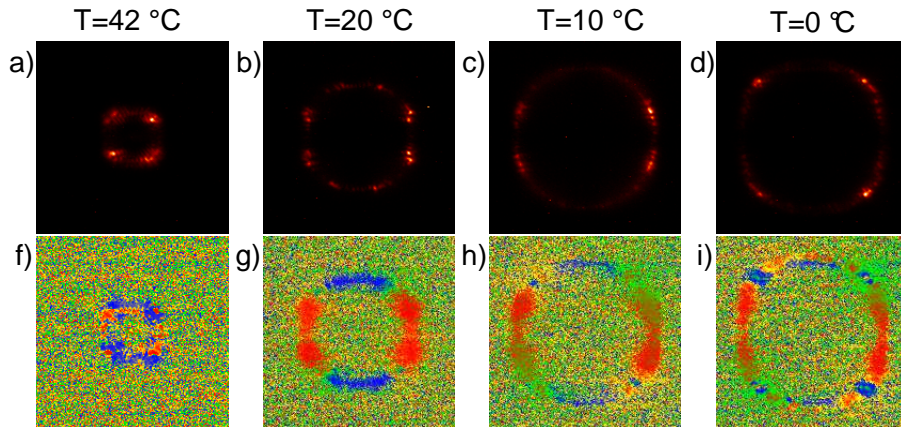


Figure 5.30: Snap-shots of a 100 ns pulse showing the far-field emission of device 40-5 at different heat sink temperatures. (a)-(d) intensity, (e)-(i) polarization angle. Exposure time 100 ns, no delay, current 30.4 mA, temperature 10°C .

less steady state. Fig. 5.29 shows images of this state. The far-field images look very similar to those shown in fig. 4.6 for the averaged case. Also the polarization distribution follows the characteristics of the time-averaged measurements very well. In addition, in fig. 5.29(g) a ring with constant polarization is visible for low wave numbers, as expected for region I emission.

5.2.8.3 Snapshots for zero time delay

To observe the laser emission as close to the onset of the current pulse as possible the camera delay is set to zero. Such snapshots of the emission at turn-on are shown in fig. 5.30 for laser 40-5. At the HP pulse generator the delay between trigger and TTL pulse is selected so that the start of the current pulse and the start of the exposure time are equal. Thus the lasing emission is detected from the very beginning of the turn-on. The measurement is repeated 21 times so that the obtained images can later be averaged.

In this way the influence of the temporal jitter of the camera trigger can be removed. The images were taken with an exposure time of 100 ns, but it was checked that with exposures of down to 25 ns no significant change in the characteristics of the transverse modes was found.

The resulting far-field images are practically identical to those shown in fig. 4.3(g), (h), and (i). Only the second image, where the temperature is set to 20 °C, is not found in fig. 4.3. Most notable is the fact that emission on the diagonal is already observed for 0 °C. Obviously on this time scales the Joule heating has not yet set in and the device temperature is about equal to the heat sink temperature.

5.3 Analysis and interpretation

In this section the results of the experiments on the polarization distribution are analyzed and interpreted on the basis of the model described in section 4.3.6 and an improved model. At first, the characteristics of the emission below threshold and the transition through the threshold are considered. This is followed by an interpretation of the measurements with temporal resolution.

The material anisotropies, important parameters for the model calculations, are extracted from optical spectra in the next section. After this, the improved model is explained and the polarization selection mechanisms of the transverse modes are investigated on the basis of this model. Finally the extent of the three regions introduced in the last chapter is estimated.

The experiments show that the three regions, defined with respect to the shape of the patterns, can be analogously defined by way of the polarization characteristics. Thus in the following analysis the definition of the regions is often understood in terms of these different polarization characteristics.

5.3.1 Polarization state below threshold and transition through threshold

In this section the mechanisms leading to the polarization behavior below threshold, which was described in section 5.2.7, are explained with help of the theory described in the previous chapter, section 4.3.6. The transition to lasing emission is compared to numerical calculations.

The reflectivity of a layered Bragg mirror depends on the angle between the plane of incidence and the polarization, due to the polarization dependence of Fresnel reflection [171]. The highest reflectivity is found for s-waves, their polarization being orthogonal to the plane of incidence. A higher reflectivity means a better resonator and thus s-waves are expected to be favored in a VCSEL above threshold. It follows that the transmissivity must be higher for p-waves. This effect can be quite pronounced, as shown by the following example: if $r_s = 0.999$ and $r_p = 0.99$ (reflectivity for s-waves, respectively for p-waves) then the transmissions are $t_s = 0.001$ and $t_p = 0.01$ (ignoring losses inside the DBRs). Ergo the transmission of the p-wave is ten times higher than that of the s-wave. The polarization of a p-wave is parallel to the wave vector of the mode.

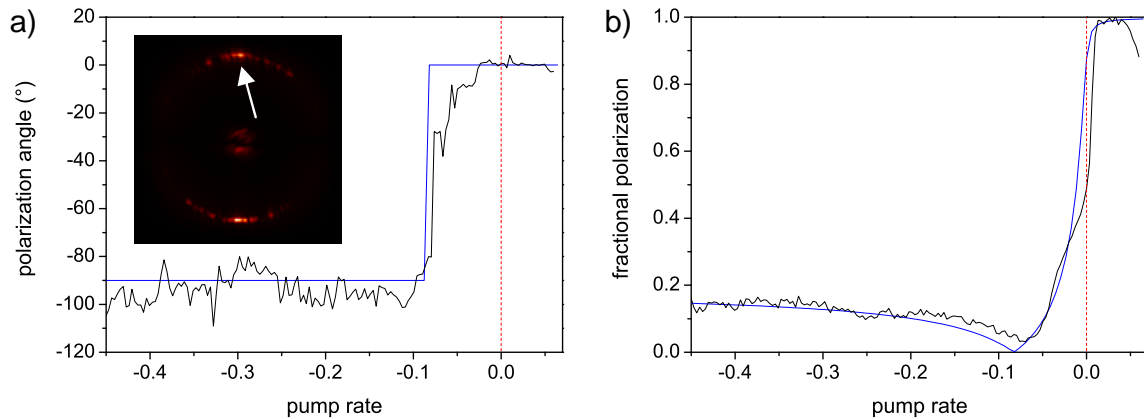


Figure 5.31: Illustration of the transition from below to above laser threshold for laser 40–9 at $T = 0^\circ\text{C}$. The plots show the experimental (black curves) and theoretical (blue) polarization angle (a) and FP (b). The local threshold ($I_{th} = 15.1\text{ mA}$) is indicated by the dotted red lines. The inset in (a) shows the corresponding far-field image. The Fourier peak taken for the plots is indicated by the arrow. The experimental data is equal to that in fig. 5.21.

The anisotropic reflection/transmission can explain the “ 0° -rule” observed for the polarization distribution of the spontaneous emission: as shown in [172] the extra-cavity light field is polarized when the intra-cavity losses are much higher than the outcoupling losses. In this case the light field inside the cavity is unpolarized, the higher transmission of p-waves results in a polarized light field outside the cavity, and the remaining polarization components not coupled out of the cavity are suppressed due to the intra-cavity losses. The result is the observed polarization distribution of the spontaneous emission.

In the following, the transition from spontaneous to lasing emission, which was illustrated in detail in section 5.2.7 for two VCSELs, is explained on the basis of the model briefly described in section 4.3.6 and published in [96, 98]. With help of numerical calculations the characteristic differences between the two transitions are analyzed and explained. A detailed description of the calculation is given in [172]. An infinite laser is sufficient for the modelling. A linear stability analysis yields the state of polarization below threshold and just at threshold. Since the model does not include carrier saturation the results above laser threshold are disregarded.

Figures 5.31 and 5.32 show the current dependence of the polarization angle and the FP for the transition from below to above laser threshold for lasers 40–9 and 40–5, respectively. The black curves correspond to the experimental data already presented in section 5.2.7. The blue curves represent the theoretical calculations.

The most significant difference between the two devices is found in the pattern formed above threshold. The far-field images of laser 40–9 show two pronounced Fourier components aligned with the vertical axis (cf. the inset in fig. 5.31(a), corresponding to stripes confined to one side of the aperture), while the pattern emitted by laser 40–5 represents the typical four-fold symmetry in the far-field images (cf. the inset in fig. 5.32(a), corresponding to vertical stripes with a small transverse wavelength modulated horizontally with a higher wavelength).

This shows that the transition in VCSEL 40–9 takes place between a state where the

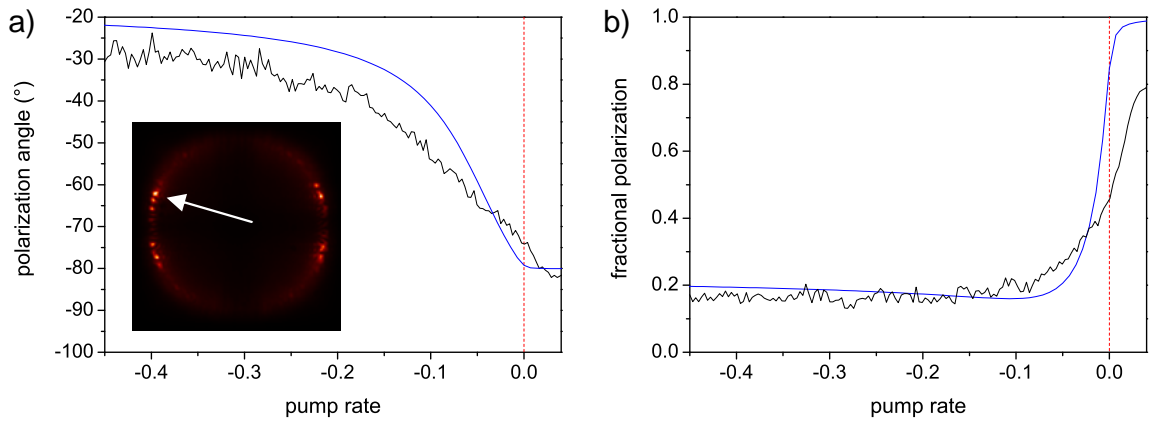


Figure 5.32: Illustration of the transition from below to above laser threshold for laser 40–5 at $T = 0^\circ\text{C}$. The plots show the experimental (black curves) and theoretical (blue) polarization angle (a) and FP (b). The local threshold ($I_{th} = 15.6\text{ mA}$) is indicated by the dotted red lines. The inset in (a) shows the corresponding far-field image. The Fourier peak taken for the plots is indicated by the arrow. The experimental data is equal to that in fig. 5.21.

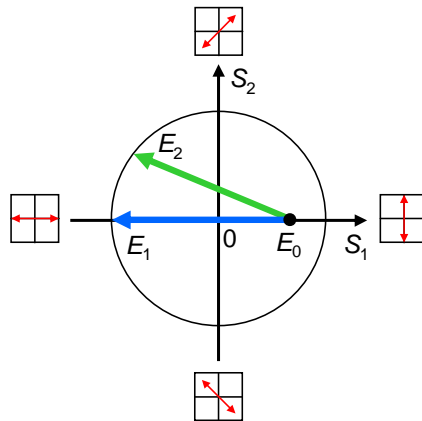


Figure 5.33: Different types of transition from below to above threshold on the plane spanned by S_1 and S_2 . The abrupt transition observed in laser 40–9 corresponds to the blue arrow, the gradual change in polarization observed for laser 40–5 corresponds to the green arrow. While the initial polarization state E_0 is the same in both cases, the states after the transition E_1 and E_2 are different. The red arrows in the boxes show the polarization state for different combinations of (S_1, S_2) . The large circle has a radius of 1 and corresponds to fully linearly polarized states.

polarization is parallel to the wave vector and a state where the polarization is orthogonal to the wave vector, i.e. in both cases the Stokes parameter S_2 is approximately zero. This is indicated in fig. 5.33 by the blue arrow between the initial state E_0 (corresponding to the polarization scenario below threshold) and the target state E_1 (corresponding to the polarization state above threshold). The abrupt polarization rotation takes place at $S_1 = 0$. In addition, the decrease of S_1 creates a drop of the FP close to the transition. At the point of the transition the FP is zero. The agreement between the experimental and theoretical curves shows that this scenario describes the reality quite well.

For laser 40–5 the transition scenario is illustrated by the green arrow in fig. 5.33. The

transition takes place between E_0 and the state E_2 , where both $S_1 \neq 0$ and $S_2 \neq 0$. It is apparent that the polarization has to change gradually between states E_0 and E_2 . Again the agreement between this scenario and the experimental observations is quite good. Nonetheless the experimentally obtained FP is considerably lower at threshold and the calculated polarization transition is somewhat faster. This can in part be explained when the state E_2 is not located on the ring with $S_1^2 + S_2^2 = 1$, but at some point inside this ring.

5.3.2 Pulsed excitation

Here the results of the pulsed excitation experiments are briefly discussed. Two effects have to be taken into account when studying the temporal evolution of the patterns emitted by the VCSELs: the turn-on behavior of the VCSEL (i.e. the time it takes for the VCSEL to start lasing after onset of the current injection) and the temperature increase due to Joule heating.

As shown in the oscilloscope traces in fig. 5.23(a) a rise of the output power is evident a few nanoseconds after the start of the current pulse. This delay is probably due to different cable lengths and the approximately two meters of optical beam path and it can be assumed that the maximum turn-on delay of the VCSEL is of the order of a few nanoseconds. However it takes up to $5 \mu\text{s}$ until the full output power is reached, as shown in fig. 5.23(b). If the amplitude of the current pulse is set high enough the initial output power of the VCSEL is enough to be detected by the CCD camera. This is evidenced by the measurements of the snapshots of 100 ns pulses shown in fig. 5.30.

It is shown in [173] that, though the increase of the temperature sets in immediately after the current is flowing through the VCSEL, it takes about $1 \mu\text{s}$ until a significant rise of the temperature is observed. As shown in [174] it may take several tenths of milliseconds until the final device temperature is reached. Thus the influence of the current on the device temperature and the emission characteristics is eliminated for time delays (between the start of the current pulse and the activation of the CCD camera) well below $1 \mu\text{s}$. In effect the effective laser temperature is then (approximately) equal to the heat sink temperature.

It can be summarized that the images of the 100 ns pulses shown in fig. 5.30 and also several other measurements presented in section 5.2.8 with time delays significantly smaller than $1 \mu\text{s}$ represent the state of the VCSEL without the influence of Joule heating. Since the observed patterns and polarization distributions do not differ from those observed in the time-averaged experiments, it can be concluded that the pattern and polarization selection mechanisms are equal with and without the influence of thermal effects.

The plots in figures 5.34 and 5.35 summarize the temporal evolution described in section 5.2.8 and the effect of the Joule heating on the characteristic length scales of the patterns. Here the time dependence of the dominant wave number is shown for laser 40–5 at different temperatures, respectively for laser 30–3 at different currents.

The first plot shows the effect of the warming up of the device due to Joule heating when starting at different wave numbers. The blue curve corresponds to emission in region I. Here the dominant wave number remains more or less constant. The other curves show a more or less pronounced decrease of the wave number over time. It shows that the higher

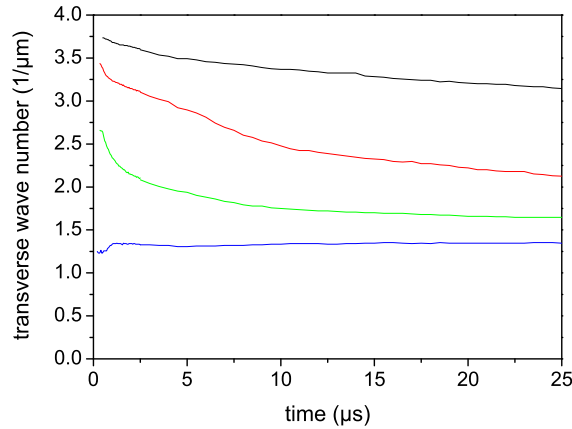


Figure 5.34: Length scale of the dominant transverse mode tracked over 25 μs for four temperatures. 0 $^{\circ}\text{C}$ (black curve), 10 $^{\circ}\text{C}$ (red), 20 $^{\circ}\text{C}$ (green), 42 $^{\circ}\text{C}$ (blue). 0.1-2.5 μs : 50ns delay steps, 2.5-25 μs : 500ns delay steps. Exposure 35 ns, current pulse amplitude 30.4 mA. Pump rates: 1.10, 1.16, 1.53, 1.72.

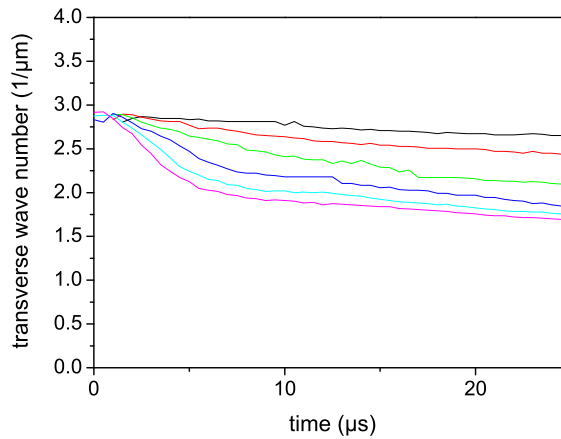


Figure 5.35: Length scale of the dominant transverse mode tracked over 25 μs for six current pulse amplitudes. 14.1 mA (black curve), 17.4 mA (red), 20.7 mA (green), 23.9 mA (blue), 27.2 mA (cyan), 30.5 mA (magenta). 500 ns delay steps, exposure 35 ns, temperature 10 $^{\circ}\text{C}$. Pump rates: 0.28, 0.58, 0.87, 1.16, 1.46, 1.76.

the wave number at the beginning of pulse the less it shrinks over time, i.e. the greatest change is visible in the green curve, the smallest in the black one. This is due to the different pump rates: for the green curve the pump rate is much higher ($p = 1.53$) than for the black curve ($p = 1.10$). The temperature rise due to Joule heating is proportional to the pump rate. Thus the device temperature increases further for higher pump rates. As was shown in the previous chapter a rising temperature leads to an increase of the dominant wave number. Also visible is the slowing down of the change in wave number with time. At $t = 25 \mu\text{s}$ the final state is reached in most cases.

In the second figure the starting condition is the same for each curve. Here the current is varied, but this does not change the dominant wave number at turn-on. With time the effect of the Joule heating sets in, shifting the wave number to lower values. This

is strongest for the highest current (magenta curve) and weakest for the lowest current (black curve).

In conclusion the characteristics of the emission observed with and without temporal resolution show only minor differences. The general structure of the patterns is equal for both types of experiments. In a few cases far-field patterns are observed in the transient images that are not found in time-averaged images of the same laser. A breakdown of the spatial coherence reported in [175] for a VCSEL driven by microsecond pulses was not observed in these experiments. The polarization distribution is in all cases equivalent and follows the same rules, namely the constant polarization along rings in region I and the locking to the boundaries for higher wave numbers in region II. The evolution of the dominant wave number with time and the comparison with the time scans shows a rather simple scenario: while the heat sink temperature defines the starting condition, i.e. the emission pattern before the Joule heating sets in, the pump rate governs the evolution with time. Especially how much the wave number decreases over time is determined by the pump rate. The main insight of these studies is that the Joule heating is very probably homogeneous over the whole laser aperture.

5.3.3 Material anisotropies

The plano-planar FPI is used to analyze certain optical spectra with a higher resolution. Most importantly the material anisotropies – birefringence and dichroism – can be obtained. These anisotropies are important parameters for the numerical model and provide some insight into the polarization selection in the VCSELs.

As was described in section 2.3 the anisotropies are induced by the electro-optic and the elasto-optic effect [2, 57, 58]. The electro-optic effect creates a small refractive index difference for waves with orthogonal polarization, which in turn results in slightly different resonance frequencies. The elasto-optic effect is induced by strain and stress that result from the fabrication process. This effect also results in a frequency splitting and can in addition lead to different gain for the orthogonal polarization components.

Since the gain is frequency-dependent, a frequency splitting between the orthogonally polarized modes results in a difference in gain. The losses can also be frequency-dependent. The resulting effective gain is anisotropic for the orthogonally polarized modes. This anisotropy is called dichroism.

Due to non-zero values of these two anisotropies the state of polarization at threshold is selected in favor of one of the fundamental polarization directions (which are in turn defined by the orientation of the anisotropies, see section 5.3.5). In this section it is considered how the anisotropies are obtained from spectral measurements and the values are compared to values found in the literature. The impact on the polarization selection scenario is discussed in section 5.3.5.

To make the calculation of the anisotropies possible the laser has to operate at parameters where both fundamental polarization directions are emitted in the same spatial mode. This is only the case for on-axis emission, and only in some lasers. Taking spectra from each polarization state the birefringence is obtained from the frequency distance between the horizontally polarized and the vertically polarized spectral lines. The dichroism is the difference in half-width of these peaks. Each anisotropy value is extracted from several

Table 5.1: Results of the experimental determination of the material anisotropies birefringence and dichroism for four VCSELs.

laser	FSR (GHz)	finesse	resolution (GHz)	birefringence (GHz)	dichroism (GHz)
30–4	100	40	2.5	19	0.3
40–1	66	110	0.6	10	≈ 0
40–5	50	100	0.5	3	≈ 0
40–7	150	40	3.75	4	≈ 0

measurements. The FSR and finesse of the FPI are given for each measurement individually since the FPI was often readjusted, especially when the VCSEL was changed. The resolution of the spectral measurement is obtained from the ratio of FSR and finesse.

Table 5.3.3 lists the values of birefringence and dichroism for four VCSELs. Values between 3 and 19 GHz are measured. Values given in [2] for $50 \times 50 \mu\text{m}^2$ VCSELs lie in the same range (5 to 20 GHz). In [169] birefringence values up to 22 GHz are reported. The author also describes that two measurements with the same laser on different mounts leads to drastically different birefringence values. This shows how sensitive the VCSELs react to stress and strain.

For values of the dichroism given as “ ≈ 0 ” different measurements yielded positive and negative numbers close to zero. The measurement for laser 30–4 was the only one that provided reproducible values for the dichroism. The positive value indicates that the width of the vertically polarized component is larger. Thus the gain for the horizontally polarized mode should be higher. The modes with small wave number in the emission of laser 30–4 are dominantly polarized horizontally, which agrees with the positive value of the dichroism. It can be summarized that the dichroism is very small, certainly smaller than 0.5 GHz. In [169] dichroism values for VCSELs between 0.1 GHz and 1.7 GHz are given, which shows that the values obtained here are realistic.

5.3.4 Description and discussion of the improved model

The experimental findings detailed in this chapter show that the model discussed in the last chapter is not sufficient to describe the polarization selection mechanisms. The polarization orientation reported in [96, 98] is parallel to the perfect stripes (i.e. orthogonal to the two wave vectors). Unfortunately, perfect stripes were never observed in the experiments reported in this work and in [18, 26, 92]. Rather the VCSELs emit modes consisting of four dominant Fourier components forming a rectangle in wave number space. Nonetheless, the authors of [18, 26] report a polarization orientation orthogonal to the four wave vectors. In the experimental section of this chapter it was shown in detail that this observation simplifies the real state considerably. In this section, the more complex polarization scenario is explained with help of numerical calculations.

In recent years I. V. Babushkin developed several simplifications to the initial model devoted to providing an analysis of the complex polarization behavior in the presence of lateral laser boundaries [99, 100, 166]. The finite size of the real VCSELs is included in form of a transverse waveguide with the amplitude [100] or the curvature of the field [166]

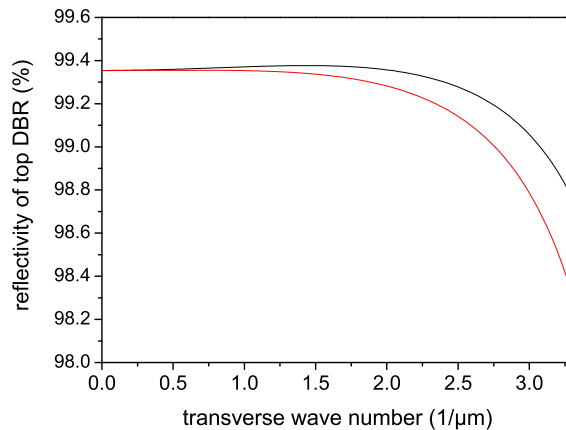


Figure 5.36: Reflectivity of the top DBR for s-waves (black curve) and p-waves (red curve) over the transverse wave number $k_{\perp} = (k_x, 0)$.

equal to zero at the boundary into the eigenvalue problem describing the growth rate (and thus the threshold) of the transverse modes. A perfect square boundary is sufficient to achieve a good agreement between numerical simulations and the experimental observations. The anisotropic reflection at the DBRs, included already in the earlier models [96, 98], adds a polarization anisotropy to the model.

It is important to state that one of the main results of the model is the pair of eigenvalues of a complex 2×2 matrix, that includes the effects like anisotropies, diffraction, gain, and losses and describes the polarization state of the light field. The two eigenvalues correspond to two polarization states at threshold. In numerical simulations the two solutions can be calculated for each point in the wave number space. One of those has a higher growth rate and is thus excited at threshold. The other has the orthogonal polarization and is disfavored at threshold. At the diagonal the growth rates are equal and the two solutions are degenerate.

When the laser boundaries are taken into account the matrix describing the polarization states has to be rewritten in terms of waveguide modes of the transverse cavity. These are two dimensional superpositions of sines and cosines, in the far-field represented by the four wave vectors (k_x, k_y) , $(k_x, -k_y)$, $(-k_x, k_y)$, and $(-k_x, -k_y)$. It is important to state that these eigenmodes of the waveguide are not eigenmodes of the reflection at the DBRs, since the incident waveguide mode can not represent a pure s- or p-wave simultaneously for all four wave vectors [166]. The result is that at reflection additional modes are created with the same wavelength as the original mode but with different wave vectors. Thus they experiences increased losses. These rescattered modes can be seen in the experiment as ripples connecting the four dominant Fourier components (cf. section 4.2.2). These modes imply that no single wave number solutions are possible, which serves as a justification of the phenomenological approach of a superposition of selected Fourier components used in [26, 27] to calculate the diamond-shaped billiard patterns.

To point out the effect of the anisotropic reflection at the DBRs on the polarization selection the reflectivity for s- and p-waves is calculated using [176] and the device parameters of the top DBR of the square lasers given in appendix B. The result is plotted in fig. 5.36 for an ideal DBR without internal losses. The absolute values of the reflec-

tivities are not equal to those of the VCSEL structure. The transverse wave number is $k_{\perp} = (k_x, 0)$, i.e. a line along the horizontal axis is selected. That means that the vertical polarization corresponds to the s-wave.

The difference in reflectivities is visible, but not very large. The effect can nonetheless be quite pronounced considering that a light wave experiences around 220 reflections at the DBRs during its lifetime (cf. appendix C). Note that at first the higher reflectivity increases slightly with the wave number. This rise may lead to slightly lower thresholds for small non-zero wave numbers. For $k_{\perp} > 2 \mu\text{m}^{-1}$ both reflectivities drop quickly. This indicates higher losses for larger wave numbers.

The orientation of the amplitude anisotropy can be misaligned with respect to the boundaries. Commonly the material anisotropy is oriented along the crystal axes of the semiconductor material [2]. In tendency the polarization should thus be parallel to the crystal axes. During the fabrication process of the VCSELs the side boundaries are approximately aligned with the crystal axes the deviation is supposed to be smaller than 5° [177]. The orientation of the principal axis (in which the matrix including the amplitude and phase anisotropies is diagonal), extracted from the experimentally obtained orientation of the polarization in region I, is used as a parameter in the numerical simulations to achieve a good agreement between experiment and theory.

Including a small amplitude anisotropy and the influence of the boundaries on the polarization of a tilted wave into the theoretical calculations the majority of the polarization effects observed in the experiment can be explained. In addition, the final transition of the light field through the top DBR has to be included, which accounts for small corrections of the polarization due to the higher transmission of p-waves (cf. section 5.3.1). The whole description of the model and the results on polarization selection can be found in [166]. In the following section examples of the numerical simulations are shown and the individual effects are explained in more details.

5.3.5 Polarization selections mechanisms: square VCSELs

From the results of the experiments and the improved model it is found that three different polarization selection mechanisms play the dominant role in the VCSELs. It is discussed in this section that these effects and their interplay are sufficient to explain most of the observed phenomena in correspondence with the behavior found within the three regions detailed in sections 5.2.3, 5.2.4, and 5.2.5. The three effects are:

1. the intrinsic material anisotropy as discussed in section 5.3.3. The values obtained in that section are used as parameters in the improved model. In addition, the orientation of the material anisotropy can modify the polarization orientation.
2. the anisotropy introduced by the DBRs due to the difference in reflectance for s- and p-waves, as shown in the previous section.
3. the influence of the reflection at the boundaries. It is shown in appendix A that a beam reflected at the side boundaries of the VCSEL does not change its polarization, i.e. the transverse reflections linearly couple the polarization between different Fourier components of a pattern. This effect counteracts the anisotropy induced by the DBRs in part, as will be shown in the following.

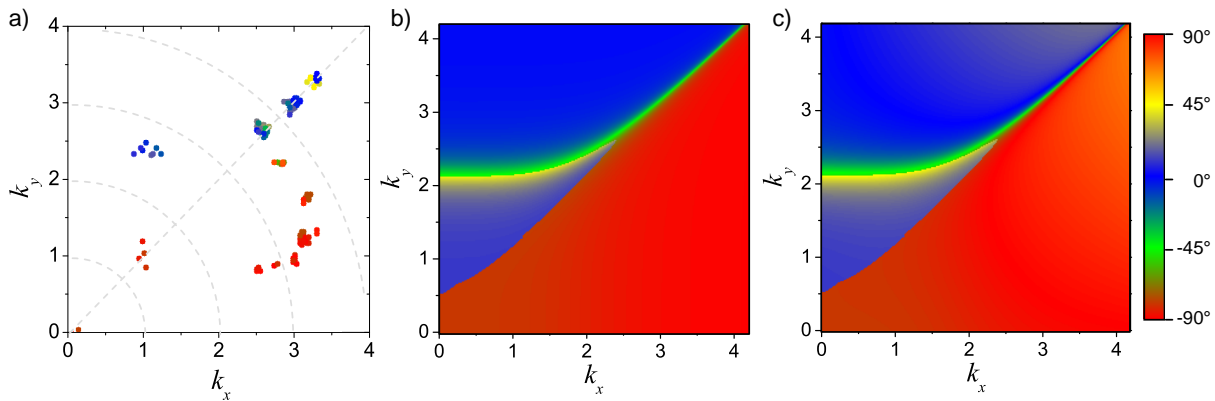


Figure 5.37: Illustration of the polarization distribution in the (k_x, k_y) plane obtained from experiments and theory. In each subfigure only the quadrant with $k_x \geq 0$ and $k_y \geq 0$ is shown. (a) Experimental data taken from VCSEL 40–5 at several temperatures and currents. Each dot represents a Fourier mode, the color corresponds to the polarization orientation of the respective mode. (b) Calculated polarization distribution of the field inside the cavity for the favored eigenstate. (c) Calculated polarization distribution after the transmission through the top DBR for the favored eigenstate. On the far right the color bar used for the polarization angles is given for reference.

Fig. 5.37 shows an example of the experimental (a) and the calculated polarization distribution inside (b) and outside of the laser (c). Both numerical images are obtained for the favored eigenstate, i.e. the eigenstate with the higher growth rate at threshold. The difference between (b) and (c) is discussed below. For reference the color bar used for the polarization is shown on the far right of the figure.

The experimental plot is similar to the mode maps described in section 4.2.4, but here each intense Fourier peak is marked by a dot colored corresponding to the polarization direction. This figure summarizes the experimentally observed polarization distribution of all three regions. For details see sections 5.2.3, 5.2.4, and 5.2.5, respectively.

The theoretical figure in fig. 5.37(b) is obtained from the improved model, that includes all effects listed above. The anisotropy values used for this calculation are $\gamma_p = 60 \text{ ns}^{-1}$ (equivalent to a birefringence of 19 GHz) and $\gamma_a = -0.1 \text{ ns}^{-1}$ (equivalent to a dichroism of -0.03 GHz). The anisotropy orientation is taken from the experimental findings and is set to -78° .

Fig. 5.37(b) mainly consists of two areas divided by the diagonal: one in which the polarization is oriented horizontally (blue) and one where it is vertical (red). For small wave numbers the border bends away from the diagonal so that the red region becomes larger. This is the area corresponding to region I. Its size is influenced by the values of the material anisotropy. The sign of the amplitude anisotropy determines if vertical or horizontal polarization orientation is selected at threshold in region I. In region II a locking of the polarization orientation to one of the laser boundaries is found, hence the plain blue and red areas. At the diagonal the two areas intersect and the polarization changes very abruptly. Here the polarization is nearly degenerate. For large wave numbers this corresponds to region III.

From the effects included into the model the mechanisms responsible for the polarization selection in the three regions can be explained: in region I the effect of the Bragg-induced anisotropy is negligible since s- and p-waves experience nearly the same reflectance for small transverse wave numbers. The polarization selection is dominated by the material anisotropy. Thus the experimentally obtained polarization orientation of modes in region I can serve as an indication of the direction of this anisotropy. As stated above in the results of the numerical simulations shown in fig. 5.37(b) and (c) the principal axis is set to -78° . The polarization of region I is oriented accordingly.

For region II the anisotropy induced by the DBRs surpasses the material anisotropy and the polarization selection is dominated by the fact that s-waves experience higher reflectivity at the DBRs. A higher reflectivity corresponds to a higher net gain (material gain minus losses) and s-waves are favored by the cavity. In principle this leads directly to the “90°-rule”, because an s-wave is polarized orthogonal to its wave vector. At this point the third effect mentioned at the beginning of this section has to be considered: the polarization of the four Fourier components is coupled linearly by the reflection at the side boundaries. The result is that eigenmodes of the waveguide and of the DBRs are not compatible, since the four wave vectors can not all be s-waves simultaneously. Thus the polarization has to lock to one of the boundaries. This is shown experimentally in appendix A. The result is, that the “90°-rule” is only valid for modes very close to one of the axes in wave number space, i.e. for modes consisting of two Fourier components.

The selection scenario found for region II results directly in an understanding of the polarization selection in region III: at the diagonal the two areas of vertical and horizontal polarization meet (cf. the green line along the diagonal for large wave numbers in fig. 5.37(b)). This results in a degenerate polarization selection: due to the sharp transition between the two areas the polarization near the diagonal changes abruptly. A mathematical explanation of this degeneracy results from the numerical calculations: as described in the last section, the growth rates of the two eigenstates of the 2×2 matrix which describes the polarization state are equal at the diagonal. Thus the polarization orientations of these two states are degenerate. This explains why the experimental observations for this region do not yield a clear rule for the polarization selection. The degeneracy can also serve as an explanation of the frequency locking between transverse modes with different polarizations reported in [27, 95].

The general characteristics of the polarization selection are thus clarified. The last building block that is necessary to explain the deviation from the locking to the boundaries observed in region II is the higher transmission of the top DBR for p-waves, which was introduced in section 5.3.1. The impact of this consideration is visible in fig. 5.37(c), especially for large wave numbers. Here the polarization distribution is shown after the transmission through the top DBR, i.e. this represents the state of polarization outside the laser. For large wave numbers the polarization is increasingly pulled toward an orientation parallel to the wave vector, visible in the discoloration of the red and blue areas. To further quantify this effect a cross-section along a circle with $3.1 \mu\text{m}^{-1}$ is plotted for the polarization distribution inside and outside of the cavity.

This plot is shown in fig. 5.38. The polarization angle φ is plotted over the angle α along the cross-section (corresponding to the angle of a Fourier mode in the (k_x, k_y) plane). The black curve represents the state inside the cavity: a nearly perfect alignment of the

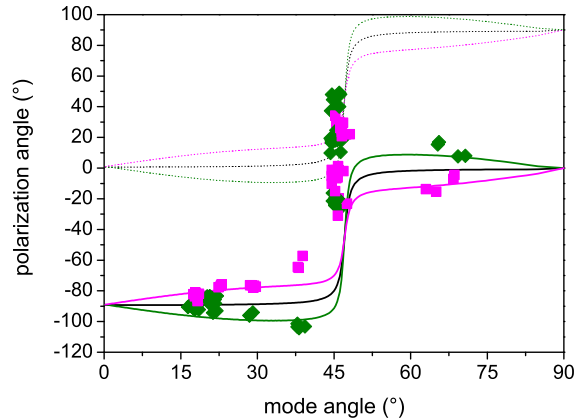


Figure 5.38: Plot of the polarization angle φ over the mode angle α including experimental and numerical data. The data points correspond to the Fourier modes included in fig. 5.37(a). The dark green diamonds represent Fourier components located in quadrants 1 and 3. The magenta squares correspond to Fourier components found in quadrants 2 and 4. The three continuous curves are cross-sections along the circle with $k_{\perp} = 3.1 \mu\text{m}^{-1}$ from the calculated polarization distribution of the favored eigenstate shown in fig. 5.37(b) and (c). The black line corresponds to the intra-cavity distribution (equal for all quadrants). The extra-cavity distribution is different for quadrants 1 and 3 (dark green curve) and quadrants 2 and 4 (magenta curve). The three dotted lines plotted in the polarization range above 0° correspond to the disfavored eigenstates (see text). Around $\alpha = 45^{\circ}$ the two eigenstates are degenerate. This explains why experimental data points are found at the diagonal for polarization angles above 0° .

polarization with the boundaries is found, i.e. the polarization is -90° for $\alpha < 45^{\circ}$ and 0° for $\alpha > 45^{\circ}$. The transition at the diagonal ($\alpha = 45^{\circ}$) is very abrupt. The other two curves represent the same cross-section for the extra-cavity polarization: the dark green curve corresponds to quadrants 1 ($k_x > 0$ and $k_y > 0$) and 3 ($k_x < 0$ and $k_y < 0$). The magenta curve represents the polarization orientation in quadrants 2 ($k_x < 0$ and $k_y > 0$) and 4 ($k_x > 0$ and $k_y < 0$). The deviation from the perfect locking to the boundaries curve is obvious. It increases for α nearing the diagonal.

The three dotted lines in the plot correspond to the polarization of the disfavored eigenstate as discussed in the previous section. They are equivalent to the curves corresponding to the favored eigenstate, but the polarization is rotated by 90° . Nearing the diagonal the growth rate of the favored eigenstate is reduced while the growth rate of the disfavored one increases. At the diagonal both eigenstates are degenerate.

The agreement between experimental data and theoretical calculations both in fig. 5.37 and fig. 5.38 is quite good and all effects found in the experiment are also found in the theoretical calculations. In the experiment region I shows mainly a homogenous polarization distribution, which is in agreement with the region I in the numerical result, though the size of region I is probably larger in the experiment than in the examples of the calculations shown here.

In region II the locking to the boundaries and the deviation from this rule for increasing mode angle α is found in both experiment and numerical simulations. Also the secondary modes excited above threshold in the experiment (the group of blue dots in the mode map, fig. 5.37(a)) fit into this characterization. This is illustrated in more detail by the

data points in fig. 5.38. They are colored in the same way as the theoretical curves. The agreement is quite good though of course the experimental data is much less smooth than the theoretical. The deviation from the locking to the laser boundaries is well visible in the experimental data and agrees in the general trends with the theory. The observation of different polarization angles for Fourier components belonging to one mode is explained in this way.

Finally the complex polarization distribution observed in region III in the experiment can be explained by the polarization degeneracy at the diagonal, as described above. The data points in the plot in fig. 5.38 near the diagonal ($\alpha \approx 45^\circ$) are scattered between -40° and 50° , in agreement with the degeneracy of the two eigenstates at the diagonal.

In conclusion, the numerical simulations helped a great deal to explain the polarization selection mechanism observed in the experiment. The improved model reveals the major building blocks necessary for this and the quantitative agreement between experiment and theory is very good.

5.3.6 Polarization selections mechanisms: circular VCSELs

The experimental observations on the polarization distribution in the circular VCSELs are presented in section 5.2.6. The scenario is apparently much less complex than that of the square lasers discussed above. First of all there are only two regions found in the emission of the circular lasers: modes with small transverse wave numbers have a (more or less) homogeneous polarization distribution, which corresponds to region I in the square lasers. Thus it follows that the mechanisms governing the polarization selection in region I are applicable to circular and square lasers.

Modes with large wave numbers show a special kind of polarization distribution that is not observed in the square devices. As shown in fig. 5.17(g) and (h) the transverse modes consist of rings in the near-field and the far-field images and the polarization of such modes rotates along these rings. In comparison the polarization orientation in the far-field pattern is rotated by 90° with respect to the near-field pattern. From the far-field polarization distribution it follows that the polarization is orthogonal to the wave vector. The “ 90° -rule”, that was found to be hardly valid for region II modes of the square lasers is essentially perfectly realized here.

For the square lasers it was found that all of the Fourier components making up one transverse mode have the same polarization orientation, that is determined by the location of the Fourier components in the (k_x, k_y) plane. This is a direct consequence of the linear coupling of the polarization for waves reflected at the transverse laser boundaries. This argument is apparently not true for the circular VCSELs, which indicates that the linear coupling is not applicable to the azimuthally modulated ring modes observed in these devices. Two reasons for this are possible: in accordance to the discussion of the gain guiding effect in these devices (cf. section 4.3.7) the observed behavior can be explained by waves travelling along the ring just inside the laser aperture which are not reflected at the side boundaries but gain-guided by the enhancement of the carrier distribution at the boundary. Another possibility arises due to the grazing incidence of the travelling waves upon the side boundary: it is conceivable that the large angle of incidence reduces the effect of the linear coupling considerably and the DBR-induced anisotropy dominates the

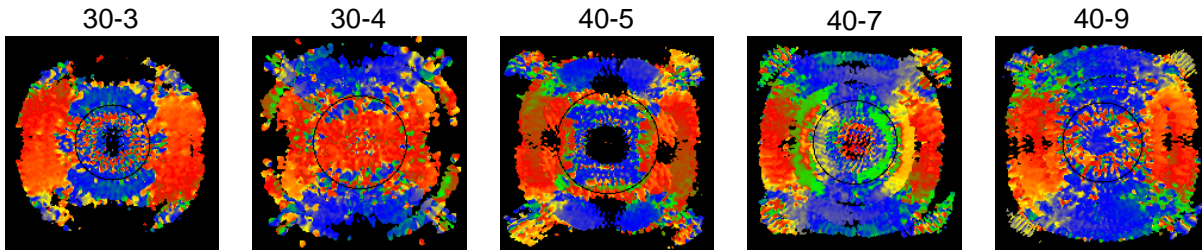


Figure 5.39: Overview of the far-field polarization distribution for several lasers. See text for details on how these images are obtained. The displayed far-field area ranges from $-4.3 \mu\text{m}^{-1}$ to $4.3 \mu\text{m}^{-1}$. The black circles indicate the estimated radius of region I.

polarization selection.

In every case, the experimental findings indicate that the eigenmodes of the transverse waveguide and those of the DBRs are compatible for region II modes in the circular lasers, though this was not explicitly calculated for these lasers. In effect this also explains why the final transition through a DBR does not influence the polarization: the transverse mode satisfies the “90°-rule” and thus forms an s-wave at each point. In this case the higher transmissivity of p-waves has no influence on the polarization of the mode.

A scenario corresponding to region III defined for the square lasers is not observed in the circular VCSELs. Of course it is possible that the temperature has to be decreased beyond the experimentally accessible minimum. Nonetheless the discussion of the dependence of the cut-off wave number on angles of incidence larger than 45° in section 4.3.2 shows that the cut-off condition and thus the reflections at the side boundaries do not play a role in the circular lasers. It is thus conceivable that the scenario explained above is valid for considerably larger transverse wave numbers than those observed in the experiments.

5.3.7 Extent of the three regions

In this section the extent of the regions, which are introduced to distinguish different mechanisms of polarization and pattern selection, is investigated for the square VCSELs. To enable an experimental approach to this investigation images are created that show an overview of the polarization distribution in the wave number space. Since for single settings of temperature and current the VCSELs only emit a limited number of transverse waves, such an overview is created from several far-field images at different settings of temperature and current. This is done in the following and the results are compared to earlier works on polarization dynamics.

At first the far-field intensity and polarization distributions at a certain setting of temperature and current are considered. For each pixel of the intensity image with a value above 5% of the global intensity maximum the polarization angle of this pixel is stored in a new image. This is repeated for several temperatures and currents, until many modes with different wave numbers more or less fill the image. Pixels of the new image are only set once. The resulting image shows an overview of the polarization distribution as a whole, since it includes the polarization distribution of many modes that are not excited in a laser for one temperature/current setting.

Again the polarization color table is used, but the color black is inserted to serve as

neutral background. Pixels of the new image that do not obtain a polarization value are set to black. Examples of the result of this method are shown in fig. 5.39.

All images in fig. 5.39 show similar features though they differ in the details. In all cases for modes with high wave numbers dominantly blue and red areas separated by the diagonals are apparent. The transition in radial direction between these areas is quite abrupt and generally at this point diagonal polarization orientation is found (corresponding to yellow and green). The central region is dominated by either red or blue. Device 30–3 and 40–9 show both colors but each one is more or less limited to certain wave number ranges. In some cases the optical axis is black, because no on-axis emission is found in those lasers. For the highest possible wave numbers the emission is only found at the diagonal and the rest of the corresponding circle is black. This corresponds to the diamond-shaped billiard patterns discussed in section 4.3.3. Also here the most complex polarization distribution is found, much more complex than at the diagonals for lower wave numbers.

The most unusual distribution is found in device 40–7, where on the left and right side of the central area segments of green and yellow circles are visible, alternating between these two colors. This unusual behavior is not discussed any further.

These images show a comprehensive overview of the polarization distribution explained in section 5.3.5. They allow an estimation of the location of the transitions between the three regions. The point of transition between region II and III is rather easy to identify: between the two regions the polarization behavior changes from a well defined locking to the boundaries (region II) to a more complex distribution (region III), which is due to the polarization degeneracy at the diagonal. In addition, diamond-shaped patterns attributed to region III are only found for wave numbers beyond $3.7 \mu\text{m}^{-1}$.

The transition between region I and II can only be estimated roughly. In general all rings having a homogeneous polarization distribution are considered to belong to region I. Good examples are found around the centers of the overview images for lasers 30–3, 30–4, and 40–9. Region II is the area where the polarization approximately locks to the boundaries. This is marked by the dominantly blue areas at the top and the bottom and the dominantly red areas at the left and right side of the images for wave numbers in the range from about 1.5 to about $3.8 \mu\text{m}^{-1}$. Another distinction between region I and II is the shape of the excited patterns: while in region I generally nearly complete rings are emitted, region II is dominated by transverse modes with four distinct Fourier peaks.

The estimation of the transition between these two regions is indicated by the black circles in the figure. In some cases there is some room for argument about the location of the transition, i.e. the radius of the circle. Nonetheless, in tendency the transition is found between 1.5 and $2.0 \mu\text{m}^{-1}$ in every laser.

As was explained in section 5.3.4 and 5.3.5 the DBRs forming the cavity of the laser introduce an amplitude anisotropy, called $\gamma_{br,a}$ here. With the relation

$$\gamma_{br,a} = (r_s - r_p) / \tau_{eff} \quad (5.11)$$

the anisotropy can be calculated (first order approximation for reflectivities close to one). r_s and r_p are the reflectivities of the s- and the p-wave at the DBR, calculated with [176]. τ_{eff} is the photon round-trip time given in appendix C. With this equation the plot in fig. 5.40 is obtained. Thus a correspondence between the transverse wave number and the

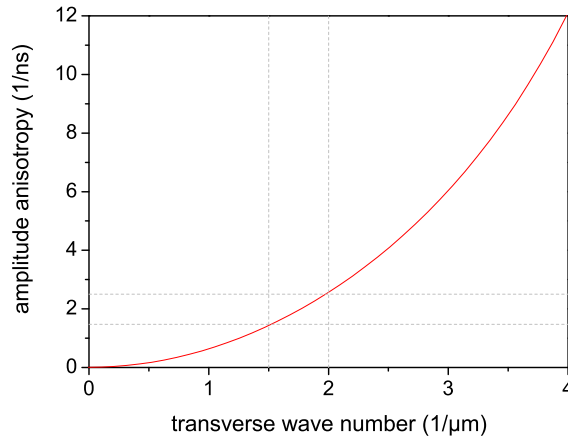


Figure 5.40: Amplitude anisotropy $\gamma_{br,a}$ (dichroism) of a DBR similar to those implemented in the VCSELs over the transverse wave number k_{\perp} . The grid lines indicate the values of the transverse wave numbers estimated for the transition between region I and II and the corresponding DBR-induced anisotropy.

DBR-induced anisotropy is found. Note that to obtain the anisotropy in GHz, as given in section 5.3.3, γ_a has to be divided by π .

The experimental findings indicate, that the polarization selection imposed by the DBRs increases with increasing transverse wave number. In region I $\gamma_{br,a}$ is still too small to dominate the polarization selection. In region II it is obviously stronger than the material anisotropy and the polarization is selected according to the anisotropic reflection of the DBRs. The experimental considerations above show that the transition is found between 1.5 and $2.0 \mu\text{m}^{-1}$. This corresponds to $\gamma_{br,a}$ between 1.5 and 2.6 ns^{-1} . These values are indicated by the grid lines in fig. 5.40

From experiments with small area VCSELs ($\leq 15 \mu\text{m}$) with and without feedback [61, 62, 72] it follows that a transition between weak polarization determinism and a strong selection of one polarization orientation is found around a material anisotropy $\gamma_a \approx 3.1 \text{ ns}^{-1}$. The same value of the Bragg-induced anisotropy is found at $k_{\perp} \approx 2.2 \mu\text{m}^{-1}$. This agrees quite well with the maximum of the estimated wave number range of the transition between region I and II.

In conclusion, it is found that though the details of the polarization distribution are different for different lasers in a rough estimation the transition between region I and II is found between wave numbers of 1.5 and $2.0 \mu\text{m}^{-1}$. This estimation agrees with studies of the dependence of polarization dynamics on the material anisotropy in small VCSELs. The transition from region II to III is easier to locate: it is found around $3.7 \mu\text{m}^{-1}$, above which the Fourier components are located at the diagonal in all square VCSELs under study.

6 Control of pattern properties with feedback

The previous experiments explained in much detail how the selection mechanisms of length scales, pattern shapes, and polarization distribution work in VCSELs. In this chapter control over these characteristics is demonstrated by submitting the VCSEL to feedback (cf. section 2.6). For this a portion of the emission of the laser is directed back into itself. The beam path forms an external cavity in which spatial filters can be inserted.

Here, the influence of frequency-selective and spatial-frequency-selective feedback on the emission of the VCSELs is investigated. The first method uses a reflection grating, that feeds only a narrow band of wavelengths back into the laser. These wavelength then have a higher gain than those that do not experience feedback (proper alignment and operation parameters assumed). For spatial-frequency-selective feedback a normal mirror is used. In addition, a Fourier filter is inserted into the feedback beam path which results in higher gain for certain Fourier modes supported by the feedback.

6.1 Experimental setup

A setup different from the one described in the previous chapters was used for the feedback experiments. It consists of a feedback and a detection beam path. The feedback is set up in Littrow configuration (compare e.g. [109]) with a 1:1 imaging of the laser onto itself. The detection again allows measurement of near- and far-field emission and optical spectra. The schematic is shown in fig. 6.1.

The VCSEL is again driven by the low-noise current source used before. It is mounted onto a heat sink with milled ribs. Since an air-tight box is not used, the temperature range is limited to about 10 °C, where water starts to condensate at the cold side of the heat sink. At 10 °C the wave number at threshold emitted from the VCSELs under study is about $2.5 \mu\text{m}^{-1}$ (cf. fig. 4.25). Thus it is sufficient to collimate the laser beam using a lens with low NA. An aspheric lens (Thorlabs) with a focal length $f = 11 \text{ mm}$ and an NA of 0.3 is used. A substrate with an anti-reflection coating on one side is used to split off a small portion (a few percent) of the beam, which is then used for detection. In this way maximum intensity is available for the feedback, which is important for the experiments involving Fourier filtering. For the detection this is of no importance, since the CCD camera is very sensitive. Two sets of polarizing elements, each consisting of a half-wave plate and a linear polarizer, are used to analyze and control the polarization state of the emission. One set is set into the detection, the other into the feedback beam path.

For the feedback beam path a lens (focal length 300 mm) is used to image the plane of the active zone of the laser onto the feedback grating or mirror, which in turn retro-reflects

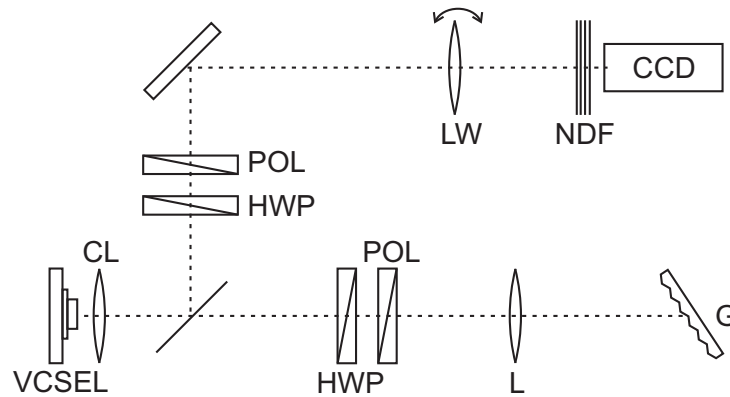


Figure 6.1: Schematic setup for the feedback experiments. The abbreviations denote the following components: CL – collimation lens, POL – linear polarizer, HWP – half-wave retardation plate, L: lens, G – feedback grating with 1800 lines/mm, LW – lens wheel, NDF – neutral density filters, CCD – CCD camera.

the beam into the VCSEL. This system then constitutes a 1:1 imaging. For frequency-selective feedback a grating from Spectrogon with 1800 lines per millimeter is used. The first order of the grating is reflected back into the VCSEL. A micrometer screw can be used to tilt the grating with respect to the vertical axis. In this way the frequency range that is fed back into the VCSEL can be adjusted. For experiments with spatial-frequency-selective feedback a standard high-reflection mirror (Thorlabs) replaces the grating. The filters have to be put into the Fourier plane of the laser. This is found in a distance of f from the collimation lens (supposed the distance between lens and laser is also f). Since the unfiltered beam is desired for the detection arm, the beam sampler has to be put between collimation lens and Fourier filters. In section 6.2.3 the different filter geometries are described.

Note that the grating is a polarizing element, since it has a significantly higher reflection for the polarization orthogonal to the grating lines, in this case the horizontal polarization. Thus the polarizer in the feedback arm is set to horizontal transmission. When the half-wave plate is rotated, the polarization state that is favored by the feedback can be selected.

The detection consists essentially of the CCD camera from SVS-Vistek, which was used for some experiments in section 5.1.1. See there for details. A lens wheel containing one lens is put into the beam path to image the far-field (without lens) or alternatively the near-field (with lens) onto the camera. The linear polarizer is set to horizontal transmission and the half-wave plate is used to select which polarization orientation is transmitted. Note that the beam splitter has a higher reflection for vertically polarized light. This has only a minor effect on the polarization of the feedback arm, since the reflectivity of the beam splitter is very low. The effect on the state of polarization detected with the CCD camera is quite pronounced and has to be taken into account when the Stokes parameters are calculated.

6.2 Experimental observations

With the feedback setup it is possible to control most of the emission characteristics directly. In the following sections it is shown that frequency-selective feedback allows control of the emission wavelength and thus of the length scales of the patterns. With Fourier filtering the shape of the pattern can also be controlled to some degree. Examples of the control of the state of polarization are shown as well.

For all experiments the feedback was adjusted with great care. The criteria for the adjustment of the feedback are the threshold reduction (i.e. the difference between the laser threshold of the free-running device and the threshold with feedback) and the increase of the output power above threshold [131, 178]. With frequency-selective feedback a maximal threshold reduction of up to 20% was measured (laser 30-2 at 42 °C). The slope efficiency was approximately equal with and without feedback, though the absolute output power was considerably higher under the influence of feedback. A more detailed description is not given since the feedback is only used as a tool here.

6.2.1 Scanning the Feedback frequency

In this section the effect of frequency-selective feedback on the emission is illustrated. It is shown that by changing the tilt angle of the feedback grating the length scales of the emission pattern can be changed. The grating tilt is adjusted with a micrometers screw. For these measurements the polarization elements in the detection beam path were removed. However the grating reflects mainly the horizontally polarized light.

In figures 6.2 and 6.3 the dependence of optical and spatial spectra of laser 40-6 on the setting of the relative feedback frequency (feedback frequency minus resonance frequency, corresponding to the tilt of the grating) is shown as spectra maps (cf. section 3.3.3). The frequency is changed by turning the micrometer screw in steps corresponding to a pitch of 12.5 μm . Each step increases the tilt angle of the grating by about 0.01°. Accordingly the feedback frequency is changed by -74 GHz which corresponds to a wavelength shift of 0.15 nm. The laser is operating slightly above threshold, so that without feedback yet no lasing emission is detected.

In the optical spectra (a) a quasi-continuous shift of the emitted wavelength is apparent. The laser emission simply follows the changing feedback frequency, i.e. the measured shift of the emission wavelength is equal to the wavelength shift induced by the tilt of the grating. Also a change in the intensity of the emission is apparent. Only for a small region of the feedback frequency the spectral lines have a high intensity. The maximum of the intensity is found at a detuning from the longitudinal resonance of around 1.4 nm at 10 °C (fig. 6.2) and around 0.6 nm at 20 °C (fig. 6.3). Comparing this to the calculated curve in fig. 4.37 the detuning values correspond to wave numbers of $1.8 \mu\text{m}^{-1}$ and $1.1 \mu\text{m}^{-1}$, respectively. Far-field images of the free-running laser 40-6 at threshold show a dominant emission at a wave number of $3.0 \mu\text{m}^{-1}$ at 10 °C, and $1.7 \mu\text{m}^{-1}$ at 20 °C. Thus the maximum intensity is not found at the same detuning for the solitary laser and the laser with feedback, as should be expected. The detuning in the case with feedback is about 1.4 nm smaller for both temperatures. Where this offset originates is not clear.

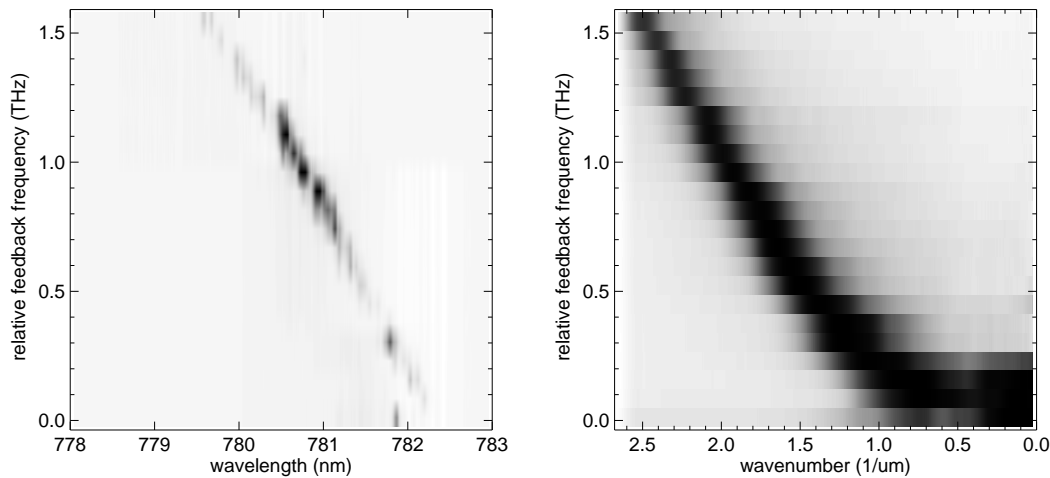


Figure 6.2: Feedback frequency dependence of the spectra of device 40–6 as grey-scale maps. (a) Optical spectra, (b) spatial Fourier spectra. Parameters $T = 10^\circ\text{C}$, $I = 15\text{ mA}$, $p = 0.07$. Black denotes highest intensity, the spectra are normalized to the global maximum and over-exposed to enhance the contrast of weak modes. The injection current is selected to be just at threshold of the free-running VCSEL, where the lasing emission is still too weak to be detected with the CCD camera.

Most of the individual spectra show more than one peak, which is visible in the spectra maps as several darker lines for some feedback frequencies. This was checked with a plano-planar FPI, where for all feedback settings multiple spectral lines were found. The transverse mode spacing found with the spectrometer is about 0.08 nm . It seems that the range of frequencies reflected by the grating and focussed back into the laser is larger than this mode spacing.

In figures 6.2(b) and 6.3(b) the corresponding spatial Fourier spectra are shown. It is apparent that the dominant length scale of the far-field changes in accordance with the feedback wavelength shift. Thus the 1:1 correspondence between emission wavelength and transverse wave number is demonstrated again. In the wave number range above $1.5\ \mu\text{m}^{-1}$ the spatial spectra maps in figures 6.2 and 6.3 are nearly identical. In the second figure, where the temperature is set to 20°C , a preference of emission close to the optical axis is found. This is explained by the observed preference of on-axis emission also in the solitary laser at this temperature. The feedback in this case is not able to fully suppress the on-axis state. Also the off-axis modes supported by the feedback have a lower intensity than the on-axis emission. The change of the transverse wave number is analyzed quantitatively in detail in section 6.3.1. Note that on-axis emission is reached near the point of zero relative feedback frequency.

When the feedback frequency is reduced further, the laser keeps emitting close to the optical axis at first, the dominant transverse wave number increases slightly. A few steps of the micrometer screw further the laser turns off. This is due to two reasons: light with a wavelength larger than the longitudinal resonance is not supported by the cavity; and

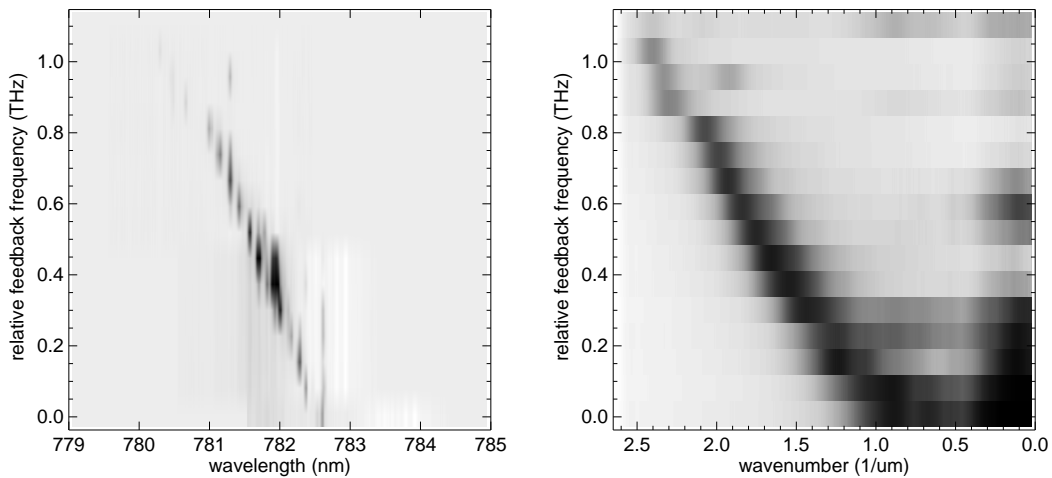


Figure 6.3: Feedback frequency dependence of the spectra of device 40–6 as grey-scale maps. (a) Optical spectra, (b) spatial Fourier spectra. Parameters $T = 20^\circ\text{C}$, $I = 13.2\text{ mA}$, $p = 0.08$. Black denotes highest intensity, the spectra are normalized to the global maximum and over-exposed to enhance contrast of weak modes. The injection current is selected to be just at threshold of the free-running VCSEL, where the lasing emission is still too weak to be detected with the CCD camera.

for this feedback setting no ASE of adequate wavelength is available to be amplified by the feedback.

Fig. 6.4 shows a similar feedback frequency scan, but here the near-field and far-field images are shown. The setting of the micrometer screw is varied in steps of $20\ \mu\text{m}$ here. The corresponding frequency and wavelength shifts are given in the caption.

It is obvious that the dominant pattern length scale is reduced during the scan: the near-field on the far left shows a finely modulated pattern, the ring in the far-field has a radius of $2.4\ \mu\text{m}^{-1}$, close to the maximum transmitted by the collimation lens. On the far right the pattern has a much larger wavelength, the wave number has shrunk accordingly.

For all settings of the feedback the far-field shows a single continuous ring. Mostly the intensity at the diagonals is slightly increased. For the first two images, where the wave number is above $2.0\ \mu\text{m}^{-1}$ and thus the pattern is supposed to belong to region II (cf. section 5.3.7), this is in contrast to the modes emitted by the solitary laser, at least at threshold. In region I emission on rings is common also in solitary lasers, in some cases with peaks at the diagonal.

For completeness it is briefly described what happens when the injection current is increase beyond threshold while the laser is subjected to frequency-selective feedback. The figures shown in this chapter are all for a current just above threshold, i.e. a small positive pump rate. Increasing the current from there, while the feedback frequency remains fixed, the radius of the ring found in the far-field grows. At the same time the intensity of the ring increases and the ring becomes broader, because additional transverse

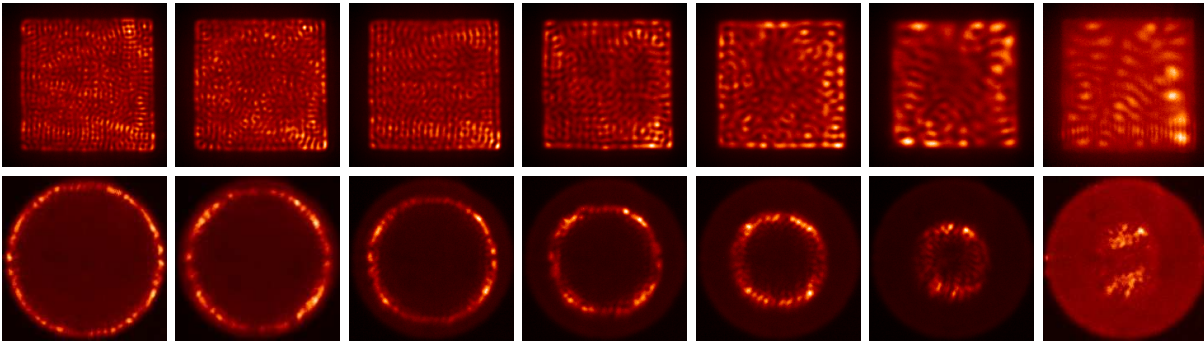


Figure 6.4: Near-fields (upper row) and far-fields (lower row) of laser 40–6 under the influence of frequency-selective feedback. From left to right the grating is tilted so that the feedback frequency is reduced. The frequency step between the images is about -120 GHz, which corresponds to 0.24 nm.

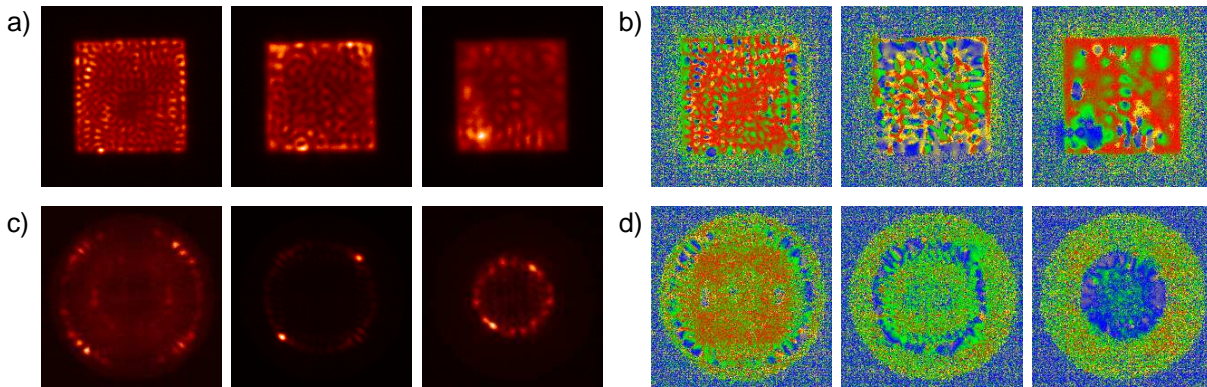


Figure 6.5: Near-field (a,b) and far-field (c,d) of the emission of laser 30–2 under the influence of frequency selective-feedback. Three settings of the feedback grating are shown with a wavelength step of 1 nm (corresponding to about 500 GHz) in between. (a) and (c) show the total intensity, (b) and (d) the polarization distribution, color-coded with the known palette.

modes are excited. The increase of the dominant wave number results from the red-shift of the longitudinal resonance with current: since the feedback wavelength is fixed, the red-shift increases the detuning between longitudinal resonance and feedback. This results in an increase of the wave number. The radius change is about $0.03 \mu\text{m}^{-1}$ per milliampere when starting at a wave number of $2 \mu\text{m}^{-1}$. This corresponds to a change of the detuning of 0.05 nm/mA (calculated with eq. (4.33)), in good agreement with the current-induced shift discussed in section 3.4.4.

6.2.2 Polarization measurements

In the following the control over the polarization state of the emission is illustrated. For this, the Stokes parameters were calculated for a horizontally polarized feedback beam. The anisotropic reflection of the beam splitter is included into the calculation of the Stokes parameters (this correction creates a dominantly horizontally polarized background noise, which is an artefact).

Fig. 6.5 shows a few near-field (a,b) and far-field (c,d) images of the emission of laser 30–2 under the influence of frequency-selective feedback. On the left side the total intensity is shown, on the right the polarization distribution. Each row of three images corresponds to three settings of the feedback frequency.

The near-field images show a rather irregular polarization distribution. When the intensity (a) and polarization (b) images are compared it becomes apparent that the areas with high intensity are all polarized horizontally (blue). The diagonally polarized (green) areas correspond to peaks with low intensity. The vertically polarized (red) areas correspond to intensity on the level of spontaneous emission. This shows that weighted with the intensity the dominant polarization is horizontal. The far-field images (d) show a predominant horizontal polarization, in agreement with this description.

Especially for the first feedback setting the polarization distribution is different from the one observed in the experiments with the VCSELs without feedback. The wave number of the mode emitted at this setting suggests that the mode belongs to region II and thus the typical locking of the polarization to the boundaries should be observed. However, the polarization is approximately homogeneous along the ring.

The feedback arm is polarized horizontally. Thus for this state the gain is higher and it is favored in the emission. The experimental observations agree with this. It is thus found that the feedback controls the state of polarization to some degree.

6.2.3 Measurements with spatial-frequency-selective feedback

To control the shape of the patterns emitted by laser 40–6 the various Fourier filters are put into the beam path just behind the beam splitter. In all cases the laser is driven close to threshold, so that without feedback the lasing emission is still too weak to be detectable. For these measurements the polarization optical elements are removed from the feedback beam path to maximize the feedback strength.

The first filter under study is a vertical slit, consisting of two small plates. One of the plates can be moved to adjust the width of the slit. The width of the slit is set to 2 mm, which corresponds to a full width in wave numbers of about $1.9 \mu\text{m}^{-1}$. The filter is carefully adjusted to be in the center of the feedback beam. With this filter frequency-selective feedback is still applicable, since one spatial degree of freedom remains available and thus the wave number can still be selected by the feedback frequency.

Scanning the feedback frequency fig. 6.6 is obtained, which is similar to the previously studied frequency scan in fig. 6.4. Comparing these two figures the effect of the filter is apparent: especially in the second and third far-field image the ring is reduced to some spots at the top and the bottom. The corresponding near-field is much more regular, rather comparable to the wavy stripe patterns observed in the solitary VCSELs. The last two images show nearly no influence of the filter, since the dominant wave number is smaller than $0.9 \mu\text{m}^{-1}$, which is smaller than the range transmitted by the slit. For example, the second to last images in figures 6.4 and 6.6 are identical.

Note that a smaller slit width does not change the emitted patterns but only reduces the output power until the laser turns off for a width lower than about half a millimeter.

Fig. 6.7 shows the effect of other Fourier filters on the laser emission. Here the feedback grating is replaced by a mirror, since the geometry of these filters is selected to transmit

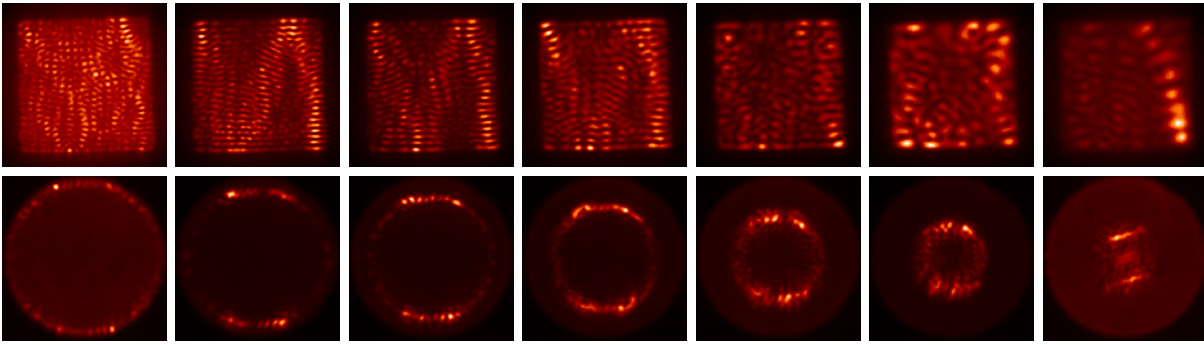


Figure 6.6: Near-fields (upper row) and far-fields (lower row) of laser 40–6 under the influence of frequency-selective feedback combined with Fourier filtering. The Fourier filter used here is a 2 mm ($1.9 \mu\text{m}^{-1}$) wide slit oriented vertically. From left to right the feedback frequency is reduced in steps of about 0.24 nm, corresponding to 120 GHz. The effect of the filtering is most apparent in comparison with fig. 6.4.

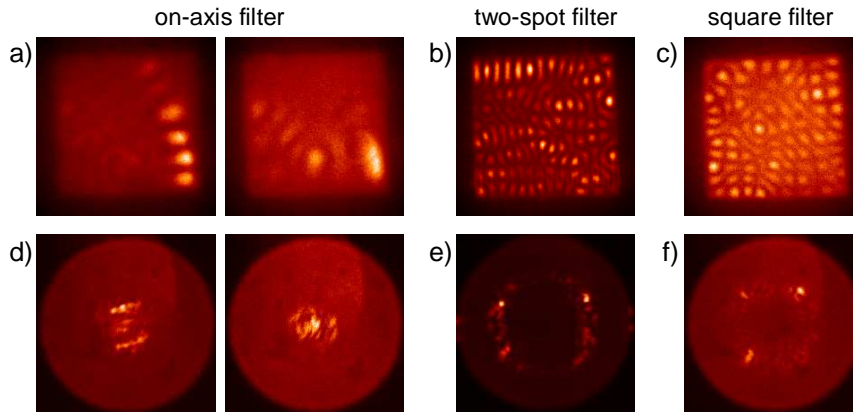


Figure 6.7: Near-field (a-c) and far-field (d-f) of laser 40–6 under the influence of spatial-frequency-selective feedback using three different Fourier filters (the name of the filter is given above the images, cf. text). The two images for the on-axis filter correspond to two adjustments of the feedback mirror. Parameters: (a) $T = 32^\circ\text{C}$, $I = 12.5 \text{ mA}$, $p = 0.09$. (b) $T = 10^\circ\text{C}$, $I = 17 \text{ mA}$, $p = 0.21$. (c) same as (a).

only certain wave numbers. Due to the correspondence of wavelength and wave number the grating is not needed any more. Ideally the mirror is adjusted so that the laser is imaged into itself. Tilting the mirror slightly results in a partially congruent feedback, so that some parts of the laser aperture experience more feedback than others.

In subfigure (a) an on-axis filter is used. This is a plate with a hole in the middle (diameter 1.5 mm) that is placed into the center of the laser beam. The filter transmits wave numbers up to $0.7 \mu\text{m}^{-1}$. The heat sink temperature is increased to 32°C for the measurement. In the figure near-field and far-field images for two settings of the feedback mirror are shown. The intensity in both cases is very weak since only a very small fraction of the feedback reaches the laser. Both images show on-axis modes similar to those found in the free-running VCSELs. The left images resemble strongly the images on the far right in fig. 6.6. Note that with an on-axis filter of larger diameter the transverse wave

number of the emission increases and a state similar to the second to last in fig. 6.6 is observed. With smaller hole diameters the laser turns off.

The next filter has two holes of 1 mm diameter, spaced 2 mm horizontally. The center between the holes is aligned with the optical axis. This filter has similar abilities as the combination of frequency-selective feedback and the slit. The spacing between the holes corresponds to a transverse mode with a radius of $0.9 \mu\text{m}^{-1}$, which is supported by the feedback. The diameter of the holes corresponds to half the width of the slit that was discussed above. Note that the two holes are aligned horizontally, i.e. orthogonal to the slit.

The resulting laser emission is not as regular as might be expected: the far-field is rather ring-shaped with two dominant peaks. The dominant wave number is around $1.1 \mu\text{m}^{-1}$. The peaks have both a nonzero k_x and k_y , though the filter is designed to force the laser on a mode with $k_y = 0$. The near-field is much more regular than comparable images without filter (cf. fig. 6.4) but shows an irregular wavy stripe pattern instead of perfect stripes.

Finally a filter with a square geometry is inserted into the beam path. It consists of four small holes with 0.5 mm diameter, arranged on a square with a side length of 2 mm, corresponding to a transverse mode with a radius of $1.3 \mu\text{m}^{-1}$. The resulting laser emission is very weak due to the small size of the holes. However the far-field shows rather clearly that the filter strongly controls the shape of the emitted patterns. Four weak Fourier components are evident, two of them slightly brighter. The dominant wave number is $1.0 \mu\text{m}^{-1}$, smaller than the one defined by the filter. The far-field emission observed with this filter is slightly different from the one observed with the two-spot filter. The near-field is partly of square symmetry, especially in the lower left and upper right corner.

6.3 Analysis and interpretation

The experiments show that the important emission characteristics – the pattern length scale and shape, the emission wavelength, and the polarization distribution – are influenced by the feedback. In fact some of these characteristics can be controlled directly, while others, like the pattern shape, allow control only to some degree. To illustrate this degree of control further the emission under influence of feedback is compared to the emission of the free-running laser. In an attempt to measure the shape of the gain curve, the modal threshold of several transverse modes at different settings of the feedback frequency is investigated.

6.3.1 Control of the length scales

First of all the length scales are considered quantitatively. This is done in the same way as in section 4.3.4, i.e. the transverse wave number of the emitted modes is plotted against the detuning between the wavelength of the feedback and the wavelength of the on-axis emission (longitudinal cavity resonance). Here the wavelength of the emitted modes is equal to the wavelength of the feedback, which is illustrated by the spectra maps (e.g. fig. 6.2). The longitudinal resonance wavelength is obtained from two sources: the

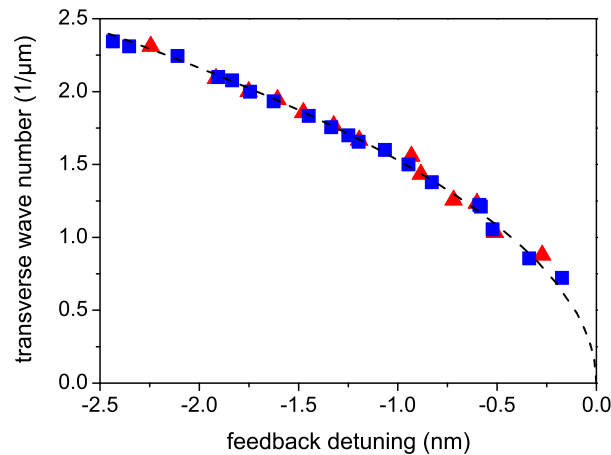


Figure 6.8: Plot of the dependence of the transverse wave number on the detuning imposed by the frequency-selective feedback. The dashed red line is identical to the one plotted in fig. 4.37. The black data points correspond to laser 40–6 at 20 °C, the red ones to 10 °C.

spectra at high temperatures without feedback and the spectra taken with the feedback set to on-axis emission. Both sources yield the same values. Again the temperature and current-induced shifts are used to shift the wavelengths to the desired operating parameters.

Fig. 6.8 shows the resulting plot for laser 40–6 at two temperatures. The dashed line is identical to the theoretical curve plotted in fig. 4.37. The experimental data points agree very well with the theory. This shows two things: 1. the correlation between the selected feedback wavelength and the pattern length scale follows the same rules as the length scale selection in the free-running VCSELs; 2. the mode spacing (indicated by the spacing of the data points) is much smaller than in the free-running laser. This shows that the feedback enables the emission of transverse modes that are not observed without feedback, at least considering the length scales. It follows that the feedback is stronger than any gain or loss mechanisms that are responsible for the transverse mode spacing in the solitary laser.

6.3.2 Control of the pattern shapes

Fourier filtering yields some promising examples of the control of the pattern shapes. All filters used in the experiments had some effect on the pattern shapes. But some limitations show up as well: the Fourier filtering is not able to force the laser on modes of perfect symmetry, like a stripe pattern or homogenous emission, though the filters are designed for this.

One example of this is the effect of the two-spot filter on the emission: the shape of the far-field emission indeed shows two bright spots, but those are not located at the transverse coordinate $(k_x, 0)$ in the wave number space, but have a nonzero k_y . When changing the vertical position of the filter the emission does not change. Apparently the filter geometry corresponds to a mode that is strongly disfavored by the laser cavity. The laser follows the feedback only to some degree and then emits a mode that only somewhat

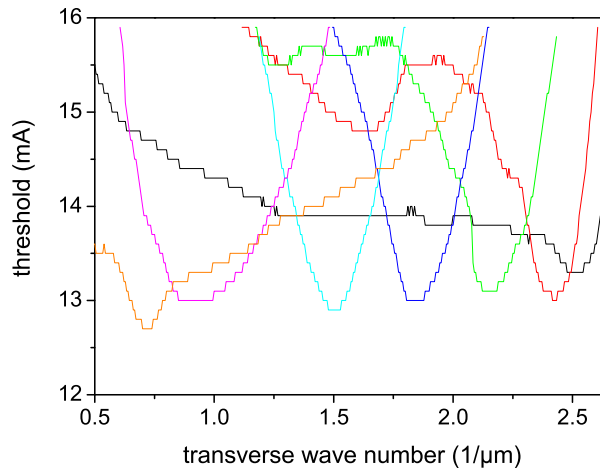


Figure 6.9: Plot of the dependence of the modal threshold on the transverse wave number for device 40-6 at 20 °C. The curves correspond to different settings of the feedback wavelength. The wavelength is increased in steps of 0.3 nm from black to orange, corresponding to a continuous decrease of the favored wave number.

resembles the filter geometry.

Both the experiments with the slit and the stripe filter were expected to force the laser to emit perfect stripes, corresponding to two Fourier components in the far-field emission. Such a pattern was neither observed in the experiments with the free-running lasers nor in experiments with feedback. This underlines the findings in chapter 4, that patterns consisting of four Fourier components are the basic building block of the pattern selection and Fourier components with $k_x = 0$ or $k_y = 0$ as well as homogeneous emission are strongly disfavored.

6.3.3 Modal threshold with frequency-selective feedback

In section 4.3.5 the mode selection was illustrated by determining the modal threshold for each transverse wave number and plotting it for several temperatures. The result shows the order in which transverse modes are excited depending on the temperature. This method can also be combined with frequency-selective feedback. Thus another quantity, the feedback frequency, is added to the parameter space. By scanning the feedback frequency it should become visible which modes are favored (thus having a lower threshold) and which are disfavored. Even modes that are not excited in the free-running laser at all can be included, since with feedback much more modes are found than without. In this way it should be possible to measure the gain curve and its shift with temperature.

Fig. 6.9 shows an example of the dependence of the modal threshold on the feedback frequency. The various curves each correspond to one setting of the feedback grating. The temperature is set to 20 °C. In contrast to fig. 4.39 here the transverse mode is not selected by the temperature but by the feedback. It shows that the minima of the curves are only marginally different. The lowest threshold is found for the mode close to the optical axis, the highest for the one with the highest wave number. The former may indicate a small preference of on-axis emission, which was already indicated by the

spectra map in fig. 6.3. The latter is probably due to the cut-off from the aperture of the collimating lens. The intermediate modes all have approximately the same threshold. The difference between maximum and minimum threshold is only 0.4 mA, the difference in the modal thresholds of the free-running device is ten times higher (cf. fig. 4.39).

Similar plots can be obtained for other temperatures, but they are not significantly different from the example above. All transverse modes have approximately the same threshold, regardless of the temperature. That shows that the losses for different transverse modes inside the cavity are not drastically different and the gain curve is quite flat. The strongest influence on the modal threshold found was due to the alignment of the feedback. That the on-axis region is in general slightly favored is probably also due to easier alignment for those modes.

7 Conclusions

In this thesis, the characteristics of transverse modes emitted by broad-area VCSELs with square and circular aperture were studied experimentally. The work focussed on the dependence of the transverse length scales on the operating parameters, the shape of the near-field and far-field patterns, and their state of polarization. In order to control these characteristics the square devices were submitted to external feedback.

Various square (30 μm and 40 μm side length) and circular VCSELs (80 μm in diameter) were investigated. It was found that though the general features are independent of the laser geometry the characteristics of the circular lasers are less complex and thus easier to understand than the characteristics of the square lasers. Thus the emphasis of the experimental works was on the VCSELs with square aperture.

From systematic measurements of the near-field and far-field intensity distribution of the transverse patterns over wide ranges of the heat sink temperature and for injection currents reaching from far below to far above threshold a characterization of the underlying mechanisms of pattern selection was achieved. The control of the detuning between maximum gain wavelength and longitudinal resonance via the operating parameters temperature and current was characterized. The square of the transverse wave number of the Fourier modes is found to be linearly dependent on this detuning [153]. The absolute values are influenced by the material compositions and growth variations (e.g. the thickness of the layers) in the VCSEL structure.

In detail the dependence of the detuning on the temperature is different for different lasers. Nonetheless all lasers of nominally equal design show the same quantitative dependence of the length scales on the detuning. This dependence is best described by a simple Fabry-Perot resonance formula derived from geometrical considerations. The linear dependence is found both for lasers with square and with circular aperture. Experiments with frequency-selective feedback proved that the length scales of externally driven modes show the same dependence of the length scale on the detuning as those of the solitary lasers. This study confirms the predictions of [24, 96, 98] and constitutes the first quantitative investigation of the length scales of self-excited tilted waves in plano-planar laser cavities.

For the study of the polarization properties of the highly divergent transverse patterns spatially resolved Stokes parameters were calculated for near-field and far-field distributions. These allow a determination of the polarization distribution with high spatial resolution, so that it was possible to identify even small spatial variations in the polarization distribution of individual Fourier modes. This type of analysis was applied to the study of laser emission for the first time to our knowledge.

The patterns observed in the emission of the VCSELs can be categorized into three regions, corresponding to areas in the wave vector plane. Each region is characterized by distinct pattern geometries and polarization distributions.

Region I contains the patterns with transverse wave numbers close to zero, characterized by far-field distributions consisting of continuous rings or small areas of emission centered around the optical axis. The corresponding near-field images show irregular long-wavelength patterns. In VCSELs with a square aperture localized intensity peaks near the corners of the aperture were also observed. The polarization of these patterns was found to be homogeneous and either approximately vertical or horizontal.

The patterns attributed to region II are different for square and circular VCSELs. In the square lasers region II contains patterns formed by superpositions of only a few Fourier modes, mostly represented by a far-field distribution consisting of four dominant peaks located at (k_x, k_y) , $(-k_x, k_y)$, $(k_x, -k_y)$, and $(-k_x, -k_y)$, with either $k_x \gg k_y$ or vice versa. The corresponding near-field patterns show wavy stripe patterns, modulated with a short wavelength in one direction and with a longer wavelength in the orthogonal direction. When the absolute value of the detuning is increased an increase of the angle between the wave vectors of two adjacent Fourier components is observed. At some point a transition to region III takes place, where the Fourier components are always located at the diagonal. The polarization of region II modes is found to be approximately aligned with one of the boundaries. The boundary is selected by the “90°-rule” established by previous publications [18, 92], which state that the polarization is oriented orthogonal to the wave vector. It was found that this rule is strictly only valid for modes with Fourier components aligned to one of the axes in the wave vector plane.

The circular lasers show modes consisting of azimuthally modulated rings in both near-field and far-field distribution. The radius of the rings in the far-field images changes when the laser is thermally tuned. The corresponding ring in the near-field images is located just inside the boundary of the circular aperture, the number of azimuthal modulations changes according to the wave number of the far-field ring. The shape of the modes is a result of the current crowding along the circular boundary of the laser, which serves as a gain-guide for the waves travelling along the ring. The polarization was found to be always orthogonal to the wave vector in the far-field distribution, representing an approximately ideal realization of the “90°-rule”. Accordingly the polarization in the near-field distribution is always parallel to the stripes along the ring.

In the emission of the square lasers a third region was observed consisting of modes with very large transverse wave numbers. These always consist of four groups of Fourier components located at the diagonals of the wave vector plane. In the near-field distribution a diamond-shaped scar of a classical closed periodic orbit was observed. These patterns were already reported in [26, 27]. In this work the description was expanded by a more in-depth study of the far-field and the polarization distribution. The latter was found to be very complex. In each group of Fourier components a rotation of the polarization direction by $n \times 180^\circ$ was found, where n is the number of Fourier components in the group.

The observed pattern shapes attributed to the three regions document a relationship found between previously only loosely connected phenomena published separately in the literature. An explanation of the underlying pattern selection mechanisms was reported in this work. In the following these mechanisms are summarized for each region.

The localized spots observed in region I in some lasers are confined in most cases to the corners of the aperture. Evidence for the influence of current crowding on the creation

of these spots was analyzed. It turned out that a combination of a weak local thermal lens and current crowding at the boundaries of the aperture is likely to be responsible for these localized spots. Spatially homogeneous emission, as predicted by theoretical works, is probably also inhibited by spatial inhomogeneities.

Most of the characteristics regarding the shape of the patterns with large transverse components of the wave vector can be explained by the mechanism of total internal reflection at the side boundaries: a tilted wave travelling inside the laser cavity undergoes total reflection as long as the transverse components of the wave vector are small. At a certain tilt angle the total reflection is lost and the losses of the wave increase drastically. The observed change of the position of Fourier components of highly divergent modes to the diagonals is explained by the resulting cut-off condition for lasers with square aperture.

The polarization selection mechanisms of the transverse patterns were explained in this work with help of numerical simulations carried out by I.V. Babushkin on the basis of his model. It shows that each of the three regions can also be defined with respect to the polarization characteristics.

The most important effect that has to be taken into account is the anisotropic reflection of the DBRs due to the properties of Fresnel reflection: s-waves, having a polarization orthogonal to the plane of incidence, experience a higher reflectivity than p-waves, having a polarization parallel to the plane of incidence. The result is that s-waves experience a higher net gain inside the cavity. For modes belonging to region I it was found that the influence of the anisotropic reflection at the DBRs is weak and the polarization selection is dominated by the material anisotropy. At some transverse wave number, determined by the magnitude of the Bragg-induced anisotropy, the polarization behavior changes to that of region II. The DBR-induced anisotropy is responsible for the “90°-rule” observed in the circular lasers.

In the square lasers an additional effect has to be taken into account to explain the observed polarization distribution: the linear coupling of the polarization upon reflection at the side boundary. Since the four Fourier components forming a transverse mode in region II can not all be s-waves simultaneously their polarization locks to one of the boundaries (i.e. the mode is either polarized horizontally or vertically). The “90°-rule” in this case only determines to which boundary the polarization is aligned. The linear coupling of the polarization also implies an incompatibility of the eigenstates of the waveguide and the DBRs. This results in the appearance of additional modes with the same wavelength but different wave number. These rescattered modes are also weakly visible in the experiment as ripples connecting the dominant Fourier components of a mode. Due to this effect no strict single wave number solutions are possible, which justifies the phenomenological approach in [26, 27] that the diamond-shaped billiard patterns are created by a superposition of selected Fourier components.

Another effect important only for the square VCSELs is the transition of the light through the top DBR when leaving the cavity. Since the reflection of the DBRs is higher for s-waves, their transmission is higher for p-waves. The result is a rotation of the polarization in direction parallel to the wave vector. This explains the deviations from horizontal and vertical orientation of the polarization for modes consisting of four Fourier components and why non-homogeneous polarization is observed within one transverse

mode.

As mentioned above modes belonging to region III are found at the diagonal of the wave vector plane. At this point a transition between the mainly horizontally and mainly vertically polarized areas forming region II has to take place. The result is that the polarization is degenerate at the diagonal. This is also implied by numerical calculations, since the two orthogonally polarized eigenstates, that are solutions of the 2×2 matrix, have equal growth rates at the diagonal. This explains the complex polarization scenario observed in the experiments. The degeneracy also serves as an explanation of the frequency locking of differently polarized diamond-shaped modes reported in [27, 95].

The experiments showed that also the amplified spontaneous emission below threshold is worth investigating. The increased transmissivity for p-waves results in a limited degree of linear polarization of this emission, though it would be expected to be unpolarized. The polarization orientation was found to be always parallel to the wave vector (“0°-rule”). The transition from this polarization selection below threshold to the polarization scenario detailed above was investigated and explained in form of a gradual change of the state of polarization on the plane spanned by the two Stokes parameters that describe the linear polarization. The experimental results were in good agreement with the numerical calculations. This shows that the model is generally valid for both the characteristics above and below laser threshold.

Measurements with temporal resolution of the order of tens of nanoseconds were analyzed and no change of the typical characteristics described above were found. Since at this time scales the temperature rise due to Joule heating has not yet set in, the state of the laser without the influence of thermal effects can be studied in this way. The results imply that the Joule heating is homogeneously distributed over the whole area of the laser aperture.

As a means to control the length scales, the pattern shapes, and the state of polarization the influence of (spatial) frequency-selective feedback was investigated. It was found that the length scales can easily be controlled by tuning the feedback frequency. The polarization of the emission followed the polarization of the feedback. An additional degree of control over the pattern shape was achieved by spatial-frequency-selective feedback, which included Fourier filters of different geometry in the feedback beam path. The filters were mainly designed to force the laser to emit transverse modes of perfect symmetry. This was only partially successful. It turned out that the VCSELs tend to operate on modes that are also observed in the emission of the solitary devices. An attempt to measure the gain curve from the thresholds of individual transverse modes showed that the losses of the different transverse modes are not drastically different and that the gain curve is apparently very flat.

Future work has to answer some of the details that could not be clarified in this thesis. The observed preference of approximately continuous rings in the far-field distribution of modes with small transverse wave numbers and the breaking of this symmetry to modes with four dominant Fourier peaks for intermediate transverse wave numbers is not fully understood. It might be related to the polarization phenomena discussed in this work. Broad-area VCSELs can also be used to study wave chaos [179]. For this subject it is of some interest if the billiard-type patterns described in [26] form an integrable system.

The shape of the nearest-neighbor frequency spacing distribution, obtained from optical spectra, is a good indicator for this. Recent studies [166] showed that square VCSELs yield a non-Poissonian distribution, which indicates that the system is not fully integrable and thus has some chaotic characteristics, despite the fact that the transverse laser boundaries are perfectly square.

A Polarization coupling for a reflection at the laser boundary

To support the claim that the polarization of a wave inside the laser cavity does not change upon reflection at the laser boundary an external laser beam was injected into a circular VCSEL with 200 μm diameter and the near-field emission was detected with a CCD camera. The setup used for this experiment is described in [110, 111]. It consists of the mounted VCSEL with a collimation lens, a tunable semiconductor laser for the injection and two CCD cameras for the detection of the near-field and far-field emission. The linearly polarized injection beam passes a half-wave plate and the collimation lens before entering the VCSEL. In the detection beam path another half-wave plate and a linear polarizer are inserted to enable the measurement of the spatially resolved Stokes parameters.

In fig. A.1 near-field (a) and far-field (b) images of the intensity and polarization distribution are shown. The injection current of the VCSEL is set below the laser threshold. The wavelength of the tunable laser is set near the longitudinal resonance of the VCSEL. The injection beam is imaged onto the VCSEL at an angle. The angle of incidence on the VCSEL and the position on the VCSEL aperture are selected so that the beam meets the VCSEL boundary at an angle of 45° . The near-field image shows the point where the injection beam enters the VCSEL on the bottom left. This point is very bright since a large portion of the intensity of the beam is reflected from the top DBR. The transverse path of the injected beam is indicated by the black arrows. Near the point where it is reflected at the transverse boundary diagonal stripes are visible, because incident and reflected beam interfere.

The path of the injection beam through the VCSEL cavity is visible because the longitudinal component of the wave vector is much larger than the transverse component and thus it is reflected back and forth along the longitudinal cavity and a portion of the intensity is coupled out of the top DBR at every reflection. Due to this the intensity of the beam is quickly decreasing after the reflection at the side boundary.

The far-field intensity image corresponds to the described scenario. The wave vectors are indicated by the black arrows which have the same orientation as those in the near-field image. The incident beam is visible on the right side, the reflected one at the top of the image.

The corresponding two images of the polarization distribution show a constant angle of polarization of 90° , i.e. the polarization is oriented vertically. This is the case because the injection beam is linearly polarized in vertical direction. Since the injection beam passes a half-wave plate before entering the VCSEL the polarization orientation inside the VCSEL can be changed.

This measurement shows that the reflection at the side boundary does not change the

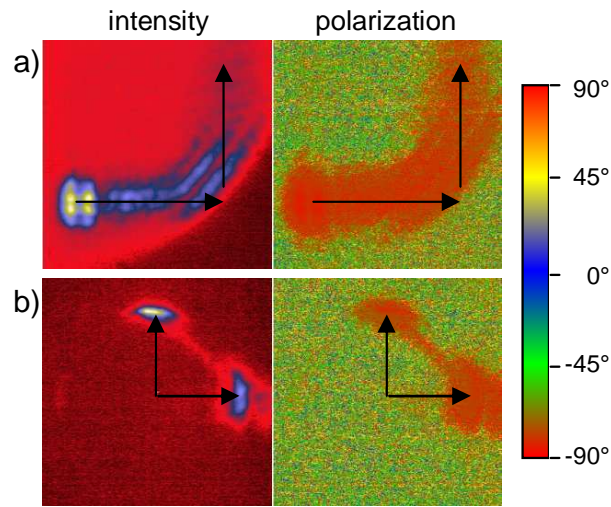


Figure A.1: Near-field (a) and far-field (b) images of the circular VCSEL with 200 μm diameter. Left column: intensity (S_0), right column: polarization distribution. Only a part of the aperture is shown in the near-field image, the boundary is visible as the circular arc at the lower right. The polarization images are color-coded using the palette shown on the right.

polarization of the injected beam. It was checked that this is not depending on the polarization orientation of the injection beam incident on the VCSEL. This observation is used in section 5.3.5 to explain the polarization selection mechanisms in the square VCSELs.

B Device structures

In several parts of the thesis parameters of the design structure of the VCSELs are needed. Firstly, the structure chart for the square devices provided by the group of K.F. Huang (National Chiao Tung University, Taiwan) together with the lasers is given in table B.2. Secondly, the chart for the circular lasers provided by ULM-Photonics is shown in table B.3. Both types of lasers mainly consist of $\text{Al}_x\text{Ga}_{1-x}\text{As}$ with different compositions x .

For each aluminum concentration x in the semiconductor material a refractive index can be obtained. The sources are discussed in 3.4.1. The values of the refractive index and the group index are given in table B.1 for all values of x that occur in the two structure charts. The respective wavelength is also given. Note that the layers in the chart of the square devices whose compositions are given as “graded” serve as a linear transition between the aluminum concentrations of the adjacent layers. For example the concentration of layer no. 4 in table B.2 is linearly changed from 0.9 to 0.3. The refractive index is then given for the average $x = 0.6$.

In many calculations throughout the thesis average values of the refractive indices of several layers are needed. To obtain the average index of such a group of layers the indices of each involved layer are weighted with their respective thickness.

Table B.1: Refractive indices of the different compositions of $\text{Al}_x\text{Ga}_{1-x}\text{As}$. The sources for these values are given in section 3.4.1.

composition	wavelength (nm)	refractive index	group index
0	780	3.911	2.953
0.11	780	3.636	4.896
0.3	780	3.461	4.481
0.36	780	3.42	4.188
0.48	780	3.33	4.103
0.6	780	3.262	3.908
0.625	780	3.242	3.893
0.9	780	3.094	3.477
0.95	780	3.048	3.76
0.97	780	3.025	3.95
0	980	3.525	4.051
0.5	980	3.251	3.528
0.99	980	2.973	3.176
1	980	2.967	3.17

Table B.2: Structure chart of the square VCSELs, which only consist of layers of $\text{Al}_x\text{Ga}_{1-x}\text{As}$ with different values of x . The layer number is given for reference. The number of repetitions indicates when layers are repeated in groups. The composition column gives the value of x in $\text{Al}_x\text{Ga}_{1-x}\text{As}$. “graded” refers to transition layers with a smooth variation of x (mostly between $x = 0.3$ and $x = 0.9$), which reduce the series resistance of the mirrors. A description is given for each group of layers. The thickness in micrometers corresponds to single layers, not accounting for the number of repetitions. The emission is directed upward.

layer no.	repetitions	composition	description	thickness (μm)
35	1	0		0.015
34	1	0.3		0.0414
33	1	graded	top DBR	0.02
32	1	0.9	layer 31	0.043
31	1	graded		0.02
30	27	0.3		0.037
29	27	graded	top DBR	0.02
28	27	0.9	layers 4 to 30	0.043
27	27	graded		0.02
26	1	0.3		0.037
25	1	graded		0.02
24	1	0.95	top DBR layer 3	0.0075
23	1	0.97	with oxide	0.03
22	1	0.95		0.0075
21	1	graded		0.02
20	1	0.3		0.037
19	1	graded	top DBR	0.02
18	1	0.9	layer 2	0.043
17	1	graded		0.02
16	1	0.3		0.037
15	1	graded	top DBR layer 1	0.02
14	1	0.9	with transition	0.053
13	1	graded		0.087
12	1	0.36		0.007
11	2	0.36	spacers and	0.008
10	3	0.11	quantum wells	0.008
9	1	0.36		0.007
8	1	graded		0.087
7	1	0.9	transition	0.053
6	1	graded		0.02
5	47	0.3		0.037
4	47	graded	bottom DBR	0.02
3	47	0.9	layers 1 to 47	0.043
2	47	graded		0.02
1	1	0	substrate	0.5

Table B.3: Structure chart of the circular VCSELs. The layer number is given for reference. The number of repetitions indicates when layers are repeated in groups. The composition column gives the value of x in $\text{Al}_x\text{Ga}_{1-x}\text{As}$. A description is given for each group of layers. The thickness in micrometers corresponds to single layers, not accounting for the number of repetitions. The emission is directed downward.

layer no.	repetitions	material	composition	description	thickness (μm)
15	1	GaAs	0		0.0695
14	33	AlAs	1	top DBR	0.0831
13	33	GaAs	0		0.0695
12	1	AlGaAs	0.5	spacer	0.135
11	1	AlAs/AIO	0.99	oxide	0.03
10	1	AlGaAs	0.5	spacer	0.135
9	1	GaAs	0	spacer	0.0485
8	2	GaAs	0	barrier	0.009
7	3	InGaAs	N/A	quantum well	0.008
6	1	GaAs	0	spacer	0.0485
5	1	AlGaAs	0.5	spacer	0.151
4	22	GaAs	0	bottom DBR	0.0695
3	22	AlAs	1		0.0831
2	1	GaAs	0	substrate	208
1	1	Si_3N_4	N/A	AR coating	0.13074

C Calculation of necessary device parameters

In this appendix several parameters of the VCSEL structure are derived from equations developed and described in [180]. The results are given in table C.1. The structural parameters necessary for the calculations can be found in the chart of the device structure in appendix B. The calculated parameters given in table C.1 are used in some of the discussion sections.

At first the DBRs (layers 2 to 5 in the chart, cf. appendix B) are considered. The length of one DBR double layer structure (including grading layers) is 120 nm, resulting in an optical length of 391.6 nm, with the average refractive index $\bar{n}_B = 3.26$. The design wavelength is then $\lambda_B = 783.2$ nm. Note that there is a slight deviation of the length of the two DBR layers from $\lambda_B/4$: one is too short, the other too long by about 1%. With $\Delta n = n_h - n_l$, where n_h is the higher, n_l the lower refractive index of the DBR double layer, and \bar{n}_{gr} the average group index, the width of the stop-band of the reflector is

$$\lambda_{stop} = \frac{2\lambda_B\Delta n}{\pi\bar{n}_{gr}}. \quad (\text{C.1})$$

The top DBR consists of $M_t = 31$ double layers, the bottom one of $M_b = 47$. Multiplying the length of the double layer stack by the number of layers yields a total mirror length of 3720 nm for the top and 5640 nm for the bottom DBR. A more precise approach uses

$$L_{t,b} = M_{t,b} \frac{\lambda_B}{4} \left(\frac{1}{n_l} + \frac{1}{n_h} \right), \quad (\text{C.2})$$

which yields the value of the total mirror lengths given in the table. With

$$R_{t,b} = \tanh \left(\frac{2\Delta n}{\lambda_B} L_{t,b} \right) \quad (\text{C.3})$$

the reflectivity of each DBR stack is obtained. Finally

$$l_{eff,t,b} = \frac{\sqrt{R}\lambda_B}{4\Delta n} \quad (\text{C.4})$$

yields the penetration depth of the incident field into the respective DBR.

Using the derived values several parameters of the cavity and the laser as a whole can be obtained. The effective length of the cavity is obtained with

$$L_{eff} = L_{cav} + l_{eff,t} + l_{eff,b}, \quad (\text{C.5})$$

Table C.1: Device parameters. Left table: l_B length of a DBR double layer, \bar{n}_B average refractive index of a DBR double layer, $\bar{n}_{gr,B}$ average group index, Δn index difference between high and low index material, λ_B resulting DBR wavelength, λ_{stop} width of DBR stop-band, \bar{R} reflection coefficient averaged over both DBRs, $M_{t,b}$ number of layers, $L_{t,b}$ overall length of DBR, $R_{t,b}$ reflection coefficient, $l_{eff,t,b}$ penetration depth. Right table: \bar{n}_{cav} average index of cavity, L_{QW} length of active quantum wells, L_{cav} length of cavity, L_{eff} effective cavity length including penetration depth into DBR, Γ_r relative confinement factor, τ_{eff} photon round trip time (with $2L_{eff}$ as path length), α_i intrinsic losses, τ_p photon lifetime, N_p number of cavity round trips during the lifetime of a photon, g_{th} threshold gain, \bar{n} averaged refractive index of the VCSEL structure, L_{all} overall length of laser structure (without substrate), F finesse, λ_M longitudinal mode spacing.

DBRs		cavity	
l_B	120 nm	\bar{n}_{cav}	3.37
\bar{n}_B	3.26	L_{QW}	24 nm
$\bar{n}_{gr,B}$	3.93	L_{cav}	228 nm
Δn	0.367	λ_{cav}	768.4 nm
λ_B	783.2 nm	L_{eff}	1294 nm
λ_{stop}	47 nm	Γ_r	1.9
\bar{R}	0.9981	τ_{eff}	3,4 fs
top DBR		α_i	20 1/cm
M_t	31	τ_p	3.75 ps
L_t	3715 nm	N_p	111
R_t	0.9962	g_{th}	805 1/cm
$l_{eff,t}$	532 nm	laser	
bottom DBR		\bar{n}	3.3
M_b	47	L_{all}	9588 nm
L_b	5633 nm	F	695
R_b	0.9999	$\Delta\lambda_m$	60 nm
$l_{eff,b}$	533 nm		

where L_{cav} is the cavity length. Note that the design wavelength of the cavity $\lambda_{cav} = L_{cav}\bar{n}_{cav}$ is much lower than both the DBR design wavelength and the wavelength of the laser emission.

The relative confinement factor, describing the overlap of the optical electric field with the active medium of the quantum wells is given by

$$\Gamma_r = 1 + \frac{\sin(2\pi\bar{n}L_{QW}/\lambda)}{2\pi\bar{n}L_{QW}/\lambda}. \quad (C.6)$$

The photon lifetime (taking into account intrinsic cavity losses, which are in general given as $\alpha_i = 20 \text{ cm}^{-1}$ [180]) is calculated from

$$\frac{1}{\tau_p} = \frac{c}{\bar{n}_{gr}} \left(\alpha_i - \frac{1}{L_{eff}} \ln \sqrt{R_t R_b} \right). \quad (C.7)$$

τ_p divided by the effective round trip time $\tau_{eff} = 2L_{eff}\bar{n}_{gr}/c$ (the time it takes a photon to cross the effective cavity length twice) yields the number of round trips N_p of a photon during its lifetime. The finesse of the cavity is then $F = 2\pi N_p$. The longitudinal mode spacing, i.e. the wavelength corresponding to the free spectral range of the laser resonator,

$$\Delta\lambda_m = \frac{\lambda^2}{2L_{eff}\bar{n}_{gr}} \quad (\text{C.8})$$

is around 60 nm (30 THz), which is larger than the width of the stop-band $\lambda_{stop} = 47$ nm (23 THz). This shows, why VCSELs always operate in a single longitudinal mode.

D Electronic circuit for pulsed excitation experiments

In section 5.1.2 the setup used for experiments on pulsed excitation is explained. In this appendix the electronic circuit used to feed the current pulses to the VCSEL is briefly described. The schematic is shown in fig. D.1. The current pulse generator is connected via a BNC jack to the open connectors at the top of the schematic. The VCSEL is connected at the indicated position, so that the conduction directions of laser and diode are opposite to each other. The diode protects the VCSEL from negative voltage by short-circuiting them. Parallel to a resistor of $47\ \Omega$ (resulting in a total load of approximately $50\ \Omega$) an oscilloscope can be connected to visualize the signal that reaches the VCSEL. The switch is used to short-circuit the VCSEL, i.e. to disconnect it from the current pulses and at the same time protect it from static discharge.

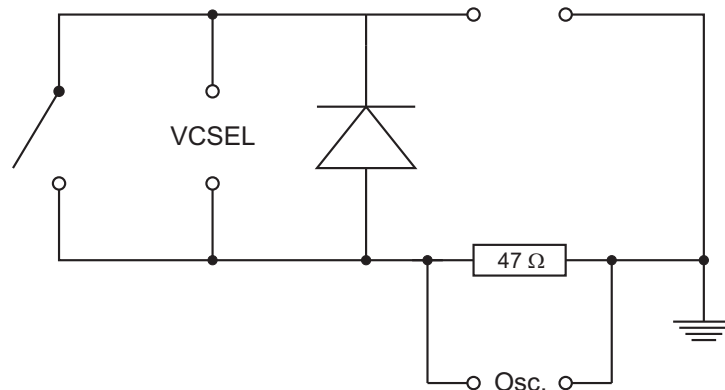


Figure D.1: Schematic of the electronic circuit used to feed the current pulses from the Hytek pulse generator to the VCSEL.

Bibliography

- [1] K. D. Choquette, R. P. Schneider Jr., K. L. Lear, and R. E. Leibenguth. *Gain dependent polarization properties of vertical-cavity lasers*. IEEE J. Sel. Top. Quantum Electron. **1**, 661–666 (1995).
- [2] M. P. van Exter, A. K. J. van Doorn, and J. P. Woerdman. *Electro-optic effect and birefringence in semiconductor vertical-cavity lasers*. Phys. Rev. A **56**(1), 845–853 (1997).
- [3] M. C. Cross and P. C. Hohenberg. *Pattern formation outside of equilibrium*. Rev. Mod. Phys. **65**, 851–1112 (1993).
- [4] E. Ammelt, D. Schweng, and H. G. Purwins. *Spatio-temporal pattern formation in a lateral high-frequency glow discharge system*. Phys. Lett. A **179**, 348–354 (1993).
- [5] P. M. Wood and J. Ross. *A Quantitative Study of Chemical Waves in the Belousov-Zhabotinsky Reaction*. Journal of Chemical Physics **82**(4), 1924–1936 (1985).
- [6] P. B. Umbanhowar, F. Melo, and H. L. Swinney. *Localized excitations in a vertically vibrated granular layer*. Nature **382**, 793–796 (1996).
- [7] Shigeru Kondo and Rihito Asal. *A reaction-diffusion wave on the skin of the marine angelfish Pomacanthus*. Nature **376**, 765–768 (1995).
- [8] F. T. Arecchi, S. Boccaletti, and P. L. Ramazza. *Pattern formation and competition in nonlinear optics*. Phys. Rep. **318**, 1–83 (1999).
- [9] G. D’Alessandro and W. J. Firth. *Spontaneous hexagon formation in a nonlinear optical medium with feedback mirror*. Phys. Rev. Lett. **66**, 2597–2600 (1991).
- [10] P. Couillet, L. Gil, and F. Rocca. *Optical vortices*. Opt. Commun. **73**(5), 403–408 (1989).
- [11] V. B. Taranenko, K. Staliunas, and C. O. Weiss. *Pattern formation and localized structures in degenerate optical parametric mixing*. Phys. Rev. Lett. **81**, 2236–2239 (1998).
- [12] M. Pesch, E. Große Westhoff, T. Ackemann, and W. Lange. *Observation of a Discrete Family of Dissipative Solitons in a Nonlinear Optical System*. Phys. Rev. Lett. **95**, 143906 (2005).
- [13] T. Ackemann and W. Lange. *Optical pattern formation in alkali metal vapors: Mechanisms, phenomena and use*. Appl. Phys. B **72**, 21–34 (2001).

- [14] C. Denz, M. Schwab, and C. Weinau. *Transverse-pattern Formation in Photorefractive Optics*. Springer, Berlin, Heidelberg, New York (2003).
- [15] L. A. Lugiato, G. L. Tredicce, J. R. Oppo, L. M. Narducci, and M. A. Pernigo. *Instabilities and spatial complexity in a laser*. J. Opt. Soc. Am. B **7**, 1019–1033 (1990).
- [16] E. Louvergneaux, D. Hennequin, D. Dangoisse, and P. Glorieux. *Transverse mode competition in a CO₂ laser*. Phys. Rev. A **53**, 4435–4438 (1996).
- [17] K. Staliunas, G. Sleky, and C. O. Weiss. *Nonlinear pattern formation in active optical systems: shocks, domains of tilted waves, and cross-roll patterns*. Phys. Rev. Lett. **79**, 2658–2661 (1997).
- [18] S.P. Hegarty, G. Huyet, J. G. McInerney, and K. D. Choquette. *Pattern formation in the transverse section of a laser with a large Fresnel number*. Phys. Rev. Lett. **82**(7), 1434–1437 (1999).
- [19] Y. F. Chen and Y. P. Lan. *Transverse pattern formation of optical vortices in a microchip laser with a large Fresnel number*. Phys. Rev. A **65**, 013802 (2002).
- [20] E. Cabrera, S. Melle, O. G. Calderón, and J. M. Guerra. *Dynamic transition from modelike patterns to turbulentlike patterns in a broad-area Nd:YAG laser*. Opt. Lett. **31**(8), 1067–1069 (2006).
- [21] E. Cabrera, S. Melle, O. G. Caldeón, and J. M. Guerra. *Evolution of the correlation between orthogonal polarization patterns in broad-area lasers*. Phys. Rev. Lett. **97**, 233902 (2006).
- [22] J. Dong and K. Ueda. *Observation of repetitively nanosecond pulse-width transverse patterns in microchip self-Q-switched laser*. Phys. Rev. A **73**, 053824 (2006).
- [23] K. Otsuka, Y. Miyasaka, T. Narita, S. Chu, C. Lin, and J. Ko. *Composite Lattice Pattern Formation in a Wide-Aperture Thin-Slice Solid-State Laser with Imperfect Reflective Ends*. Phys. Rev. Lett. **97**, 213901 (2006).
- [24] P. K. Jakobsen, J. V. Moloney, A. C. Newell, and R. Indik. *Space-time dynamics of wide-gain-section lasers*. Phys. Rev. A **45**, 8129–8137 (1992).
- [25] J. Lega, P.K. Jakobsen, J.V. Moloney, and A.C. Newell. *Nonlinear transverse modes of large-aspect-ratio homogeneously broadened lasers: II. Pattern analysis near and beyond threshold*. Phys. Rev. A **49**, 4201–4212 (1994).
- [26] K. F. Huang, Y. F. Chen, H. C. Lai, and Y. P. Lan. *Observation of the wave function of a quantum billiard from the transverse patterns of vertical cavity surface emitting lasers*. Phys. Rev. Lett. **89**, 224102 (2002).
- [27] Y. F. Chen, K. F. Huang, and Y. P. Lan. *Localization of wave patterns on classical orbits in a square billiard*. Phys. Rev. E **66**, 046215 (2002).

- [28] T.H. Maiman. *Stimulated optical radiation in ruby*. Nature **187**(4736), 493–494 (1960).
- [29] R. N. Hall, G. E. Fenner, J. D. Kingsley, T. J. Soltys, and R. O. Carlson. *Coherent Light Emission From GaAs Junctions*. Phys. Rev. Lett. **9**(9), 366–369 (1962).
- [30] K. Iga. *Surface-emitting laser — its birth and generation of new optoelectronic fields*. IEEE J. Sel. Top. Quantum Electron. **6**(6), 1201–1215 (2000).
- [31] J. K. Guenter, R. A. Hawthorne, D. N. Granville, M. K. Hibbs-Brenner, and R. A. Morgan. *Reliability of proton-implanted VCSELs for data communications*. Proc. SPIE **2683**, 102–113 (1996).
- [32] Y. Hayashi, M. B. Panish, P. W. Foy, and S. Sumski. *Junction lasers which operate continuously at room temperature*. Appl. Phys. Lett. **17**(3), 109–111 (1970).
- [33] R. Dingle, W. Wiegmann, and C. H. Henry. *Quantum states of confined carriers in very thin $Al(x)Ga(1-x)As$ - $GaAs$ - $Al(x)Ga(1-x)As$ heterostructures*. Phys. Rev. Lett. **33**(14), 827–830 (1974).
- [34] Y. Nakano, Y. Luo, and K. Tada. *Facet reflection independent, single longitudinal mode oscillation in a $GaAlAs/GaAs$ distributed feedback laser equipped with a gain-coupling mechanism*. Appl. Phys. Lett. **55**(16), 1606–1608 (1989).
- [35] K. Utaka, K. Kobayashi, K. Kishino, and Y. Suematsu. *1.5-1.6 μm $GaInAsP/InP$ integrated twin-guide lasers with first-order distributed Bragg reflectors*. Electron. Lett. **16**(12), 455–456 (1980).
- [36] F.A. Kish, S.J. Caracci, N. Holonyak, J.M. Dallesasse, K.C. Hsieh, M.J. Ries, S. C. Smith, and R.D. Burnham. *Planar native-oxide index-guided $Al(x)Ga(1-x)As$ - $GaAs$ quantum-well heterostructure lasers*. Appl. Phys. Lett. **59**(14), 1755–1757 (1991).
- [37] K. Iga, F. Koyama, and S. Kinoshita. *Surface emitting semiconductor lasers*. IEEE J. Quantum Electron. **24**, 1845–1855 (1988).
- [38] H. Soda, K. Iga, C. Kitahara, and Y. Suematsu. *$GaInAsP/InP$ surface emitting injection lasers*. Jpn. J. Appl. Phys. **18**, 2329–2330 (1979).
- [39] D. I. Babic and S. W. Corzine. *Analytic expression for the reflection delay, penetration depth, and adsorptance of quarter-wave dielectric mirrors*. IEEE J. Quantum Electron. **28**(2), 514–524 (1992).
- [40] K. L. Lear, R. P. Schneider, K. D. Choquette, and S. Kilcoyne. *Index Guiding Dependent Effects in Implant and Oxide Confined Vertical-Cavity Lasers*. IEEE Photon. Technol. Lett. **8**(6), 740–742 (1996).
- [41] P. Zhou, J. Cheng, C. F. Schaus, S. Z. Sun, K. Zheng, E. Armour, C. Hains, W. Hsin, D. R. Myers, and G. A. Vawter. *Low series resistance high-efficiency $GaAs/AlGaAs$ vertical-cavity surface-emitting lasers with continuously graded mirrors grown by MOCVD*. IEEE Photon. Technol. Lett. **3**(7), 591–593 (1991).

- [42] Hoi-Jun Yoo, J. R. Hayes, N. Andreadakis, E. G. Paek, G. K. Chang, J. P. Harbison, L. T. Florez, and Young-Se Kwon. *Low series resistance vertical-cavity front-surface-emitting laser diode*. Appl. Phys. Lett. **56**(20) (1990).
- [43] M. Grabherr, M. Miller, R. Jäger, R. Michalzik, U. Martin, H. J. Unold, and K. J. Ebeling. *High-Power VCSEL's: Single Devices and Densely Packed 2-D-Arrays*. IEEE J. Selected Topics Quantum Electron. **5**(3), 495–502 (1999).
- [44] R. A. Morgan, K. Kojima, T. Mullally, G. D. Guth, M. W. Focht, R. E. Leibenguth, and M. T. Asom. *High power coherently coupled 8×8 vertical cavity surface emitting laser array*. Appl. Phys. Lett. **61**, 1160–1162 (1992).
- [45] M. V. R. Murty, L. M. F. Chirovsky, S. Y. Hu, D. Venables, M. Cheng, and C. M. Ciesla. *Performance and reliability of 12.5-Gb/s oxide-free 850-nm mesa VCSELs*. IEEE J. Quantum Electron. **44**(3), 226–231 (2008).
- [46] C. Affolderbach, A. Nagel, S. Knappe, C. Jung, D. Wiedenmann, and R. Wynands. *Nonlinear spectroscopy with a vertical-cavity surface-emitting laser (VCSEL)*. Appl. Phys. B **70**, 407–413 (1999).
- [47] G. Hasnain, K. Tai, L. Yang, Y. H. Wang, R.J. Fischer, J. D. Wynn, B. Weir, N. K. Dutta, and A. Y. Cho. *Performance of Gain-Guided Surface Emitting Lasers with Semiconductor Distributed Bragg Reflectors*. IEEE J. Quantum Electron. **27**(6), 1377–1385 (1991).
- [48] W. W. Chow, K. D. Choquette, M. H. Crawford, K. L. Lear, and G. R. Hadley. *Design, fabrication, and performance of infrared and visible vertical-cavity surface-emitting lasers*. IEEE J. Quantum Electron. **33**, 1810–1824 (1997).
- [49] K. L. Lear and R. P. Schneider. *Uniparabolic mirror grading for vertical cavity surface emitting lasers*. Appl. Phys. Lett. **68**(5), 605–607 (1996).
- [50] J. J. Jewell, J. P. Harbison, A. Scherer, Y. H. Lee, and L. T. Florez. *Vertical-cavity surface-emitting lasers: design, growth, fabrication, characterization*. IEEE J. Quantum Electron. **27**, 1332–1346 (1991).
- [51] J.M. Dallesasse, N. Holonyak, A.R. Sugg, T.A. Richard, and N. El-Zein. *Hydrolyzation oxidation of $Al(x)Ga(1-x)As-AlAs-GaAs$ quantum well heterostructures and superlattices*. Appl. Phys. Lett. **57**, 2844–2846 (1990).
- [52] D. Wiedenmann, R. King, C. Jung, R. Jäger, R. Michalzik, P. Schnitzer, M. Kicherer, and K. J. Ebeling. *Design and analysis of single-mode oxidized VCSEL's for high-speed optical interconncts*. IEEE J. Selec. Top. Quantum Electron. **5**(3), 503–511 (1999).
- [53] M. Grabherr, R. Jäger, M. Miller, C. Thalmaier, J. Herlein, and K. J. Ebeling. *Bottom-emitting VCSELs for high-CW optical output power*. IEEE Photon. Technol. Lett. **10**, 1061–1063 (1998).

- [54] M. Miller, M. Grabherr, R. King, R. Jäger, R. Michalzik, and K. J. Ebeling. *Improved performance of high-power VCSELs*. IEEE J. Selec. Top. Quantum Electron. **7**(2), 210–216 (2001).
- [55] S. Barland, J. R. Tredicce, M. Brambilla, L. A. Lugiato, S. Balle, M. Giudici, T. Maggipinto, L. Spinelli, G. Tissoni, T. Knödel, M. Miller, and R. Jäger. *Cavity solitons as pixels in semiconductors*. Nature **419**, 699–702 (2002).
- [56] A. E. Siegman. *Lasers*. University Science Books, Mill Valley, California (1986).
- [57] A. K. van Doorn, M. P. van Exter, and J. P. Woerdman. *Elasto-optic anisotropy and polarization orientation of vertical-cavity surface-emitting semiconductor lasers*. Appl. Phys. Lett. **69**, 1041–1043 (1996).
- [58] A. K. van Doorn, M. P. van Exter, and J. P. Woerdman. *Strain-induced birefringence in vertical-cavity semiconductor lasers*. IEEE J. Quantum Electron. **34**, 700–706 (1998).
- [59] M. Sondermann, M. Weinkath, and T. Ackemann. *Polarization Switching to the Gain Disfavored Mode in Vertical-cavity Surface-emitting Lasers*. IEEE J. Quantum Electron. **40**, 97–104 (2004).
- [60] M. P. van Exter, M. B. Willemsen, and J. P. Woerdman. *Polarization fluctuations in vertical-cavity semiconductor lasers*. Phys. Rev. A **58**, 4191–4205 (1998).
- [61] M. Sondermann, H. Bohnet, and T. Ackemann. *Low Frequency Fluctuations and Polarization Dynamics in Vertical-cavity Surface-emitting Lasers with Isotropic Feedback*. Phys. Rev. A **67**, 021802 (2003).
- [62] M. Sondermann, M. Weinkath, T. Ackemann, J. Mulet, and S. Balle. *Two-frequency emission and polarization dynamics at lasing threshold in vertical-cavity surface-emitting lasers*. Phys. Rev. A **68**, 033822 (2003).
- [63] A. V. Naumenko, N. A. Loiko, M. Sondermann, K. F. Jentsch, and T. Ackemann. *Abrupt turn-on and hysteresis in a VCSEL with frequency-selective optical feedback*. Opt. Commun. **259**(2), 823–833 (2005).
- [64] K. Panajotov, B. Ryvkin, J. Danckaert, M. Peeters, H. Thienpont, and I. Veretenicoff. *Polarization switching in VCSEL's due to thermal lensing*. IEEE Photon. Technol. Lett. **10**, 6–8 (1998).
- [65] T. Ackemann and M. Sondermann. *Characteristics of polarization switching from the low to the high frequency mode in vertical-cavity surface-emitting lasers*. Appl. Phys. Lett. **78**, 3574–3576 (2001).
- [66] M. Sondermann, T. Ackemann, J. Mulet, S. Balle, and K. Panajotov. *Experimental and theoretical investigations on elliptically polarised dynamical transition states in polarisation switching of vertical-cavity surface-emitting lasers*. Opt. Commun. **235**, 421–434 (2004).

- [67] J. Paul, C. Masoller, Y. Hong, P. S. Spencer, and K. A. Shore. *Experimental study of polarization switching of vertical-cavity surface-emitting lasers as a dynamical bifurcation*. Opt. Express **31**(6), 748–750 (2006).
- [68] J. Martín-Regalado, F. Prati, M. San Miguel, and N. B. Abraham. *Polarization properties of vertical-cavity surface-emitting lasers*. IEEE J. Quantum Electron. **33**, 765–783 (1997).
- [69] Z. G. Pan, Shijun Jiang, M. Dagenais, R. A. Morgan, Keisuke Kojima, M. T. Asom, R. E. Leibenguth, G. D. Guth, and M. W. Focht. *Optical injection induced polarization bistability in vertical-cavity surface-emitting lasers*. Appl. Phys. Lett. **63**, 2999–3001 (1993).
- [70] W. W. Chow. *Nonequilibrium and many-body Coulomb effects in the relaxation oscillation of a semiconductor laser*. Opt. Lett. **20**, 2318–2320 (1995).
- [71] M. P. van Exter, A. Al-Remawi, and J. P. Woerdman. *Polarization fluctuations demonstrate nonlinear anisotropy of a vertical-cavity semiconductor laser*. Phys. Rev. Lett. **80**, 4875–4878 (1998).
- [72] A. V. Naumenko, N. A. Loiko, M. Sondermann, and T. Ackemann. *Description and analysis of low frequency fluctuations in vertical-cavity surface-emitting lasers with isotropic optical feedback by a distant reflector*. Phys. Rev. A **68**, 033805 (2003).
- [73] M. S. Torre, C. Masoller, and P. Mandel. *Transverse and polarization effects in index-guided vertical-cavity surface-emitting lasers*. Phys. Rev. A **74**, 043808 (2006).
- [74] P. Besnard, M. L. Charès, G. M. Stéphan, and F. Robert. *Switching between polarized modes of a vertical-cavity surface-emitting laser by isotropic optical feedback*. J. Opt. Soc. Am. B **16**, 1059–1063 (1999).
- [75] L. Fratta, P. Debernardi, G. Bava, C. Degen, J. Kaiser, I. Fischer, and W. Elsässer. *Spatially inhomogeneously polarized transverse modes in vertical-cavity surface-emitting lasers*. Phys. Rev. A **64**, 031803 (2001).
- [76] S. Jiao, G. Yao, and L. V. Wang. *Depth-Resolved Two-Dimensional Stokes Vectors of Backscattered Light and Mueller Matrices of Biological Tissue Measured With Optical Coherence Tomography*. Appl. Opt. **39**(34), 6318–6324 (2000).
- [77] D. F. Elmore, B. W. Lites, S. Tomczyk, A. Skumanich, R. B. Dunn, J. A. Schuenke, K. V. Streander, T. W. Leach, C. W. Chambellan, H. K. Hull, and L. B. Lacey. *Advanced Stokes polarimeter: a new instrument for solar magnetic field research*. Proc. SPIE **1746**, 22–33 (1992).
- [78] J. T. Oh and S. W. Kim. *Polarization-sensitive optical coherence tomography for photoelasticity testing of glass/epoxy composites*. Opt. Express **11**(14), 1669–1676 (2003).

- [79] L. A. Lugiato, Wang Kaige, L. M. Narducci, G. L. Oppo, M. A. Pernigo, J. R. Tredicce, D. K. Bandy, and F. Prati. *Cooperative frequency locking and spatial structures in lasers*. J. Opt. Soc. Am. B **5**, 879–888 (1988).
- [80] J. Lega, J.V. Moloney, and A.C. Newell. *Universal Description of laser dynamics near threshold*. Physica D **83**, 478–498 (1995).
- [81] G. K. Harkness, W. J. Firth, J. B. Geddes, J. V. Moloney, and E. M. Wright. *Boundary effects in large-aspect-ratio lasers*. Phys. Rev. A **50**, 4310–4317 (1994).
- [82] P.K. Jakobsen, J. Lega, Q. Feng, M. Staley, J.V. Moloney, and A.C. Newell. *Nonlinear transverse modes of large-aspect-ratio homogeneously broadened lasers: I. Analysis and numerical simulation*. Phys. Rev. A **49**, 4189–4200 (1994).
- [83] G. L. Oppo, M. Brambilla, and L. A. Lugiato. *Formation and evolution of roll patterns in optical parametric amplifiers*. Phys. Rev. A **49**, 2028–2032 (1994).
- [84] W. J. Firth and A. J. Scroggie. *Spontaneous pattern formation in an absorptive system*. Europhys. Lett. **26**, 521–526 (1994).
- [85] A. V. Mamaev and M. Saffman. *Pattern formation in a linear photorefractive oscillator*. Opt. Commun. **128**, 281–286 (1996).
- [86] U. Bortolozzo, P. Villoresi, and P. L. Ramazza. *Experimental evidence for detuning induced pattern selection in nonlinear optics*. Phys. Rev. Lett. **87**(27), 274102 (2001).
- [87] A. Esteban-Martín, J. Garcia, E. Roldán, V. B. Taranenko, G. J. de Valcárcel, and C. O. Weiss. *Experimental approach to transverse wave-number selection in cavity nonlinear optics*. Phys. Rev. A **69**, 033816 (2004).
- [88] Hua Li, T. L. Lucas, J. G. McInerney, and R. A. Morgan. *Transverse modes and patterns of electrically pumped vertical-cavity surface-emitting semiconductor diodes*. Chaos, Solitons & Fractals **4**, 1619–1636 (1994).
- [89] H. Deng, Q. Deng, and D. G. Deppe. *Native-oxide laterally confined whispering-gallery mode laser with vertical emission*. Appl. Phys. Lett. **69**(21), 3120–3122 (1996).
- [90] D. L. Huffaker, H. Deng, Q. Deng, and D. G. Deppe. *Ring and stripe oxide-confined vertical-cavity surface-emitting lasers*. Appl. Phys. Lett. **69**, 3477–3479 (1994).
- [91] C. Degen, I. Fischer, and W. Elsässer. *Transverse modes in oxide confined VCSELs: Influence of pump profile, spatial hole burning, and thermal effects*. Opt. Express **5**, 38–47 (1999).
- [92] S.P. Hegarty, G. Huyet, P. Porta, J. G. McInerney, K. D. Choquette, K. M. Geib, and H. Q. Hou. *Transverse-mode structure and pattern formation in oxide-confined vertical-cavity surface-emitting lasers*. J. Opt. Soc. Am. B **16**(11), 2060–2071 (1999).

- [93] T. Ackemann, S. Barland, M. Cara, S. Balle, J. R. Tredicce, R. Jäger, P. M. Grabherr, M. Miller, and K. J. Ebeling. *Spatial mode structure of bottom-emitting broad-area vertical-cavity surface-emitting lasers*. J. Opt. B: Quantum Semiclass. Opt. **2**, 406–412 (2000).
- [94] T. Ackemann, S. Barland, J. R. Tredicce, M. Cara, S. Balle, R. Jäger, P. M. Grabherr, M. Miller, and K. J. Ebeling. *Spatial structure of broad-area vertical-cavity regenerative amplifiers*. Opt. Lett. **25**, 814–816 (2000).
- [95] Y. F. Chen, K. F. Huang, H. C. Lai, and Y. P. Lan. *Observation of vector vortex lattices in polarization states of an isotropic microcavity laser*. Phys. Rev. Lett. **90**, 053904 (2003).
- [96] N. A. Loiko and I. V. Babushkin. *Competition between spatial Fourier modes in a wide-aperture vertical-cavity surface-emitting semiconductor laser*. Quantum Electronics **31**(3), 221–226 (2001).
- [97] M. San Miguel, Q. Feng, and J. V. Moloney. *Light polarization dynamics in surface-emitting semiconductor lasers*. Phys. Rev. A **52**, 1728–1739 (1995).
- [98] N. A. Loiko and I. V. Babushkin. *Competition of orthogonally polarized transverse Fourier modes in a VCSEL*. J. Opt. B: Quantum Semiclass. Opt. **3**, S234–S243 (2001).
- [99] I. V. Babushkin, N. A. Loiko, and T. Ackemann. *Complexity of Polarized Spatial Patterns in Large Aperture VCSEL* (2007), arxiv.org:nlin/0702004v1.
- [100] I. V. Babushkin, N. A. Loiko, and T. Ackemann. *Eigenmodes and symmetry selection mechanisms in circular large-aperture vertical-cavity surface-emitting lasers*. Phys. Rev. E **69**, 066205–1–14 (2004).
- [101] R. A. Morgan, G. D. Guth, M. W. Focht, M. T. Asom, K. Kojima, L. E. Rogers, and S. E. Callis. *Transverse Mode Control of Vertical-Cavity Top-Surface-Emitting Lasers*. IEEE Photonics Technology Letters **4**, 374–377 (1993).
- [102] E. Miyai, K. Sakai, T. Okano, W. Kunishi, D. Ohnishi, and S. Noda. *Lasers producing tailored beams*. Nature **441**, 946 (2006).
- [103] J.M. Ostermann, P. Debernardi, C. Jalics, A. Kroner, M. Riedl, and R. Michalzik. *Surface gratings for polarization control of single- and multi-mode oxide-confined vertical-cavity surface-emitting lasers*. Opt. Commun. **246**(4-6), 511–519 (2005).
- [104] J. Gustavsson, A. Haglund, J. Vukusic, J. Bengtsson, P. Jedrasik, and A. Larsson. *Efficient and individually controllable mechanisms for mode and polarization selection in VCSELs, based on a common, localized, sub-wavelength surface grating*. Opt. Express **13**(17), 6626–6634 (2005).
- [105] M. Dabbicco, T. Maggipinto, and M. Brambilla. *Optical bistability and stationary patterns in photonic-crystal vertical-cavity surface-emitting lasers*. Appl. Phys. Lett. **86**, 021116 (2005).

- [106] M. Brambilla, L. A. Lugiato, F. Prati, L. Spinelli, and W. J. Firth. *Spatial soliton pixels in semiconductor devices*. Phys. Rev. Lett. **79**, 2042–2045 (1997).
- [107] L. Spinelli, G. Tissoni, M. Brambilla, F. Prati, and L. A. Lugiato. *Spatial solitons in semiconductor microcavities*. Phys. Rev. A **58**, 2542–2559 (1998).
- [108] X. Hachair, S. Barland, L. Furfaro, M. Giudici, S. Balle, J. Tredicce, M. Brambilla, T. Maggipinto, I. M. Perrini, G. Tissoni, and L. Lugiato. *Cavity solitons in broad-area vertical-cavity surface-emitting lasers below threshold*. Phys. Rev. A **69**, 043817 (2004).
- [109] Y. Tanguy, T. Ackemann, and R. Jäger. *Characteristics of bistable localized emission states in broad-area vertical-cavity surface-emitting lasers with frequency-selective feedback*. Phys. Rev. A **74**, 053824 (2006).
- [110] Y. Tanguy, T. Ackemann, W. J. Firth, and R. Jäger. *Realization of a semiconductor-based cavity soliton laser* (2007), arxiv.org:0709.2575v1.
- [111] Y. Tanguy, T. Ackemann, and R. Jäger. *Characteristics of switching dynamics in a semiconductor-based cavity-soliton laser*. Opt. Express **15**(25), 16773–16780 (2007).
- [112] S. Jiang, Z. Pan, M. Dagenais, R. A. Morgan, and K. Kojima. *Influence of external optical feedback on threshold and spectral characteristics of strong vertical-cavity surface-emitting lasers*. IEEE Photon. Technol. Lett. **6**, 34 (1994).
- [113] I. Fischer, G. H. M. van Tartwijk, A. M. Levine, W. Elsässer, E. Göbel, and D. Lenstra. *Fast pulsing and chaotic itinerancy with a drift in the coherence collapse of semiconductor lasers*. Phys. Rev. Lett. **76**, 220–223 (1996).
- [114] G. Vaschenko, M. Giudici, J. J. Rocca, C. S. Menoni, J. R. Tredicce, and S. Balle. *Temporal dynamics of semiconductor lasers with optical feedback*. Phys. Rev. Lett. **81**, 5536–5539 (1998).
- [115] G. Giacomelli, F. Marin, and M. Romanelli. *Multi-time-scale dynamics of a laser with polarized optical feedback*. Phys. Rev. A **67**, 053809 (2003).
- [116] S. Wolff, D. Messerschmidt, and H. Fouckhardt. *Fourier-optical selection of higher order transverse modes in broad area lasers*. Opt. Express **5**, 32–36 (1999).
- [117] J. Dellunde, A. Valle, and K. A. Shore. *Transverse-mode selection in external-cavity vertical-cavity surface-emitting laser diodes*. J. Opt. Soc. Am. B **13**(11), 2477–83 (1996).
- [118] F. Marino, S. Barland, and S. Balle. *Single-mode operation and transverse-mode control in VCSELs induced by frequency-selective feedback*. IEEE Photon. Technol. Lett. **15**(6), 789–791 (2003).
- [119] M. G. Littman. *Single-mode operation of grazing-incidence pulsed dye laser*. Opt. Lett. **3**(4), 138–140 (1978).

- [120] T. W. Hänsch. *Repetitively pulsed tunable dye laser for high resolution spectroscopy*. Appl. Opt. **11**(4), 895 (1972).
- [121] K. C. Harvey and C. J. Myatt. *External-cavity diode laser using a grazing-incidence diffraction grating*. Opt. Lett. **16**, 910–912 (1991).
- [122] D. Wandt, M. Laschek, A. Tünnermann, and H. Welling. *Continuously tunable external-cavity diode laser with a double-grating arrangement*. Opt. Lett. **22**(6), 390–392 (1997).
- [123] C. J. Hawthorn, K. P. Weber, and R. E. Scholten. *Littrow configuration tunable external cavity diode laser with fixed direction output beam*. Rev. Sci. Instrum. **72**(12), 4477–4479 (2001).
- [124] D. Wandt, M. Laschek, K. Przyklenk, A. Tünnermann, and H. Welling. *External cavity laser diode with 40 nm continuous tuning range around 825 nm*. Opt. Commun. **130**, 81–84 (1996).
- [125] Y. F. Chen, K. F. Huang, and Y. P. Lan. *Quantum manifestations of classical periodic orbits in a square billiard: Formation of vortex lattices*. Phys. Rev. E **66**, 066210 (2002).
- [126] R. S. Geels, S. W. Corzine, J. W. Scott, D. B. Young, and L. A. Coldren. *Low threshold planarized vertical-cavity surface-emitting lasers*. IEEE Photon. Technol. Lett. **2**, 234–236 (1990).
- [127] R. Michalzik, M. Grabherr, and K. J. Ebeling. *High-power VCSELs: Modeling and experimental characterization*. Proc. SPIE **3286**, 206–219 (1998).
- [128] C. Degen, I. Fischer, W. Elsässer, L. Fratta, P. Debernardi, G. Bava, M. Brunner, R. Hövel, M. Moser, and K. Gulden. *Transverse modes in thermally detuned oxide-confined vertical-cavity surface-emitting lasers*. Phys. Rev. A **63**, 23817 (2001).
- [129] J. Martín-Regalado, S. Balle, and M. San Miguel. *Polarization and transverse-mode dynamics of gain-guided vertical-cavity surface-emitting lasers*. Opt. Lett. **22**, 460–462 (1997).
- [130] H. Ströker. *Stabilisierung der Emissionsfrequenz und Reduzierung der Linienbreite von Halbleiterlasern durch Rückreflexion von einem Stufengitter in Littrow-Anordnung*. Diploma thesis, Westfälische Wilhelms-Universität Münster (1995).
- [131] K. F. Jentsch, M. Sondermann, and T. Ackemann. *Analysis and optimization of coupling to external cavities in feedback experiments with vertical-cavity surface-emitting lasers*. Opt. Commun. **281**(6), 1396–1400 (2007).
- [132] Guotong Du, J. Lin, J. K. Gamelin, B. Wu, J. J. Talghader, S. Wang, Y. J. Yang, T. G. Dziura, and S. C. Wang. *Ohmic heating and series resistance of a vertical-mircocavity surface-emitting laser*. Appl. Phys. Lett. **59**(3), 265–267 (1991).

- [133] E. Towe, R.F. Leheny, and A. Yang. *A Historical Perspective of the Development of the Vertical-Cavity Surface-Emitting Laser*. IEEE J. Selec. Top. Quantum Electron. **6**(6), 1458–1464 (2000).
- [134] L. A. Coldren and S. W. Corzine. *Diode Lasers and Photonic Integrated Circuits*. Wiley, New York (1995).
- [135] T. E. Sale. *Cavity and reflector design for vertical cavity surface emitting lasers*. IEE Proc.-Optoelectron. **142**(1) (1995).
- [136] S. Adachi. *GaAs, AlAs, and Al(x)Ga(1-x)As: Material parameters for use in research and device applications*. J. Appl. Phys. **58**(3), R1–R29 (1985).
- [137] E. F. Schubert. *Materials - Refractive index and extinction coefficients* (2004), <http://www.rpi.edu/~schubert/Educational-resources/Educational-resources.htm>.
- [138] U. Das and P. K. Bhattacharya. *Variation of refractive index in strained In(x)Ga(1-x)As-GaAs heterostructures*. J. Appl. Phys. **58**(1), 341–344 (1985).
- [139] ILX Lightwave. *The Differences Between Threshold Current Calculation methods* (2003).
- [140] W. W. Chow, S. W Koch, and M. Sargent III. *Semiconductor laser physics*. Springer, New York (1994).
- [141] K. L. Lear, K. D. Choquette, R. P. Schneider, S. P. Kilcoyne, and K. M. Geib. *Selectively oxidised vertical cavity surface emitting lasers with 50% power conversion efficiency*. Electron. Lett. **31**(3), 208–209 (1995).
- [142] J. S. Blakemore. *Semiconducting and other major properties of gallium arsenide*. J. Appl. Phys. **53**, R123–R182 (1982).
- [143] M. Bertolotti, V. Bogdanov, A. Ferrari, A. Jascow, N. Nazorova, A. Pikhtin, and L. Schirone. *Temperature dependence of the refractive index in semiconductors*. J. Opt. Soc. Am. B **7**(6), 918–922 (1990).
- [144] C. Tanguy. *Temperature dependence of the refractive index of direct band gap semiconductors near the absorption threshold: Application to GaAs*. J. Appl. Phys. **80**(8), 4626–4631 (1996).
- [145] Jang Pyo Kim and A. M. Sarangan. *Temperature-dependent Sellmeier equation for the refractive index of Al(x)Ga(1-x)As*. Opt. Lett. **32**(5), 536–538 (2007).
- [146] J. Talghader and J. S. Smith. *Thermal dependence of the refractive index of GaAs and AlAs measured using semiconductor multilayer optical cavities*. Appl. Phys. Lett. **66**(3), 335–337 (1995).
- [147] J. Talghader and J. S. Smith. *Erratum: Thermal dependence of the refractive index of GaAs and AlAs measured using semiconductor multilayer optical cavities [Appl. Phys. Lett. 66, 335 (1995)]*. Appl. Phys. Lett. **69**(17), 2608 (1996).

- [148] P.L. Gourley, S.K. Lyo, T. M. Brennan, B. E. Hammons, C. F. Schaus, and S. Sun. *Lasing Threshold in Quantum Well Surface-Emitting Lasers: Many-Body Effects and Temperature Dependence*. Appl. Phys. Lett. **55**(26), 2698–2700 (1989).
- [149] W. W. Chow, K. D. Choquette, and P.L. Gourley. *Effects of quantum well subband structure on the temperature stability of vertical-cavity semiconductor lasers*. Appl. Phys. Lett. **66**(24), 3266–3268 (1995).
- [150] B. Tell, K. F. Brown-Goebeler, R. E. Leibenguth, F. M. Baez, and Y. H. Lee. *Temperature dependence of GaAs-AlGaAs vertical cavity surface emitting lasers*. Appl. Phys. Lett. **60**, 683–685 (1992).
- [151] K. D. Choquette, W. W. Chow, M. H. Crawford, K. M. Geib, and R. P. Schneider. *Threshold investigation of oxide-confined vertical-cavity laser diodes*. Appl. Phys. Lett. **68**(26), 3689–3691 (1996).
- [152] W. Nakwaski. *Current spreading and series resistance of proton-implanted vertical-cavity top-surface-emitting lasers*. Appl. Phys. A **61**, 123–127 (1995).
- [153] M. Schulz-Ruhtenberg, I. V. Babushkin, N. A. Loiko, T. Ackemann, and K. F. Huang. *Transverse patterns and length-scale selection in vertical-cavity surface-emitting lasers with a large square aperture*. Appl. Phys. B **81**(7), 945–953 (2005).
- [154] M. Brunner, K. Gulden, R. Hövel, M. Moser, and M. Illegems. *Thermal lensing in small oxide confined vertical-cavity surface-emitting lasers*. Appl. Phys. Lett. **76**, 7–9 (2000).
- [155] A. Yariv. *Quantum Electronics*. Wiley, New York, 3rd edition (1989).
- [156] G. R. Hadley. *Effective index model for vertical-cavity surface-emitting lasers*. Opt. Lett. **20**, 1483–1485 (1995).
- [157] I. V. Babushkin. *Cut-off transverse wavevector in 3-dimensional resonator (internal report)* (2006).
- [158] Group of J.V. Moloney, Arizona Center For Mathematical Sciences. *Program for the calculation of the effective index of a VCSEL structure*.
- [159] T. Ackemann, W. Grosse-Nobis, and G. L. Lippi. *The Gouy phase shift, the average phase lag of Fourier components of Hermite-Gaussian modes and their application to resonance conditions in optical cavities*. Opt. Commun. **189**, 5–14 (2001).
- [160] Simin Feng and H. G. Winful. *Physical origin of the Gouy phase shift*. Opt. Lett. **26**(8), 485–487 (2001).
- [161] L. G. Gouy. *Sur une propriété nouvelle des ondes lumineuses*. C. R. Acad. Sci. Paris **110**, 1251 (1890).
- [162] T. Ackemann. *Internal communication based on a program from ULM Photonics* (2006).

- [163] Yu. A. Logvin, N. A. Loiko, S. I. Turovets, P. S. Spencer, and K. A. Shore. *Modeling transverse optical pattern dynamics of vertical-cavity surface-emitting lasers beyond the rate equation approximation*. Laser Physics **7**(6), 1160–1167 (1997).
- [164] N. A. Loiko and I. V. Babushkin. *Polarized patterns in broad-area VCSEL*. Proc. SPIE **4751**, 382–388 (2002).
- [165] I. V. Babushkin, N. A. Loiko, and T. Ackemann. *Secondary bifurcations and transverse standing wave patterns in anisotropic microcavity lasers close to the first laser threshold*. Phys. Rev. A **67**, 013813 (2003).
- [166] I. V. Babushkin, M. Schulz-Ruhtenberg, N. A. Loiko, K. F. Huang, and T. Ackemann. *Coupling of polarization and spatial degrees of freedom of highly divergent emission in broad-area square vertical-cavity surface-emitting lasers*. accepted for publication in Phys. Rev. Lett. (2008).
- [167] T. Rössler, R. A. Indik, G. K. Harkness, and J. V. Moloney. *Modeling the interplay of thermal effects and transverse mode behavior in native-oxide confined vertical-cavity surface-emitting lasers*. Phys. Rev. A **58**, 3279–3292 (1998).
- [168] A. K. van Doorn, M. P. van Exter, A. M. van der Lee, and J. P. Woerdman. *Coupled-mode description for the polarization state of a vertical-cavity semiconductor laser*. Phys. Rev. A **55**, 1473–1484 (1997).
- [169] M. Sondermann. *On polarization dynamics in vertical-cavity surface-emitting lasers: solitary devices and lasers with isotropic feedback*. Phd thesis, Westfälische-Wilhelms Universität Münster (2004).
- [170] J. Martín-Regalado, M. San Miguel, N. B. Abraham, and F. Prati. *Polarization state selection and switching in VCSELs*. Proc. SPIE **2693**, 213–220 (1996).
- [171] M. Born and E. Wolf. *Principles of Optics*. Pergamon, Oxford (1980).
- [172] M. Schulz-Ruhtenberg, I. V. Babushkin, N. A. Loiko, and T. Ackemann. *Polarization properties in the transition from below to above lasing threshold in broad-area vertical-cavity surface-emitting lasers*. Unpublished (2008).
- [173] S. K. Mandre, W. Elsässer, I. Fischer, M. Peeters, and G. Verschaffelt. *Determining the temporally and radially resolved temperature distribution inside a pulsed broad-area vertical-cavity surface-emitting laser cavity*. Appl. Phys. Lett. **89**, 151106 (2006).
- [174] R. Mehandru, G. Dang, S. Kim, F. Ren, W.S. Hobson, J. Lopata, S.J. Pearton, W. Chang, and H. Shen. *Finite difference analysis of thermal characteristics of CW operation 850 nm lateral current injection and implant-apertured VCSEL with ip-chip bond design*. Solid State Electronics **46**, 699–704 (2002).
- [175] M. Peeters, G. Verschaffelt, H. Thienpont, S. K. Mandre, I. Fischer, and M. Grabherr. *Spatial decoherence of pulsed broad-area vertical-cavity surface-emitting lasers*. Opt. Express **13**(23), 9337–9345 (2005).

-
- [176] I. V. Babushkin. *Program for the calculation of the reflectance of s- and p-waves at a distributed Bragg reflector* (2007).
- [177] K. F. Huang. *Personal communication* (2007).
- [178] M. Giudici, S. Balle, T. Ackemann, S. Barland, and J. R. Tredicce. *Polarization dynamics in vertical-cavity surface-emitting lasers with optical feedback: experiment and model*. *J. Opt. Soc. Am. B* **16**, 2114–2123 (1999).
- [179] T. Gensty, K. Becker, I. Fischer, W. Elsässer, C. Degen, P. Debernardi, and G. Bava. *Wave Chaos in Real-World Vertical-Cavity Surface-Emitting Lasers*. *Phys. Rev. Lett.* **94**, 233991 – 233904 (2005).
- [180] K. J. Ebeling. *Analysis of vertical cavity surface emitting laser diodes (VCSELs)*. In A. Miller, M. Ebrahimzadeh, and D. M. Finlayson, editors, *Semiconductor quantum optoelectronics: From quantum physics to smart devices*, pages 295–338. SUSSP Publications and Institute of Physics Publishing, Bristol (1999).

Acknowledgments

First of all, I would like to thank Dr. Thorsten Ackemann for the supervision of the scientific work leading to this thesis and the many fruitful discussions. I am very grateful to Prof. Wulfhard Lange for his support and the opportunity to work in his group.

The theoretical work presented in this work was done by Dr. Igor Babushkin and I want to thank him for this input and the helpful discussions about this subject over the years. For his help and the introduction into the scientific field during the first year I would like to thank Dr. Markus Sondermann.

Thanks to all my colleagues in the institute, who provided a very amicable atmosphere, especially Karl Jentsch, Dr. Matthias Pesch, Dr. Jens Schüttler, Dr. Florian Huneus from the group of Prof. Lange; and Dr. Petra Groß, Nicoletta Brauckmann, Niklas Andermahr, and Till Walbaum from the Optical Technologies group. A special thanks goes to Prof. Carsten Fallnich for providing office and lab space during the last year of my work. I would also like to thank the members of the workshops and secretaries of the institute for their help.

During the work for this thesis I had the opportunity to work with several scientists from international institutes. For their support and fruitful discussions I would like to thank Natalia Loiko (National Academy of Sciences, Belarus), Kai-Feng Huang (National Chiao Tung University, Taiwan), Xavier Hachair (Institute Non Linéaire de Nice, France), and Yann Tanguy (University of Strathclyde, Scotland).

For their financial support I would like to thank the “Deutsche Forschungsgemeinschaft”, the “Graduiertenkolleg Nichtlineare kontinuierliche Systeme und deren Untersuchung mit numerischen, qualitativen und experimentellen Methoden”, and the “Deutscher Akademischer Austauschdienst”.

For her support in all non-scientific things and her ability to motivate me during stressful times I am very grateful to my wife Insa. Thanks to my son Armin for providing distraction when it was needed, and also when it was not needed. Finally, I would like to thank my parents, my brother and sister, and my friends for all their support and friendship.

Curriculum vitae

Malte Schulz-Ruhtenberg

Geburtsdatum	03. Juli 1978
Geburtsort	Berlin
Staatsangehörigkeit	deutsch
Eltern	Dr. med. Conrad Schulz-Ruhtenberg Sabine Schulz-Ruhtenberg, geb. v. Mühlendahl

Schulausbildung

1984 bis 1988	Domschule Minden
1988 bis 1997	Bessel-Gymnasium Minden
11. Juni 1997	Allgemeine Hochschulreife

Wehrdienst

September 1997 bis Juni 1998	Wehrdienst in Ahlen
------------------------------	---------------------

Studium

1998 bis 2003	Studium der Physik an der Georg-August-Universität, Göttingen
16.10.2000	Diplomvorprüfung
März 2002 bis Juli 2003	Diplomarbeit am Laser-Laboratorium Göttingen zum Thema "Mikromaterialbearbeitung von optischen Materialien mit Excimer-Lasern"
11.07.2003	Diplomprüfung

Promotionsstudium

Dezember 2003	Beginn der Dissertation am Institut für Angewandte Physik unter der Betreuung von HDoz. Dr. T. Ackemann
---------------	---------------------------------------------------------------------------------------------------------

Berufstätigkeit

März 2002 bis Juli 2003	Studentische Hilfskraft am Laser-Laboratorium Göttingen
April 2004 bis Juli 2007	Wissenschaftliche Hilfskraft am Institut für Angewandte Physik, Universität Münster

